

Investigations on the variations in helium abundance in the solar wind

A thesis submitted in partial fulfilment of
the requirements for the degree of

Doctor of Philosophy

by

Yogesh

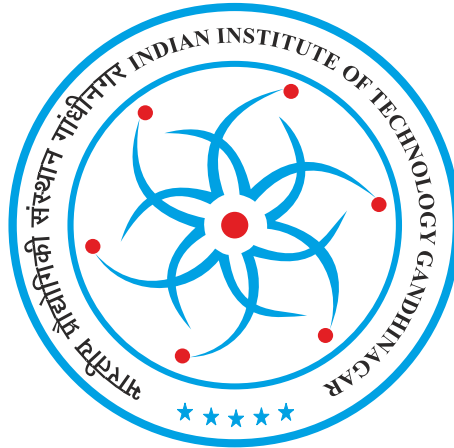
(Roll No. 18330028)

Under the guidance of

Prof. Dibyendu Chakrabarty

Space & Atmospheric Sciences Division

Physical Research Laboratory, Ahmedabad, India



Department of Physics

Indian Institute of Technology Gandhinagar

2023

Dedicated to
my family

Declaration

I declare that this written submission represents my ideas in my own words and where others' ideas or words have been included, I have adequately cited and referenced the original sources. I also declare that I have adhered to all principles of academic honesty and integrity and have not misrepresented or fabricated or falsified any idea/data/fact/source in my submission. I understand that any violation of the above can cause disciplinary action by the Institute and can also evoke penal action from the sources which have thus not been properly cited or from whom proper permission has not been taken when needed.

Yogesh

(Roll No: 18330028)

Certificate

I feel great pleasure in certifying that the thesis entitled “**Investigations on the variations in helium abundance in the solar wind**” by **Mr. Yogesh** has been carried out under my supervision and this work has not been submitted anywhere else for any degree or diploma.

Prof. Dibyendu Chakrabarty

(Thesis supervisor)

Physical Research Laboratory

Ahmedabad-380009, Gujarat, India

Acknowledgements

First and foremost, I express my heartfelt gratitude to my esteemed advisor, Prof. Dibyendu Chakrabarty, for his unwavering support throughout my Ph.D. research. I am deeply thankful for his patience, motivation, enthusiasm, and extensive knowledge, which have been instrumental in guiding me through the highs and lows of my doctoral journey. Prof. Chakrabarty's academic support has been invaluable, providing guidance at every stage of my research and thesis writing. I am truly indebted to him for his exceptional mentorship and guidance during my Ph.D. studies. His visionary outlook, dedication, and motivation have profoundly inspired me, and he has imparted not only valuable research methodologies but also emphasized the importance of presenting research findings clearly and effectively. I am forever appreciative of his significant contributions to my academic and professional development.

I am deeply grateful to the esteemed members of my Doctoral Studies Committee (DSC), Prof. Nandita Srivastava, Prof. Santosh Vadawale, and Dr. Sanjay K. Mishra, for their unwavering support, thought-provoking questions, and invaluable insights. Their guidance and constructive feedback have played an indispensable role in enriching my understanding of the subject matter. The engaging discussions and interactions with them have profoundly influenced my research journey. I extend my heartfelt thanks to Prof. Nandita Srivastava for her exceptional suggestions and continuous support throughout my research.

I extend my deepest appreciation for the invaluable scientific interactions I have had with esteemed individuals, namely Prof. Nat. Gopalswamy, Dr. Seiji Yashiro, Dr. Nicholeen M Viall, Dr. I.G. Richardson, Dr. S. Wallace, P. Makela, S. Akiyama, and H. Xie from GSFC NASA, Prof. Martin Laming from Naval Research Laboratory, and Dr. P. Mostafavi from Johns Hopkins University Applied Physics Laboratory. Your insightful feedback and valuable suggestions have made a significant impact on my research journey, and I am truly grateful for the privilege of benefiting from your expertise and guidance. I would also like to express my sincere gratitude to Prof. Kazuo Shiokawa, the SCOSTEP chairman, and late Prof. Patricia Doherty, the SCOSTEP scientific secretary, for selecting me in the SCOSTEP visiting scholar program. My heartfelt thanks go to Dr. Nat. Gopalswamy and his team for hosting me and for the fruitful discussions. Additionally, I am grateful to Dr. Seiji Yashiro for his dedicated efforts in coordinating all the necessary arrangements during my visit to the GSFC, NASA, USA.

I also thank the principal investigators of SWE, MFI on-board WIND; SWICS,

SWIMS, MAG on-board ACE; and SWEAP, FIELDS on-board PSP spacecraft for their commitment to open data.

I am deeply grateful to the Director, Dean, Registrar, Head academic services, and Academic Committee of PRL for their support and guidance throughout my research journey. Their steadfast commitment and assistance have been instrumental in ensuring the smooth progression of my research. I would also like to extend my heartfelt appreciation to all the esteemed faculties of PRL for their valuable insights and perspectives. The continuous support and provision of necessary facilities by the staff members of PRL's Computer center, Library, Administration, Accounts, Canteen, and CMG are deeply appreciated. Their dedication and efforts have played a crucial role in facilitating a conducive research environment. I am also grateful to the medical facility at PRL and to Dr. Samir Dani and Dr. Sheetal Patel for their availability and assistance whenever needed. Their care and support have been invaluable during my time at PRL. Additionally, I would like to express my thanks to the academic and administrative personnel of IITGn for their support and efficient handling of official formalities, which have greatly contributed to the smooth progress of my research endeavours.

I am thankful to my esteemed colleagues in the Space and Atmospheric Sciences division, including Prof. D. Pallamraju, Prof. S. Ramachandran, Prof. L. Sahu, Prof. S. Sharma, Dr. H. Gadhvi, Dr. A. Guharay, Dr. N. Ojha, Dr. R. P. Singh, Dr. T. A. Rajesh, Dr. K. Venkatesh, Mr. S. Venkataramani, Mr. A. Manke, Mr. M. Bhavsar, Mr. T. K. S. Kumar, Mr. Malaidevan, Dr. Tanzil, Dr. Subarna, Dr. Narayan, Sneha di, Pradip, Shashank, Pankaj, Vishnu, Chithra, Mohit, and Aniket. Their contributions and support have created an exceptional working environment for me.

I am indebted to my present and past fellow labmates and colleagues, Kuldeep, Sandeep, Suman, Aaditya, Rahul, Jacob, Abhishek, Anil, Ankit, Bijoy, Mitesh, and Sumanjit. Your presence in the lab has truly enhanced the vibrancy and enjoyment of our working environment. I deeply appreciate the time we have spent together, the valuable interactions, and the unforgettable moments we have shared, including the memorable parties.

I would like to extend my heartfelt thanks to my fellow batchmates, Sunil, Dayanand, Vikas, Deepak, and Arijit. The time spent with them has been truly unforgettable, and I am grateful for the bonds we have formed. I would also like to express my gratitude to Meghna, Monika, Naba, Ayushi, Supriya, Siddharth, Deepak Rai, Naval, Akanksha, Anju, Yash, Namita, Binal, Anupam, Sandeep, Pranav, Deva, Partha, and Sanjit for sharing wonderful moments with me. Your presence has made my journey all the more special, and I appreciate the memories

we have created together.

I would like to extend my heartfelt appreciation to my seniors Kuldeep, Suman, Subir, Ankit, Sovan and Deepak Kumar for their companionship during parties, trips, and late-night walks. Your presence and camaraderie have added countless joyful moments to my PhD experience. I am truly grateful for the encouragement and support I have received from a group of seniors, including Diptirana-jan, Deepak Karan, Deepak, Pravin, Ramanuj, Amit, Milan, Atif, Anshika, and Alka. Their motivation has played a significant role in my journey. Additionally, I would like to express my gratitude to my juniors, including Bijoy, Kshitiz, Gourav, Yogesh Kumar Maurya, Sourav, Bharti, Santanu, Rithvik, Mansi, Kam-ran, Dharmendra, Aakansha, Debashis, Gurucharan, Sandeep, Malika, Kiran, Harithasree, Shreya, Aakash, Sandip, Komal, and Nitin. The time spent together in the hostel has been truly unforgettable, filled with moments of playing table tennis, cricket, and celebrating festivals. These memories and the bonds we have formed will hold a special place in my heart.

I extend my heartfelt gratitude to my friends Kaushlendra, Punit, Praveen, Nagendra, Ajay, Pankaj, Sagar, Roshan, and Shubham for their unexpected visits, constant love, and unwavering support.

Last but not least, I would like to express my deepest gratitude to my parents, Mr. Jaipal Sharma and Mrs. Meera Devi, for their unwavering love, support, and countless sacrifices they have made to help me reach this milestone. I am forever indebted to them for their constant encouragement and belief in me. I also want to extend my love to my grandfather, late Sh. Khushi Ram Sharma, and my grandmother, Smt. Sara Devi, who have always been a source of inspiration and strength. To my beloved sisters, Ritu, Pooja, and Chanchal, and my brothers-in-laws, Mr. Rupesh Sharma and Mr. Kapil Sharma, I express my heartfelt gratitude for their love, support, and understanding in every situation. I would also like to convey my love and appreciation to my nephews and nieces, Bhumi, Daksh, Pihu, and Piyush, whose presence brings immense joy to my life. I am also grateful to all my paternal and maternal uncles, aunties, and my cousins, as well as my brothers and sisters, for their blessings, love, and continuous support.

Finally, I would like to express my gratitude to all the individuals who have supported me directly or indirectly in completing this research work.

Yogesh

Abstract

The abundance of doubly ionized helium ions (alpha particles) to singly ionized hydrogen ions (protons), expressed as $A_{He}=100 * n_{\alpha}/n_p$ (in percentage), varies significantly in different layers of the Sun. Further, the alpha-proton ratio in the solar wind has been shown to respond to solar cycle variation, to have dependence on solar wind velocity, and also seen to have been enhanced in the interplanetary coronal mass ejection (ICME) structures. In addition, this ratio has also been observed to vary in the Stream/Corotating Interaction Regions (SIRs/CIRs). Despite a number of studies in the past, the processes that lead to the variations in helium abundance in the background solar wind, in ICME and SIR/CIR structures are not well-understood. Another intriguing aspect is that the helium abundance changes at various time scales starting from 11-year time scale associated with solar cycle to the time scales corresponding to the passage of ICME or SIR/CIR structures at 1 AU. In terms of magnitude of change, it is often seen that while helium abundance changes to very high values (sometimes A_{He} exceeding 30%) in some ICMEs, it drops down to very low values (less than 0.05%) on some occasions. The present thesis work addresses the above issues (e.g. source processes, magnitude and time scale of changes) related to the A_{He} variations in the solar wind in a comprehensive and systematic manner.

One of the major outcomes of the thesis is to demonstrate that the A_{He} variations are distinctively different in solar cycle 24 compared to the previous three cycles. The frequency of $A_{He} = 2 - 3\%$ events is found to be significantly higher in slow/intermediate solar winds in solar cycle 24 as opposed to the dominance of the typical $A_{He} = 4 - 5\%$ events in the previous three cycles. Also, the changes in the delay between A_{He} and sunspot numbers variation are less sensitive to changes in solar wind velocity in cycle 24. The investigation suggests that the coronal large-scale magnetic field configuration started undergoing systematic changes from cycle 23. This result is also probably indicative of the variation in the sources of the solar wind starting from cycle 23. It is suggested that these changes affected the way helium got injected and processed in the solar atmosphere.

Earlier studies suggested that A_{He} is significantly enhanced (compared to

the background solar wind) in ICMEs on many occasions. Systematic correlation studies between A_{He} and other ICME signatures suggest that coronal temperature and the FIP effects are not the only factors that control the A_{He} enhancement in ICMEs. The timing and strength of solar flares connected with the CMEs play an essential role in A_{He} enhancement. While the solar flares closer to the launch of CME affects A_{He} through chromospheric evaporation, gravitational settling of helium determines how much helium is available that could be injected into the solar wind by the chromospheric evaporation process. Therefore, it is argued that time scales of these processes are important to determine whether A_{He} enhancement occurs in ICMEs or not.

A_{He} can get changed in the interplanetary medium as well. The interaction between different solar wind streams, i.e. SIRs/CIRs, can modify A_{He} . Higher modifications are observed in the fast wind regions of SIRs compared to the slow wind regions. The angle between bulk velocity vector and local magnetic field and differential velocity of protons and alphas are shown to have important roles in changing A_{He} inside SIRs. These changes of A_{He} variations in SIRs during maxima and minima of solar cycles 23 and 24 are also brought out.

In general, A_{He} variation in the background solar wind (slow and fast) is found to be 2-5%. Particularly, A_{He} is low in the slow solar wind. However, it is seen that there are occasions when it can go even below 1% in the solar wind. This very low A_{He} is found near the heliospheric current sheet. The possible reasons responsible for these very low A_{He} events are investigated.

Overall, this thesis work takes a comprehensive approach to understand the variations in A_{He} by shedding light on diverse processes that contribute to the changes in A_{He} .

Keywords: Solar wind, photosphere, chromosphere, transition region, corona, active regions, quiet streamers, coronal holes, solar abundances, First Ionisation Potential (FIP) effect, Coulomb drag, gravitational settling, solar cycle, Interplanetary Coronal Mass Ejections (ICMEs), flares, Stream/Co-rotating Interaction Regions (SIRs/CIRs).

List of Abbreviations and Acronyms

Abbreviation	Definition
ACE	Advance Composition Explorer
ADAPT	Air Force Data Assimilative Photospheric Flux Transport
AR	Active Regions
BAD	Bulk velocity Angle Distribution
CH	Coronal Holes
CIR	Co-rotating Interaction Region
CME	Coronal Mass Ejection
CRIS	Cosmic Ray Isotope Spectrometer
EPACT	Energetic Particles: Acceleration, Composition and Transport
EPAM	Electron, Proton, and Alpha-particle Monitor
EPI	Energetic particle Instruments
ESA	Electrostatic Analyzer
FC	Faraday Cup
FI	Flare Index
FIELDS	Electromagnetic Field Investigation
FIP	First Ionization Potential
FWR	Fast Wind Region
GCN	Gamma ray Coordinates Network
HCS	Heliospheric Current Sheets
HDR	High-Density Regions
HET	High Energy Telescope
HMRS	High Mass Resolution Spectrometer
ICME	Interplanetary Coronal Mass Ejection
IMF	Interplanetary Magnetic Field
IMP	Interplanetary Monitoring Platform
IP	Inter-Planetary

IS \odot IS	Integrated Science Investigation of the Sun
L1	first Lagrangian point of Sun Earth system
LET	Low Energy Telescope
MASS	High-resolution MASS spectrometer
MCPs	Micro Channel Plates
MFI	Magnetic Field Investigation
MHD	Magnetohydrodynamic
PAD	Pitch Angle Distribution
PFSS	Potential Source Field Surface
PSP	Parker Solar Probe
QS	Quiet Sun
R \odot	Radius of Sun
RTSW	Real-Time Solar Wind
SA	Sunspot Area
SC	Solar Cycle
SCS	Schatten Current Sheet
SEPICA	Solar Energetic Particle Ionic Charge Analyzer
SIR	Stream Interaction Region
SIS	Solar Isotope Spectrometer
SPA	Superposed Epoch Analysis
SPAN	Solar Probe Analyzer
SPC	Solar Probe Cups
SSN	Sunspot Number
SWE	Solar Wind Experiment
SWEAP	Solar Wind Electron Alpha and Protons
SWEPAM	Solar Wind Electron, Proton and Alpha Monitor
SWICS	Solar Wind Ion Composition Spectrometer
SWIM	Solar Wind Ions Mass Spectrometer
SWR	Slow Wind Region
TOF	Time of Flight
ULEIS	Ultra Low Energy Isotope Spectrometer

VDF	Velocity Distribution Functions
VEIS	Vector Electron and Ion Spectrometer
VSSW	Very Slow Solar Winds
WISPR	Wide-field Imager for Solar Probe
WSA	Wang-Sheeley-Arge

Contents

Acknowledgements	ix
Abstract	xiii
Abbreviations	xv
Contents	xix
List of Figures	xxiii
List of Tables	xxvii
1 Introduction	1
1.1 Solar Wind	1
1.2 Solar wind composition	4
1.2.1 Helium Abundance	5
1.2.2 Importance of Helium Abundance	6
1.3 Physical processes	10
1.3.1 First Ionization Potential (FIP) effect	14
1.3.2 Gravitational settling	18
1.3.3 Coulomb Drag	21
1.3.4 Wave-particle interaction	22
1.4 Large-scale solar processes causing helium abundance changes	25
1.4.1 Solar Flares	25
1.4.2 Coronal Mass Ejections	26
1.4.3 Stream Interaction Region/Corotating Interaction Region	28

1.5	Techniques to measure helium abundance	29
1.6	Aim and overview of the thesis	30
2	Techniques, Datasets and Models	33
2.1	Introduction	33
2.2	<i>Wind</i> Spacecraft	34
2.3	Solar wind Experiment (SWE)	35
2.3.1	Working Principle	36
2.4	<i>Wind</i> Magnetic Field Investigation (MFI)	39
2.5	<i>ACE</i> Spacecraft	42
2.6	Solar Wind Ion Composition Spectrometer (SWICS)	43
2.6.1	Principle of Operation	43
2.6.2	Deflection analyzer	44
2.6.3	Time-of-flight vs energy system	45
2.7	Solar Wind Ions Mass Spectrometer (SWIMS)	46
2.7.1	Principle of Operation	46
2.7.2	SWIMS Time-of-flight High Mass Resolution Spectrometer	48
2.8	Magnetic Field Experiment (MAG)	49
2.9	The Parker Solar Probe (PSP)	49
2.10	OMNI Database	51
2.11	ADAPT-WSA model	52
3	Helium abundance variation in solar wind	53
3.1	Introduction	54
3.2	Data Section	56
3.3	Results	56
3.3.1	Frequency of A_{He} events in the last four SCs	57
3.3.2	Frequency of A_{He} events higher than 10% in the last four SCs	60
3.3.3	Solar cycle variation of $A_{He} \leq 10\%$	60
3.3.4	Phase offset and correlation between A_{He} and SSN for the last four SCs	61

3.4	Discussion	65
3.5	Summary	69
4	Helium abundance variation in ICMEs	71
4.1	Introduction	72
4.2	Data and ICME selection	76
4.3	Role of background conditions	77
4.4	Relationship of A_{He} with different proxies	78
4.4.1	Relationship between A_{He} and the average charge states	79
4.4.2	Relationship between A_{He} and number density ratio of different charge states of a given element	80
4.4.3	Relationship between A_{He} and FIP elemental ratios	82
4.5	Chromospheric evaporation and Sludge effect	87
4.6	Summary and Conclusions	93
5	Helium abundance variation in SIRs	95
5.1	Introduction	96
5.2	Selection of SIR events and other datasets	99
5.3	Results and Discussion	100
5.3.1	Superposed Epoch Analysis (SPA) of the total events during solar maxima and minima	100
5.3.2	Superposed epoch Analysis of number densities of alphas and protons	102
5.3.3	Bulk velocity Angle Distribution(BAD)	104
5.3.4	Distribution of velocity difference between alphas and protons	109
5.3.5	Validity of magnetic mirror hypothesis	113
5.3.6	Uncertainties associated with alpha particle measurements	114
5.4	Discussion	114
5.5	Conclusion	117
6	Very Low Helium Abundances in solar wind	119
6.1	Introduction	120
6.2	Data Section and Model details	122

6.3	Results	123
6.3.1	In-situ measurements of Low helium abundance events	123
6.3.2	Sources of low A_{He} events	128
6.4	Discussion	132
6.5	Conclusions	136
7	Summary and Future works	139
7.1	Summary	139
7.2	Future works	140
	Bibliography	145
	List of Publications	169
	Publications Attached with Thesis	173

List of Figures

1.1	Solar wind speed as a function of helio-latitudes	3
1.2	A_{He} as a function of solar wind speed	8
1.3	Schematic of the various processes that control elemental abundances in corona and solar wind	12
1.4	Variation of plasma parameters, i.e. plasma beta (black), temperature (red) and hydrogen density (blue) in the solar atmosphere .	13
1.5	Schematic diagram for the FIP effect	15
1.6	Histogram of T_a/T_p	24
1.7	A schematic diagram of chromospheric evaporation	26
1.8	Three-part structure of the ICMEs	27
1.9	Interaction between the slow and fast wind	29
2.1	The cross-section of the Faraday Cup sensor	37
2.2	Schematic of Faraday cup	38
2.3	Ring core induction magnetometer.	40
2.4	Simple principle of operation of Fluxgate magnetometers.	41
2.5	Schematic of the measurement technique used in SWICS	44
2.6	Cross section of the SWICS sensor	45
2.7	SWICS time-of-flight system	46
2.8	Schematic of the SWIMS instrument	47
2.9	Schematic of the high mass resolution section of the SWIMS instrument.	48
3.1	Helium abundance variation in last fifty years	57
3.2	Frequency of distribution of A_{He}	58

3.3	Frequency of $A_{He} > 10\%$ events	59
3.4	Variation of $A_{He} \leq 10\%$	61
3.5	Sensitivity analysis - 1	62
3.6	Sensitivity analysis- 2	63
3.7	Delay and correlation between $A_{He} (\leq 10\%)$ and SSN	64
4.1	The variation of A_{He} and SSN for ICMEs only	78
4.2	Correlations between the average charge state of different elements with A_{He}	81
4.3	Correlations between the number density ratios of the different charge states of carbon and oxygen with A_{He}	82
4.4	Correlations between the FIP elemental ratios with A_{He}	84
4.5	Correlations of Mg/O, Si/O, Ne/O with Fe/O	86
4.6	Three classes of CMEs	90
5.1	Schematic of two high-speed streams and the associated variations in some of the plasma parameters at 1AU	98
5.2	The general properties of SIRs	101
5.3	The SPA of proton and alpha densities.	104
5.4	Probability Distribution of Bulk velocity Angles for Slow Wind Region	106
5.5	BADs of alpha particles are shown here in solar wind (proton) frame	107
5.6	The BAD for the FWR	108
5.7	The BAD for the FWR for equal events (60)	109
5.8	The BAD for the FWR in solar wind frame	110
5.9	The distribution of differential velocity for SWR	111
5.10	Same as Figure 5.9 but for FWR	112
6.1	The low helium abundance event observed by Wind spacecraft in December 2019	125
6.2	The low helium abundance event observed by PSP in January 2020	126
6.3	ADAPT-WSA model output for CR 2225 and CR 2226	129
6.4	ADAPT-WSA model output vs the satellite observation	130

LIST OF FIGURES

6.5	The Fe/O vs A_{He} density distributions	134
6.6	The Fe/O vs A_{He} density distributions	135

List of Tables

1.1	A few solar wind parameters and their ranges	2
1.2	Spatial scales and relevant processes which modify the solar wind composition and its kinetic Properties	11
3.1	Linear fit parameters between the phase offset and velocity for different A_{He} limits	65
4.1	ICME signatures	74
4.2	The collective results from the detailed correlation exercises of A_{He} with FIP elemental ratios, average charge states, and charge state ratios	85
4.3	List of ICMEs with other relevant details	88
4.4	The statistics of A_{He} enhancement events according to the associated flare class (in red). The column shows the percentage of enhancements of A_{He} for at least one hour for different	92
6.1	The low helium abundance events ($A_{He} < 1\%$) observed by WIND and PSP spacecrafts	127
6.2	The solar wind sources of the events shown in the table 6.1	131

Chapter 1

Introduction

1.1 Solar Wind

The Sun illuminates our world with light, but it also releases particles that are invisible to the naked eye. The Sun emits one million tons of singly ionized hydrogen per second as part of the solar wind. The solar wind is a flow of plasma streaming out supersonically from the Sun ([Parker, 1965](#)). This plasma primarily consists of electrons, protons, alpha particles and a tiny fraction of heavier ions with the kinetic energy of the wind lying between 0.2 to 10 keV. So to say, solar wind pervades the Inter-Planetary (IP) medium.

Solar wind varies in density, speed and temperature over time, solar latitude and longitude depending on the nature of the source regions. The solar wind particles can escape the Sun's gravity because of their high energy. This high energy results from the high coronal temperature or solar coronal heating. The solar wind starts from the solar corona and merges with the interstellar medium at the heliopause. Heliosphere is a region which is mainly affected by the activity of the Sun. The effects of solar rotation (27 days), activity cycle (11 years) and magnetic cycle (22 years) can be observed in the variations of solar wind across the heliosphere.

The general properties of the solar wind are captured by a few parameters measured at the first Lagrangian point (henceforth, L1 point) of the Sun-Earth system and shown in [Table 1.1](#).

Parameter	Range	Typical value	unit
Bulk speed (V)	300-800	400	Km/s
Thermal speed (w)	10-300	30	Km/s
Number density (n)	0.1-100	10	Protons/ cm^3
Magnetic field (B)	0.5-50	5	nT
Helium abundance (N_{He}/N_H)	0.5-30	5	In percentage

Table 1.1: A few solar wind parameters, their ranges of variations and the typical values along with the respective units are shown.

Solar wind achieves speeds of 250–750 km/s at a distance of a few solar radii from the Sun. Solar wind can be classified into two types - the slow solar wind and the fast solar wind. These two types of winds differ in speed and show different physical properties, e.g. temperature, composition etc. Additionally, the sources of slow and fast winds are also different. Observations around the L1 point show that the slow solar wind has a velocity of 300–500 km/s, a temperature of ~ 100 MK, and a composition nearly matching with corona. On the other hand, the fast-solar wind has a velocity of 750 km/s (600-900 km/s), a temperature of 800 MK, and its composition nearly matches the photosphere (Geiss et al., 1995). The density of slow solar wind is twice as high as fast wind and is more variable than the fast solar wind.

The sources of the slow solar wind are thought to be the streamer belt, quiet Sun, and active regions. However, there are still debates on the sources of the slow solar wind (Fisk, 2003). Figure 1.1, taken from McComas et al. (2003), shows that emission of the slow solar wind occurred at lower latitudes (up to 30° – 35°) during the solar minimum (low solar activity, 1992-1998). The distribution of slow wind expanded towards the poles during the period of higher activity (1998-2003). The sources of the fast solar wind are coronal holes (Zirker, 1977). Figure 1.1 also shows that fast solar wind mainly comes from coronal holes. The coronal holes are primarily characterized by the open field lines (Cranmer, 2009).

There are various ways to investigate the solar processes occurring closer to the solar surface and at different layers (e.g. photosphere, chromosphere, tran-

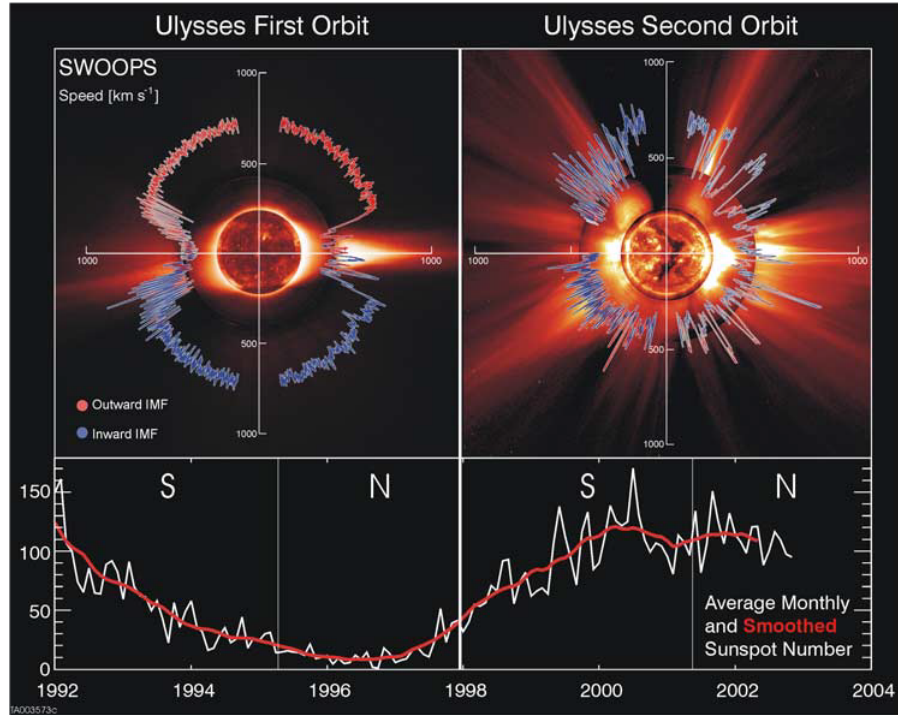


Figure 1.1: Solar wind speed as a function of helio-latitudes is shown. The two vertical panels are for *Ulysses*' first two orbits. Sunspot number (horizontal bottom panel) shows that the first and second orbits occurred during the solar cycle's declining and ascending phases. The observed velocity is plotted over solar images on a typical day during solar minimum (17 August, 1996) and that during solar maximum (07 December 2000). (Courtesy: [McComas et al., 2003](#))

sition region, and corona) of the Sun or in the IP medium. Researchers use a combination of remote sensing and in-situ measurements to investigate various solar processes. Remote sensing of the Sun involves the use of telescopes, spectrometers, coronagraphs, and other instruments to probe the Sun from a distance. On the other hand, in-situ measurements involve sending spacecraft/instruments to physically sample the solar wind. Remote sensing and in-situ measurements, when combined together, provide a comprehensive understanding of the Sun and its various processes.

In-situ measurements of solar wind provide crucial information about the composition, temperature, magnetic field, and dynamics of the solar wind as well as solar processes. In-situ measurements are primarily used in this thesis. On certain occasions, remote sensing observations are used to understand the possible

sources of solar wind near the Sun.

1.2 Solar wind composition

The solar photosphere primarily consists of hydrogen ($\sim 95\%$ in terms of abundance) and helium ($\sim 4\%$ in abundance) is the second most abundant element. The other heavier elements are much smaller in abundance ($< 1\%$). [Grevesse and Sauval \(1998\)](#) and [Asplund et al. \(2009\)](#) comprehensively discuss heavier elemental abundance measurements and observation methods. Spectroscopic observations show the presence of heavy ions and atomic nuclei: He, C, N, O, Ne, Mg, Si, S, and Fe in the corona ([Feldman et al., 1998](#)). In-situ measurements by the *ACE/Ulysses/Wind* satellites give details regarding the solar wind abundance ratio (He/O, Mg/O, Fe/O, Si/O, He/H etc.), total charge states (Q_{Fe} , Q_C , Q_O etc.) as well as charge state ratios (O^{7+}/O^{6+} , C^{5+}/C^{4+}). The in-situ compositions observed by *Ulysses* (e.g. [Geiss et al., 1995](#)) and *ACE* spacecraft (e.g. [Stakhiv et al., 2016](#)) are helpful in understanding the solar wind origin and acceleration.

Ion charge states and abundance ratios are important markers to understand solar wind formation. The charge states reveal the source of the solar wind and shed light on the physical processes occurring in the lower solar corona. Different types of solar wind originating from various sources show different ionization states, which have been extensively studied by researchers ([Neugebauer et al., 2016](#); [Cranmer et al., 2017](#); [Fu et al., 2017](#); [Zhao et al., 2017](#)). The ionization equilibrium of the coronal plasma at a specific height in the solar atmosphere allows the charge states to provide information about the local electron temperature. Near the Sun, the recombination and ionization time scales are less compared to the expansion time of the solar wind. As the solar wind travels outward, the recombination time scale increases because of the rapid decrease in the electron density ([Hundhausen et al., 1968](#)) with height. At a particular height, when the recombination time scale becomes larger than the expansion time scale of the plasma structure, the ionization states of a species get frozen. The temper-

ature at which the charge states get frozen is known as the freeze-in temperature. The height at which this happens is known as the freeze-in height. The freeze-in heights differ for different elements depending on the specific ionic state and the electron concentration at that height. The elevated total ion charge (e.g. Q_{Fe} , Q_{Si} etc.) states are also used to understand the Interplanetary Coronal Mass Ejections (ICMEs) characteristics (Gruesbeck et al., 2011, 2012). These aspects are again discussed and used in chapter 4.

The underlying cause(s) of abundance anomalies, such as the enhancement or reduction of certain elements in the solar corona, has (have) remained poorly understood despite their observations for the past 50 years (e.g., Pottasch, 1963). The study of abundances can provide clues regarding the solar coronal heating and the role of waves in the solar atmosphere.

1.2.1 Helium Abundance

In this thesis, the primary focus is on the helium abundance of solar wind. It is already stated that helium is the second most abundant element in the solar atmosphere. Despite that, the direct measurements of relative helium abundances in the solar atmosphere eluded the researchers because helium does not emit or absorb radiations in the photosphere (too cold) or corona (too hot). The only regions where helium radiates are the chromosphere, transition region, and prominences. Helium was first observed in the above-said regions during an eclipse in 1868 (Hirshberg, 1973). Except for spectroscopy, there are other methods for determining the helium abundance in the solar atmosphere that includes measurements of solar wind and cosmic rays from space, solar neutrino flux (that involves nuclear reactions and can be used to determine the core's helium abundance), and helioseismology to examine the photospheric abundance of helium (Hirshberg, 1973; Basu and Antia, 2004). The Coronal Helium Abundance Experiment (CHASE), conducted onboard Spacelab 2, provided the initial direct measurement of helium abundance near the Sun (Patchett et al., 1981). The obtained value of 7.9% at $1.15R_{\odot}$ (solar radii) was in agreement with the photospheric values. However, the accuracy of these measurements was compromised

by the elevated background stray light which was higher than anticipated.

Helium abundance is generally denoted by $A_{He} = (n_{He}/n_H) * 100$, where n_H is the number density of hydrogen and n_{He} is the helium number density. Please note that hydrogen, singly ionized hydrogen and proton are used interchangeably in the literature in the context of assessment of helium abundance. Similarly, helium, doubly ionized helium, and alpha particles are also used interchangeably. In the present thesis, we will also use the terms “alpha” (a, α) and “helium” (He) interchangeably to refer to doubly ionized helium ions and “hydrogen” (H) and “proton” (p) to refer to singly ionized hydrogen ions. The helium abundance is 8.5% in the photosphere (Grevesse and Sauval, 1998; Asplund et al., 2009) and 4 - 5% in the solar corona (Laming and Feldman, 2001, 2003; Mauas et al., 2005). Solar wind consists of 95% of protons and 2 - 5% alpha particles. A_{He} varies with solar wind velocity as well as solar cycle (Ogilvie and Hirshberg, 1974; Feldman et al., 1978; Aellig et al., 2001; Kasper et al., 2007, 2012; Alterman and Kasper, 2019). The above researchers used different satellite data to show the solar cycle variation of A_{He} in the solar wind. A_{He} gets enhanced and can exceed even 30% in some ICMEs (Hirshberg et al., 1972; Borrini et al., 1982; Fu et al., 2020). The primary goal of the thesis is to investigate how different sources as well as solar and interplanetary processes influence variations in helium abundance in the solar wind.

1.2.2 Importance of Helium Abundance

Helium constitutes 25% mass flux of the solar wind and plays an important role in the structure and dynamics of the solar wind, corona, and interior of the Sun. The simple models (mainly two fluids) of solar wind generation in solar corona predict that the flux and speed of protons should increase sharply with the increase in the temperature or heating rate of the solar corona. However, it is observed that the proton flux in the interplanetary medium is roughly constant and independent of solar wind speed (Feldman et al., 1978; Neugebauer, 1981). To resolve this problem, researchers used a multifluid model (Geiss et al., 1970; Bürgi, 1992; Hansteen et al., 1994, 1997) and not only found the constancy of the

solar wind hydrogen flux but also suggested that helium plays a regulatory role in the corona and is primarily responsible for the constant hydrogen flux in the solar wind.

[Kasper et al. \(2007\)](#), based on statistical analyses, brought out another important result that suggested that solar wind may cease to exist when helium abundance in solar wind approaches zero. The upper panel of [Figure 1.2](#) shows helium abundance variation with proton speed. The lower panel shows the frequencies of speed observed by the *Wind* spacecraft until the publication of [Kasper et al. \(2007\)](#). There is a 6-month periodicity because of the Earth's (and the *Wind's*) annual variation in heliographic latitude. This interval is shown in light grey, and the 6-month modulations are removed while deriving the linear relationship. The helium vanishing speed is calculated by extending the linear fit between the A_{He} and the solar wind velocity. The value of helium vanishing speed turns out to be 259 ± 12 km/s. The velocity distribution shown in the lower panel of [Figure 1.2](#) also indicates that the minimum speed observed by *Wind* spacecraft is also coming in the same interval. This matching between the lowest speed observed and helium vanishing speed suggests that helium probably plays a very important regulatory role in the solar wind flux.

The helium abundance reduces from the photosphere to the corona and can undergo further changes from the corona to the solar wind. Helium is less affected by the gravitational and pressure gradients in the corona compared to hydrogen due to the dominance of other processes acting on helium. Therefore, helium does not experience the classical Parker solar wind acceleration mechanism that accelerates coronal hydrogen to supersonic speeds ([Parker, 1958](#)). There are other processes which cause the acceleration of helium ions as well as variation in their abundance. These processes will be discussed in the next section. The fast and slow solar wind have different helium abundances. Therefore, it is not surprising that A_{He} changes across the stream interface when interaction between different solar wind parcels take place ([Durovcová et al., 2019](#)). Another important aspect is the enhancement of A_{He} in CME/ICME structures on many occasions ([Fu et al., 2020](#), and references therein). Therefore, helium abundance can be used

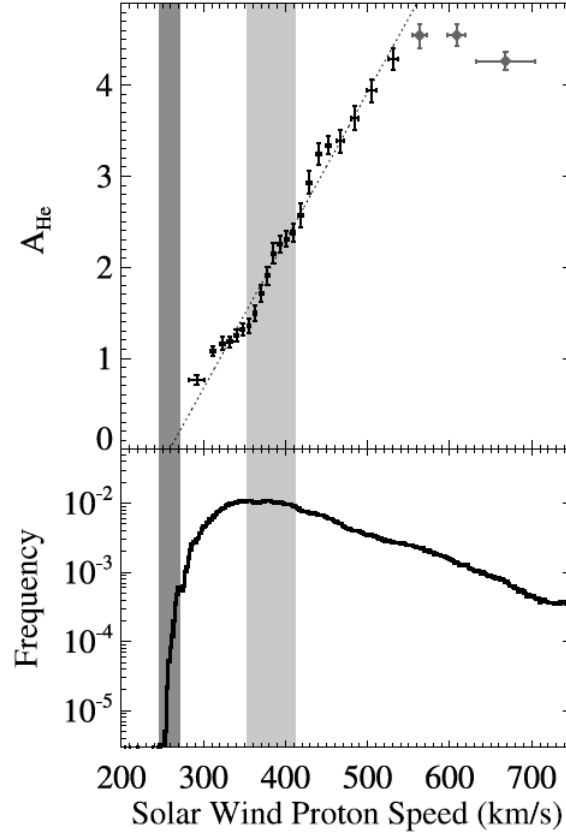


Figure 1.2: (Top Panel) A_{He} as a function of solar wind speed. The helium abundance, which shows heliospheric modulation, is highlighted with a light grey band in both panels. The dotted line is the best fit for the slow-speed component. This does not include the three highest speed points. This linear fit is extended to the velocity limit, where the A_{He} approaches to zero. The zero-helium speed or helium vanishing speed is 259 ± 12 km/s. This vanishing speed is indicated in both panels with a dark grey band. (Bottom Panel) The histogram for all solar wind speeds measured by the *Wind* spacecraft for full mission duration (until the publication of Kasper et al., 2007). The frequency of solar wind velocity observations drops by three orders within one sigma of the helium vanishing speed. (Courtesy: Kasper et al., 2007)

as a potential compositional proxy to mark the arrival of ICME at the L1 point. Not only that since A_{He} is different in slow and fast winds, variations in A_{He} can be used to understand the source regions of solar Wind (Kasper et al., 2007; Fu et al., 2018). Further, A_{He} variation can also be used to understand the wave-particle interaction in solar wind (Bochsler, 2000). In recent times, it has been shown (Kasper et al., 2019; Huang et al., 2023) that the properties of magnetic

switchbacks and their effect on the solar wind can also be studied using helium abundances.

The study of helium abundance in the solar wind began with the onset of the satellite era. Previous studies have primarily focused on investigating the variation of helium abundance within one or two solar cycles (Aellig et al., 2001; Kasper et al., 2007; Alterman and Kasper, 2019). However, when it comes to investigating the A_{He} variation across all the solar cycles when measurements are available and identifying the characteristic changes, if any, across the cycles remain unaddressed. Further, although helium abundance is considered to be an important signature for identifying ICMEs at the L1 point (Richardson and Cane, 2004, 2010), the physical processes that cause enrichment of helium in ICMEs remain poorly understood except a few studies wherein the role of gravitational settling (Hirshberg et al., 1970; Neugebauer and Goldstein, 1997), chromospheric evaporation (Fu et al., 2020) have been brought out in isolated manners. Although the roles of these processes have been indicated in these works, the interplay of many of these processes that determine the variability of helium abundance in ICME remain an enigma till date.

Similarly, there has been limited focus on the processes that determine the variation of helium abundance in Stream Interaction Regions (SIRs). Previous studies by Gosling et al. (1978) and Durovcová et al. (2019) have indicated changes in helium abundance near SIRs, with Durovcová et al. (2019) suggesting the potential role of pitch angle and differential velocity in altering helium abundance. However, it is not clear how these processes varied over the past solar cycles and during different activity phases of the Sun. Another outstanding problem is the very low (much lower than what is found in slow solar wind) helium abundance in the solar wind. These are intervals when A_{He} goes below 1% and these events stand at the opposite end of the large enhancement of helium abundance in ICMEs. Indirect evidences of these low A_{He} events can be found in studies such as Borrini et al. (1981); Suess et al. (2009); Sanchez-Diaz et al. (2016); Vasquez et al. (2017). However, comprehensive investigation addressing the identification of sources and processes responsible for low helium abundance

(A_{He}) is currently lacking. The thesis aims to address these identified gap areas mentioned above. To effectively fill these gaps, it is essential to have a comprehensive understanding of the fundamental processes that control helium abundance. These processes will be thoroughly discussed in the upcoming sections.

1.3 Physical processes

Table 1.2 shows the active processes operational at different heights in the solar atmosphere. The rightmost column of the table shows the solar wind properties that are mostly affected by each process. These are the major processes that control the solar atmospheric and wind composition.

Different processes control the solar wind acceleration and composition at three different transition layers in the solar atmosphere. The first transition happens at the lower chromosphere. At this height, the pressure changes its nature from being predominantly thermal to magnetically dominated. The sound speed and Alfvénic speeds are equal at this region. The wave mode conversion and other wave-wave interactions can also occur in this region. Solar wind acceleration due to Magnetohydrodynamic (MHD) waves derived from solar convection also takes place in this region. Beyond this region, the separation between ions and neutrals starts. The second transition layer appears higher up in the chromosphere, where the transition from neutral gas to ionized plasma occurs that ultimately forms the solar wind and corona. The transition causes a strong density gradient, resulting in waves' reflection and refraction. This reflection and refraction of Alfvén waves and interaction with this density gradient generate the ponderomotive force (Laming, 2012, 2015; Laming et al., 2019). The Alfvénic waves are magnetic in nature. Therefore, this force will only affect the charged particles, which is the primary reason behind the charge-neutral separation. This process gives rise to elemental fractionation in the Sun's upper atmosphere. This whole phenomenon of elemental fractionation driven by the effects of the ponderomotive forces on the ions is known as the first ionization potential (FIP) effect. The third transition layer is at higher distances where the solar wind plasma becomes

collisionless. This is the region where the solar plasma evolves from a dominantly fluid state to primarily kinetic state.

Distance From Solar Surface	Site	Process	Most Affected Solar Wind Property
$-0.3R_{\odot}$	boundary radiative/convective zone	gravitational settling/convective mixing	elemental and isotopic composition
$< 1R_{\odot}$	upper chromosphere lower transition region	ion-neutral separation	elemental composition
$1 - 3R_{\odot}$	inner corona	electronic collisions	ionic charge state
$1 - 10R_{\odot}$	upper transition region, corona	Coulomb collisions/gravitational stratification	He/H ratio, elemental and isotopic composition
$1 - 10,000R_{\odot}$	interplanetary medium	wave-particle interaction stream-stream interaction	bulk speed, ionic velocity distributions bulk speed, ionic velocity distributions

Table 1.2: Spatial scales and relevant processes which modify the solar wind composition and its kinetic Properties. (Courtesy: [Bochsler, 2000](#))

Returning to helium abundance, it changes from photosphere to corona to solar wind, and Parker’s solar wind model cannot explain it. The helium ions are, on many occasions, controlled, modulated, processed, and accelerated by processes that do not work the same way or in the same degree for hydrogen. For example, the helium ions are accelerated by coupling with accelerated hydrogen through Coulomb collisions ([Geiss et al., 1970](#); [Bürigi, 1992](#)). In addition, helium may undergo cyclotron resonance with cascading turbulent Alfvénic fluctuations in the corona. These fluctuations and variable intensities of Alfvénic waves can change the interplanetary A_{He} ([Bochsler, 2000](#)).

The primary process controlling the A_{He} in the solar wind can be seen in Figure 1.3. The First Ionization Potential (FIP) effect and gravitational settling are the dominant processes near the solar surface ($\leq 1.5R_{\odot}$). The modulation in particle abundances due to wave-particle interaction dominates at higher heights ($\geq 3 - 5R_{\odot}$). The coulomb collisions or drag control these abundances at the intermediate heights ($1.5R_{\odot} \leq \text{distance (R)} \leq 3 - 5R_{\odot}$).

To understand the variation of plasma parameters with the regions of dominance of the processes shown in Figure 1.3, a composite plot has been made with data from the published literature. Figure 1.4 represents the variation of different solar wind parameters, i.e. plasma beta (ratio of thermal pressure and magnetic

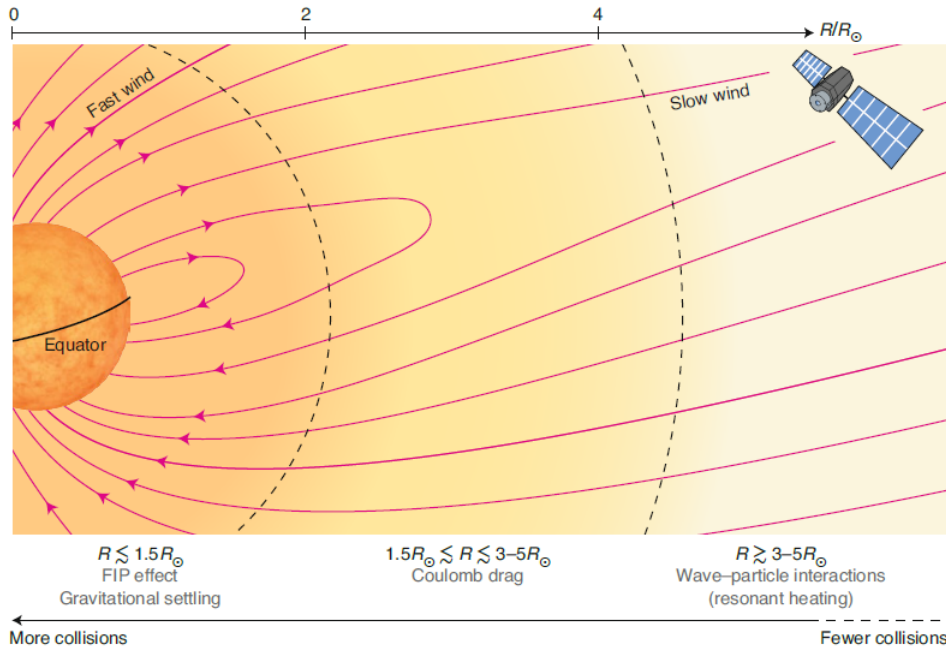


Figure 1.3: Schematic of the various processes that control elemental abundances in corona and solar wind. The density and proton–ion collision rates decrease, and flow speed increases as the distance increases. These changes cause the dominance of different processes. Near the solar surface, gravitational settling and the FIP effect are dominant. Coulomb drag becomes important at intermediate heights. Wave–particle interactions can preferentially modulate and accelerate the ions at higher heights (Courtesy: [Hahn, 2020](#); [Moses et al., 2020](#)).

pressure), temperature, and hydrogen density. The variations in plasma beta with height is taken from [Gary \(2001\)](#), while the height variations in temperature and hydrogen density are obtained from [Withbroe \(1981\)](#). The processes depicted in [Figure 1.3](#) play important roles in determining the composition of the solar wind. These processes exhibit different regions of dominance, approximately shown by violet lines and texts in [Figure 1.4](#). The charge states in the solar wind are generally fixed between 1–5 R_{\odot} ([Landi et al., 2012](#), and references therein). This region is shown by the green rectangular box. However, these freezing heights change to 4–10 R_{\odot} in CMEs ([Gruesbeck et al., 2011, 2012](#)).

It can be seen that major change in the solar wind parameters generally happens near the transition region, where the ionization of elements starts dominating the neutral particles. Its impact on composition will be discussed in the

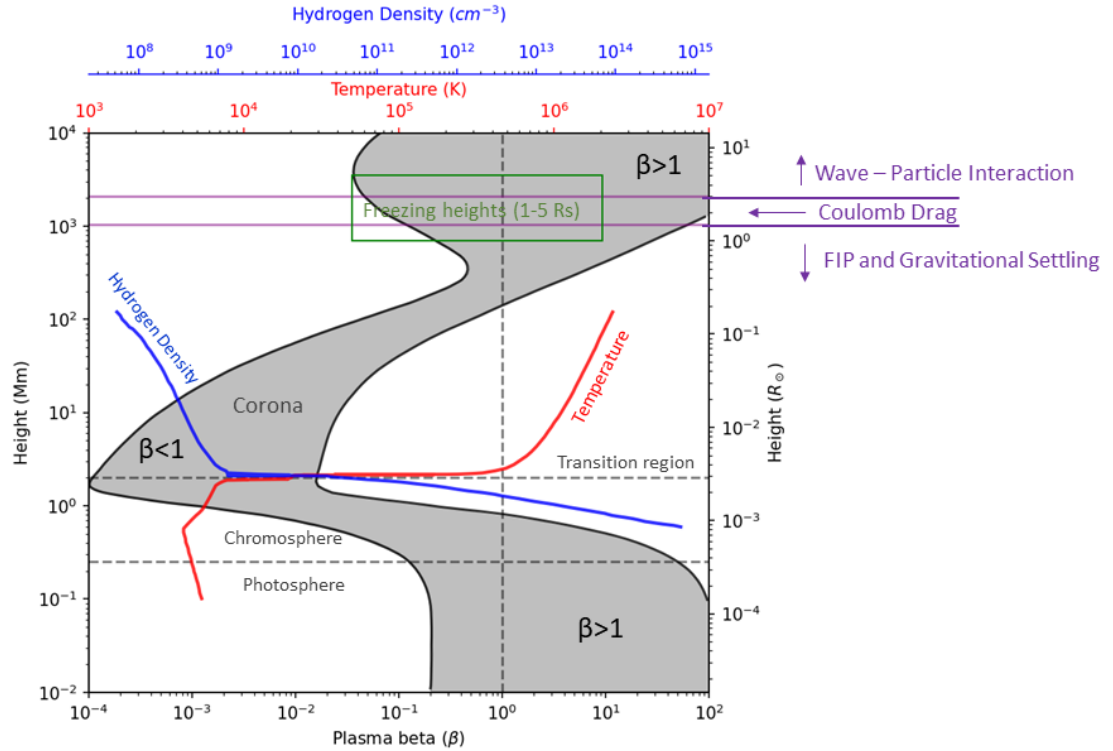


Figure 1.4: Variation of plasma parameters, i.e. plasma beta (black), temperature (red) and hydrogen density (blue) in the solar atmosphere. The boundaries of photosphere and chromosphere are also marked by the dashed horizontal lines in black. The dominance of different processes at different heights (violet) is also approximately shown. The region of freezing-in of the charge states is shown by the rectangular box in green color. This Figure is constructed based on the results published in Gary (2001) (for plasma beta), Withbroe (1981) (for Hydrogen density and temperature), Hahn (2020); Moses et al. (2020) (for region of dominance of different processes) and Landi et al. (2012) and references therein (for the fixing of the charge states).

context of FIP effect. Also, the freezing-in height closer to the dominance of wave-particle interaction dominated region implies that the wave-particle interaction is primary mechanism which the ions are affected at these heights. These important processes like FIP, gravitational settling, Coulomb drag and wave-particle interactions play important roles in fixing the abundance ratio in the solar wind (including alpha-proton ratio) and are discussed in the next section.

1.3.1 First Ionization Potential (FIP) effect

The abundance of elements with First Ionization Potential (FIP) below 10 eV are generally enhanced in the corona as compared to photosphere and slow solar wind by a factor of about 3 (can vary from 2 to 5). This enhancement in the abundance of low FIP elements is observed by both remote sensing (i.e., spectroscopic) and in situ measurements. At the same time, the coronal holes and the fast-solar wind coming from them show less FIP fractionation than the quiet corona and slow wind (e.g., [Bochsler, 2007](#); [Feldman, 1998](#)). To solve this mystery of FIP bias, i.e. enhancements of low (<10eV) FIP elements and reduction of high FIP (>10eV) elements in corona, researchers have used various theories. The primary approaches to understand FIP bias are diffusion, thermoelectric driving, chromospheric reconnections, ion cyclotron wave heating and pondermotive force. The details and drawbacks regarding these theories/models can be found in [Laming \(2015\)](#) and references therein. Among these theories/models, the pondermotive force model has been the most popular and successful in explaining elemental abundances. Therefore, we will only invoke the pondermotive force model here to understand the FIP effect.

The pondermotive force caused by the magneto-hydrodynamics (MHD) waves separate the neutrals and ions in the solar atmosphere. According to [Lundin and Guglielmi \(2006\)](#), the word “pondermotive” comes from the Latin words *pondus* (*ponderis*), meaning “heaviness” and *motor*. The pondermotive forces are time-averaged nonlinear forces. These forces are active on the medium in the presence of oscillating non-uniform electromagnetic fields. The FIP effect depends on propagation and strength (energy density) of the electromagnetic waves. A simple case is presented in [Figure 1.4](#) to understand the FIP effect due to the pondermotive force in the solar atmosphere. A coronal loop having a footpoint at the chromosphere is considered. The curvature effects of the loop are ignored to understand the propagation of Alfvén waves. The model assumes the steady evaporation of plasma from the chromosphere to the corona, having a speed less than the local Alfvénic speed. The model also ignores the transient effects e.g. flare heating, CME eruption etc. This is done because if the Alfvén waves

produced by a heating event in the corona reach the chromosphere before the heat conduction front, the chromospheric flow velocity required for fractionation to occur will be significantly lower than what is required. If the opposite of this scenario happens, then no fractionation will be there.

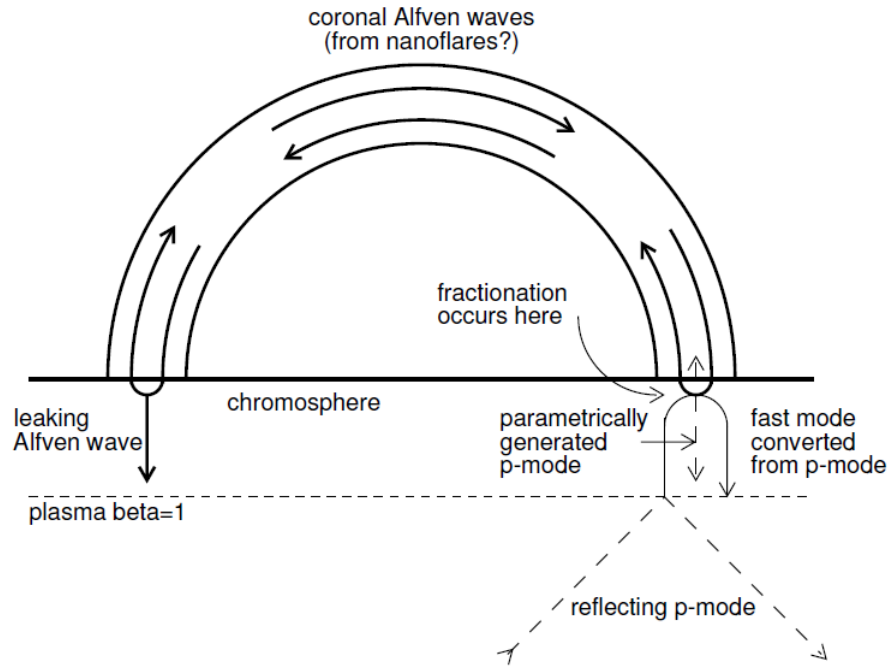


Figure 1.5: Schematic diagram for the FIP effect. The Figure shows the coronal loop having foot points in the chromosphere. The region of fractionation, Alfvénic waves transport and fast mode converted from p-mode (pressure – mode, Helioseismology notation) acoustic waves are shown. (Courtesy: [Laming, 2012](#))

The pondermotive model starts with the assumption that the chromosphere is unfractionated. This means there is sufficient turbulence to overcome any kind of diffusion, including gravitational settling. There will be a thermal force caused by heating in tandem with the pondermotive force. However, the acceleration due to the thermal force is 1-10% of the acceleration provided by the pondermotive force. The thermal acceleration is mass dependent, whereas the pondermotive acceleration is independent of mass. The comparison of thermal and pondermotive acceleration is necessary because these two majorly define the plasma movement in the solar atmosphere.

The derivation and discussion regarding the pondermotive force can be found

in the [Laming \(2009, 2015\)](#). This force is a second-order force which depends on the second-order changes in the fields. The expression of this can be seen below.

$$F_i = \frac{q_i^2}{4m_i(\Omega_i^2 - \omega^2)} \frac{d\delta[E_p(z_i)^2]}{dz} \quad (1.1)$$

Here, F_i is the force on the i th ion present in the region where this force is active. The q_i , m_i , Ω_i , ω and δE_p are charge, mass, ion cyclotron frequency, frequency of wave and peak electric field, respectively. 'z' is the coordinate along the magnetic field. Therefore, for the low-frequency plasma ($\omega \ll \Omega_i$), the pondermotive acceleration (F_i/m_i) is mass and charge-independent. The simplified form of pondermotive acceleration ([Laming, 2017](#)) is

$$a = \frac{c^2}{2} \frac{\partial}{\partial z} \left(\frac{\delta E^2}{B^2} \right) \quad (1.2)$$

where δE , B , c , and z are the wave electric field, ambient magnetic field, speed of light, and a coordinate along the magnetic field respectively. Therefore, the pondermotive acceleration depends on the gradient of the wave electrical energy.

Let us now go back to the fractionation process of different elements. [Figure 1.5](#) shows the different processes at each foot-point of a coronal loop. The Alfvén waves generated inside the coronal loop are shown as thick solid lines. These waves bounce back and forth from the loop foot-points. There is a finite probability of leaking out and being transmitted deeper into the chromosphere at each bounce (left foot-point). These reflecting Alfvén waves can also produce slow mode (“p-mode”, Helioseismology notation) waves by a parametric process (right foot-point). These waves are shown by using thin dashed lines. The other p-mode acoustic waves propagating inside the solar envelope can convert into fast-mode waves at chromospheric heights where the Alfvénic speed and sound speed become equal (nearby the plasma $\beta = 1$). These converted waves are shown in a thin solid line at the right foot-point. These waves are refracted back into the chromospheric region, where the Alfvénic speed increases with height. These fast-mode waves may also convert to Alfvén waves. Depending on the frequency of these waves, they can then propagate up to the loop to be transmitted or reflected. The transmission and reflection depend on the match between the loop

resonance and their frequencies. The above are the primary ways the Alfvén waves can generate and propagate in the coronal loops.

The pondermotive acceleration depends on the gradient of wave electric energy. The gradient in the wave energy is generated because of the change in density inside the chromosphere. The heating of the chromosphere is mainly caused by the processes responsible for coronal heating. The chromosphere is cooled in the region where the maximum FIP fractionation happens. This cooling primarily occurs because of the radiations in H Lyman α . As hydrogen gets ionized in this region, its ability to cool through radiative cooling decreases, which causes an increase in temperature. The density falls drastically, corresponding to this increase in temperature. This gradient in density is steeper than the typical hydrostatic scale height. All these changes, i.e. H atoms getting ionized, generation of strong density gradient, reduction in radiative cooling etc., happen at the same location. Hence, this is where the pondermotive force is the most effective.

The fractionation caused by this pondermotive force can be calculated from the momentum equation for ions and neutrals in the background of protons and neutral hydrogen. The final expression for ratio (f_k) of densities ρ_k for element k at lower (z_l) and upper (z_u) boundaries of the fractionation region can be seen below.

$$f_k = \frac{\rho_k(z_u)}{\rho_k(z_l)} = \exp \left\{ \int_{z_l}^{z_u} \frac{2\xi_k a \nu_{kn} / [\xi_k \nu_{kn} + (1 - \xi_k) \nu_{ki}]}{2k_B T / m_k + v_{\parallel, \text{osc}}^2 + 2u_k^2} dz \right\} \quad (1.3)$$

Where ξ_k is the element ionization fraction, a , ν_{ki} and ν_{kn} are pondermotive acceleration, collision frequencies of ions and neutrals with the background gas of neutral hydrogen and protons. The k_B , T , and m_k represents Boltzmann's constant, temperature, and mass of element k, respectively. $k_B T / m_k (= v_z^2)$ represents the square of the element's thermal velocity along the z-direction. u_k is the upward flow speed and $v_{\parallel, \text{osc}}$ is a longitudinal oscillatory speed, corresponding to upward- and downward-propagating sound waves. A slight change of ξ_k from unity can result in significant decreases in the fractionation because $\nu_{ki} \gg \nu_{kn}$ in the fractionation region at the top of the chromosphere. More detailed discussion and derivation of fractionation because of the pondermotive force can be found

in [Laming \(2009, 2015, 2017\)](#); [Laming et al. \(2019\)](#).

In simple words, the FIP effect is a phenomenon where elements with low first ionization potentials (such as iron, magnesium, and silicon) are overabundant in the solar corona relative to their abundances in the photosphere. As the temperature increases with increasing height in the chromosphere, the low FIP elements start ionizing. So, the low FIP elements are preferentially transported up by pondermotive acceleration, resulting in their over-abundance in the corona. In contrast, the elements with high FIP (helium, neon etc.) show a reduction in abundance at coronal heights. This is because these elements become ionized at upper heights. [Rakowski and Laming \(2012\)](#) show the depletion in the He/O. They also shown that this depletion is maximum when wave frequency matches the loop resonance. This causes the limit on the pondermotive acceleration up to the top of the chromosphere. Therefore, oxygen, which has a lower FIP than He, is ionized and transported to coronal heights, whereas helium being neutral, remains at the lower height resulting in a reduction in the He/O ratio. In the same way, the decrease in A_{He} from the photosphere to the corona can be understood using a similar argument. However, FIP is only valid for smaller reductions in A_{He} in background corona or solar wind. Other active processes can dominate over FIP effect under some specific conditions. These processes are discussed in the upcoming sections.

1.3.2 Gravitational settling

The gravitational settling is primarily active in two regions of the Sun's interior and the atmosphere. The settling-dominated interior is at the boundary between radiative and convection zones ([Bochsler, 2000](#)) and external or atmospheric settling is active in the lower part of the chromosphere ([Vauclair and Meyer, 1985](#)). The interior gravitational settling causes depletion of helium of typically 10% in the convection zone compared to its initial abundance at the time of formation. In the present thesis, we are more interested in the effects of the gravitational settling in the chromosphere as this causes the reduction in the helium (as well as other heavier elements).

The physical mechanism of gravitational settling can be understood by using a simple scenario. There are two major opposing forces on the minor ions. One force is downward due to gravitational pull which is balanced by the momentum transfer through collisions with the surrounding electron-proton gas. Without friction or momentum transfer between heavy ions and electron-proton gas, the heavy ions would drop rapidly into the solar atmosphere. However, the presence of collisional interaction causes a reduction in the drift of particles in the solar atmosphere.

Vauclair and Meyer (1985) investigated diffusion processes to explain the compositional changes in chromosphere and corona. The diffusion of a gas with negligible abundance in mixture of gases is used to understand the role of diffusion. They stated that when a gas mixture is exposed to pressure, temperature, or concentration gradients, or other forces (e.g. radiative force etc.), the gas components undergo diffusion relative to each other. These authors treated the effects of pressure, temperature, and concentration separately on the downward velocity of the less abundant species. This downward diffusion velocity (v_D) can be represented as follows.

$$v_D = D (\nabla \ln c - k_p \nabla \ln p - k_T \nabla \ln T + F/kT) \quad (1.4)$$

In the above expression, D is the diffusion coefficient, c is the concentration of heavy ion (in this case, helium) considered, and k_p and k_T are the pressure diffusion and thermal diffusion factors. p and T stand for pressure and temperature respectively. The first, second, third and fourth terms on the right-hand side represent diffusion in the concentration, gravitational settling (pressure diffusion term), thermal diffusion and any additional force (like radiation force) respectively.

In the chromosphere, the temperature and concentration gradients are negligible. Further the radiation gradient is not large enough to compete with pressure diffusion term. Therefore, the composition of minor species in solar chromosphere are controlled by gravitation settling. So, the above equation becomes

$$v_D = D(k_p \nabla \ln p) \quad (1.5)$$

However, in the transition region, this scenario changes because of the sharp gradient in temperature and concentration. In addition, the forces due to magnetic field becomes dominant because of the complete ionization of particles.

Recently, [Laming et al. \(2019\)](#) calculated periods corresponding to gravitational settling for different elements. These authors assumed a coronal loop collisionally coupled to the solar disk to remove the complication because of the transition to the collisionless plasma. The continuity equation used by them is as follows.

$$\frac{\partial n_k}{\partial t} = -\nabla \cdot (n_k v_k) \simeq -2n_k v_k / L \quad (1.6)$$

where L , v_k and n_k are the coronal loop length, settling velocity, and number density respectively. v_k can be calculated from the equation ([Laming et al., 2019](#)) below:

$$v_k = V_H - \frac{3\sqrt{\pi}}{4} \frac{m_p}{4\pi e^4 \ln \Lambda} \frac{k_B T}{n} \sqrt{\frac{A+1}{A}} \frac{2k_B T}{m_p} \times \left(V_H \frac{dV_H}{dr} + \frac{GM_\odot}{r^2} \right) \left(\frac{2A - Z - 1}{2Z^2} \right) \left(\frac{A+1}{A} \right) \quad (1.7)$$

where V_H , m_p , A , Z , $\ln \Lambda$, k_B , T , G , and M_\odot are velocity of hydrogen, mass of the proton, atomic mass of selected heavy ion, the charge of the heavy ion, collision cut-off parameter, the Boltzmann's constant, temperature, gravitational constant and mass of the Sun respectively. This equation is derived from [Geiss et al. \(1970\)](#) and is valid only for the collisional plasma.

The solution of the continuity equation is

$$n_k \propto \exp(-2v_k t / L) \quad (1.8)$$

[Laming et al. \(2019\)](#) assumed $n \sim 10^9 \text{ cm}^{-3}$, $T \sim 10^6 \text{ K}$ and $L=75000 \text{ km}$ and found the gravitational settling time for He, O, and Ne are 1.5, 3.6, and 5.0 days respectively. These settling times are essential in understanding the helium

abundance enhancements in the ICMEs. The details regarding this and the role of gravitational settling in A_{He} enhancement are taken up in Chapter 4.

1.3.3 Coulomb Drag

Coulomb drag is a process that occurs when charged particles interact with each other in a plasma. In the solar wind, Coulomb drag plays an essential role in the plasma dynamics. Solar wind plasma expands and cools down as it moves away from the Sun. In addition, the solar wind particles become increasingly collisionless as they go out. However, Coulomb drag continues to operate and can be the dominant force affecting the plasma dynamics at a height range of 1.5 to 3-5 R_{\odot} . Coulomb drag arises from the interaction between charged particles in the plasma. The Coulomb interaction causes the particles to exchange momentum, resulting in energy transfer from one particle to another.

To understand the Coulomb friction, consider an ion with mass M (Let us assume alpha particle) surrounded by small ions (Let us assume protons). The protons surrounding the alpha particle will exert Coulomb's force on the alpha particle, and the system will eventually be in equilibrium. However, if a parcel of protons moves away, the equilibrium will get disturbed, and the alpha particle will experience a force in the direction of movement of the protons. This is the simplest explanation of Coulomb drag. The strength of Coulomb drag depends on the charge and mass of the particles involved and the relative velocity between them. In the solar wind, Coulomb drag is the most effective when the heavier ions of the solar wind plasmas are considered. The general formula of Coulomb drag (Geiss et al., 1970) is written below.

$$C = \frac{4\pi e^4 \ln \Lambda}{m_p} \frac{nZ^2}{kTA} G \left\{ \frac{A}{A+1} \frac{m_p}{2kT} (V-v) \right\} \quad (1.9)$$

where,

m_p - the mass of the proton, v - velocity of the proton,

n - number density of protons, V - velocity of heavier ions,

Z - atomic number of heavier ions, A - atomic mass of heavier ions,

Λ - collision cut-off parameter (derived from Rutherford scattering, $\ln \Lambda = 22$)

(Parker, 1963))

T- temperature, k- Boltzmann's constant, and

G – function introduced by Chandrasekhar (1943) to explain the dynamic friction

Bürgi (1992) used the Coulomb drag to explain the constant proton flux at 1 AU. They created three fluid models, which include the electrons, protons and alphas. The additional term used in this model was Coulomb friction on the alpha particles due to protons and vice-versa. This is given by

$$f_{\alpha p} \propto \frac{n_p}{T^{3/2}} (v_p - v_\alpha) \quad (1.10)$$

where $f_{\alpha p}$ is frictional force on alpha particles caused by protons, T, n_p , v_p , and v_α are temperature, proton number density, proton velocity, and alpha velocity respectively.

Coulomb drag is an important force to reckon with closer to the Sun. It is known that alphas move faster than protons near the solar surface. However, closer to 1 AU, alphas and protons have comparable velocities (Mostafavi et al., 2022). As Coulomb friction depends on the velocity difference of protons and alphas, it is more effective closer to the Sun (up to ~ 0.3 AU) beyond which wave-particle interaction controls the interaction between the alphas and protons (Wang, 2016).

1.3.4 Wave-particle interaction

In the solar atmosphere and solar wind, there are various types of waves, such as Alfvén waves, magneto-ionic waves, and plasma waves etc. These waves can interact with the particles in the solar wind, leading to energy transfer between the waves and particle and vice versa. One of the important consequences of wave-particle interaction is the acceleration of particles. These accelerated particles can then contribute to the heating of the solar wind. Wave-particle interaction can also lead to the generation of turbulence in the solar wind. This interaction can also change the properties of alphas and protons in the solar wind.

As mentioned earlier, the alphas move faster than the protons in solar wind (Mostafavi et al., 2022) and the differential velocity between alphas and protons

is higher near the Sun (Marsch et al., 1982; Mostafavi et al., 2022). The Coulomb drag cannot explain the higher velocity of alphas (Dusenbery and Hollweg, 1981) near the Sun. It is also observed that the heavier ions also have velocities higher than the alpha particles (Schmidt et al. 1979). The differential velocity between the alphas and protons ($V_\alpha - V_p$) usually does not exceed the Alfvén velocity (V_A) (Neugebauer and Feldman, 1979). Moreover, the kinetic temperature of alpha particles is higher than protons (Robbins et al., 1970; Kasper et al., 2008). The temperature anisotropies in alpha and protons also depend on the $(V_\alpha - V_p)/V_A$ (Kasper et al., 2008, 2013; Cranmer, 2014).

The reason for the velocity limit of the differential velocity is believed to be caused by the interaction between waves and particles, which is driven by instabilities caused by the interaction of alpha-proton with waves. The ion-cyclotron waves can preferentially accelerate the alphas via resonance scattering. The alpha and proton have different resonance factors for interacting with waves and therefore have different momentum and energy transfer rates (Hu and Habbal, 1999). This interaction reduces the differential velocity to the Alfvén speed, which is further explained in the works of Gary et al. (2000) and Verscharen et al. (2013).

An evidence for the interaction between Alfvén-cyclotron waves and helium can be seen in Figure 1.6 (Kasper et al., 2008). This Figure shows the breakdown in temperature equilibrium of proton and alpha in the solar wind. Figure 1.6 represents the histogram of alpha (T_α) and proton (T_p) temperatures for millions of observations from the *Wind* spacecraft. This distribution/histogram shows the maximum peak at $T_\alpha/T_p = 1$, representing the isothermal plasma. Another peak at $T_\alpha/T_p = 4$ represents the equal thermal speed of the alpha and protons. This equal thermal velocity in place of equal temperature represents the violation of the principle of energy equipartition, which states that the total energy of a system is equally distributed among all available degrees of freedom. This suggests that the solar wind deviates from ideal gas behavior. In addition, a part of the distribution (23%) shows $T_\alpha/T_p \geq 5$. This additional high temperature of helium suggests that the resonant heating through waves is preferential for alphas compared to protons.

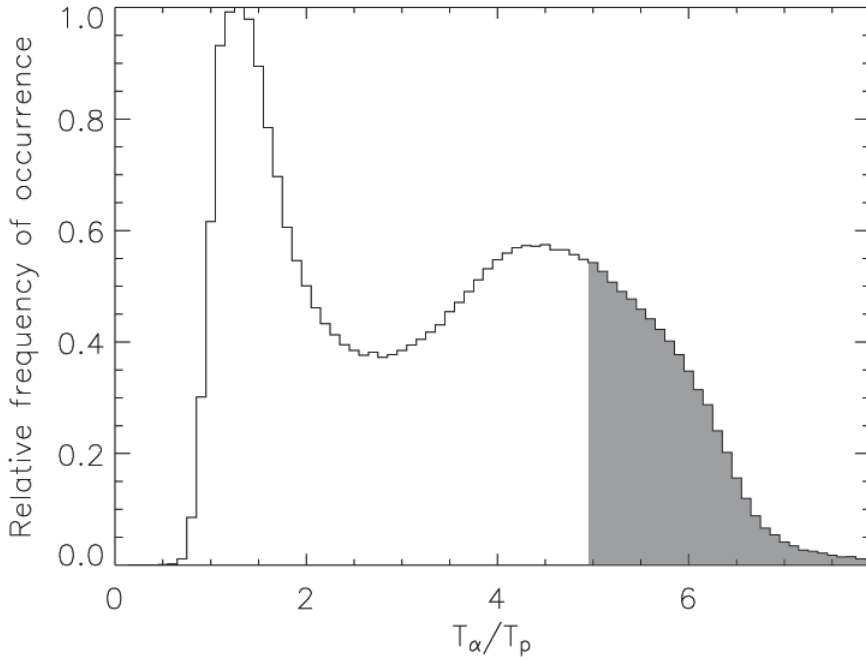


Figure 1.6: The histogram of T_α/T_p is shown. This Figure represents the bimodal nature of the dominant components of the solar wind plasma. The first peak is at $T_\alpha/T_p = 1$ meaning isothermal plasma. The second peak is near $T_\alpha/T_p = 4$, representing similar thermal speed. The 23% of the observations show $T_\alpha/T_p \geq 5$ which indicates the preferential heating of alphas over protons. (Courtesy: [Kasper et al., 2008](#))

The large amplitude Alfvén waves cause preferential heating (via resonance with ions) and dissipation. During the interaction, these resonant ions will be accelerated in the direction perpendicular to the ambient solar magnetic field. The primary reasons behind these resonances can be the drop in gyrofrequencies of the ions with increasing height or the power transfer to smaller kinetic scales by long wavelength waves via turbulence ([Kasper et al., 2008](#), and references therein). These interactions of alphas and protons with waves can alter the ions' energies/temperature and velocities. These interactions lead to temperature anisotropies.

The processes continuously altering the abundance, distribution, velocity, temperature etc. of protons, alphas and heavier ions are discussed in the previous section. In the ensuing section, we discuss briefly processes like solar flares,

CMEs and SIRs/CIRs that are relevant for the theme of the thesis.

1.4 Large-scale solar processes causing helium abundance changes

1.4.1 Solar Flares

A solar flare is a sudden, intense burst of energy and radiation that originates from the Sun. The primary cause behind the solar flare is the rapid release of the stored magnetic energy. This rapid release of energy causes the acceleration of particles and the emission of radiation in the broad electromagnetic spectrum, from radio to gamma rays. Figure 1.7 shows various features associated with a typical solar flare. Magnetic reconnection is the primary cause of energy release in the solar flare. We are more interested in the changes in the helium abundance caused by the solar flare. Therefore, we will focus on chromospheric evaporation which is a process that occurs during a solar flare. More observational details regarding solar flare can be found in [Fletcher et al. \(2011\)](#) and the modelling details can be found in [Priest and Forbes \(2002\)](#).

As the name suggests, chromospheric evaporation is the evaporation of the chromospheric material because of the energy released during the flaring process. This process starts with the magnetic reconnection which is marked as 1 in Figure 1.7. The energy produced will energize the electrons in both upward and downward directions. The downward moving non-thermal electrons are represented by 2. These electrons will move along the magnetic loops and reach toward the loop's foot-points, which are situated at the chromospheric heights. These electrons will produce the hard X-rays and Gamma rays and heat the chromospheric material, which will be evaporated (see number 3). The evaporated material is moved to higher heights (number 4). This material will contain the chromospheric abundances of helium. Therefore, solar wind affected by chromospheric evaporation may have higher helium abundance.

The chromospheric evaporation can enhance the A_{He} up to the chromospheric

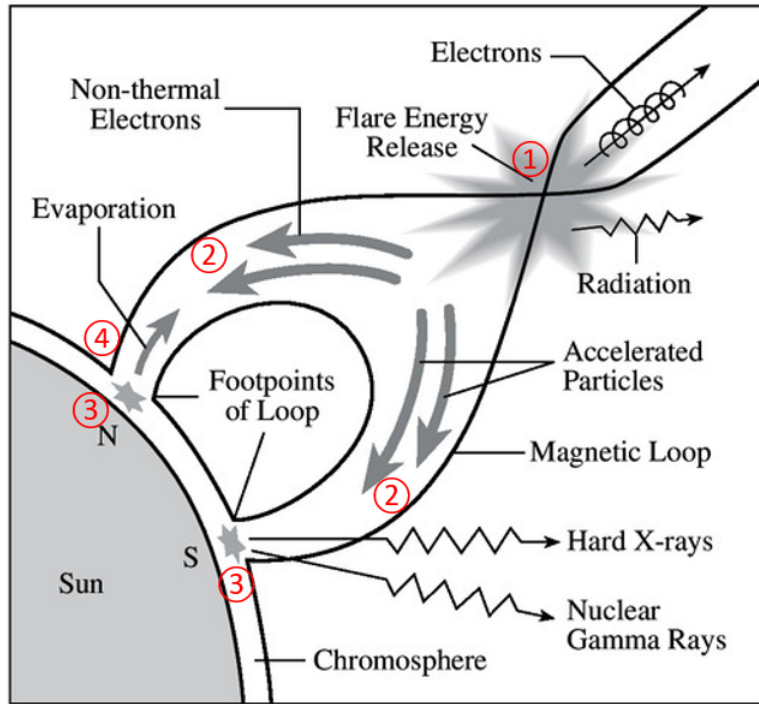


Figure 1.7: A schematic diagram of the processes that occurs during solar flare leading to chromospheric evaporation. The numbers are used to indicate different stages. (Courtesy: Lang, 2000)

level, i.e. 8%. The importance of the process in modulating the helium abundance and its contribution to A_{He} enhancement are discussed in Chapter 4. The critical roles of flare strength and its timing will also be addressed in the context of the results presented in Chapter 4.

1.4.2 Coronal Mass Ejections

Coronal Mass Ejections (CMEs) are massive eruptions of plasma and magnetic fields from the Sun's corona. These events are often associated with solar flares and can release billions of tons of material into space at speeds ranging from a few hundred to over 2000 km/s. The details regarding the modelling and observations of CMEs can be found in Chen (2011). The interplanetary counterpart of CMEs is known as ICMEs. The helium abundance is usually found to be enhanced in ICMEs.

Figure 1.8 shows the three-part structure of a typical ICMEs that contains

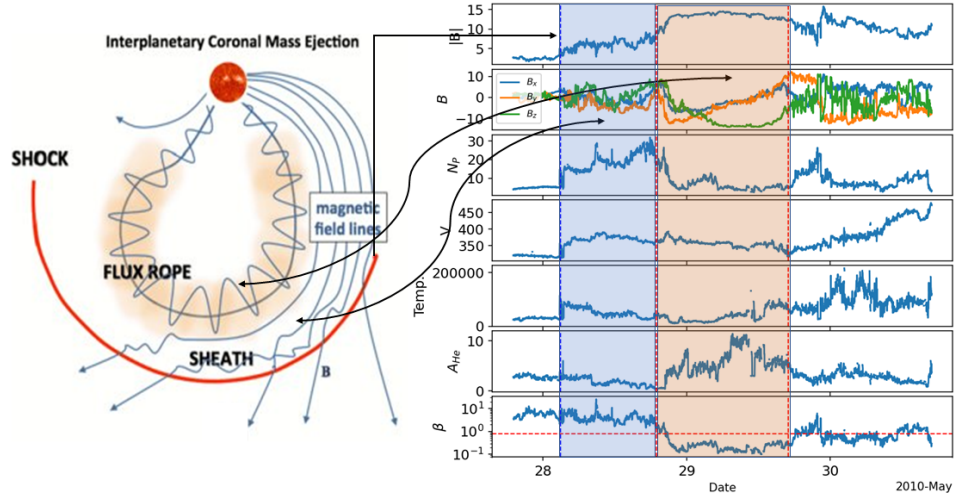


Figure 1.8: The three-part structure of the ICMEs, i.e., shock, sheath and flux rope is shown on the left-hand side. The typical observational counterparts of an ICME are shown on the right side. The schematic of ICME is taken from Kilpua et al. (2017). The right side shows the magnetic field and its components (\mathbf{B} , B_x , B_y , B_z), velocity (V), number density (N), temperature, helium abundance (A_{He}) and Plasma beta (β).

shock, sheath and magnetic flux rope. The observational counterparts are also shown in the right side of Figure 1.8. The schematic of ICME shown in Figure 1.8 is taken from Kilpua et al. (2017). The right side of Figure 1.8 shows the magnetic field and its components (B and B_x , B_y , B_z), velocity (V), number density (N), temperature, helium abundance (A_{He}) and Plasma beta (β). The sudden jump in the various parameters, i.e., magnetic field, velocity, number density etc., can be seen as the shock arrives at the location of the satellite. The structure of the sheath is complex and highlighted with blue colour. The orange colour shows the flux rope structure of the ICME, also known as the magnetic cloud (MC). The magnetic cloud shows an evident rotation in the magnetic field components and has low plasma beta. The A_{He} enhancement during the ICME (observed on 28-29 May 2010) can be seen in Figure 1.8.

More details regarding the ICMEs can be found in Kilpua et al. (2017) and references therein. A_{He} can be enhanced up to 30% during the arrival of the ICMEs at the first Lagrangian point (L1) of the Sun-Earth system, but the reason behind these enhancements is not understood fully. Although, there are a few

works (e.g. [Fu et al., 2020](#), and references therein) that suggest the important role of chromospheric evaporation, a holistic picture regarding the enhancement of A_{He} in ICMEs is suggested in Chapter 4.

1.4.3 Stream Interaction Region/Corotating Interaction Region

The processes discussed in the earlier sections are usually active near the Sun. However, interplanetary modulations can also show changes in the helium abundance. The significant interplanetary modulations are caused by Stream /Corotating interaction regions (SIRs/CIRs). The SIRs are formed when fast wind streams coming from coronal holes interact with slow wind streams ahead of them. If the SIR corotates and survive one full solar rotation (~ 27 days) owing to the long lifetime of coronal holes, it is known as a CIR. More details regarding the formation and properties of SIR can be found in [Richardson \(2018\)](#) and references therein. The major signatures of SIRs are discussed in Chapter 5.

Except a few studies (e.g. [Durovcová et al., 2019](#); [Gosling et al., 1978](#), etc.), the changes in helium abundance in the SIRs have not been investigated comprehensively till date. Although enhancements in A_{He} are observed in SIRs on several occasions, the degree of enhancements are not as dramatic as seen in ICMEs. [Gosling et al. \(1978\)](#) and [Wimmer-Schweingruber et al. \(1999\)](#) suggested that the resultant changes in the A_{He} in SIRs are because of the interaction of different streams having their own variation in helium abundances. They indicated that the A_{He} is enhanced in SIRs because the fast stream has higher A_{He} than the slow stream. But, recently, [Durovcová et al. \(2019\)](#) have shown that interaction regions do affect A_{He} as well. Figure 1.9 is taken from [Durovcová et al. \(2019\)](#) and it shows that the alphas move slower and faster than protons in slow and fast wind respectively. They considered that CIRs are analogous to magnetic bottles and argued that the pitch angles of alpha particles within the magnetic bottle play important roles in determining the A_{He} . In Chapter 5 we treat the alpha and proton interfaces separately and show how it can help in addressing the changes in A_{He} in SIRs.

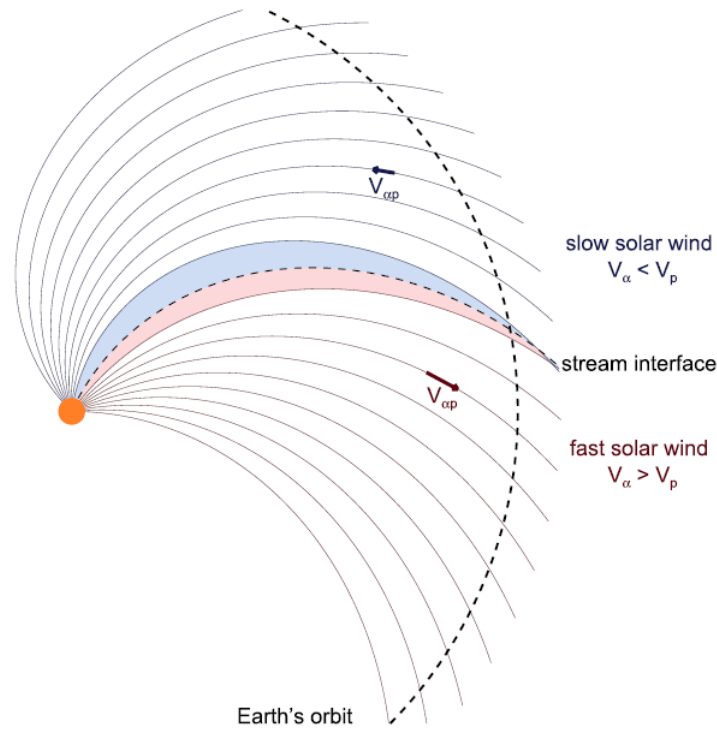


Figure 1.9: The interaction between the slow and fast wind is shown. The slow and compressed side is shown in blue and red, respectively. The slow wind has an alpha velocity higher/equal to protons, whereas alphas move fast in the fast wind. The stream interface and Earth's orbits are also shown. (Courtesy: [Durovcová et al., 2019](#))

1.5 Techniques to measure helium abundance

There are three main techniques which are used to measure the properties of the ions. The first technique involves the use of a Faraday Cup, which is composed of an electrically grounded metal cup or collector. When charged particles enter this cup, they transfer their charge to the cup's surface. The accumulated charge is then measured as an electric current. This current will be proportional to the incoming charged particles.

The second method includes Time of Flight (TOF) in combination with an Electro-Static Analyzer (ESA). TOF is a method commonly used in mass spectrometry to determine the mass-to-charge ratio of ions. In a TOF mass spectrometer, ions are accelerated by an electric field and enter a drift region where they travel to a detector. The time it takes for ions to reach the detector is measured,

and from this information, the mass-to-charge ratio can be calculated. TOF mass spectrometers are known for their high sensitivity and fast data acquisition capabilities.

The third technique introduces the Top Hat Analyzer (THA), which is used together with the magnetic assembly to separate ions of varying masses and detector for measuring these ions. Notably, THAs have the unique capability of measuring ions within a two-dimensional plane, differentiating them from Faraday Cups and TOF, which require the spacecraft to rotate to achieve a full 180-degree coverage. These techniques play a crucial role in space missions and scientific research, where accurate ion measurements are essential. The THA assembly and FC were used in the Wind and PSP spacecraft. The ACE spacecraft has TOF as a major particle detector. The ADITYA-L1 spacecraft have a TOF (PAPA Payload) and the THA assembly (SWIS subsystem of ASPEX payload). The THA assembly will measure the particles in 360°.

To improve helium measurements, the researchers are developing more effective ionization methods, improving electronics and detectors, improved design and reducing noise.

1.6 Aim and overview of the thesis

The abundance of helium in the solar wind shows various features, such as dependence on solar activity, on solar wind velocity, enhancement in coronal mass ejection (CME) structures, and alteration during the interaction of different solar wind streams (i.e., Stream/Co-rotating Interaction Regions, or SIRs/CIRs). Although some of these aspects are addressed in the past, many aspects of the variation of helium abundance in background solar wind, Interplanetary CME (ICME) and SIR/CIR structures and at various time scales are not known in great detail.

This thesis work addresses the changes in helium abundance (A_{He}) ranging from 0.01% to more than 30%. In doing so, various physical processes that may cause these changes have been discussed in Chapter-1. The results presented in

this thesis provide new insights into the processes closer to the Sun as well as to the Earth, transport processes through the interplanetary medium and also, how these processes may change the helium abundance at both shorter and longer time scales. Chapter-2 of the present thesis introduces the techniques, data, and models used to carry out this research work. This chapter contains information about the relevant instruments onboard different satellites at the L1 point of the Sun-Earth system (WIND and ACE), together with their basic principles. A brief description of the Air Force Data Assimilative Photospheric Flux Transport - Wang-Sheeley-Arge (ADAPT-WSA) model is also given.

It is well known that helium abundance varies with solar activity. However, a 4-cycle long perspective of the changes in the solar wind helium abundance was missing before this work. The variation in helium abundance in the last four solar cycles (cycle 21- cycle24) is described in chapter-3. This chapter shows that the helium processing changed in solar cycle 24 (SC24) because of the changes in the topologies and the dynamics of the large-scale coronal magnetic field. The investigation also suggests the important role of the possible changes in the sources of the slow and fast solar winds in the last four solar cycles.

The helium abundance is, in general, 4-5% in the corona, but it can increase to 8% or more in ICMEs measured by the L1-satellites. A holistic view of all the processes responsible for this enhancement in helium abundance is presented in Chapter-4. This chapter also describes the critical role of timing and strength of solar flares associated with the ICME measured from the L1 -satellites. It is suggested that chromospheric evaporation associated with solar flares coupled with gravitational settling can enhance A_{He} to 30% or more. Chapter-5 is focused on helium abundance variation in the SIRs/CIRs. While Chapters 3 and 4 contain the results related to the changes in A_{He} because of the near Sun processes, Chapter 5 comprises of the results that capture the processes that cause interplanetary alteration in A_{He} . It is shown that the modifications in the pitch angles of alphas and protons as well as their velocity differences play important roles in the enhancement of A_{He} towards the fast wind side of the SIRs.

The above chapters focus on the variation of A_{He} from $\sim 2\%$ to $\sim 30\%$. How-

ever, there are instances when A_{He} goes even lower than 1%. The potential source region characteristics and the associated processes that may cause very low abundance of helium are discussed in Chapter-6. Therefore, Chapters 3 to 6 of this thesis cover the entire range of solar wind helium abundance variation.

In a nutshell, this thesis comprehensively addresses the changes in helium abundance caused by various processes, sources, and interactions at various time scales.

Chapter 7 of this thesis provides a brief discussion of the potential areas of future research based on the findings and insights reported in this work.

Chapter 2

Techniques, Datasets and Models

2.1 Introduction

The science problems addressed in this doctoral work have been addressed by utilizing a range of solar wind parameters such as magnetic field, number densities, temperature, and others. These parameters are obtained from multiple satellites, including those in orbits at the first Lagrangian point (L1) of the Sun-Earth system, as well as satellites located near Earth (e.g. Interplanetary Monitoring Platform (IMP) and Geotail) and the Sun (e.g. Parker Solar Probe or PSP). These satellites have various instruments designed to measure directly (e.g. magnetic field) or to provide information on velocity distribution functions the moments of which provide the bulk parameters (e.g. density, velocity, temperature etc.). A variety of measurement techniques are used in these instruments and it is pertinent to introduce in this chapter brief descriptions of some of these techniques. Furthermore, the thesis also utilizes model outputs to connect the interplanetary observations obtained from satellites (*Wind* and PSP) to the surface of the Sun and it is also relevant to present briefly the basic description of these models. Therefore, this chapter, by providing the basic principles of measurement techniques, datasets and models, will prepare the context for the results that are to be presented in the subsequent chapters.

2.2 *Wind* Spacecraft

The *Wind* spacecraft (https://wind.nasa.gov/inst_info.php) was launched on November 1, 1994, at 09:31 UT. In early 2004, the *Wind* satellite was transitioned into a Lissajous orbit around the L1 point following multiple orbits through the magnetosphere. The defined mission life was three years, but it is still working. The primary payloads in the *Wind* spacecraft are as follows:

- ⇒ Solar Wind Experiment (SWE, [Ogilvie et al., 1995](#))
- ⇒ Magnetic Field Investigation (MFI, [Lepping et al., 1995](#))
- ⇒ Plasma Analyser instrument (3DP, [Lin et al., 1995](#); [Wilson et al., 2018, 2019](#))
- ⇒ SMS Suprathermal Particle Data (STICS, MASS, SWICS, [Gloeckler et al., 1995](#))
- ⇒ Energetic Particles: Acceleration, Composition and Transport (EPACT, [Von Rosenvinge et al., 1995](#))
- ⇒ WAVES ([Bougeret et al., 1995](#))
- ⇒ *Wind* KONUS and TGRS Data ([Aptekar et al., 1995](#); [Owens et al., 1995](#))

In this thesis SWE (majorly Faraday cup) data is used to understand the helium as well as proton properties in the solar wind. This instrument provides different proton and alphas parameters, i.e. 3-D velocities, number densities, thermal velocities, flow angles etc. In addition, the MFI instrument provided the details regarding the magnetic field observations. The MFI data having a similar resolution to SWE is also provided on the Coordinated Data Analysis Web (<https://cdaweb.gsfc.nasa.gov/>). The details regarding these two instruments are discussed in subsequent sections.

2.3 Solar wind Experiment (SWE)

SWE has two subsystems – one, for the ion measurements, and the other for measurement of electrons. The SWE contains two instruments, i.e. Vector Electron and Ion Spectrometer (VEIS) and Faraday Cup sensors.

Ion measurements

The SWE contains two Faraday Cup (FC) subsystems that measure solar wind thermal protons and heavier positive ions. The details of the Faraday cup subsystem can be found in [Ogilvie et al. \(1995\)](#). The details of this subsystem will be taken up further in the next section. We have used mostly the *Wind* SWE data for the thesis work. The details regarding the procedures and algorithms used to generate the FC data products can be found in [Kasper \(2002\)](#). The details regarding the systematic uncertainties in measurements using calibration against other *Wind* instruments and using the basic physical principles are discussed in [Kasper et al. \(2006\)](#). Together with the Faraday cup, the VIES also provides ion measurements.

Electron measurements

Another part of SWE is used to measure the solar wind electrons. This electron subsystem consists of two electrostatic analyzers, i.e., the vector spectrometer (VEIS) and the Strahl spectrometer. These instruments are designed to measure the distribution function of electrons in the solar wind. The detectors used in the instrument are described in detail in [Ogilvie et al. \(1995\)](#). In 2001, the high-voltage power supply of the VEIS instrument failed. Afterwards, the Strahl detector underwent reconfiguration to restore the majority of its measurement capabilities. Details of SWE electron instruments can be found at <https://wind.nasa.gov/swe/index.html>.

The central theme of this thesis is to investigate the variations in the alpha-proton ratio in the solar wind and therefore, we will only be discussing the FC in the ensuing section.

The FC contains a set of planar grids and two semi-circular collector plates. These semi-circular plates collect the solar wind and measure the current generated by the solar wind ions. Figure 2.1 shows the general FC assembly and cross-

sectional view of the sensor. A DC-biased time-varying high voltage (200Hz) is applied to a highly-transparent metal grid (modulator plate). This high voltage is used to remove the photoelectric current. This high voltage also helps determine ion energy and the discrimination between the charged particles and photoelectric current. The waveform can vary from $V+dV$, where this $V+dV$ can have a value of 8kV, and dV can have a maximum value of 1kV. The suppressor grid is biased at -120V to escape the secondary electrons from collector plates. The multiple plates grounded grids are used to reduce the effect of capacitive-coupling of the plates caused by the time-varying voltages. The front two outermost grids minimize the emission of time-varying electric fields from the sensor's front. The resultant current from the collector grid is used to construct the solar wind velocity distribution functions. The major features of the FC sensor system are:

- a The energy/charge bandwidth can be changed using the change in dV .
- b The precision in flow direction can be as good as 1° .
- c High cadence measurements
- d Measurements of 3-D velocity distribution functions

2.3.1 Working Principle

Faraday Cups' operation principle can be understood from Figure 2.2. The modulator plate selects a particular range of perpendicular velocities depending on the specific voltage applied on it. Therefore, nearly mono-energetic ions are selected by the modulator. It is to be noted that some of the particles that are incident on the FC with an angle will not be able to overcome the applied field. The simulated current variations with angle can be found in [Ogilvie et al. \(1995\)](#).

The different parameters of solar wind can be derived by using the current observed. The modeled velocity distribution function and nonlinear least square fitting on currents can be used to derive the speed, density, and temperature. The equation below shows the equivalence of observed current to isotropic Maxwellian

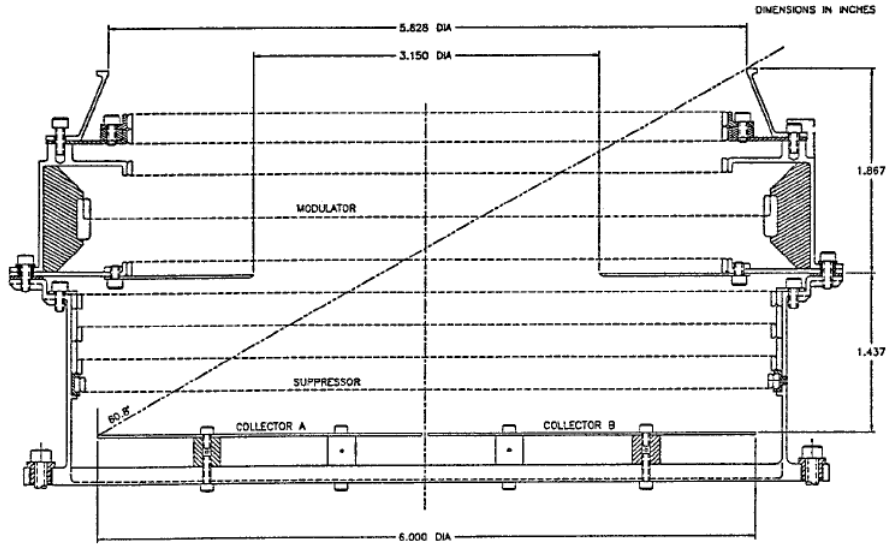


Figure 2.1: The cross-section of the Faraday Cup sensor is shown. All the grids except the modulator are at ground potential. The modulator grid has a time-varying voltage applied to it. The functioning of different grids is described in the text. (Image courtesy: [Ogilvie et al., 1995](#))

distribution. Following [Kasper \(2002\)](#), the differential amount of current dI produced by a small element of plasma with velocity \vec{v} in the frame of the FC (and speed $v_z = \vec{v} \cdot \hat{z}_c$ normal to cup) is given by

$$dI = A(\vec{v}/v)qv_z f(\vec{v})d^3\vec{v} \quad (2.1)$$

Equation 2.1 is a general form of the current seen by the simple FC. Now, inserting isotropic Maxwellian distribution and integrated over all energy/velocities windows:

$$I_{iso} = \frac{Anq}{\pi^{3/2}w^3} \iiint_{\text{window}} v_z e^{-\frac{(\vec{v}-\vec{U})^2}{w^2}} d^3\vec{v} \quad (2.2)$$

Here, I_{iso} is the isotropic current observed, A is the collecting area of FC, n is number density, q is the charge, w is thermal width, U is bulk velocity, v is the velocity in FC's frame, and v_z is the velocity in the normal direction. The integration is over the energy window. The above expression can be used to calculate the velocity distribution function. Further details regarding the calculations of solar wind parameters can be found in [Kasper \(2002\)](#) and [Verscharen et al.](#)

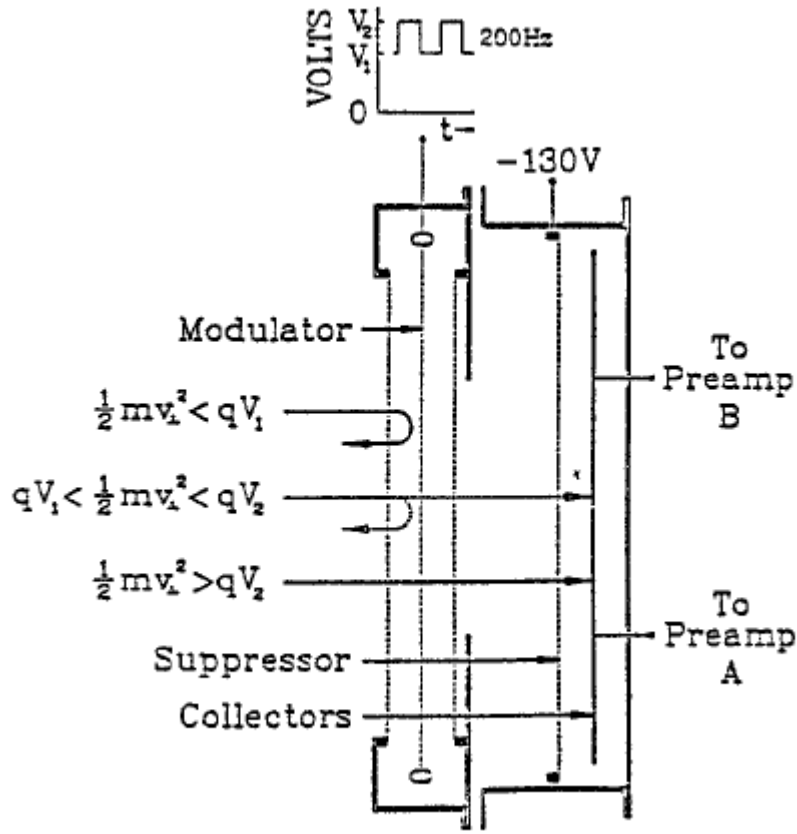


Figure 2.2: The schematic of Faraday cup. Note, the voltage applied on the grid helps in selecting particles with a particular of energy. (Courtesy: [Ogilvie et al., 1995](#))

(2019). In short, if the velocity distribution function is $f(r, v, t)$, the solar wind parameters can be calculated using moment analysis and can be seen below.

Starting with equation 2.1, we will use moment analysis technique to calculate the bulk parameters. The most significant approximation of the moment analysis technique is that $f(\vec{v})$ does not vary much over the width of the speed window V , so we may approximately write the total current I as

$$\Delta I \simeq A q v f(v) \Delta V \quad (2.3)$$

The phase space density f_i of the reduced distribution function along $\hat{\mathbf{n}}$ for the i th window at $(V_i; \Delta V_i)$ is then approximately

$$f_i = \frac{\Delta I_i}{AqV_i\Delta V_i} \quad (2.4)$$

We can calculate the bulk parameters using this phase space density using following equations:

Zeroth moment: - The density, $n(\vec{r}, t)$:

$$n(\hat{n}) = \sum_i \frac{\Delta I_i}{AqV_i\Delta V_i} \quad \text{or} \quad n(\vec{r}, t) \equiv \int f(\vec{r}, \vec{v}, t) d^3\vec{v} \quad (2.5)$$

First moment: - The bulk velocity, $\vec{U}(\vec{r}, t)$:

$$U(\hat{n}) = \frac{1}{n(\hat{n})} \sum_i f_i V_i \quad \text{or} \quad \tilde{U}(\vec{r}, t) \equiv \frac{1}{n(\vec{r}, t)} \int f(\vec{r}, \vec{v}, t) \vec{v} d^3\vec{v} \quad (2.6)$$

Second moment: Thermal speed, w_{ij} (Tensor quantity)

$$w(\hat{n}) = \sqrt{2} \left(\frac{\sum_i f_i (V_i - U(\hat{n}))^2}{n(\hat{n})} \right)^{1/2} \quad \text{or} \quad w_{ij}^2 \equiv \frac{1}{n(\vec{r}, t)} \int f(\vec{r}, \vec{v}, t) (v_i - U_i) (v_j - U_j) d^3\vec{v}, \quad (2.7)$$

The tensorial temperature (T_{ij}) can be calculated as $k_B T_{ij} = 1/2 m w_{ij}^2$.

2.4 *Wind* Magnetic Field Investigation (MFI)

The MFI ([Lepping et al., 1995](#)) observations are used in tandem with the SWE observations. The MFI comprises dual, wide-range (± 0.001 to ± 6536 nT) tri-axial fluxgate magnetometers. These magnetometers are placed at 2/3 and the end of a 12m boom. The length of the boom is sufficient to reduce the spacecraft's magnetic field by up to ± 0.1 nT at the sensor located at the end. The dual configuration eliminates the real-time dipolar part of the spacecraft's magnetic field components. The basic principle of these magnetometers is magnetic induction. The induction magnetometer does not respond to steady or stationary magnetic fields. The induction magnetometer sensitivity increases linearly with the frequency. Therefore, this kind of magnetometer is used in fluctuating (ac) magnetic field measurement. The mathematical details of induction magnetometers can be found in [Ness \(1970\)](#). The MFI uses the ring-core induction

magnetometer. The schematic of the ring-core induction magnetometer can be seen in Figure 2.3.

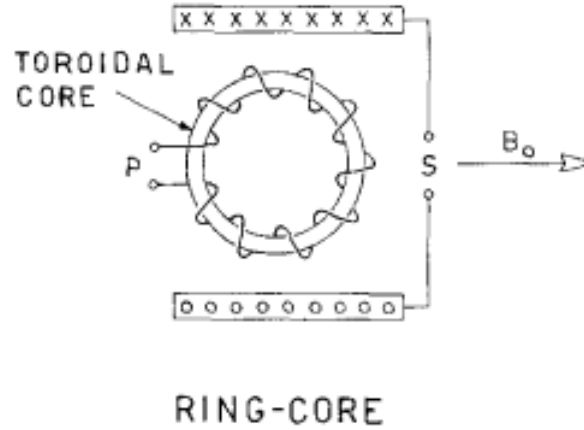


Figure 2.3: Ring core induction magnetometer. (Courtesy: Ness, 1970)

The P and S in Figure 2.3 represent the primary and secondary coils, respectively. The primary coil is wound on the core. Generally, P is used as an input, and S is used as the magnetometer output.

The nonlinear characteristics of a magnetically saturable transformer, a sensing element, are important factors for the operation of a flux-gate magnetometer. The second harmonics of the input can directly give direct details of the external magnetic field. The general principle of operation of fluxgate magnetometers can be seen in Figure 2.4. The nonlinear B-H curve is assumed to be a combination of linear parts. A triangular wave having a frequency of $1/T$ and amplitude of H_D is used as input on the primary coil. The core material inside the primary coil saturates when magnetic field strength, H reaches $\pm H_C$ (See Figure 2.4) and the magnetic induction B reaches $\pm B_S$. Although a sinusoidal wave is generally used, a simple triangular wave is shown here for the sake of simplicity and it will not invalidate the principle of operation (Ness, 1970). Here, it is assumed that the $+\Delta H$ is the bias caused by the external magnetic field.

The secondary/sensing coil observes the resultant waveform and can be seen as B_R in Figure 2.4. The sensing coil works on Faraday's law of magnetic induction and its input depends on the B-H curve of the core material. The induced output

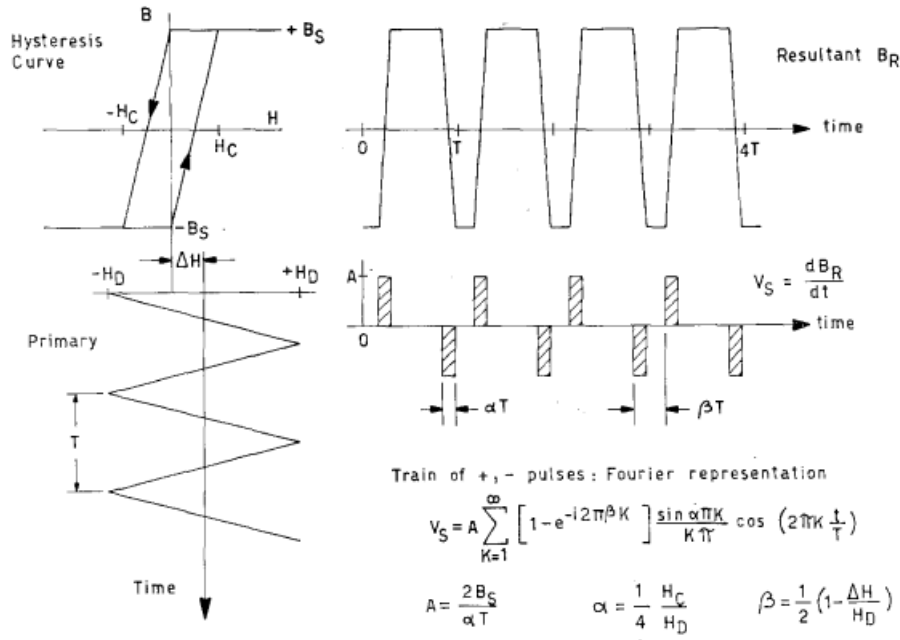


Figure 2.4: Simple principle of operation of Fluxgate magnetometers. (Courtesy: Ness, 1970)

signal in the sensing coil depends on the change in flux, i.e., the time derivative of B_R . This output will be observed when the flux varies, and zero output will be observed when the flux is gated to positive or negative saturation levels. A consistent wave of positive and negative pulses can be seen in Figure 2.4. The width of these pulses is considered as αT , and the separation between successive pulses is βT or $(1 - \beta)T$. The alternating saturation of the core in the opposite direction causes the ‘gated flux’, which is sensed by the secondary coil. The Fourier analysis of the output waveform leads to formulas shown in Figure 2.4. It can be noted that the α is independent of ΔH and β depends on the $\Delta H/H_D$. In case of no external field ($\Delta H=0$), the term in the square bracket of V_S becomes

$$[1 - \cos(k\pi)] = \begin{cases} +2 & k = 1, 3, \dots \text{ odd} \\ 0 & k = 0, 2, \dots \text{ even} \end{cases} \quad (2.8)$$

This suggests that even harmonics come only when the external perturbation ($\Delta H \neq 0$) is present. The second harmonics is used in the calculation because of the decrease in the amplitude of higher harmonics. The amplitude of second

harmonics is the most crucial parameter in calculating the ambient magnetic field direction and magnitude. Now, to identify the relationship between the harmonics and ΔH , some approximations, i.e., $\alpha \ll 1$ and H_D is much larger than ΔH , are used. By taking the ratio of second to first harmonics (r) and by using these approximations, it can be found that the ratio (r) is:

$$r = \frac{1 - 1 + i \sin(2\pi\Delta H/H_D)}{1 + 1 - i \sin(\pi\Delta H/H_D)} = i \frac{\Delta H}{H_D} \pi \quad (2.9)$$

This suggests that the second harmonics is 90° out of phase with the first/primary harmonics. The amplitude of the second harmonics depends on the $\Delta H/H$. So, this overall operation explains the fluxgate magnetometer's principle. More details regarding the more refined measurements can be found in [Ness \(1970\)](#).

2.5 *ACE* Spacecraft

The Advanced Composition Explorer (ACE) was launched on August 25, 1997 at the L1 point for a mission duration of 5 years. However, it is still working and continuously giving solar wind information. The following are the payloads on board *ACE* spacecraft:

- ⇒ Cosmic Ray Isotope Spectrometer (CRIS, [Stone et al., 1998a](#))
- ⇒ Solar Isotope Spectrometer (SIS, [Stone et al., 1998b](#))
- ⇒ Ultra Low Energy Isotope Spectrometer (ULEIS, [Mason et al., 1998](#))
- ⇒ Solar Energetic Particle Ionic Charge Analyzer (SEPICA, [Möbius et al., 1998](#))
- ⇒ Solar Wind Ions Mass Spectrometer and Solar Wind Ion Composition Spectrometer (SWIM and SWICS, [Gloeckler et al., 1998](#))
- ⇒ Electron, Proton, and Alpha-particle Monitor (EPAM, [Gold et al., 1998](#))
- ⇒ Solar Wind Electron, Proton and Alpha Monitor (SWEPAM, [McComas et al., 1998](#))

⇒ Magnetometer (MAG, [Smith et al., 1998](#))

⇒ Real-Time Solar Wind monitors (RTSW, [Zwickl et al., 1998](#))

The data from SWICS and SWIMS are used in this thesis. These two instruments in combination provide the helium and other elemental abundances, charge state of heavier ions in the solar wind etc. The details of these instruments are provided in the next sections.

2.6 Solar Wind Ion Composition Spectrometer (SWICS)

SWICS consists of electrostatic analyzer (ESA), post-acceleration, time of flight (TOF), and energy measurements (Figure 2.5). The details of the SWICS instrument can be found in [Gloeckler et al. \(1998\)](#).

2.6.1 Principle of Operation

The working principle of SWICS can be understood from Figure 2.5. The ions having kinetic energy E , charge Q , and Mass M enter the sensor through a multi-slit collimator with a large aperture. The collimator ensures that only particles with appropriate entrance trajectories are selected. The ions that have a particular E/Q ratio are chosen by the electrostatic analyzer (ESA). A stepped deflection voltage determines these E/Q values. The ESA also uses a UV radiation trap. Subsequently, the ions are accelerated and directed to enter the time-of-flight section. The energy gained by these ions is sufficient to be detected by a solid-state detector at the end of the sensor. The time of flight section provides the speed of different ions based on the time taken by the ion from the start to the end point of the system (distance of 10 cm). The particle energy is measured by the solid-state detector, which completes the identification of the particles. The equations below can be used to identify the ions in the ambient solar wind.

$$M = 2(\tau/d)^2 (E_{res}/\alpha) \quad (2.10)$$

$$Q = (E_{res}/\alpha) / (V_a + E'/Q) \quad (2.11)$$

$$M/Q = 2(\tau/d)^2 (V_a + E'/Q) \quad (2.12)$$

$$E = Q \cdot (E'/Q) \quad (2.13)$$

$$V_{ion} = 438 \cdot (E/M)^{1/2} \quad (2.14)$$

Where M , Q , E , V_{ion} are Mass, charge, energy, velocity of ion. The d is distance between start and end detector (10.5 cm) and t is flight time taken by ion to cover this distance. E_{res} is residual energy, V_a is acceleration potential, α is nuclear defect in solid state detector (Ipavich et al., 1978), E'/Q takes care of the energy loss in the start detector V_{ion} is in km/s and E/M in keV/amu. E' is the energy after a small portion of energy is lost in the carbon foil.

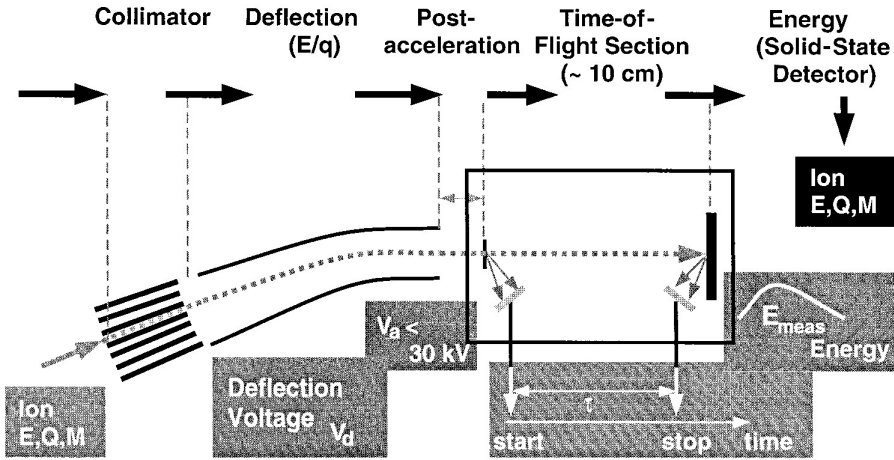


Figure 2.5: The schematic of the measurement technique used in SWICS, illustrating the functions of each basic element involved in the process. (Courtesy: Gloeckler et al., 1998)

2.6.2 Deflection analyzer

An electrostatic deflection analyzer is used in SWICS. There are two separate deflection regions (channels) of the analyzer. One is for H & He, and the other

for all ions. Both the analyzers have 18 plates with a limit of 0.5% dispersion. The resolution of the H/He channel is 5.2%, and that of the main channel 6.4%. Deflection voltage in case of H/He channel varies from 6.91 to 945 V, but in the main channel, it is 46.09 to 6300 V.

The H/He region generally covers the energy range from 0.16 to 15.05 keV/charge. These low-energy particles are accelerated and measured by a single rectangular solid-state detector. Stepping-up of voltage provides the separated E/Q spectra. The main channel has an energy range of 0.49 to 100.0 keV/charge. Figure 2.6 shows both H/He and the main channel of the analyzer.

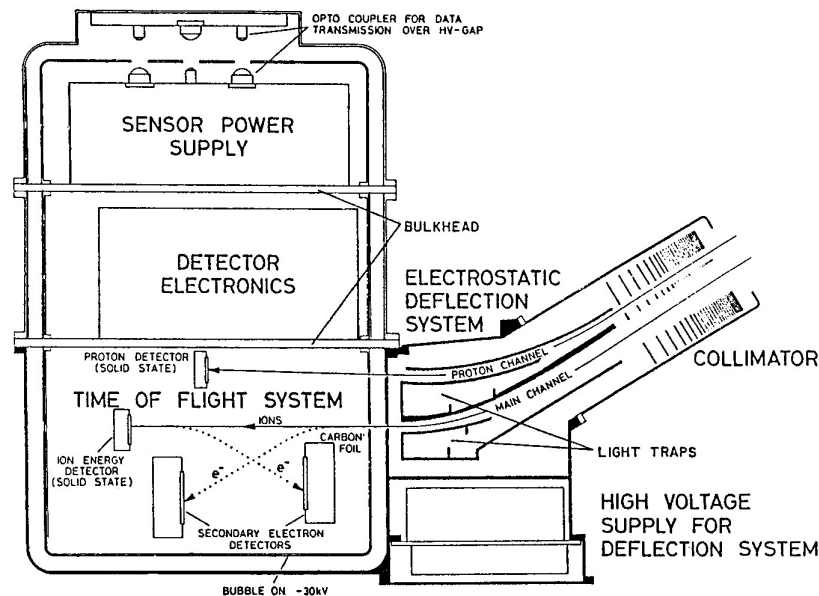


Figure 2.6: Cross section of the SWICS sensor illustrating the key components including the collimator, two-channel deflection system, deflection power supply, time-of-flight system, He/H detector, analogue electronics, and sensor bias and power supply. (Courtesy: Gloeckler et al., 1998)

2.6.3 Time-of-flight vs energy system

For the time of flight system, SWICS uses a carbon foil as a start detector and a solid-state detector (AuSi) as the stop detector as well as the detector for the residual energy measurement. Electrons generated from the start and stop detector are accelerated by 1 kV and collected by the front surface of each chevron-

assembly micro-channel plate (MCP).

A slight difference of 0.2 ns in flight time is generated because of the path difference of the electrons, which is less than ~ 0.5 ns FWHM of analogue electronics. The ion's trajectory will not be significantly affected because of its higher energy. The measurement of residual energy is carried out using one of the three rectangular solid-state detectors. Time of flight system can be understood from Figure 2.7.

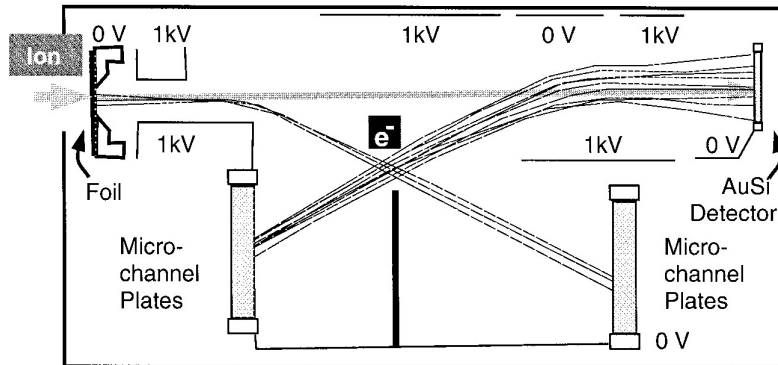


Figure 2.7: Time-of-flight vs energy telescope of SWICS displaying computer-generated trajectories of secondary electrons emitted from the carbon foil and solid-state detector. (Courtesy: Gloeckler et al., 1998)

2.7 Solar Wind Ions Mass Spectrometer (SWIMS)

SWIMS measure solar wind particles with the exceptionally high isotopic resolution of $M/\Delta M > 100$. It determines the density of the elements and their isotopes lying between 3 to 60 amu.

2.7.1 Principle of Operation

Like SWICS, ions with Energy E , mass M , and charge Q enter the electrostatic analyser, which selects a particular E/Q channel. The ESA also acts as a UV trap. Ions passing through the slit are chosen using a Wide-Angle, Variable Energy/charge (WAVE) passband deflection system, as shown in Figure 2.8. WAVE plates are connected with variable voltage supply, which varies in 60 logarithmic

steps (0.6 kV to 12.2 kV). The walls of WAVE also trap UV radiation. E/Q resolution of this system is 5%.

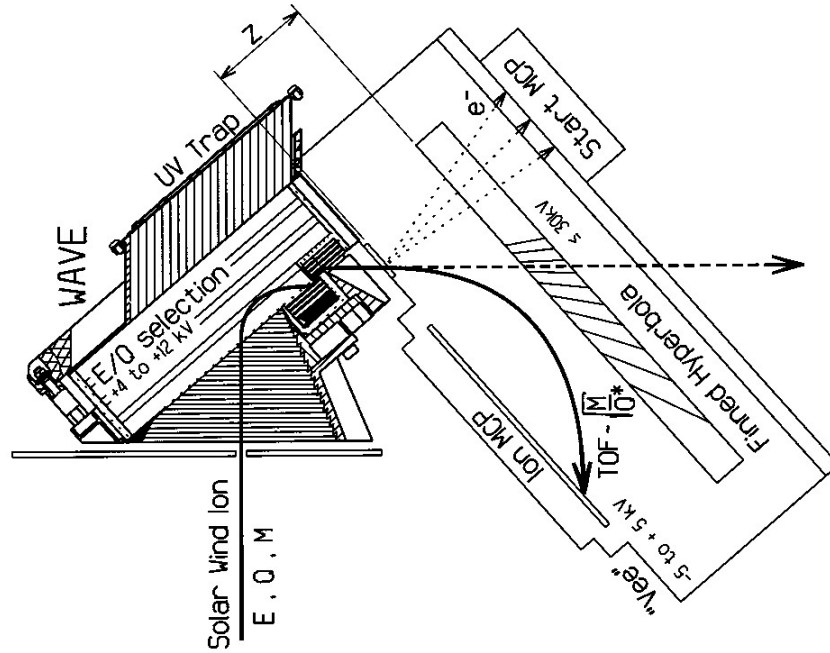


Figure 2.8: Schematic of the SWIMS instrument illustrating the WAVE entrance system, start MCP location, hyperbolic deflection surface, position-sensing stop MCP, and a typical ion trajectory. (Courtesy: Gloeckler et al., 1998)

These ions with specific E/Q ratios will pass through a thin carbon foil and then enter the High Mass Resolution Spectrometer (HMRS) for time-of-flight measurements. The secondary electrons generated from carbon foil will give the start time trigger for the time of flight HMRS system. Subsequently, these positive charges are deflected by the static retarding harmonic potential (V). This voltage (V) applied in the time of flight system is proportional to the square of the perpendicular distance from MCP, i.e. Z ($V \propto Z^2$), as shown in Figure 2.8. Time of flight (τ) in this type of potential depends only on the mass (M) and charge state (Q^*) remaining after the crossing of carbon foil, as written below.

$$\tau \propto (M/Q^*)^{1/2} \quad (2.15)$$

The ions passing from the carbon foil will remain neutral or have a charge of +1 with a minor fraction of +2 and -1 charge states. The above equation and the

2.8 Magnetic Field Experiment (MAG)

The MAG instrument is almost similar to the *Wind*/MFI instrument. The only change is in the Input/Output (I/O) data board. The I/O data board were replaced to change (reduce) the sampling rate of the instrument from 44 vectors s^{-1} to 24 vectors s^{-1} . The basic principle of operation can be seen from the MFI instrument in section 4. The other details regarding the MAG observations can be seen in [Smith et al. \(1998\)](#).

2.9 The Parker Solar Probe (PSP)

The Parker Solar Probe (PSP) was launched on August 12 2018. PSP's main objective is to study the Sun's outer atmosphere, i.e., the solar corona. The probe follows a highly elliptical orbit around the Sun. It carries four suites of scientific instruments, which are discussed below. The spacecraft has a heat shield to withstand intense heat and radiation. The instruments on-board PSP are described below. There are four instruments onboard PSP. But the data from FIELDS and SWEAP are used in thesis.

Electromagnetic Field Investigation (FIELDS)

This instrument measures the electric and magnetic fields. FIELDS measures the electric field using five antennas. Four out of five antennas are fixed beyond the spacecraft's heat shield. The length of these antennas is two meters. The fifth antenna sticks out perpendicular to others in the shade of the heat shield. These five antennae provide the 3D measurements of electric fields. Two identical fluxgate magnetometers, i.e., MAGi and MAGo, are used to measure the magnetic fields. The working principle of MAGi and MAGo is similar to *Wind*'s MFI. More details regarding this instrument can be found in [Bale et al. \(2016\)](#).

Solar Wind Electron Alpha and Protons (SWEAP)

The major constituents of the SWEAP instrument are Solar Probe ANalyzers (SPAN) and Solar Probe Cups (SPC). The SPAN is an electrostatic analyzer, and SPC is a Faraday Cup sensor. The basic principle of SPC is similar to the *Wind*/SWE. The FC is situated at the top of the heat shield. It faces all the

light, heat, and energy from the Sun.

The SPAN is composed of SPAN-A and SPAN-B instruments. These instruments have a wide field-of view. The ions crossing through the ESA are deflected by a series of deflectors and voltages which separate particles based on their mass and charge. SPAN-A measures electrons and ions, whereas SPAN-B only measures the electrons. Further information and additional details can be found in [Kasper et al. \(2016\)](#).

Integrated Science Investigation of the Sun (IS \odot IS)

The instrument consists of two parts: Energetic particle Instruments (EPI) -Lo and EPI-Hi. EPI-Lo measures electron and ion spectra, covering a wide field-of-view with 80 viewfinders. It measures ions from 0.02 MeV/n to ~ 15 MeV total energy and electrons from 25–1000 keV. EPI-Hi measures protons and He nuclei from ~ 1 to ~ 100 MeV/n, with higher energies for heavier elements. It has three telescopes for a wide energy range and field of view: High Energy Telescope (HET), Low Energy Telescope -1 (LET1), and LET2. Further details can be found in [McComas et al. \(2016\)](#).

Wide-field Imager for Solar Probe (WISPR)

The WISPER (Wide-field Imager for Solar Probe) is an optical telescope that takes images of the corona and heliosphere. The WISPER consists of two cameras having radiation-hardened active pixel sensor CMOS detectors. The full detailed description can be found in [Vourlidis et al. \(2016\)](#).

These were the primary instruments from which the data are used in this thesis work. The compiled data (OMNI database) of various solar wind parameters from multiple satellites are also used in Chapter 3. The time duration of the OMNI database is more than 50 years. The details of the OMNI database can be found in the next section.

2.10 OMNI Database

The OMNI web contains two sets of data, i.e., Low-Resolution OMNI (LRO) and High-Resolution OMNI (HRO). All the details of the OMNI database of OMNI web can be found at <https://omniweb.gsfc.nasa.gov/>. The details of LRO can be found at https://omniweb.gsfc.nasa.gov/html/ow_data.html and HRO at <https://omniweb.gsfc.nasa.gov/html/HR0docum.html>. The LRO data have an hourly cadence and HRO data have a 1-minute and 5-minute cadence. We have used the LRO dataset in Chapter 3.

The Low-Resolution OMNI (LRO) dataset is available from 1963 to the present date. This dataset is compiled based on the measurements from a number of spacecrafts. These satellites are/were either in geocentric or orbits around the L1 (Lagrangian point) point. The data have been extensively cross-normalized between different satellites for overlapping periods. The data of the following satellites are used in creating the dataset: IMP 1 to IMP 8, AIMP 1 & 2, HEOS 1 & 2, VELA 3, OGA 5, ISEE 3 & 1, PROGNOZ 10, *Wind*, *ACE* and Geotail. Further details regarding time shift, satellite parameterization, cross-normalization etc. can be found at https://omniweb.gsfc.nasa.gov/html/ow_data.html. *ACE* and *Wind* satellites are significant contributors to this data set. The removal of the outliers are also present e.g., they have taken a simple approach to eliminating most of magnetic field outliers by rejecting any 3-sec record with a magnetic field magnitude or component in excess of 70 nT. For SWE data, they have run a despiking routine requiring (to be a non-spike) that the difference between a parameter value and the mean of the two preceding and two following values should be less than four times the standard deviation. Various methods are employed to calibrate velocities, utilizing different windows. The correlation between spacecraft velocities for distinct velocity windows was established as part of the OMNI data generation techniques. Additional information can be found on the OMNI website. Also, The cross normalization between *ACE* and *Wind* can be found in [King and Papitashvili \(2005\)](#).

2.11 ADAPT-WSA model

we have used the Air Force Data Assimilative Photospheric Flux Transport - Wang-Sheeley-Arge (ADAPT-WSA; [Arge et al., 2010](#)) coronal and solar wind model to identify the sources of solar wind. This model is a combined empirical and physics-based model. This model is an upgraded version of the original WS model ([Wang and Sheeley, 1992](#); [Wang et al., 1995](#)). The ADAPT model produces global synchronic photospheric field maps, which are subsequently utilized as input for the WSA model. The ADAPT model uses magnetic flux transport model ([Worden and Harvey, 2000](#)) for the differential rotation particularly when the observations are unavailable. After getting the input from ADAPT maps, the WSA uses the traditional Potential-field Source-Surface (PFSS) model to determine the coronal fields from the source surface height, i.e., $2.5R_{\odot}$ ([Hoeksema et al., 1983](#)). The outputs of the PFSS model are used as the input to the Schatten Current Sheet (SCS) model ([Schatten, 1971](#)). This SCS model will give us more realistic magnetic field topologies of the corona.

The WSA used with ADAPT provides twelve solutions of solar wind parameters. These solutions represent the comprehensive state of the coronal field and connectivity from a spacecraft to $1R_{\odot}$ for a given time. The optimal output is selected by comparing the model-derived magnetic field and solar wind speed with the observed values. Further details regarding the identification of solar wind sources can be found in work by [Wallace et al. \(2019, 2020\)](#).

Chapter 3

Changes in the helium abundance of the solar wind over the last four solar cycles

Abstract

This chapter deals with the behaviour of helium abundance in solar wind during the last four solar cycles. Fifty years of inter-calibrated A_{He} data obtained from multiple satellites (OMNI) is used to understand the A_{He} behaviour. We show that A_{He} variations and phase offset between the variations in A_{He} and sunspot number change in solar cycle 24 (hereafter, SC24) compared to the last three cycles (hereafter, SC21,22, 23). The solar wind velocity is divided into five windows to understand the change in the frequency distribution of A_{He} . We find that slow and intermediate solar wind shows the maximum changes. The median of the frequency distribution of helium abundance is shifted toward lower values ($A_{He} = 2-3\%$) in SC24 from higher values ($A_{He} = 4-5\%$) in the previous three SCs. This investigation also shows a disproportionate drop in the percentage of events with $A_{He} > 10\%$ in SC24. Further, the changes in the delay of A_{He} with respect to sunspot numbers are less sensitive to changes in velocity in SC24. These distinctive changes started from SC23 and became conspicuous in SC24. Our investigation suggests that the global coronal magnetic field configuration started

undergoing systematic changes started from SC23 and continued in the SC24. These changes in magnetic field configuration affected helium processing in the solar atmosphere and caused changes in its abundance. The role of the changes in the sources of slow and fast winds that are known to have low and high helium abundances respectively, is also believed to be a potentially important factor.

3.1 Introduction

The particles coming out of the Sun constitute what is known as the solar wind (Parker 1965). Solar wind generally has $\sim 95\%$ proton (H^+) as the principal constituent and $\sim 5\%$ helium nuclei (He^{2+}) or alpha particle as the second major constituent. Helium abundance in the solar wind is represented by $A_{He} = (n_{He}/n_p) * 100$, where n_{He} and n_p are the alpha and proton concentrations in the solar wind. Analysis of helium abundance in the solar wind can provide essential clues to the solar processes, the origin of the slow and fast solar wind, and heating processes in the solar corona (Neugebauer et al., 1996; Kasper et al., 2012, 2007). A_{He} in the photosphere is nearly 8.5% (Grevesse and Sauval, 1998; Asplund et al., 2009). However, it remains about 4 – 5% in the solar corona (Laming and Feldman, 2001, 2003). It is also found that the alpha particles have higher velocities than the protons in the solar wind. These higher velocities are reported based on the measurements from Ulysses (Neugebauer et al., 1996; Reisenfeld et al., 2001), Wind (Steinberg et al., 1996), and ACE (Berger et al., 2011).

The variation of A_{He} with solar activity was first indicated by Hirshberg (1973) and Ogilvie and Hirshberg (1974) by comparing these with the variations in the Sunspot numbers (SSN). These authors used multiple satellite data to show the relationship between A_{He} and SSN. Subsequently, Feldman et al. (1978) used IMP satellite data to extend the result of Ogilvie and Hirshberg (1974) and found a delay between the variations in A_{He} and SSN. These authors also realized that A_{He} of fast and slow solar wind needed to be treated differently. Aellig et al. (2001) extended the SC variation of A_{He} using WIND data and found a linear

relationship between the velocity and the A_{He} for the slow solar wind. No such strong association was found to exist for the fast-solar wind. It was also found that the linear relationship between the solar wind velocity and the A_{He} for the slow solar wind is strong during minima however weak during maxima. These authors explained higher values of A_{He} during solar maxima and lower during minima using the expansion factor of the solar magnetic field and Coulomb drag (Aellig et al., 2001).

Further, to understand the variation of A_{He} for slow solar wind, Kasper et al. (2007, 2012) investigated the solar activity variation of A_{He} for approximately one entire SC. These authors proposed two types of slow solar wind sources- one from the streamer belt and the other from the active regions. The active region and the streamer belt sources dominate during solar maxima and minima periods, respectively. As the origins of the fast-solar wind are generally known to be only the coronal holes, these authors attributed the minimal variability of the A_{He} of the fast solar wind with SSN to the coronal hole processes.

The above studies indicate a connection between the sources of the solar wind, their characteristics, and relative abundances at various stages of solar activity and the A_{He} variation. Extending arguments in these lines, Fu et al. (2018) discussed three sources of the solar wind quiet Sun, active regions, and coronal holes. These authors also showed differences in properties of these sources using A_{He} and velocity difference between alpha and proton in the solar wind. They found that coronal holes (CH) generally have higher A_{He} and higher velocity differences. On the other hand, quiet sun (QS) has low A_{He} and low-velocity differences. Interestingly, it was also shown that the composition of the solar wind originating from active regions (AR) and the velocity difference of alpha and proton depend on the phase of the SC. These authors discussed three types of solar wind based on velocity - slow (< 400 km/s), intermediate (between 400 to 500 km/s), and fast (> 500 km/s).

In addition to the dependence on sources, the earlier studies right from the work of Feldman et al. (1978) suggested that it is essential to understand the delay between A_{He} and SSN. The delay between different solar activity indicators like

sunspot numbers (SSN), sunspot area (SA), solar radio flux (F10), solar flare index (FI) etc., were studied by [Ramesh and Vasantharaju \(2014\)](#) and references cited therein. They found that the delay between the solar indices for the three SCs starting from SC21 to SC23 varies from 0 days to 23 months. In recent times, [Alterman and Kasper \(2019\)](#) investigated the delay in A_{He} variation with respect to the variations in SSN and found a linear relationship between the solar wind velocity and the delay. These authors used approximately two SC data from the WIND satellite, extended the work of [Kasper et al. \(2007, 2012\)](#), and found that the delay varies from 100 to 400 days.

The above discussion suggests that although some progress has been made in understanding the relationship of A_{He} with sunspot variation and solar wind velocity, there has been no attempt to investigate these aspects for a more extended period that includes more than two solar activity cycles' of observation. This is important as this will help in evaluating the SC-to-SC variations in A_{He} . This is achieved by extensively analyzing the cross-normalized OMNI dataset for 49 years, available at <https://cdaweb.gsfc.nasa.gov>. The results obtained are discussed in the upcoming sections. The implications of these results are also discussed in the later parts of this chapter.

3.2 Data Section

We have used the OMNI data set. The details of the OMNI data can be found in Chapter 2.

3.3 Results

SC24 is one of the weakest cycles in the last hundred years ([Hathaway, 2015](#)). We performed several extensive analyses of A_{He} data to evaluate the changes in the solar wind helium abundance in SC24 compared to the previous three SCs. A_{He} data is taken at a 1-hour cadence from the OMNI database spanning over half a century encompassing the last four cycles (SC21 to SC24). The general variation of helium abundance in the previous SC can be seen in Figure 3.1. The yearly

averaged A_{He} (red color), and the sunspot number (blue colour) are shown for the years from 1971 to 2022. It can be seen that the A_{He} varies with the SC. If we consider only A_{He} 's maxima value, it decreases from SC21 to SC24. Further detailed analyses are discussed in upcoming subsections.

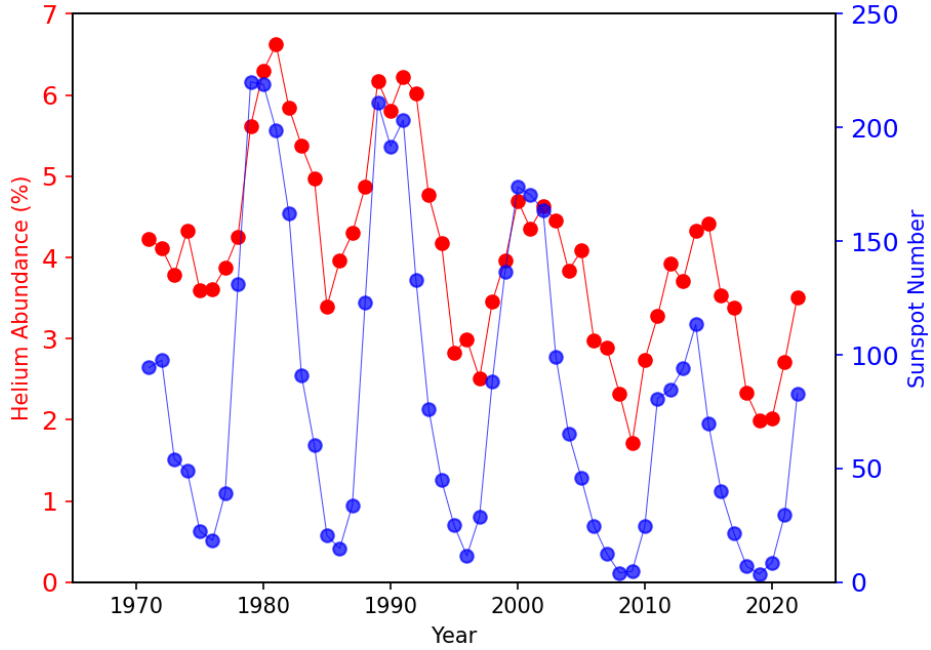


Figure 3.1: Variation in helium abundance: A comparison of the variation in the helium abundance (Red color) with sunspot number (Blue color) in the last 52 years. It is clear that variation in helium abundance follows SC variation.

3.3.1 Frequency of A_{He} events in the last four SCs

To analyze the distribution of A_{He} , we divided the one hourly A_{He} data for each SC in five velocity bins, viz. (1) < 300 km/s, (2) 300-400 km/s, (3) 400-500 km/s, (4) 500-600 km/s, and (5) ≥ 600 km/s. The frequency distributions of A_{He} events are found by using the percentage of occurrence (Frequency) of A_{He} events in a number of A_{He} bins (0-1, 1-2 etc.) in different velocity windows. We note that the frequency distributions could be well-approximated by Log-normal distributions for all the velocity bins except for the bin 300 km/s (Figure 3.2).

$$Frequency = \frac{A}{\sigma\sqrt{2\pi}} \exp\left\{-\frac{(\log(A_{He}) - \mu)^2}{2\sigma^2}\right\} \quad (3.1)$$

$$m = \exp(\mu) \quad (3.2)$$

Equation 3.1 is a general log-normal distribution function where A is the normalization factor, σ is the standard deviation (shape parameter), and μ is the centre (median) of the distribution. Equation (3.2) converts μ from log scale to linear scale. The m in equation 3.2 is the linear counterpart of μ , and this is the median value. The corresponding A , m and μ values are mentioned in each subplot of Figure 3.2 below.

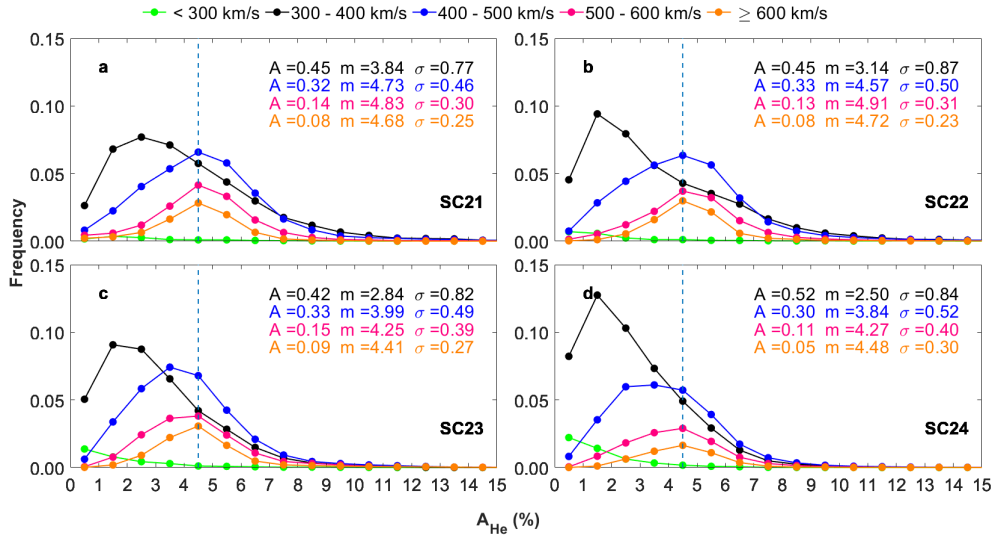


Figure 3.2: Frequency of distribution of A_{He} : Frequency distribution of A_{He} events for four velocity bins, viz. (1) < 300 km/s (2) 300-400 km/s (3) 400-500 km/s (4) 500-600 km/s (6) ≥ 600 km/s in SC21 (a), SC22 (b), SC23 (c) and SC24 (d). Velocity windows are marked with different colours and are shown at the top of the Figure. The frequency distributions are fitted with Log-normal distributions where A (normalization coefficient), σ (standard deviation) and m (median in linear scale) are the fit parameters. The median (m) monotonically decreased for 300-400 km/s and 400-500 km/s velocity windows from SC21 to SC24. Further, the velocity window 400-500 km/s shows a shift in the peak A_{He} from the usual 4-5% (in SC21 and SC22) to 2-3. In addition, an increase in the frequency in the 300-400 km/s velocity bin in SC24 can be observed. The vertical dashed sky-blue lines mark A_{He} of 4.5. It can be seen that the frequency of occurrence of higher A_{He} events ($> 10\%$) events are insignificant in the statistical sense.

The velocity bins 300-400 km/s and 400-500km/s show the maximum change in A_{He} distribution. In addition, these bins contribute almost 75% to the solar

wind. It can be seen that the median value of A_{He} monotonically decreased for 300-400 km/s and 400-500 km/s velocity bin as one goes from SC21 to SC24. However, the median value increased in SC22 for the other two velocity bins before dropping again in SC23 and 24. The most important feature to be noted is the shift of the peak A_{He} in the 400-500 km/s velocity range from the usual 4-5% in SC21 and 22 to 3-4% in SC23, and then this peak shifted towards lower value, i.e., 2-3% in SC24. In addition, there is an increase in the frequency (See parameter A in the Figure 3.2) in the 300-400 km/s velocity range in SC24. It can also be seen that there are a few events above 10%. Therefore, based on Figure 3.2, we fix the upper limit of A_{He} for slow and intermediate winds at 10% and proceed to evaluate the other properties of A_{He} variations for the four SCs in upcoming sections.

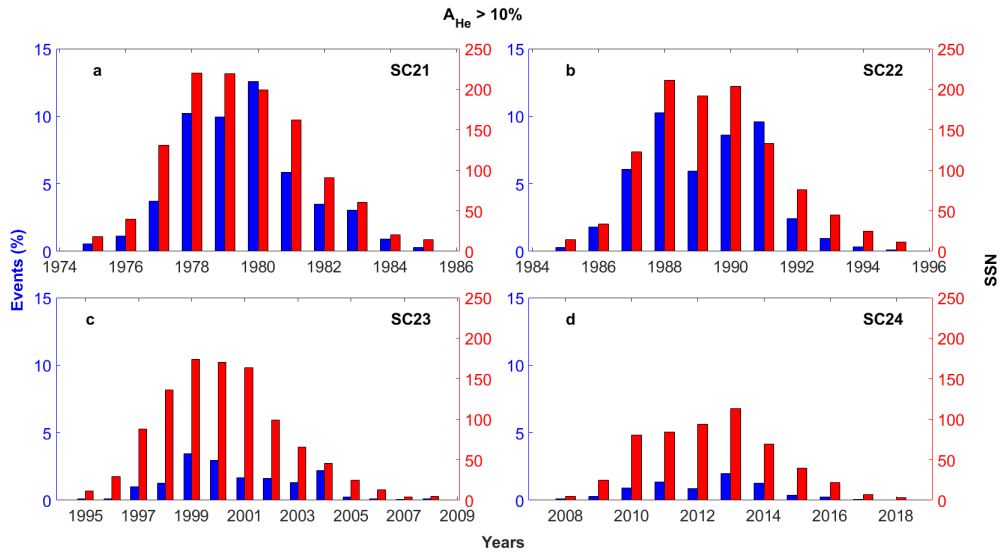


Figure 3.3: Frequency of $A_{He} > 10\%$ events: The yearly frequency of higher A_{He} events ($> 10\%$) events (blue vertical bars) and Sunspot number (red vertical bars) in the last four SCs are shown in subplots a, b, c and d, respectively. This frequency is the ratio of $A_{He} > 10\%$ with respect to the number of all A_{He} events in a particular year. The peak value of the A_{He} frequencies is 12.55%, 10.25%, 3.44% and 1.98% from SC21 to 24. A drastic change in the higher A_{He} event can be observed.

3.3.2 Frequency of A_{He} events higher than 10% in the last four SCs

The higher A_{He} events are usually associated with solar eruptive events (Borrini et al., 1982). The higher events can be used as a proxy for the distribution of the eruptive events. The yearly events distribution having a higher A_{He} value ($>10\%$) is shown in Figure 3.3. It can be observed that these events are drastically reduced in SC24. It can also be noted that these events started reducing significantly from SC23, and by SC24, the frequency of these events did not exceed 2%.

3.3.3 Solar cycle variation of $A_{He} \leq 10\%$

This section divides the solar wind velocity in each SC into 12 quantiles. This division in the quantiles is essential because the number of observations varies according to the solar wind velocity. The fastest and slowest quantiles are neglected to avoid possible measurement uncertainties and expanding velocity range. These analyses are primarily related to slow and intermediate solar wind velocities. The A_{He} and SSN are first averaged for 250 days for each velocity quantile for all the SCs. This exercise is repeated for each SC, and the results can be seen in the subplot of Figure 3.4. The mid-point of each quantile and the corresponding Spearman Rank Correlation co-efficient (CC) between A_{He} and SSN are shown as a legend in each subplot. It can be seen that CC maximizes at 369 km/s, 372 km/s, and 373 km/s in SCs 21, 22 and 23, respectively. In comparison, the CC value maximizes at 401 km/s in SC24. Therefore, CC maximizes at a higher velocity in SC24 compared to the previous three SCs. It is also interesting to note that the variation of CC across different velocity bins and mainly in higher velocity bins are significantly less in SC24. This is not the case in the previous three SCs. There is a continuous decrease of CC in higher velocity bins in SC23-SC24.

We also note a phase offset (delay) between the A_{He} and SSN, however this offset decreases in SC23 and eventually becomes negligible in SC24. The details of this delay and its dependency on solar wind velocity are explored in the next part.

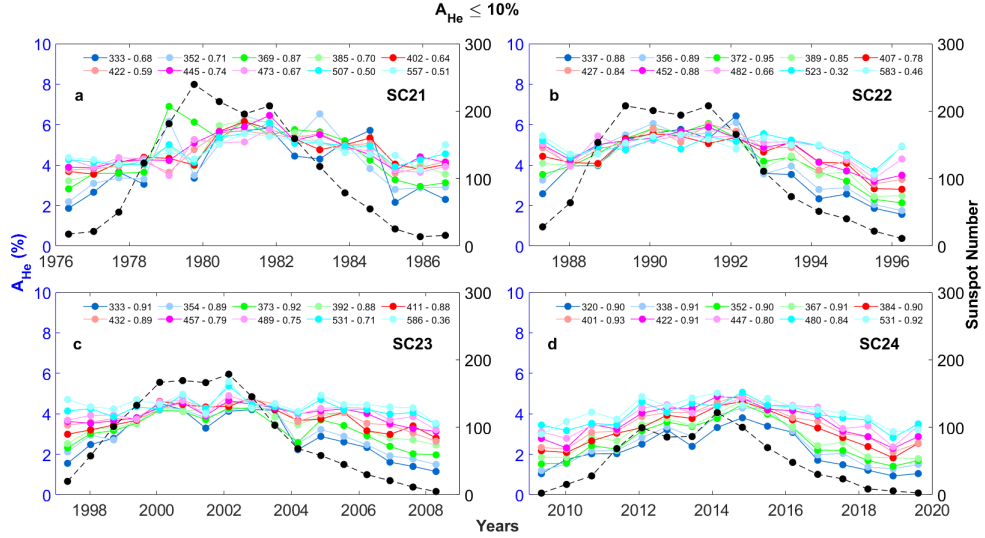


Figure 3.4: Variation of $A_{He} \leq 10\%$: - The variation of averaged (for 250 days) A_{He} and averaged Sunspot number are shown for four SCs. The A_{He} variation is shown for ten velocity quantiles. The Spearman Rank Correlation (CC) between A_{He} and sunspot numbers (SSN) for each velocity quantile in the last four SCs are calculated. Results for SC21 to SC24 are represented in a, b, c and d, respectively. The correlation coefficients (CC) and the mid-point of each velocity quantile are shown as legend on the top of each panel. Different colours mark each velocity quantile (see legend), and SSN variations are marked by black. It can be observed that the velocity 369 km/s, 372 km/s, and 373 km/s have the highest CC in the SCs 21-23, respectively. In contrast, the velocity of 401 km/s shows the highest correlation in SC24.

3.3.4 Phase offset and correlation between A_{He} and SSN for the last four SCs

In this section, we have calculated the time delay between the A_{He} and the SSN. To derive the phase offsets between A_{He} and SSN for four SCs, the A_{He} and SSN were 1-day averaged. However, the major problem was that this phase offset varied with the A_{He} and SSN smoothing window. Therefore, we have done a sensitivity test to choose a proper smoothing window. We have calculated the variation in the delays between the SSN and the A_{He} for the different smoothing windows in steps of 40 days. We have also computed Spearman's correlation coefficients for each smoothing window. The variation in the delay with smoothing

varies for lower smoothing windows, and the variation varies less for the higher smoothing window. This exercise was repeated for all the quantiles for all the SCs. Similar behaviour was observed for most of the velocity quantiles except a few.

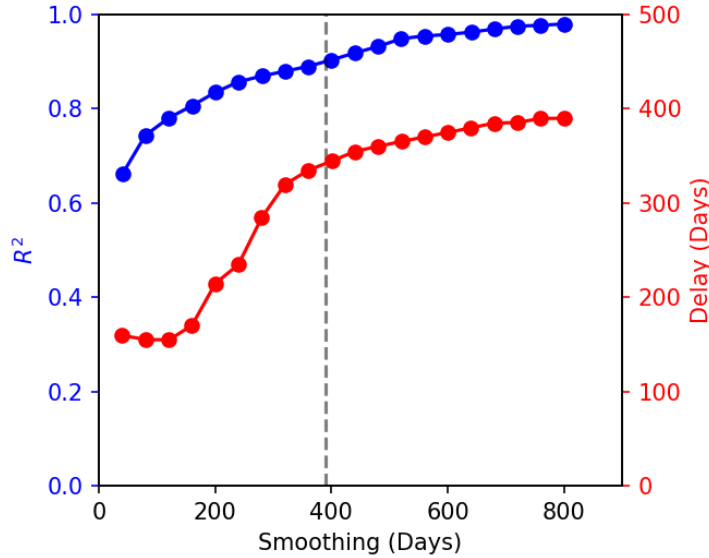


Figure 3.5: Sensitivity analysis - 1: This sample case is for the 456.5 km/s velocity quantile of SC23. The variation of R^2 and the delay (in days) with respect to smoothing applied. The dashed black vertical line is at 390 days. It can be noted that the variation in delay is not significant when smoothing beyond 390 days is applied.

Two sample cases are presented below in Figures 3.5 and 3.6. The sample cases are 456.5 km/s velocity quantile from SC23 and 401 km/s velocity quantile from SC24 with A_{He} limit of 10%. It can be seen from Figures 3.5 and 3.6 that there is no significant variation in the delay as we go towards higher smoothing window. After the sensitivity analysis, we decided to use 390 days (13 months) of smoothing. Ramesh and Vasantharaju (2014) also used the 13 months' of smoothing for calculating the delay/phase offset between different solar activity indicators like sunspot numbers (SSN), sunspot area (SA), solar radio flux (F10), solar flare index (FI) etc.

Note that smoothing window of 13 months also helps to remove the discreteness in the data. In addition, there is a six-monthly periodicity in the helium

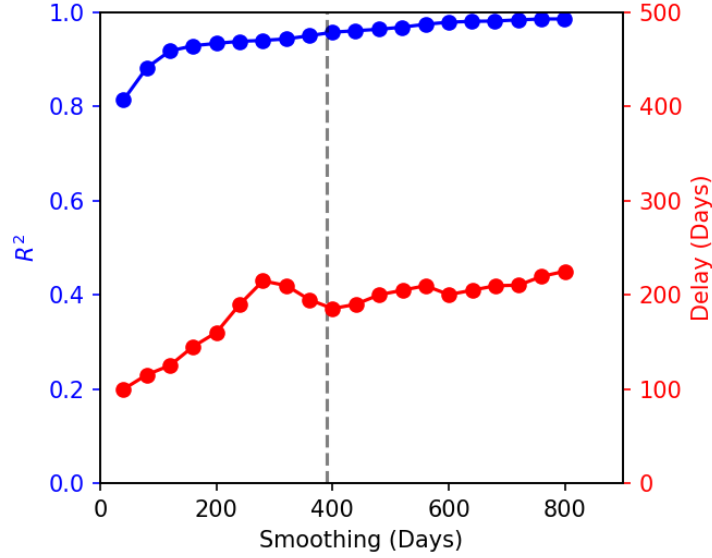


Figure 3.6: Sensitivity analysis- 2: This sample case is for the 401 km/s velocity quantile of SC24. The variation of R^2 and the delay (in days) with respect to smoothing applied. The dashed black vertical line is at 390 days. Similar to the previous case, the variation in delay with the smoothing period is small when we increase the smoothing beyond 390 days.

abundance data (Kasper et al., 2007) because of the orientation of the heliospheric current sheet with respect to the satellites. A 13 month’s smoothing window also removes this six-monthly periodicity.

To calculate the delay, SSNs are shifted in steps of 10 days starting from 0 to 600, and the peak Spearman rank correlation coefficients, CC, are obtained for each velocity quantile. The delay for this peak CC corresponds to the delay for the given velocity quantile. These results are plotted in Figure 3.7, which shows CC without delay in the dashed blue line and the peak CC with delay in the solid blue line for each velocity quantile. The delays at different velocity quantiles are marked in filled black circles joined by the dashed line. The positive delay means changes in A_{He} follow the changes in SSN. The standard deviations are also plotted. It can be observed that the CC maximizes between 350-400 km/s in all four SCs. However, the slopes of the linear fits (the fit equations are mentioned in the subplots of Figure 3.7) for delay are significantly reduced in SCs 23-24. We note that the delay for even the highest velocity quantile does

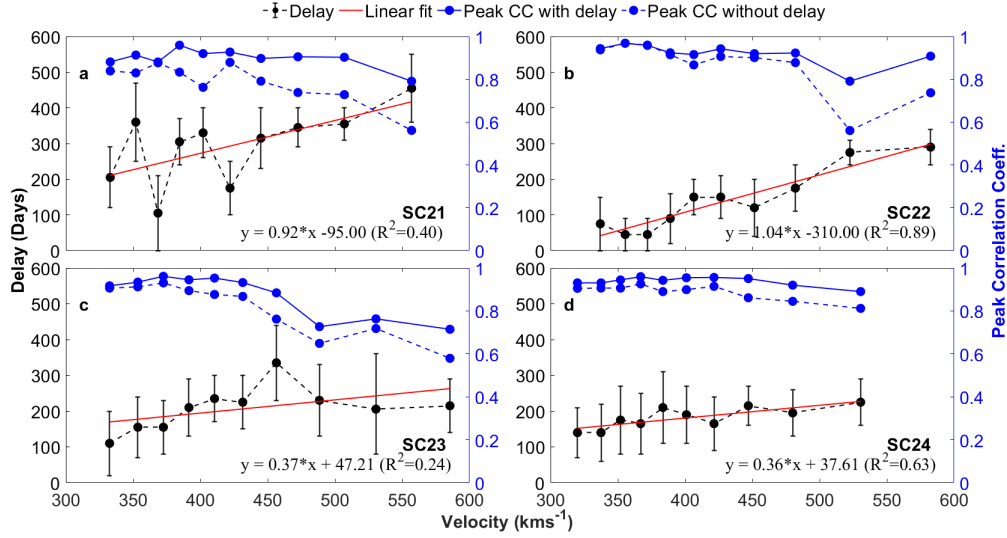


Figure 3.7: Delay and correlation between A_{He} ($\leq 10\%$) and SSN. The delay variation (dashed black line) between SSN and A_{He} for each velocity quantile. These variations are marked by a, b, c and d for SCs 21 to 24, respectively. Peak correlation coefficients between SSN and A_{He} with (solid blue line) and without (dashed blue line) delay for each velocity quantile are also plotted for each SC. A linear line is fitted (red colour) in the delay variation, and the fitting equation and R^2 values are shown in each panel. The maximum peak correlation coefficient between 350-400 km/s in all four SCs can be observed. However, the slopes of the linear fit equations in SCs 23-24 and particularly in SC24 are significantly less than the previous two SCs, i.e., SC21-22. It can be observed that the dependence of delay on velocity is considerably less, or the delay for each velocity quantile is not varying much in SC24.

not exceed 200 days in the case of SC24. Not only that, the differences in delay between the lowest and highest quantiles are not significantly different. This suggests that the dependence of delay on velocity is reduced in SC24.

We varied A_{He} from 4% to 10%, and linear fit parameters were obtained in each case. Here, the 4% bin encompasses all A_{He} values below 4%. All the other bins are constructed in a similar manner, representing A_{He} values below their respective percentage thresholds. The fitting parameters are shown in Table 3.1. In the table, m is the slope, c is the intercept, and R^2 is the linear regression coefficient. Slopes are highlighted in grey colour. It is found that the slopes remain consistently higher (close to 1 or more) in SCs 21 and 22 and consistently

lower (the highest value of the slope is 0.64 at $A_{He} = 5\%$) in SC24 for all values of A_{He} .

SC	Modelled parameters	A_{He} limit						
		4%	5%	6%	7%	8%	9%	10%
21	m	1.85	1.12	1.34	1.58	1.35	1.11	0.92
	c	-508.24	-56.89	-157.70	-285.37	-262.95	-143.45	94.93
	R^2	0.39	0.22	0.42	0.54	0.61	0.61	0.40
22	m	2.06	2.22	2.04	1.69	1.27	1.08	1.04
	c	-671.54	-756.51	-688.91	-543.61	-389.24	-310.99	-309.99
	R^2	0.75	0.0.84	0.82	0.64	0.86	0.85	0.89
23	m	0.99	1.90	1.66	1.95	0.60	0.30	0.30
	c	-153.54	-498.31	-419.18	-531.84	-28.42	78.65	47.21
	R^2	0.56	0.97	0.75	0.94	0.35	0.16	0.24
24	m	0.35	0.64	0.62	0.55	0.43	0.32	0.36
	c	55.19	-54.05	-50.91	-22.36	16.14	56.87	37.61
	R^2	0.21	0.81	0.69	0.50	0.63	0.41	0.63

Table 3.1: Linear fit parameters between the phase offset and velocity for different A_{He} limits: The limit of A_{He} is varied from 4% to 10% in steps of 1%, and the corresponding delays are estimated. The linear fit parameters can be seen in the Table. These parameters include slope (m), intercept (c) and the goodness of fit coefficient (R^2). The rows corresponding to the slope in each SC have a grey background. It is found that the slopes remain consistently higher (close to 1 or more) in SCs 21 and 22, whereas the slopes are always lower (the highest value of the slope is 0.64 at $A_{He} = 5\%$) in SC24 for all the limits of A_{He} . In SC23, the slopes remained higher when A_{He} was between 4%-7% and decreased when A_{He} was between 8% to 10%.

3.4 Discussion

The helium abundance varies significantly in the solar atmosphere. The photospheric value of helium abundance is nearly 8.5% (Grevesse and Sauval, 1998), however it depletes at higher heights in the solar atmosphere. This A_{He} value

reduces to 4 – 5% in the solar corona (Laming and Feldman, 2001). The A_{He} value can vary in solar wind depending on the SC activity. This value can vary depending on the processing of helium at different longitude, latitude and heights in the solar atmosphere (Moses et al., 2020). This general reduction in helium abundance suggests that the helium abundance is depressed by processes occurring in the chromosphere, transition region and corona. Helium is heavier than hydrogen, therefore it does not follow the Parker Mechanism (Parker 1965) of solar wind. The helium feels more gravitational pull and experiences enhanced gravitational settling (Hirshberg, 1973). The other essential processes which can contribute to this depletion are First Ionisation Potential (FIP) effect (Laming, 2015) and Coulomb drag (Geiss et al., 1970).

The FIP effect is the primary process that can alter the solar atmosphere's composition. In this process, the elements with lower FIP get enhanced, and the higher FIP elements are depleted in the closed magnetic field regions. In simple words, the ions are lifted upward because of the pondermotive forces caused by the upward or downward propagating waves in the solar corona and solar chromosphere (Laming, 2012; Rakowski and Laming, 2012). Therefore, the ions (Low FIP elements), which are ionized at lower heights, are lifted towards higher altitudes and enhanced. The low FIP ions are released into the corona whenever these magnetic loops open up due to magnetic reconnection. This phenomenon enhances the abundance of lower FIP elements in the corona, implying that it reduces the higher FIP elements. Therefore, this effect suggests that if there are any changes in the coronal magnetic loop configuration from one SC to another, these changes will be reflected in the helium processing and its abundance in the solar atmosphere.

It is also important to understand the sources of the solar wind, which can have helium abundance variation. Generally, the fast wind comes from the coronal holes. The streamers, quiet Sun and active regions are considered the sources of slow and intermediate wind (Fu et al., 2018). Similar sources, i.e. streamer belt and active region, are also proposed by Kasper et al. (2007). The active regions have stronger magnetic fields compared to the streamer belt. At the same time,

streamer belts have longer magnetic loops as compared to the active regions. It was suggested that helium is processed more inside the streamer belts because of the higher loop length, and this higher processing causes the lower value of helium abundance. These authors also suggested that A_{He} is higher in the solar wind coming from the active region. The interplay between the dominance of streamer belt and active region causes the SC activity variation in the helium abundance. This interplay between sources and the processing of helium abundance leads to the delay or phase shift with respect to the sunspot numbers variation. Interestingly, this delay is solar wind velocity dependent (Alterman and Kasper, 2019). However, we found out that this processing seems to have become less sensitive to solar wind velocity starting from SC23.

In addition, pseudostreamers are considered slow wind sources (Crooker et al., 2012). The pseudostreamers generally have only a one-foot point with a single magnetic polarity, whereas streamers have two-foot points corresponding to different magnetic field polarities. The occurrence of pseudostreamers is higher during the minimum of the SC23, whereas these structures almost disappeared in the SC21 and SC22 (Owens et al., 2014). These authors also showed that the dipole streamers were less tightly confined to the solar equator at the end of SC23 compared to the previous two SCs. These differences in the sources, i.e., pseudostreamers and dipole streamers properties at the end of SC23 with respect to the earlier SCs 21 and 22, may have caused the changes in the solar wind helium processing. These changes are reflected in the helium abundance distributions and phase offset.

Some researchers suggest the boundaries of the coronal holes as slow solar wind sources (Levine et al., 1977; Wang and Sheeley, 1990). In a general picture, the magnetic field expansion from the coronal holes decides the bulk flow speed of solar wind. The expansion of magnetic field lines and bulk speed of solar wind are anti-correlated. This reduction in the bulk flow speed results in the low proton flux coming out from the boundaries of the coronal holes. This reduced proton flux beyond $2.5 R_{\odot}$ can be one of the reasons for the decrease in the alpha particle abundance in the solar wind because of the reduction in momentum transfer

via Coulomb collisions (Bürigi, 1992). This process is particularly dominant for the solar minimum when these magnetic flux tubes undergo strong expansion. We hypothesize that global scale magnetic flux tube topologies are changed in SC24, which started from SC23. These changes affected the processing of helium together with the velocity dependence of the phase offset between helium enrichment and sunspot number. This hypothesis gets indirect support from Janardhan et al. (2018) where these authors showed the unusual reversal of the polar field.

The higher A_{He} events are generally associated with transient coronal disturbances like solar flares, coronal mass ejections, eruptive prominences etc. (Borrini et al., 1982). The details of these are discussed in chapter 4 also. The frequency of occurrence of such transient events is approximately in phase with the SC (Borrini et al., 1982). A similar observation can be seen in Figure 3.3. The drop in high A_{He} events can be because of the reduction in the number of X, M and C-class flares in SC23 compared to the earlier SCs 21 and 22 (Hudson et al., 2014). The number of these flares is even lesser in SC24.

As discussed earlier, SC24 has been the weakest in the last century. The observations from Ulysses from its first (SC22) and third orbit (SC23) revealed that the solar wind in the minimum of SC23 was weaker than SC22 (McComas et al. 2008). These changes in SC23 can be characterized by number density reduction, cooler wind and momentum flux compared to the first orbit during the solar minimum in SC22. Earlier researchers have also shown the distinctiveness of the SC24 (Antia and Basu, 2013). Janardhan et al. (2011) and Choudhuri et al. (2007) highlighted the declining solar activity from SC23 onwards based on observations and dynamo models, respectively. Therefore, combining these results with our results suggests that the Sun's global large-scale coronal magnetic field topology changed significantly in SC24. The changes in helium processing and phase offset are the product of these magnetic field changes.

To summarize, helium abundance can be used as a proxy to understand the strength of solar activity SC. The claim of the onset of SC25 based on the variation in helium abundance is reinforced by Alterman et al. (2021).

3.5 Summary

The present chapter can be summarised in the form of the following points.

1. The median of the frequency distribution of helium abundance is shifted towards a lower value in SC24 compared to SC21 to 23.
2. The higher A_{He} events ($>10\%$) are also reduced in SC24.
3. The delay between the A_{He} and sunspot variation is reduced in SC24 as compared to SC21-SC23
4. This delay is velocity dependant and this dependence of delay on velocity is reduced in SC24.
5. Our results suggest that large-scale global coronal magnetic fields started changing in SC23, which became conspicuous in SC24. This change determined the way helium got processed in the solar corona through FIP effect.
6. The changes in the sources of solar winds can also play a significant role in the A_{He} variations observed during SC24.

Chapter 4

Changes in the Helium abundance in the interplanetary Coronal Mass Ejection structures

Abstract

The relative abundance of alpha particles with respect to protons is known to respond to solar activity and solar wind velocity. The A_{He} is 8% in the photosphere and can go up to 30% in ICMEs. This chapter contains the study of A_{He} enhancement inside the interplanetary Coronal Mass Ejection (ICME) structures. The relationships between different compositional proxies of ICME and A_{He} are explored in detail and this exercise suggests that local coronal heating and the FIP effects are not the only factors that control the A_{He} enhancement in ICME. We show that the timing and strength of the flares preceding the ICMEs are important drivers that control A_{He} enhancement in the ICMEs. We propose that chromospheric evaporation combined with the sludge effect (sludge of enhanced helium formed due to gravitational settling) determine the degree of A_{He} enhancement in ICME structures.

4.1 Introduction

In the last chapter, we discussed about the helium abundance (A_{He}) variation in the ambient solar wind. It is known that A_{He} follows the solar cycle variation and depends on the solar wind velocity. It was also found that there is a delay between the sunspot number variation and the A_{He} variation. It was observed that background solar wind properties have changed in solar cycle 24 in terms of A_{He} variations (Chapter-3). These differences in the A_{He} variations during solar cycle 24 suggest a significant change in the large-scale coronal magnetic field topologies and dynamics as well as the sources of the slow and fast winds. In Chapter 3, events with $A_{He} > 10\%$ are not considered to remove eruptive events from the database.

This chapter deals with the variation of A_{He} during the passage of interplanetary coronal mass ejections (ICMEs) at the L1 point. Earlier works showed that A_{He} enhancement could be used to identify the ICMEs (Hirshberg et al., 1972; Borrini et al., 1982). In this context, it is essential to note that various proxies are reported in the literature to identify the arrival of ICMEs in the heliosphere. These proxies are discussed by Zurbuchen and Richardson (2006). In their work, the ICME signatures are divided into several broad categories based on the variations in the magnetic field (B), plasma dynamics (P), plasma composition (C), plasma waves (W), and suprathermal particles. Our primary focus here is the compositional signatures of ICMEs. A few of these reported signatures are (a) high Helium abundance (Hirshberg et al., 1972; Borrini et al., 1982), (b) enhancement in the minor ions, (e.g., Bame et al., 1979; Wurz et al., 2001), (c) enhanced charge states of iron (Bame et al., 1979; Lepri and Zurbuchen, 2004) and oxygen (Galvin, 1997; Rodriguez et al., 2004), (d) enhancement in FIP bias in low FIP elements (Fe/O, Mg/O) (Zurbuchen et al., 2016), as well as (e) He^+ enhancement (Gosling et al., 1980) in some cases. To make things complicated, not all the ICMEs show all the compositional signatures discussed above.

The compositional anomalies of ICMEs hold important clues to the conditions prevalent near the solar surface during the CME initiation process. As a consequence, ionic charge states are essential proxies for understanding the formation

of ICMEs. These charge states carry information about the electron temperature near the solar surface ($1 - 5R_{\odot}$). Near the Sun, the recombination and ionization time scales are less than the expansion time of the ejecta/magnetic cloud associated with CME. As the CMEs expand, the recombination time scale increases because of the rapid decrease in the electron density (Hundhausen et al., 1968) with height. At a particular height, when the recombination time scale becomes more than the expansion time scale of the plasma structure, the ionization states of a species get frozen (Gruesbeck et al., 2011, 2012). This is known as the freeze-in temperature. The freeze-in heights differ for different elements depending on the specific ion and electron concentration. Therefore, if the coronal plasma is in ionization equilibrium at any given height in the solar atmosphere, the charge states can throw light on the local electron temperature. Usually, the average charge states of other elements are elevated in the CMEs. Such enhancement or anomalies exist in 85% or more CMEs (Richardson and Cane, 2004; Zurbuchen and Richardson, 2006). Henke et al. (1998, 2001) observed the high oxygen charge states in the ICMEs, and Reinard et al. (2001) characterized ICMEs on the basis of $O^{7+}/O^{6+} > 1.0$. A correlation was shown between the charge states and associated flare magnitude, indicating the enhanced charge states originate from the flare-heated region of the corona.

Zurbuchen et al. (2016) showed the enhancement of the lower FIP elements (Mg/O, Si/O, Fe/O) together with Ne/O and S/O for ICMEs in the Carrington rotation 1975 (CR1975) in 2001. They also found that the C/O ratio depletes in ICMEs. They also found a strong correlation between the low FIP proxies, and the correlation is found to improve when the compositionally hot CMEs ($Q_{Fe} > 12$) are considered. There are also reports of a good correlation between Mg/O and the average Q_{Fe} or O^{7+}/O^{6+} (Richardson and Cane, 2004). A good correlation was observed between the Fe/O and the Ne/O, which was unexpected as Ne is a high FIP element and Fe is a low FIP element (Zurbuchen et al., 2016). Correlations between compositional proxies related to FIP and coronal temperature can help to understand the processes that cause the enhancement of a particular proxy. This, in turn, can help to understand the coronal processes in

Table 4.1: The table is taken from [Zurbuchen and Richardson \(2006\)](#). The in-situ signatures of ICMEs are collected from various authors. These signatures are divided in several broad categories based on the variations in the magnetic field (B), plasma dynamics (P), plasma composition (C), plasma waves (W), and suprathermal particles (S).

Signature	Description	Selected references
B1: B Rotation	$\gg 30^\circ$, smooth	Klein and Burlaga (1982)
B2: B Enhancement	$> 10\text{nT}$	Hirshberg and Colburn (1969); Klein and Burlaga (1982)
B3: B Variance decrease		Pudovkin et al. (1979); Klein and Burlaga (1982)
B4: Discontinuity at ICME boundaries		Janoo et al. (1998)
B5: Field line draping around ICME		Gosling and McComas (1987); McComas et al. (1989)
B6: Magnetic clouds	(B1, B2 and $\beta = \frac{\sum nkT}{B^2/(2\mu_0)} < 1$)	Klein and Burlaga (1982); Lepping et al. (1990)
P1: Declining velocity profile/expansion	Monotonic decrease	Klein and Burlaga (1982); Russel and Shinde (2003)
P2: Extreme density decrease	$\leq 1\text{ cm}^{-3}$	Richardson et al. (2000a)
P3: Proton temperature decrease	$T_p < 0.5T_{\text{exp}}$	Gosling et al. (1973); Richardson and Cane (1995)
P4: Electron temperature decrease	$T_e < 6 \times 10^4\text{ K}$	Montgomery et al. (1974)
P5: Electron Temperature increase	$T_e \gg T_p$	Sittler and Burlaga (1998); Richardson et al. (1997)
P6: Upstream forward shock/"Bow Wave"	Rankine-Hugoniot relations	Parker (1961)
C1: Enhanced α / proton ratio	$\text{He}^{2+}/\text{H}^+ > 8\%$	Hirshberg et al. (1972); Borrini et al. (1982a)
C2: Elevated oxygen charge states	$\text{O}^{7+}/\text{O}^{6+} > 1$	Henke et al. (2001); Zurbuchen et al. (2003)
C3: Unusually high Fe charge states	$\langle Q \rangle_{\text{Fe}} > 12; Q_{\text{Fe}}^{>15+} > 0.01$	Bame et al. (1979); Lepri et al. (2001); Lepri and Zurbuchen (2004)
C4: Occurrence of He^+	$\text{He}^+/\text{He}^{2+} > 0.01$	Schwenn et al. (1980); Gosling et al. (1980); Gloeckler et al. (1999)
C5: Enhancements of Fe/O	$\frac{(\text{Fe}/\text{O})_{\text{CMH}}}{(\text{Fe}/\text{O})_{\text{phloghtere}}} > 5$	Ipavich et al. (1986)
C6: Unusually high $^3\text{He}/^4\text{He}$	$\frac{(^3\text{He}/^4\text{He})_{\text{cME}}}{(^3\text{He}/^4\text{He})_{\text{chotosobone}}} > 2$	Ho et al. (2000)
W1: Ion acoustic waves		Fainberg et al. (1996); Lin et al. (1999)
S1: Bidirectional strahl electrons		Gosling et al. (1987)
S2: Bidirectional \sim MeV ions	2nd harmonic $> 1^{\text{st}}$ harmonic	Palmer et al. (1978); Marsden et al. (1987)
S3: Cosmic ray depletions	Few % at $\sim 1\text{GeV}$	Forbush (1937); Cane (2000)
S4: Bidirectional cosmic rays	2nd harmonic > 1 st harmonic	Richardson et al. (2000 b)

more detail. The scientific objective of the work in this chapter is to understand the possible reasons behind the enhancement of A_{He} for some ICMEs and the absence of enhancements for others. As stated, the physical processes behind the enhancements or lack thereof are not understood comprehensively to this date (Manchester et al., 2017). Elliott et al. (2018) showed A_{He} is a good indicator for ICMEs in the outer heliosphere. However, it is known that A_{He} shows solar cycle variation at slow and intermediate solar wind velocities (Kasper et al., 2007; Alterman and Kasper, 2019). Therefore, it is difficult to identify a threshold level beyond which A_{He} enhancements can be seen as a true enhancement associated with the ICME as it passes through the L1 point since A_{He} in the ICME is mixed up with the A_{He} in the ambient solar wind Richardson et al. (2003). Further, although helium is a high FIP element, it shows photospheric values in many ICMEs. Therefore, it is crucial to understand the physical processes that cause enhancements in A_{He} in some ICMEs.

Enhanced A_{He} at 1 AU was also observed in the past and was associated with interplanetary (IP) shocks (e.g., Borrini et al., 1982). However, some authors (e.g., Fenimore, 1980) reported that A_{He} enhancement can also happen without preceding IP shock. Borrini et al. (1982) suggested that enhanced A_{He} in the solar wind at 1 AU indicates the arrival of ejecta from the solar eruptive events. They concluded based on the high ionization temperature observed during these events. The ejecta brings out additional loads of gravitationally settled helium (Hirshberg et al., 1970). Neugebauer and Goldstein (1997) proposed the 'sludge effect' in which the eruptive events take out gravitational settled helium. As gravitational settling is always present, it is unclear how the enhancement of A_{He} selectively occurs in certain ICMEs and not in a few other ICMEs. On the other hand, Fu et al. (2020) suggested that the enhancement in helium abundance is caused by chromospheric evaporation. As chromospheric abundance of helium is not expected to be drastically different from the photospheric abundance of A_{He} which is known to be $\sim 8\%$ (Grevesse and Sauval, 1998), it is obvious that chromospheric evaporation alone cannot explain the enhancement in A_{He} above 8%. Therefore, the variability of A_{He} enhancements in ICMEs, particularly

enhancements beyond 8% or the absence of enhancement on some occasions, remain unresolved till date. In this chapter, we take a holistic approach, evaluate all the processes that may cause A_{He} enhancements in ICMEs and address this issue of variability of A_{He} enhancements in ICMEs.

4.2 Data and ICME selection

The measurements from the Solar Wind Ion Composition Spectrometer (SWICS) instrument onboard the ACE (Advanced Composition Explorer) satellite are used in the present study. The details of SWICS–ACE can be found in Chapter 2. Here we have used the two-hourly data of different elemental compositions and charge states. This data set contains data from 04 February 1988 to 21 August 2011 for several elements and their charge states. On 22 August 2011, ACE/ SWICS entered a different state due to hardware degradation caused by radiation-induced defects. After this incident, another approach (Shearer et al., 2014) was used to get the compositional data. A few compositional observations were possible using this indirect and modified approach. Details on the data before and after the change in approach can be found at <http://www.srl.caltech.edu/ACE/ASC/level12/index.html>. The one-hourly helium and hydrogen ratios are used from the ACE/SWEPAM data (McComas et al., 1998).

In this work, the ICME catalogue compiled by Richardson and Cane (2004, 2010) and available at <http://www.srl.caltech.edu/ACE/ASC/DATA/level13/icmetable2.htm> is used to identify the ICME events and their arrival at the L1 point. The ICME selection criterion is based on multiple ICME indicators like enhancement in O^{7+}/O^{6+} , average Q_{Fe} , magnetic field signatures, streaming bi-directional electrons, etc. The details regarding the selection criteria can be found in Richardson and Cane (2004). The start and end times of the passage of ICMEs at the L1 point are determined based on the behaviours of different compositional indicators or plasma/magnetic field observations (Richardson and Cane, 2010; Cane and Richardson, 2003). The ICME list is categorized into three classes: ICME with full magnetic cloud (MC) characteristics, ICMEs showing

magnetic rotation but lacking few properties like enhancements in the magnetic field (Partial MC), and ICMEs without most of the MC characteristics (Ejecta).

In addition, we have considered only those events for which the data are available for more than 6 hours. The parameters used in this work are averaged for the entire duration of the passage of ICME through the L1 point, i.e., each point corresponds to a particular ICME. The ICME boundaries are marked based on the timings provided in [Richardson and Cane \(2010\)](#). A total of 319 ICMEs are considered in the present work, out of which ICMEs with more than 6 hours of data are found to be 275. The number of ICMEs having magnetic cloud (MC), partial MC and ejecta are 86, 92 and 97, respectively. The ambient solar wind data are averaged for 24 hrs and the averaging stops 12 hours before the ICME event. If two conjugative ICMEs exist, then no ambient solar wind reaching the trailing ICME is considered. The number of ambient solar wind events is 184.

4.3 Role of background conditions

Background conditions can play an important role in controlling the A_{He} value. Background A_{He} is solar cycle-dependent ([Kasper et al., 2007](#); [Alterman and Kasper, 2019](#)). Therefore, the solar cycle variation of A_{He} for the ICME duration is investigated for SC23 and 24 to understand the background contribution in the A_{He} enhancements during ICMEs. This is done as the ICME related enhancements of A_{He} are expected to be over and above the background A_{He} . In the upper panel of [Figure 4.1](#), the red and black lines in the background show the individual ICME averaged A_{He} and sunspot number (SSN). The red and black dots are the yearly averaged SSN and A_{He} averaged over the ICME durations for a given year.

Interestingly, the yearly ICME averaged A_{He} , and SSN shows a good correlation ($R^2 = 0.63$), as shown in the lower panel of [Figure 4.1](#). If we consider a 95% confidence level, the correlation coefficient spans from 0.31 to 0.82. Similarly, at a 68% confidence level or $1-\sigma$, the correlation coefficient ranges between 0.48 and 0.74. Therefore, the CC ($R^2 = 0.63$) in present case (lower panel of [Figure 4.1](#)) is

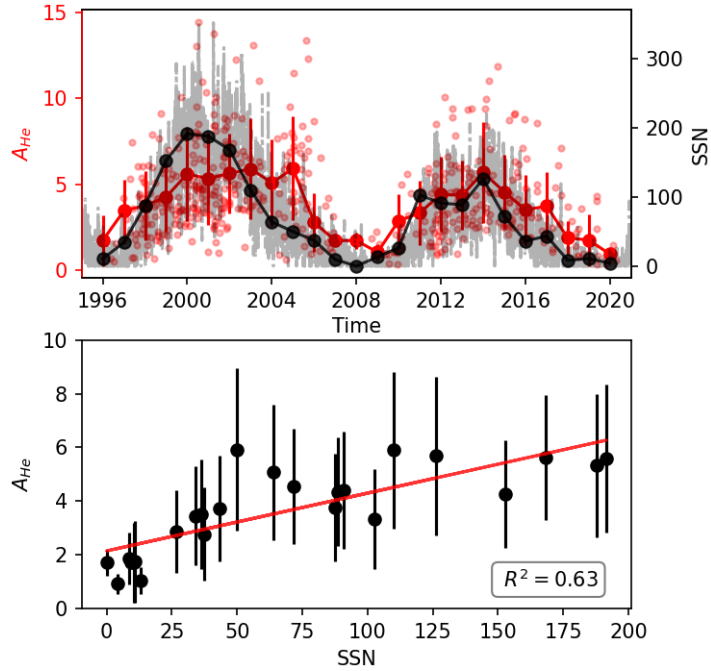


Figure 4.1: Upper panel: The variation of A_{He} and SSN: The variation of individual ICME averaged A_{He} (in red) and Sunspot number (SSN) (in black) respectively. Lower panel: correlation between SSN and A_{He} : The linear correlation between the annually averaged A_{He} , and SSN for the ICME duration is shown.

modest with respect to 95% confidence level but quite good with respect to 68% confidence level. This solar cycle variation suggests that the processes controlling the A_{He} in the background solar wind do contribute to the ICME A_{He} values as well. Therefore, if the background A_{He} is already high (high solar activity period), enhancements in A_{He} in ICMEs are expected to be more pronounced. Another important point to observe from Figure 4.1 is the higher ICME averaged A_{He} in 2005. A similar kind of enhancement in the flare production by the active region and CME eruption rate in 2004-2005 is seen by [Hudson et al. \(2014\)](#) and [Mishra et al. \(2019\)](#), respectively. The possible flare connection in A_{He} enhancement will be discussed in the upcoming sections.

4.4 Relationship of A_{He} with different proxies

It is observed ([Zurbuchen et al., 2016](#)) that the low- FIP elements are enhanced during the ICMEs as compared to the ambient SW. These authors suggested that

either FIP bias is more significant during the CME or a different type of plasma is injected into the CME. It is known that the magnetic energy is converted into kinetic and thermal energies through magnetic reconnection in the corona during the CME initiation process (Forbes et al., 2006; Wimmer-Schweingruber et al., 2006). The flares associated with these events can alter the compositions of the ICMEs. The temperature-dependent compositional proxies that include charge states and the charge state ratios, get frozen in the corona at higher heights (generally, above $2.5 R_{\odot}$) because there are effectively no collisions beyond these heights. CME throws out this plasma with frozen compositions from the corona into the interplanetary medium (Gruesbeck et al., 2011, 2012). Therefore, it is essential to evaluate the relationship of A_{He} with average charge states, charge state ratios, and FIP elemental ratios. This comparison can shed light on the A_{He} enhancement during ICMEs.

This section is divided into three parts. In the first part, the relationship between the average charge state (Q_X where the subscript "X" stands for C, O, Mg, Si, Fe) and A_{He} is evaluated, in the second part, the relationship between the number density ratio for different charge states for a particular element (C^{6+}/C^{4+} , C^{6+}/C^{5+} , and O^{7+}/O^{6+}) and A_{He} is investigated. The relationship between A_{He} and FIP elemental ratio is evaluated in the last and final part.

4.4.1 Relationship between A_{He} and the average charge states

As discussed earlier, the charge states are good proxies for ICME identification. In this section, we compare the relationship between A_{He} and the different charge states during the ICME events. Figure 4.2 shows the correlation coefficients of the average charge state of elements, i.e., Carbon (C), Oxygen (O), Magnesium (Mg), Silicon (Si), and Iron (Fe) with A_{He} in each row, respectively. Column one is for ambient solar wind, column 2nd is for ejecta, column 3rd is for the event that does not fulfil all MC criteria, and the 4th column is for the MC. It can be observed from Figure 4.2 that there is almost zero correlation between the A_{He} and charge proxies for ambient solar wind. In contrast to the ambient solar wind, A_{He}

shows varying degrees of correlations with the average charge states of different elemental species with the exception of carbon. The correlation coefficients (CC characterized by R^2) and the parameters for the linear fits are mentioned in each subplot. The 1- sigma variations are also shown along with the mean values.

A few important points can be inferred from Figure 4.2. First, the R^2 value is found to be maximum for Q_{Si} . Second, the R^2 values for Q_{Fe} , Q_{Mg} and Q_O are found in descending order, but the values are not significantly different. Third, although not significantly different, the R^2 values for ejecta are less than their MC and partial MC counterparts. Fourth, Q_C is uncorrelated with A_{He} . The higher R^2 for MCs (partial and complete) compared to ejecta and ambient SW suggests modification in A_{He} by localized coronal heating due to magnetic reconnection processes. This may be the reason for the improvement in the linear relationship between A_{He} and averaged charge state proxies. Together with this, the Spearman Correlation Coefficients (Sp CCs) are higher than linear correlations. These higher Sp CCs suggest the involvement of processes other than localized coronal heating for the A_{He} enhancements in ICMEs. This, in turn, means contributions from other processes in A_{He} enhancements that cannot be explained by the charge state only.

4.4.2 Relationship between A_{He} and number density ratio of different charge states of a given element

In the second part of this section, the ratios of the number density of different charge states of carbon and oxygen are compared with A_{He} . This is shown in Figure 4.3. It is noted that similar to the average charge state of carbon (shown in the previous subsection), the ratio of the number density of different charge states of carbon (C^{6+}/C^{4+} and C^{6+}/C^{5+}) also do not show any correlation with A_{He} . This can be seen from the first two rows of Figure 4.3. However, the third row reveals that the number density ratio of the Oxygen charge states (O^{7+}/O^{6+}) show reasonable correlation with A_{He} for ICMEs compared to the ambient solar wind. The ejecta have a lower correlation coefficient than the partial MCs and MCs. Similar to the previous section, SP CCs are also calculated here. The

4.4 Relationship of A_{He} with different proxies

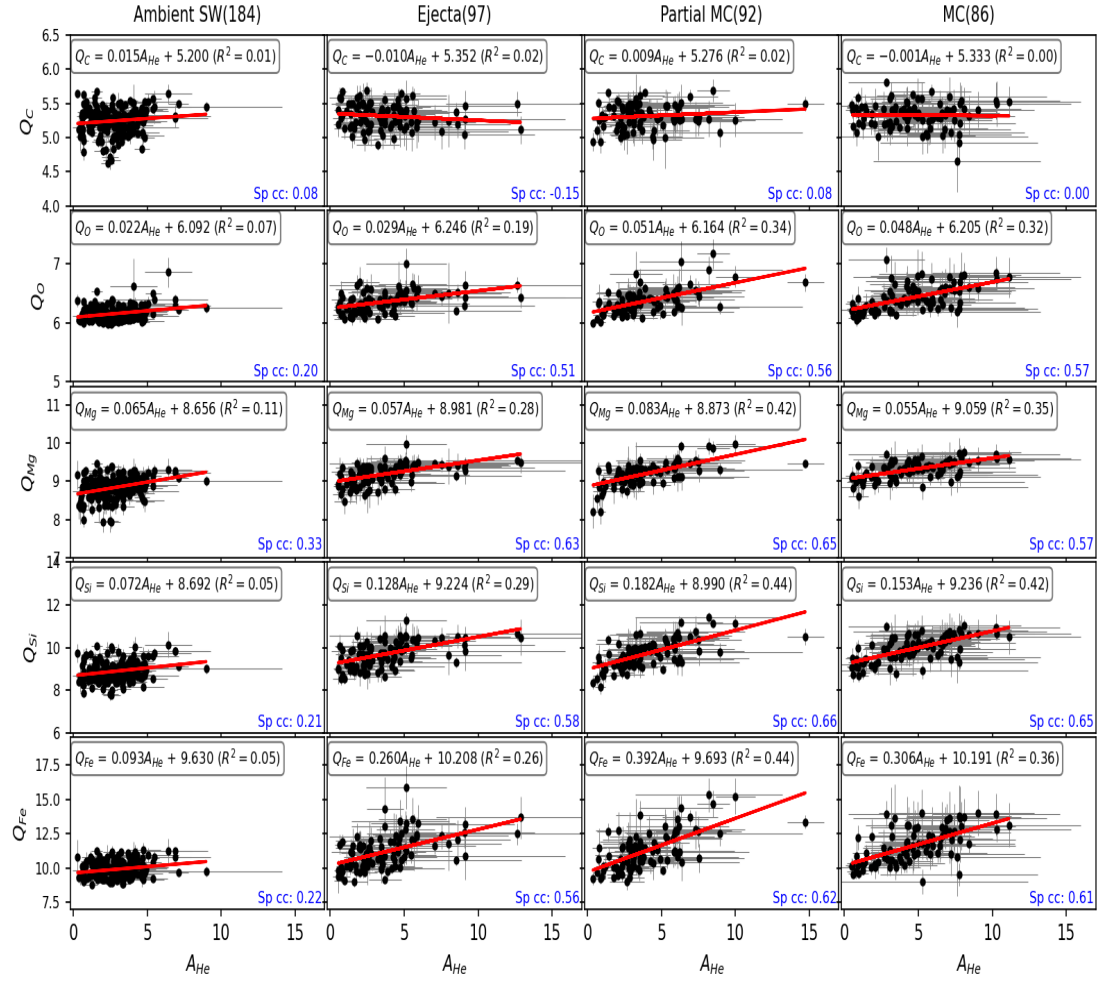


Figure 4.2: Correlations between the average charge state of different elements with A_{He} : Average charge states of Carbon (C), Oxygen (O), Magnesium (Mg), Silicon (Si), and Iron (Fe) are shown in rows starting from the top to the bottom. Column 1: Ambient solar wind (184), Column 2: Ejecta - ICMEs without MC characteristics (97), Column 3: Partial MC - ICMEs with partial MC characteristics (92), Column 4: MC - ICMEs with MC characteristics (86). These correlations include the data from the duration of 1998-2011. The linear fitted line (red colour) and associated parameters, including R^2 values, are mentioned in each plot. The Spearman correlation coefficients are mentioned in blue colour. It can be noted that the average charge states (except carbon) show reasonable correlations with A_{He} in the case of partial MCs and MCs. In contrast, there is a negligible correlation in the case of ambient solar wind.

enhanced value of Sp CC with respect to CC can be seen in the case of O^{7+}/O^{6+} . The slope of the linear fits is higher in the case of ICMEs compared to ambient

Solar wind. It can be seen that the 1-sigma variations during the ICMEs are also higher as compared to the ambient solar wind. This suggests that the variations of the proxies are much higher in the case of ICMEs compared to the ambient SW. These results also indicate contributions from factors other than localized coronal heating for the A_{He} enhancements in ICMEs.

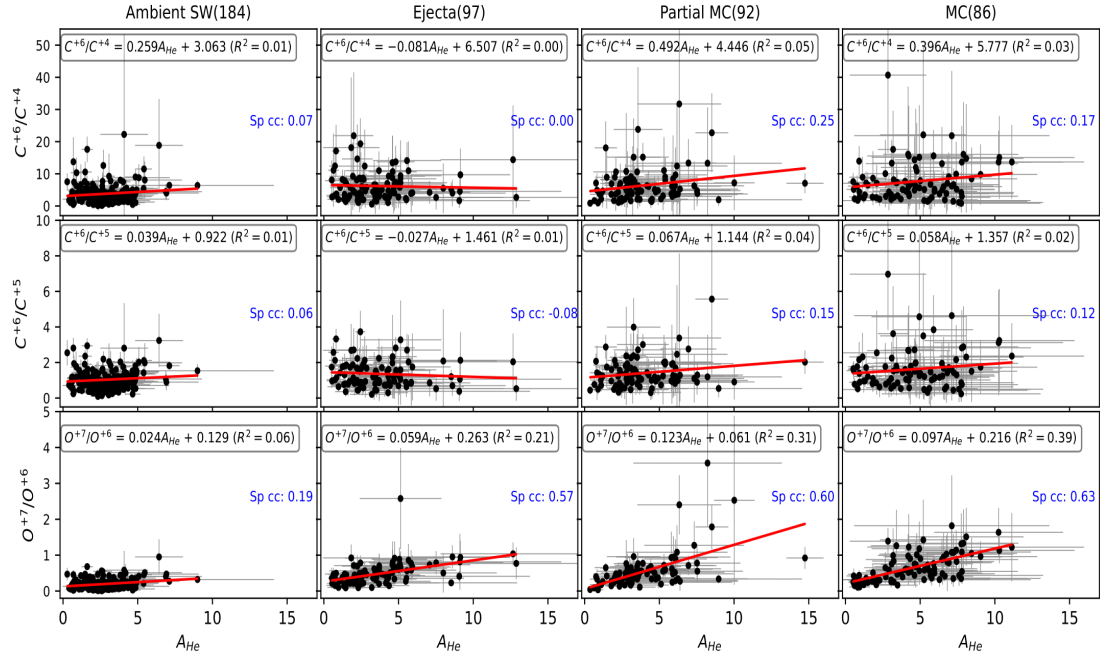


Figure 4.3: Correlations between the number density ratios of the different charge states of carbon and oxygen with A_{He} . The C^{6+}/C^{4+} , C^{6+}/C^{5+} , and O^{7+}/O^{6+} are shown in rows from the top to the bottom. Similar to Figure 4.2, the four columns represent ambient solar wind, ejecta, partial-MC and MC events from left to right. The linear line is fitted, and the associated parameters are written in the figure. The Spearman correlation coefficients are mentioned in blue colour. A reasonable correlation can be found between the event-averaged O^{7+}/O^{6+} and A_{He} . The number density ratios of different charge states of carbon, i.e., average C^{6+}/C^{4+} and average C^{6+}/C^{5+} and average A_{He} , do not show any correlations.

4.4.3 Relationship between A_{He} and FIP elemental ratios

This section deals with the relationship of A_{He} with different FIP elemental ratios (like Mg/O, Fe/O, Si/O, C/O, Ne/O and He/O) for the background solar wind, ejecta, partial MC and MC varieties of ICMEs. The FIP elemental ratios are

arranged in Figure 4.4 in accordance with the ascending values of the FIP from top to bottom. It is to be noted that the FIP of Mg, Fe, Si, C, Ne, He and O are 7.6, 7.9, 8.2, 11.3, 21.6, 24.6 and 13.1 eV, respectively. Similar to previous sections, it can be observed that there is a negligible correlation in the case of the ambient solar wind. The reason behind this may be the inclusion of all the sources of the solar wind, i.e., active region, coronal holes, streamers, quiet Sun etc., in calculating parameters for the ambient wind.

Figure 4.4 reveals that the correlation coefficients are low for He/O and negligible for C/O regardless of ejecta, partial or MC variety. In case of He/O and A_{He} , a higher correlation is expected because both the H and O have FIP of 13.6 eV. The other FIP ratios show a higher correlation for MC when compared with the ejecta and partial-MC categories. The higher correlations are indicative of the presence of well-defined structure of the magnetic cloud. The correlation coefficients are nearly comparable for Mg/O, Fe/O, and Si/O. The similar FIP values of these elements may be the reason behind the similar correlation coefficients. The correlation coefficient corresponding to Ne/O is the highest compared to other elements.

Similar to the previous cases, Sp CCs are more than linear CCs. This again indicates the role of non-linear processes in the A_{He} enhancement. In order to verify further, we have additionally computed the significance levels for the correlation of each signature. Our analysis revealed that the significance bands of the correlation coefficients (CCs) overlap for ejecta, partial MC and MC in nearly all cases. However, when comparing the CC with its significance band to the Sp CC with significance, we observed that a significant number of events do not overlap. These significance levels significantly support our argument regarding the engagement of non-linear processes.

It can be seen from figure 4.2-4.4 that the carbon proxies do not show any kind of CC with the A_{He} . Song et al. (2021) showed the solar cycle variation of C^{6+}/C^{5+} and C^{6+}/C^{4+} . In their study, C/O exhibits a negative but low correlation with SSNs. The solar cycle variation observed in C^{6+}/C^{5+} and C^{6+}/C^{4+} may be linked to temperature changes in solar atmosphere due to solar activity.

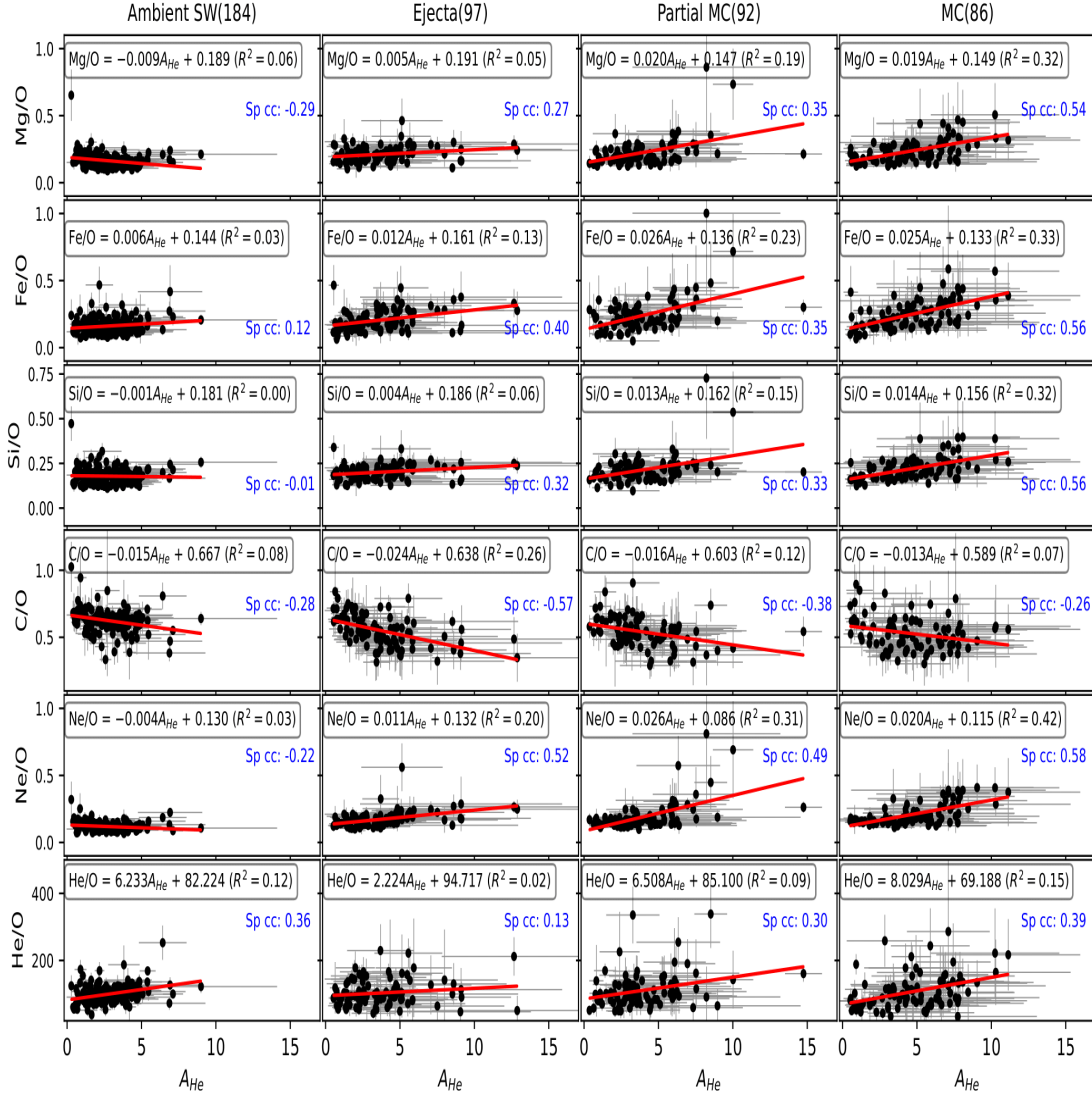


Figure 4.4: Correlations between the FIP elemental ratios with A_{He} . The Mg/O, Fe/O, Si/O, C/O, Ne/O, and He/O are shown in rows from top to bottom. Similar to Figures 4.2 and 4.3, the three columns represent ambient solar wind, non-MC and MC events from left to right. The Spearman's correlation coefficients, linear fitting, and associated parameters are mentioned in blue and black colour, respectively. A significant enhancement in correlation can be seen between FIP proxies and average A_{He} for the MCs except for He/O and C/O.

Additionally, they found that C/O does not show any correlation with C^{6+}/C^{5+} and C^{6+}/C^{4+} . Similarly, in our study, C/O, C^{6+}/C^{5+} , C^{6+}/C^{4+} , and Q_C do not show correlation with He/H. This is consistent with Song et al. (2021) and also suggest that the carbon requires a separate investigation.

All the above results are summarized in Table 4.2. This table contains the

4.4 Relationship of A_{He} with different proxies

Table 4.2: The collective results from the detailed correlation exercises of A_{He} with FIP elemental ratios, average charge states, and charge state ratios - Linear correlation coefficient (CC - parameterized by the Coefficient of determination, R^2) and the Spearman's Correlation coefficients (Sp. CC) are calculated and tabulated for ambient SW, Ejecta, partial MC as well as MC. The correlation of A_{He} in ICME is non-existent for ambient SW and maximum for MC. Importantly, Sp. CC consistently exceeds CC, indicating other processes' vital role in determining the abundance of A_{He} in ICMEs.

	Ambient SW (184)		Ejecta (97)		Partial MC (92)		MC (86)	
Average charge States								
	CC	Sp CC	CC	Sp CC	CC	Sp CC	CC	Sp CC
Q_c	0.01	0.08	0.02	-0.15	0.02	0.08	0.00	0.00
Q_o	0.07	0.20	0.19	0.51	0.34	0.56	0.32	0.57
Q_{Mg}	0.11	0.33	0.28	0.63	0.42	0.65	0.35	0.57
Q_{si}	0.05	0.21	0.29	0.58	0.44	0.66	0.42	0.65
Q_{Fe}	0.05	0.22	0.26	0.56	0.44	0.62	0.36	0.61
Charge state ratios								
	CC	SpCC	CC	SpCC	CC	SpCC	CC	Sp CC
C^{+6}/C^{+4}	0.01	0.07	0.00	0.00	0.05	0.25	0.03	0.17
C^{+6}/C^{+5}	0.01	0.06	0.01	-0.08	0.04	0.15	0.02	0.12
O^{+7}/O^{+6}	0.06	0.19	0.21	0.57	0.31	0.60	0.31	0.63
FIP elemental ratios								
	CC	Sp CC	CC	SpCC	CC	Sp CC	CC	SpCC
Mg/O	0.06	-0.29	0.05	0.27	0.19	0.35	0.32	0.54
Fe/O	0.03	0.12	0.13	0.40	0.23	0.35	0.33	0.56
Si/O	0.00	-0.01	0.06	0.32	0.15	0.33	0.32	0.56
C/O	0.08	-0.28	0.26	-0.57	0.12	-0.38	0.07	-0.26
Ne/O	0.03	-0.22	0.20	0.52	0.31	0.49	0.42	0.58
He/O	0.12	0.36	0.02	0.13	0.09	0.30	0.15	0.39

linear CC and the Sp CC for the ambient solar wind, ejecta, partial MCs and MCs.

The results presented in sections 4.3-4.4 reveal that the correlation coefficients between ICME signatures and A_{He} in ICMEs are not very high when viewed in

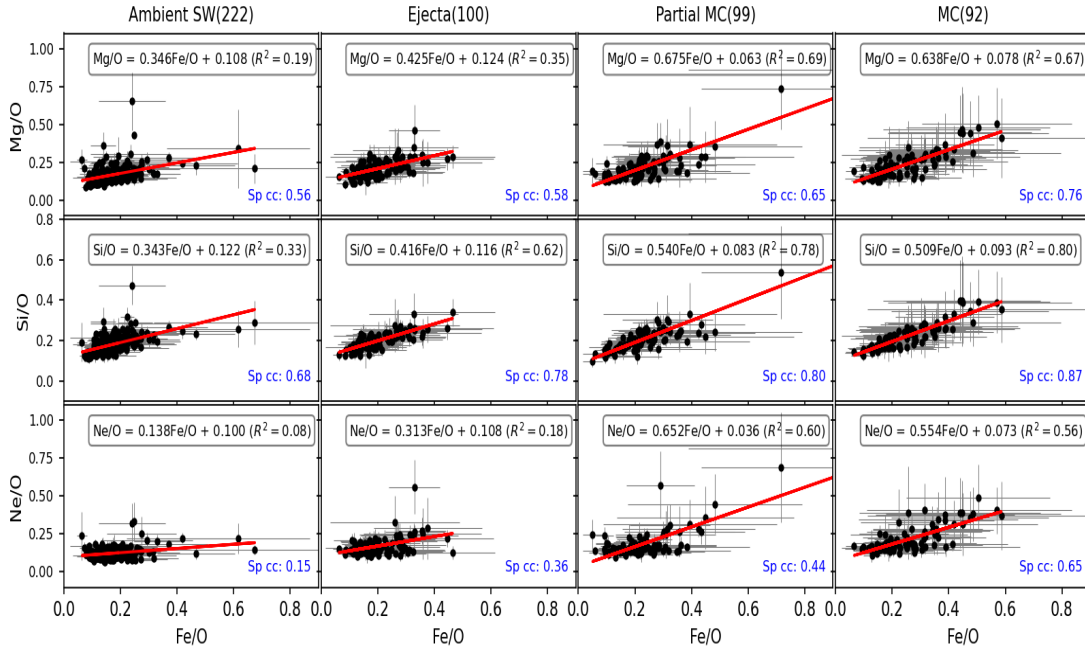


Figure 4.5: Correlations of Mg/O, Si/O, Ne/O with Fe/O - Relationships between the average elements abundance ratio (Mg/O, Si/O, and Ne/O) with Fe/O are explored. The four columns represent the ambient solar wind, Ejecta, Partial MC, and MC from left to right. Spearman's correlation coefficients (Sp. CC) are mentioned in blue colour. It can be seen that all the ICME events show higher correlation coefficients (R^2) compared to the ambient solar wind. The Mg/O and Si/O show an excellent correlation with Fe/O. Also, the difference between linear CC and Sp CC are narrowed down to particularity for MCs and partial MCs. This is probably because of the FIP effect, as the First ionization potentials are not significantly different for Mg(7.65 eV), SI (8.15), and Fe(7.9 eV). However, Ne/O correlates positively with Fe/O in partial and complete MC events. The reason behind this is not apparent, as the Ne (21.56 eV) is a high FIP element.

isolation. However, these can be considered reasonably higher with respect to the ambient solar wind. One way to validate these results is to test these exercises on analogous proxies and check if the correlation coefficients increase significantly. We tried this and found a very high correlation coefficient ($R^2 = 0.67$) between Mg/O and Fe/O and Si/O and Fe/O ($R^2 = 0.80$) in the case of magnetic clouds. The correlation coefficient for partial MCs and MCs are comparable and higher than ambient solar wind and ejecta. In addition, the R^2 values are also found to be closer to Sp CC as one considers ICMEs. These results can be seen in

Figure 4.5. This exercise suggests that if the process is same (in this case, the FIP effect), one can expect significantly higher correlations.

These results suggest that processes like FIP effect (that determines the elemental abundances) and localized coronal heating (that determines the average charge states as well as charge state ratios) may contribute to the changes in A_{He} in ICMEs to a certain degree. The higher Sp CC (compared to the linear CC) strongly suggests the possible role of contributions from non-linear processes. This makes chromospheric evaporation and sludge effect important factors to be considered. This aspect is discussed in the next section.

4.5 Chromospheric evaporation and Sludge effect

In this section, we evaluate the relationship between the A_{He} enhancements in ICME and the occurrence of flares. To do that, we identify the flares and the corresponding NOAA active regions associated with these flares using SOHO/LASCO CME catalogue https://cdaw.gsfc.nasa.gov/CME_list/halo/halo.html. The number of flares associated with each active region are considered along with the strength of the flares around the eruption of CME. The information on the number of CMEs and the occurrence of flares for each CME are available for 63 cases. All these 63 cases are listed in Table 4.3. This table includes the ICME start time, end time, associated CME onset time, classes (discussed later in this section), peak A_{He} , Average A_{He} and flare class. Out of these 63 cases, 17 cases are associated with X-class flares, 29 with M-class, 16 with C-class, and 1 with B-class flare. We find (marked in red in Table 4.4) that approximately 88% (15/17) of the ICMEs associated with X-class flares show A_{He} enhancement at the L1 point for at least an hour. The corresponding numbers for ICMEs with M and C-class flares are $\sim 76\%$ and 50% , respectively.

Further, 46 out of 63 events ($\sim 73\%$) show $A_{He} > 8\%$ for at least one hour, and this number increases to 59 ($\sim 94\%$) if ∓ 12 hours are considered with respect to the ICME start and end times respectively. These additional 12 hours are taken

because of the difference in the compositional and magnetic start and end times (Gopalswamy et al., 2013) corresponding to ICMEs. A similar observation can be seen in the catalogue compiled by Richardson and Cane (2010), where the compositional start and end times differ from the magnetic start and end times.

Table 4.3: List of ICMEs with other relevant details: The list of 63 events used in this work is presented below. The table includes ICME start time, end time, associated CME onset time, classes (discussed later in this section), peak A_{He} , Average A_{He} and flare class.

ICME Start	ICME End	CME Onset	Class	Peak A_{He}	Avg A_{He}	Flare class
1997/04/110600	1997/04/111900	1997/04/071427	1	8.6	5.34	C68
1997/05/150900	1997/05/160000	1997/05/120530	1	10.5	7.45	C13
1999/06/272200	1999/06/290400	1999/06/241331	1	19.1	5.5	C41
2000/04/070600	2000/04/080600	2000/04/041632	1	9.8	3.64	C97
2000/07/281200	2000/07/301300	2000/07/250330	1	13.1	7.82	M80
2000/11/061700	2000/11/080300	2000/11/031826	1	7.9	3.73	C32
2000/12/230000	2000/12/231200	2000/12/181150	1	2.8	1.76	C70
2001/03/281700	2001/03/301800	2001/03/251706	1	7.5	4.34	C90
2001/10/010800	2001/10/020000	2001/09/280854	1	8.6	4.72	M33
2001/11/061200	2001/11/090300	2001/11/041635	1	9.8	5.56	X10
2002/05/111500	2002/05/120000	2002/05/081350	1	6.4	4.31	C42
2002/09/080400	2002/09/082000	2002/09/051654	1	5.2	3.52	C52
2004/12/122200	2004/12/131900	2004/12/82026	1	15.6	8.03	C25
2005/02/201200	2005/02/220700	2005/02/170006	1	6.1	4	C49
2012/01/222300	2012/01/230700	2012/01/191436	1	3.6	1.95	M32
2012/07/090000	2012/07/091400	2012/07/041724	1	10.9	8.89	M18
2012/07/150600	2012/07/170500	2012/07/121648	1	16.4	9.4	X14
2013/04/141700	2013/04/152300	013/04/110724	1	15.6	9.36	M65
2014/04/052200	2014/04/070500	2014/04/021348	1	14.9	11.02	M65
2014/09/122200	2014/09/140200	2014/09/101800	1	17.3	11.86	X16
1997/11/070400	1997/11/091200	1997/11/040610	2	11.5	5.39	X21
1998/11/072200	1998/11/090100	1998/11/04 0754	2	10.9	5.85	C16
2000/06/081200	2000/06/101700	2000/06/061554	2	16.1	9.5	X23
2001/01/240900	2001/01/260700	2001/01/202130	2	8.2	3.25	M 77
2001/04/281400	2001/05/010200	2001/04/261230	2	13.9	10.07	M78
2001/10/212000	2001/10/251000	2001/10/191650	2	14.2	7.52	X16
2002/08/191200	2002/08/211400	2002/08/161230	2	12.9	6.95	M52
2003/05/302200	2003/06/010100	2003/05/290127	2	13.2	4.4	X12
2005/01/161400	2005/01/170700	2005/01/131754	2	10.8	7.71	C42
2005/05/300100	2005/05/302300	2005/05/261506	2	12.1	5.86	B75
2005/08/241400	2005/08/242300	2005/08/220131	2	13.6	5.48	M26
2006/08/201300	2006/08/211600	2006/08/161630	2	2.6	1.64	C36
2010/02/110800	2010/02/120300	2010/02/070354	2	5	2.51	M64

4.5 Chromospheric evaporation and Sludge effect

2011/02/181900	2011/02/200800	2011/02/150236	2	14.9	7.79	X22
2011/08/062200	2011/08/072200	2011/08/040412	2	4.2	1.4	M93
2012/06/162300	2012/06/171200	2012/06/141412	2	9.1	6.13	M19
2014/02/160500	2014/02/161600	2014/02/120612	2	13.3	9.97	M37
2014/12/220400	2014/12/221700	2014/12/170500	2	4.7	2.48	M87
2015/03/171300	2015/03/180500	2015/03/150236	2	15.3	8.75	C91
2015/06/251000	2015/06/260600	2015/06/221836	2	12.4	9.11	M65
1998/05/020500	1998/05/040200	1998/04/291658	3	14	7.87	M68
1998/05/041000	1998/05/072300	1998/05/021406		13.5	6.01	X11
2000/02/121200	2000/02/130000	2000/02/100230	3	7	5.37	C73
2000/02/141200	2000/02/160800	2000/02/120431		9.6	4.33	M17
2000/07/131300	2000/07/141500	2000/07/111327	3	7.4	4.6	X10
2000/07/151900	2000/07/170800	2000/07/141054		19.1	14.45	X57
2001/03/310500	2001/03/312200	2001/03/281250	3	18.4	13.79	M43
2001/04/010400	2001/04/031500	2001/03/291026		13	9.07	X17
2001/04/081400	2001/04/090400	2001/04/061930	3	5.8	2.41	X56
2001/04/112200	2001/04/130700	2001/04/100530		17.2	7.79	X23
2001/04/130900	2001/04/141200	2001/04/111331		13.1	8.45	M23
2001/11/192200	2001/11/211300	2001/11/170530	3	6.1	2.54	M28
2001/11/241400	2001/11/252000	2001/11/222330		18.5	8.74	M99
2002/04/171600	2002/04/191500	2002/04/150350	3	35.6	12.27	M12
2002/04/200000	2002/04/211800	2002/04/170826		12.6	6.76	M26
2004/07/221800	2004/07/240800	2004/07/201331	3	16.2	7.85	M86
2004/07/270200	2004/07/272200	2004/07/251454		6.8	5.88	M11
2004/09/141500	2004/09/161200	2004/09/120036	3	10	6.15	M48
2004/09/181200	2004/09/200000	2004/09/141010		14.1	6.68	M15
2004/11/092000	2004/11/112300	2004/11/071654	3	11	6.88	X20
2004/11/120800	2004/11/132300	2004/11/100226		8.5	4.03	X25
2012/03/090300	2012/03/110700	2012/03/070024	3	18.8	10.06	X54
2012/03/151700	2012/03/161000	2012/03/131736		3.7	2.28	M79

The statistics of A_{He} enhancement during different kinds of flares can be seen in Table 4.3. This exercise tells that the stronger the flare, the higher the chances of A_{He} enhancement in ICMEs. This indicates that energetic flares are associated with stronger chromospheric evaporation processes leading to higher probability of A_{He} enhancement. However, chromospheric evaporation can at the most enhance A_{He} up to the chromospheric levels of A_{He} ($\sim 8\%$) but it cannot explain the higher A_{He} values ($>8\%$) that are also observed in the ICMEs at the L1 point. This suggests that the additional processes are at play. Various researches indicate that helium accumulates in the chromosphere and/or lower

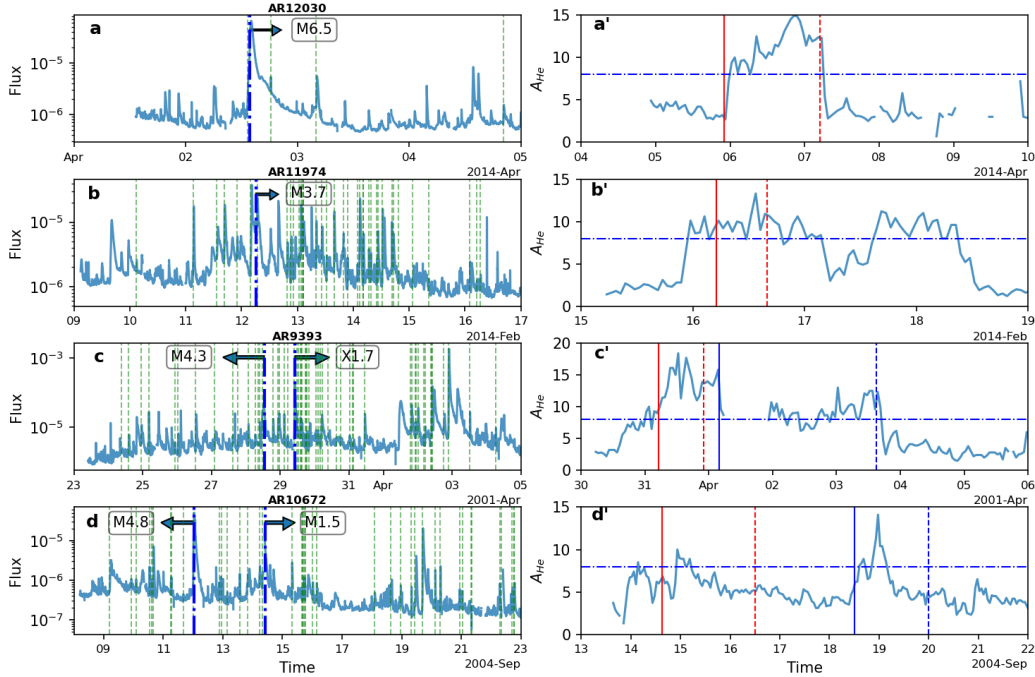


Figure 4.6: The first column shows GOES X-ray flux variation, and the dotted dashed blue line indicates the CME eruption time. The green dashed lines are for all the flares originating from the same NOAA region. The flare class with the NOAA number is also written. The second column represents the A_{He} variation for the associated ICME. The solid and dashed lines in 2nd column are for the ICME start and end time. The red and blue lines represent different events. The horizontal dotted dashed line represents the $A_{He} = 8\%$ level. Panel a and a' are for the CME erupted on 2014/04/02. These belong to Class 1 (see the text). The second row, i.e., b, b', represents Class 2. Panels b and b' correspond to the CME eruption on 2014/02/12. The third and fourth rows, i.e., c, c' and d, d', represent Class 3. The events pair that erupted on 2001/03/28 and 2001/03/29 (panels c and c') as well as 12/09/2004, and 14/09/2004 (panels d and d') are used for Class 3.

corona (Geiss et al., 1970) during the fractionation in the solar wind. The physical mechanism proposed by the authors is the inefficient Coulomb drag, i.e., the smaller proton drag force on helium compared to other heavy ions causing the bulging of helium in the chromosphere and/or lower corona. The other mechanism can be the gravitational settling (Hirshberg et al., 1970; Laming et al., 2019) which can also help in the accumulation of helium. The 'Sludge effect' proposed by Neugebauer and Goldstein (1997) is effectively the removal of this excess helium

by CMEs. The 'cleaning out' of this accumulated helium in lower corona by CMEs can contribute to the higher values of A_{He} (Wimmer-Schweingruber et al., 2006) in ICMEs.

To understand the effect of chromospheric evaporation together with the sludge effect, we divide the CME events (see Table-4.3 and 4.4) into three classes. Under Class-1, we consider the CMEs (20 events) with a nearly concurrent flare event before the CME and no previous flare activities from the same active region (except the concurrent one) for 12 hours before the CME. Under Class-2, we consider CMEs (20 events) with multiple flares before the CME from the vicinity of the same active region. Class-3 is for the multiple CMEs (23 events-11 active regions, one or more CMEs per active region) erupting from a single active region. One typical example of Class 1 and 2 is shown in the 1st and 2nd row of Figure 4.6. The 3rd and 4th rows are examples of Class 3. The 1st column of Figure 4.6 shows the GOES X-ray flux variation. The green vertical dashed lines show the times of flares that originated from the same NOAA region and from which the CME erupted. Blue vertical dashed lines mark the eruption time of CMEs. The 2nd column shows the A_{He} variation in the ICMEs as measured from the L1 point. The solid and dashed lines in 2nd column are for the ICME start and end time. The red and blue lines represent different events. The horizontal dotted dashed line represents the $A_{He} = 8\%$ level. It is a general observation from the statistical analysis that CMEs having multiple flares nearby (class 2) shows the highest probability $A_{He} > 8\%$ as compared to CME with a single flare nearby (class 1). This may be because there is a continuous supply of material from the lower heights of the solar surface due to continuous chromospheric evaporation caused by multiple flares. Class-1 shows the least enhancement probability (65%) as a single flare is connected to CME. The probability of A_{He} enhancement is highest (80%) in Class-2. Class-3 shows medium probability (74%) because it is a mixture of Class 1 and 2 based on the multiple CMEs (and not flares) from a single active region. The details of enhancement probability for different Classes and flares can be seen in Table 4.4.

The CMEs originated on 2014/04/02 (panels a and a' of Figure 4.6), and

Table 4.4: The statistics of A_{He} enhancement events according to the associated flare class (in red). The column shows the percentage of enhancements of A_{He} for at least one hour for different

	X	M	C	B	
Class 1	3/3 (100%)	5/6 (83.3%)	5/11 (45.5%)		13/20 (65%)
Class 2	5/5 (100%)	7/10 (70%)	3/4 (75%)	1/1 (100%)	16/20 (80%)
Class 3	7/9 (78%)	10/13 (77%)	0/1 (0%)		17/23 (74%)
	15/17 (88%)	22/29 (76%)	8/16 (50%)	1/1 (100%)	46/63 (73%)

2014/02/12 (panels b and b') are used as representatives of Class 1 and 2. For Class-3, the events that erupted on 2001/03/28 and 2001/03/29 (panels c and c') & 12/09/2004 and 14/09/2004 (panels d and d') are taken. These two events are chosen based on the time difference between the two CME eruptions. The first one has the least time difference (21 hour 36min) among all the events of multiple CMEs originating from the same active region. The second one has a time difference of 2 day 9 hour and 34 min. between the successive CMEs.

These multiple events from a single active region can help us understand the 'Sludge effect'. We know that the gravitational settling time for helium is 1.5 days (Laming et al., 2019). If two events erupts in close succession (less than 1.5 days) from the same active region, A_{He} in the first ICME should be higher as there will not be sufficient time for the gravitational settling to take place before the second CME erupts. We assume here no change in the solar background conditions between the two CMEs. We have only two cases with a time difference of less than 1.5 days. Panel c' shows a similar observation, i.e., the first event shows higher A_{He} and the second event shows lesser A_{He} . It is expected that most of the helium will settle down if the time between two successive CMEs is higher than 1.5 days, and under that condition, the two ICMEs can show any value depending on the background condition at the eruption time. An example of CME events having a higher time difference can be seen in panels d and d' of Figure 4.6.

This analysis suggests that chromospheric evaporation working in tandem with the sludge effect can enhance A_{He} beyond 8%. The interplay between these

two processes determine the variability of the A_{He} enhancements in ICMEs. Having said this, we also see that there exists a class of ICMEs that do not show any A_{He} enhancement. Further investigations are needed to address this issue.

4.6 Summary and Conclusions

1. These results show that solar activity level, FIP effect, and coronal temperature contribute to A_{He} enhancements in ICMEs to certain degrees.
2. The chromospheric evaporation during solar flares, assisted by the gravitational settling of helium, determines the enhancement and variability of A_{He} in ICMEs.
3. We show that the intensity and timing of the preceding flares from the same active region where the CME erupts are important factors in determining the A_{He} enhancements in ICMEs.
4. A subset of ICMEs does not show any enhancement at all. Studies of these events will be taken up in future.

Chapter 5

Variations in Helium abundance in the Stream/Co-rotating Interaction Regions (SIRs/CIRs)

Abstract

The helium abundance in solar wind, in general, gets fixed near the Sun by a number of processes that are discussed in the earlier two chapters. However, a few recent studies suggest that helium abundance can also change in the Stream/Co-rotating Interaction Regions (SIRs/CIRs) present in the interplanetary medium. In this chapter, we show that the angles between bulk velocity and local magnetic field (henceforth, bulk velocity angle) as well as their differential velocities play important roles in determining A_{He} enhancements in SIRs. The fast wind regions of the SIRs show higher modification in A_{He} as compared to the slow wind regions. Our results suggest that the frequency of alpha particles having higher bulk velocity angles is more than protons in the fast wind region. This investigation also shows the difference between background solar wind and SIR in terms of the velocities of alphas and protons. The study suggests that the changes in the differential velocity of alphas and protons as well as changes in the bulk velocity angle distribution cause A_{He} enhancement. Another important result is that the variations in helium abundance within the SIR are not influenced by the levels of

solar activity, but rather by the bulk velocity angle and the differential velocity of alphas and protons.

5.1 Introduction

Stream/Corotating interaction regions (SIRs/CIRs) are formed by the interaction of fast solar wind with slow solar wind in the interplanetary medium (Sarabhai, 1963; Belcher and Davis, 1971). The fast solar wind, in general, originates from the coronal holes. The interaction region forms the compressed plasma along with the leading edge (Richardson, 2018). This interaction region is approximately twisted into an Archimedean spiral because of the solar rotation. Since the fast wind sources, i.e., coronal holes, sustain for a long time (often persisting for a few months), the interaction regions are generally observed at regular intervals that coincide with the time period of solar rotation (~ 27 days). Owing to this, the interaction regions are usually referred to as Corotating Interaction Regions (CIRs). The fast and slow wind do not mix because of the frozen-in principle (Alfvén, 1942). The faster stream interacts with slow stream and deflects the slower flow towards the west, while the slower stream deflects the faster flow towards the east. As a result, a compression region is created with the increases in the magnetic field intensity and plasma density, forming the stream interaction region.

Observations of interfaces separating low and high-speed flows in the solar wind were first reported in 1971 (Belcher and Davis, 1971) using Mariner 5 data. Additionally, the typical profiles of plasma parameters at 1AU related to stream interaction regions were summarized in Figure 5.1 taken from Belcher and Davis (1971). The upper section of Figure 5.1 illustrates two high-speed streams that are co-rotating with the Sun, as viewed from above the solar north pole. The spiral regions of compressed plasma are formed at the leading edges of these fast streams. The dotted lines in the figure indicate representative magnetic field lines corresponding to the slow and fast solar wind. The variations of plasma parameters observed by a spacecraft at ~ 1 AU are shown in the lower part of

Figure 5.1.

These authors identify four regions which are as follows:

1. The ambient, undisturbed, slow solar wind (S);
2. Slow compressed solar wind (S');
3. Fast compressed solar wind (F');
4. The ambient, undisturbed, fast-solar wind (F).

In this chapter, we have focused on three specific components of Stream Interaction Regions (SIRs) - the region of slow wind (compressed), the stream interface region, and the region of fast wind (compressed). The stream interface (SI) is usually identified based on the sharp changes in solar wind parameters across it. Abrupt drop in density, increase in the solar wind pressure and temperature, and a change in velocity with a large gradient (Burlaga, 1974) are, in general, observed across the SI. The characteristic changes of various solar wind parameters like solar wind density, interplanetary magnetic field, solar wind dynamic pressure etc. across the stream interface region have been discussed in detail by Richardson (2018) and references therein. However, the effects of stream interaction on plasma composition has not been explored comprehensively. One of the important compositional parameters in this context is helium abundance, which is often used to understand various solar processes but the behavior of which has not been extensively studied across the SI region.

As already discussed in the previous chapters, the Helium abundance, $A_{He} = N_a/N_p * 100$, is an important parameter for identifying the solar wind sources (e.g., Borrini et al., 1981; Kasper et al., 2008). Different regions of solar atmosphere are characterized by different A_{He} . While A_{He} in photosphere is $\sim 8\%$, it is 4-5% in the corona. A_{He} varies in solar wind according to solar cycle activity level and solar wind velocity (Kasper et al., 2007; Alterman and Kasper, 2019). In general, higher A_{He} values are observed in the fast wind as compared to the slow wind. Further, the variations in A_{He} values are larger in the case of the slow solar wind, whereas the variations are significantly smaller in the case of the fast wind. It

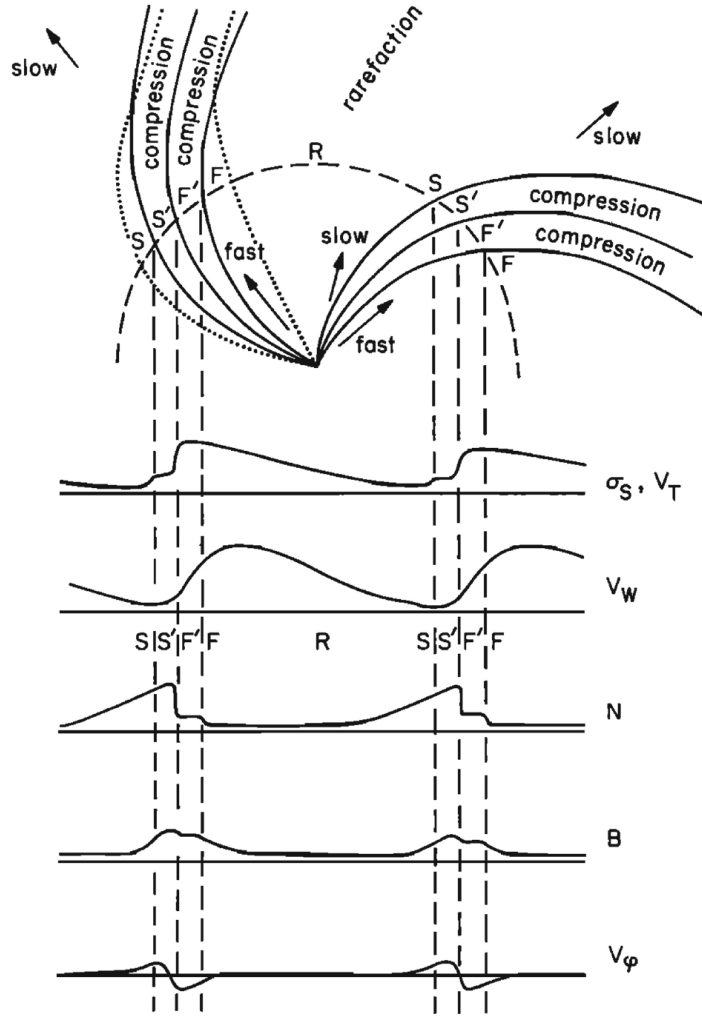


Figure 5.1: Schematic of two high-speed streams and the associated variations in some of the plasma parameters at 1AU: Thermal velocity (V_T), magnetic field fluctuation level (σ_s); solar wind speed (V_W); density (N); magnetic field intensity (B); and the transverse component of the solar wind velocity (V_ϕ). The indicated regions include the unperturbed slow solar wind (S), compressed and accelerated slow solar wind (S'), compressed and decelerated fast solar wind (F'), unperturbed fast solar wind (F), and rarefaction in the region of declining solar wind speed (R). The interaction region is formed by S' and F', with the stream interface situated at the S'-F' boundary. Dotted lines represent magnetic field lines in the slow and fast solar wind. (Courtesy: [Belcher and Davis, 1971](#))

is already discussed that A_{He} values often go above 8% in the case of ICMEs ([Borrini et al., 1982](#); [Fu et al., 2020](#)). The changes (enhancement in general) in A_{He} in SIR were earlier thought to be only because of the transition in the type of solar wind ([Gosling et al., 1978](#); [Wimmer-Schweingruber et al., 1999](#)).

However, recently, [Durovcová et al. \(2019\)](#) suggested that some other physical processes may also be responsible for the changes in the helium abundance in SIR. They suggested that the SIR's magnetic configuration is similar to a large-scale magnetic mirror in which the curvature of the magnetic field lines changes with the bulk solar wind speed. The pitch angle and velocity of alphas in the proton frame can help in explaining the variations in A_{He} in SIRs ([Durovcová et al., 2019](#)). These authors have studied the A_{He} behaviour for SIR using data from the Helios and *Wind* satellites.

We have studied the properties of alphas and protons individually inside the SIRs. Additionally, helium abundances are also investigated in the context of fast and slow wind, solar minima, and maxima of SC23 and 24 to understand whether the changes in A_{He} are due to changes in the interplanetary interaction and/or solar wind sources. In the upcoming sections, we will discuss the behavior of alpha and protons in terms of bulk velocity angle and differential velocity distributions of helium and hydrogen for different solar activity conditions.

5.2 Selection of SIR events and other datasets

For this study, we utilized data from the Solar Wind Experiment (SWE) onboard the Wind spacecraft ([Ogilvie et al., 1995](#)). This dataset provides observations with a temporal resolution of approximately 92 seconds. Magnetic field data were obtained from the Magnetic Field Investigation (MFI) experiment ([Lepping et al., 1995](#)).

The SIR events used in our analysis are the same events as reported in the work by [Chi et al. \(2018\)](#). Detailed information regarding event selection, start and end times of the SIR events can be found in [Chi et al. \(2018\)](#) and references therein. The catalogue initially contained 866 SIR events spanning from 1995 to 2016. We excluded events with incomplete data coverage and those with possible influence from Interplanetary Coronal Mass Ejections (ICMEs) occurring one day before the start time and one day after the end time. The ICME events were obtained from the Richardson & Cane catalogue ([Richardson and Cane, 2010](#)).

Applying these criteria resulted in a final set of 436 events which is used for our analysis.

The SIR events were categorized into four groups for further analysis: SC23 minima (1996-1998, 2006-2009), SC23 maxima (1999-2005), SC24 minima (2010-2011, 2016), and SC24 maxima (2012-2015). It should be noted that the SIR event data beyond 2016 is not included in this catalogue that has resulted in a smaller number of SIR events in SC24 compared to SC23. However, we have compared the results obtained based on the available SIR events (For example, Figure 5.6) with those obtained by ensuring an equal number of SIR events in each solar epoch (For example, Figure 5.7). This comparison does not point towards any significant change in the results. This suggests that the scientific conclusions drawn in this study remain consistent regardless of the equality or non-equality of the number of SIR events in each epoch. This is probably because of the already large number of events that are used in this work. Therefore, we have used the entire available database in this work in order to be more comprehensive.

5.3 Results and Discussion

5.3.1 Superposed Epoch Analysis (SPA) of the total events during solar maxima and minima

Figure 5.2 shows the general properties of SIRs based on superposed epoch analysis (SPA). The data cadence is changed from the 92s to two minutes to generate the SPA plot. The stream interface is the intermediate part between the slow and fast wind. Throughout this work, the slow wind side will be referred to as the Slow Wind Region (SWR), and the fast wind side will be described as the Fast Wind Region (FWR). It can be noted from Figure 5.2 that although SPA mixes measurements from inside the SIRs with those from outside the SIRs, the characteristic changes related to SI occur mostly within an interval of ± 10 hours with respect to zero epoch line. Note, in our investigation, the duration of 80% of SIR events are more than 20 hours. Therefore, we believe that the results presented in this work are statistically valid.

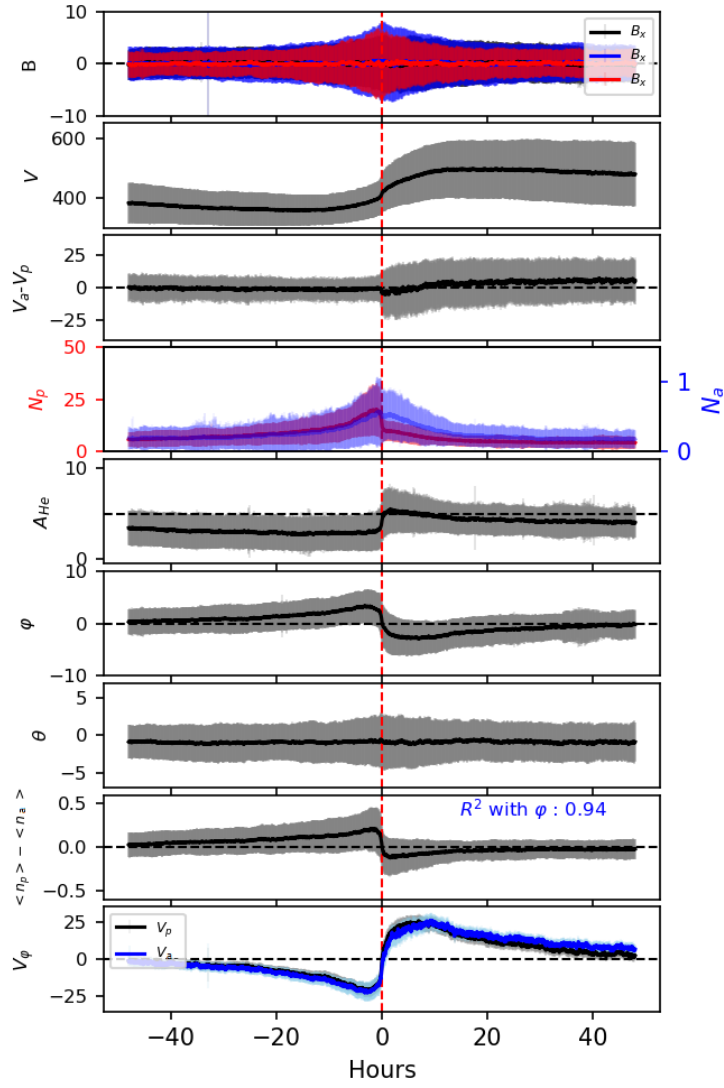


Figure 5.2: The general properties of SIRs can be seen in this figure. The red dashed line is the epoch time (SI). The epoch time is the time when signatures of SI are seen. The upper seven rows of each panel show the magnetic field components (B_x , B_y , B_z), velocity (V), the difference between the alpha and proton velocities ($V_a - V_p$), the number density of alpha and proton (N_a , N_p), Helium abundance (A_{He}), East-West GSE bulk Flow Angle (ϕ) and North-South flow angle (θ). Row eight shows the difference between scaled ($\langle N_p \rangle = (n_p - n_{p,min}) / (n_{p,max} - n_{p,min})$) proton number density and scaled alpha number density ($\langle N_a \rangle = (n_a - n_{a,min}) / (n_{a,max} - n_{a,min})$). Row nine shows the East-West velocity of alphas and protons ($V_\phi(p)$, $V_\phi(a)$). The ϕ and V_ϕ are good indicators for the change in the solar wind type, i.e., from slow to fast wind or in other words, the ϕ and V_ϕ can be used to identify the Stream Interface. The R^2 between $\langle N_p \rangle - \langle N_a \rangle$ and ϕ is very high (more than 90%). This indicates that the pile-up of protons dominates in the slow wind region, whereas the alpha pile-up dominates in the fast wind region.

The variation in the magnetic field, number density, and velocity across the stream interface (SI) can be observed in the SPA (Figure 5.2). An important point from this figure is that the difference between the scaled proton number density and scaled alpha density shows a very high correlation (see figure 5.2) with the East-West flow angle. These high correlations suggest that the pile-up of protons is dominant over alpha in the SWR, whereas pile-up of alphas dominates towards FWR. This is the primary cause of enhancement of A_{He} during SIRs. The reason behind the pile-up of alpha or protons is discussed in upcoming subsections. It is to be noted here that the east-west component of velocity difference is finite and small (and not zero) in the lowermost panel of Figure 5.2 in this context, Marsch et al. (1982) have shown that the differential velocity is about one half of the Alfvén velocity. However, Marsch et al. (1982) considered the bulk velocities and azimuthal components of velocities are considered here. Note as the azimuthal velocity is less compared to radial velocity in solar wind, the differences in azimuthal velocities of alpha and protons are very small but non-zero. Since azimuthal velocities are considered, the orientation of differential velocity along the magnetic field (e.g., in Němeček et al., 2020) is not expected. Further, we have considered different solar activity levels to understand if the changes in the properties of alphas and protons are due to interplanetary interactions or just a manifestation of two different types of solar winds.

5.3.2 Superposed epoch Analysis of number densities of alphas and protons

In this section, we focus on the variation of the number density of alphas and protons. The zero-epoch time is the time when the signatures of SI are identified. A period of 2 days before and after the zero-epoch time is shown. Figure 5.3 shows the variation of proton and alpha in red and blue colour, respectively, with one sigma (standard deviations) variations. The four panels correspond to SC23 minima, SC23 maxima, SC24 minima and SC24 maxima, respectively. The dashed black line is the zero-epoch time. The red and blue dashed vertical lines represent the peak proton number density towards SWR and the peak alpha

number density towards FWR, respectively.

Figure 5.3 reveals distinct additional SIs (peak) towards the FWR for alphas during SC24, both in the minima and maxima phases, whereas this additional SI appears to be absent in SC23. In SC23, the SI of alphas either coincides with the SI of protons in the maxima or is noticeably separated as the primary SI in the FWR region during the minima. Regardless of whether it is the primary or additional alpha SI, there is an approximate 2-hours separation from the proton SI. Therefore, considering the well-separated nature of the alpha SIs (except for SC23 maxima) based on a statistically significant dataset, we consider these alpha SIs to be genuine. Further, there is no abrupt decline in the alpha number density near SI, whereas protons show a sharp decrease across it. It is perplexing that alpha density doesn't drop abruptly at the so-called SI similar to protons as can be seen in figure 5.3. The discussion regarding this is taken up in section 5.3.5. Therefore, an enhanced helium abundance can be observed near the SI towards the FWR. The alpha peak is higher toward SWR in the case of maxima of SC23. This can be understood as the A_{He} value is higher in the slow wind during solar maxima. The SWR peak and FWR peak of alpha particles are similar in SC24, whereas the SWR peak of alpha is higher than its FWR peak in SC23 maxima. This may be associated with the strength of the solar cycle, i.e., the SC23 is a strong cycle, and SC24 is weak. In case of solar minima, the peak of alpha particles is higher towards FWR. There seems to be a second alpha peak towards FWR in all the solar epochs except for the SC23 maxima, for which this feature is not very conspicuous.

Durovcová et al. (2019) considered SIRs as equivalent to magnetic mirror assemblies. The pitch angle and the velocity of ions are important parameters which control the charged particles' motion in curved magnetic fields. In this work, instead of pitch angle, we have considered angle between bulk velocity vector and local magnetic field vector and differential velocity between alphas and protons. We have evaluated how these parameters affect the alpha and proton number density. This exercise is repeated for the maxima and minima of SC23 and SC24. It can be noted from Figures 5.2 and 5.3 that the behaviours

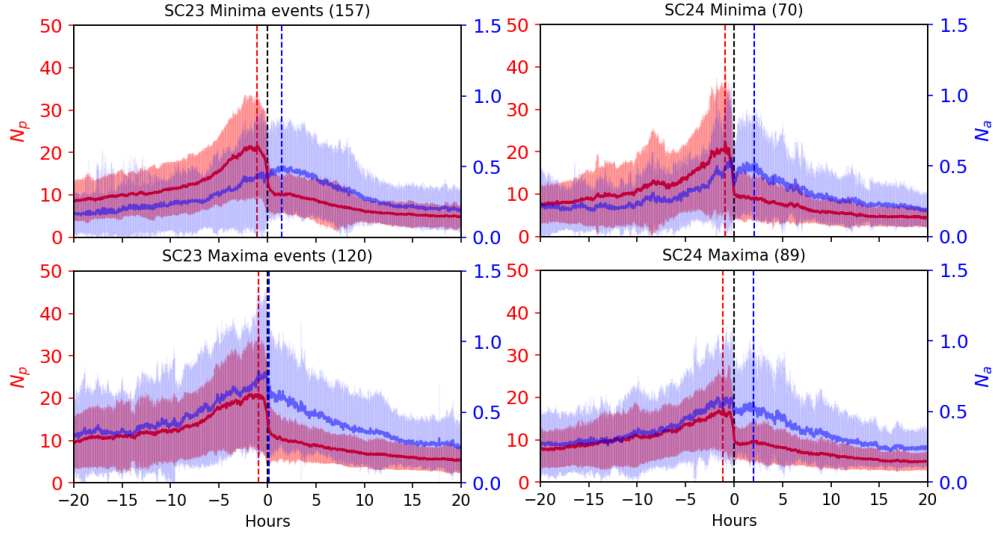


Figure 5.3: The SPA of proton and alpha densities. Protons and alphas are marked in red and blue colour, respectively, with one sigma error bar superimposed on the variations. The four panels show the SC23 minima, SC24 maxima, SC24 minima, and SC24 maxima, respectively. The number of events used to construct each subplot is mentioned at the top. The dashed black, red, and blue vertical lines represent the stream interface (SI), the peak proton density towards the SWR, and the peak alpha density towards the FWR. The additional peak of alpha particles towards fast wind suggests the differential behaviour of alphas and protons across the stream interface. This additional peak of alpha particles is considered as the alpha SI.

of alphas and protons are different in the SWR and FWR. Therefore, both SWR and FWR are analyzed separately and the results are presented in the upcoming subsections.

5.3.3 Bulk velocity Angle Distribution(BAD)

We define bulk velocity angle with respect to the local magnetic field (in short, BA) for both protons and alphas and construct Bulk velocity Angle Distribution (BAD). Note, BAD is different from Pitch Angle Distribution or PAD as BAD deals with the angle of bulk velocity of ions with respect to the local magnetic field direction while PAD deals with the angles between the individual ion velocity with respect to the local magnetic field direction. BA is defined as follows:

$$(BA) = \cos^{-1}\left(\frac{\vec{B} \cdot \vec{V}}{|\hat{B}||\hat{V}|}\right) \quad (5.1)$$

Here B is the magnetic field vector and V is the bulk velocity vector. Subsequently, BADs are calculated from 0° to 90° . The BAD between 90° to 180° is the mirror image of BAD between 0° to 90° and this aspect is taken care by the modulus inside the cosine inverse in the expression for BA. Figure 5.4 represent the BAD for minima and maxima of SC23 and SC24 for SWR. The frequency in Figure 5.4 (similar in Figure 5.4-5.10) represents the rate of occurrence with respect to the total number of observations. The BAD of SIRs is compared to the background BAD to understand the effects of the Stream interaction. The data with velocities less than 400 km/s is used here as the background for slow wind, whereas the speed higher than 500 km/s is used as the background for the fast wind. The solar wind having velocities between 400-500 km/s are not considered to avoid the overlapping between slow and fast wind. The ICMEs and SIRs are removed from the data to estimate the background properties.

In Figure 5.4, the red and blue colours represent the protons and alphas respectively. In each panel of Figure 5.4, the upper part shows the BAD for SWR in a dotted line, and the dotted dashed line shows the BAD for the background wind. In each panel, the dashed vertical lines represent the point where the SWR and background BADs intersect. The bottom part of the panel illustrates the difference between the BAD of the SWR and the BAD of the background slow solar wind. The green line shows the difference or residue between the BADs of alphas and protons for SWR.

Figure 5.4 reveals a few important points. It can be seen that a portion of the lower BAD shifts towards higher values after the crossover point. This shift appears to be more during the maximum period of SC24. The crossover point is nearly 50° for SC23 and SC24. The crossover points are almost identical in SC23 and SC24 except for SC23 minima wherein a difference of 2.7° is noticed. The green line is near zero, i.e., there is little difference between the BADs of alphas and protons. Therefore, it is apparent that there is not much difference between the BADs of alphas and protons for the SWR. Additionally, there are

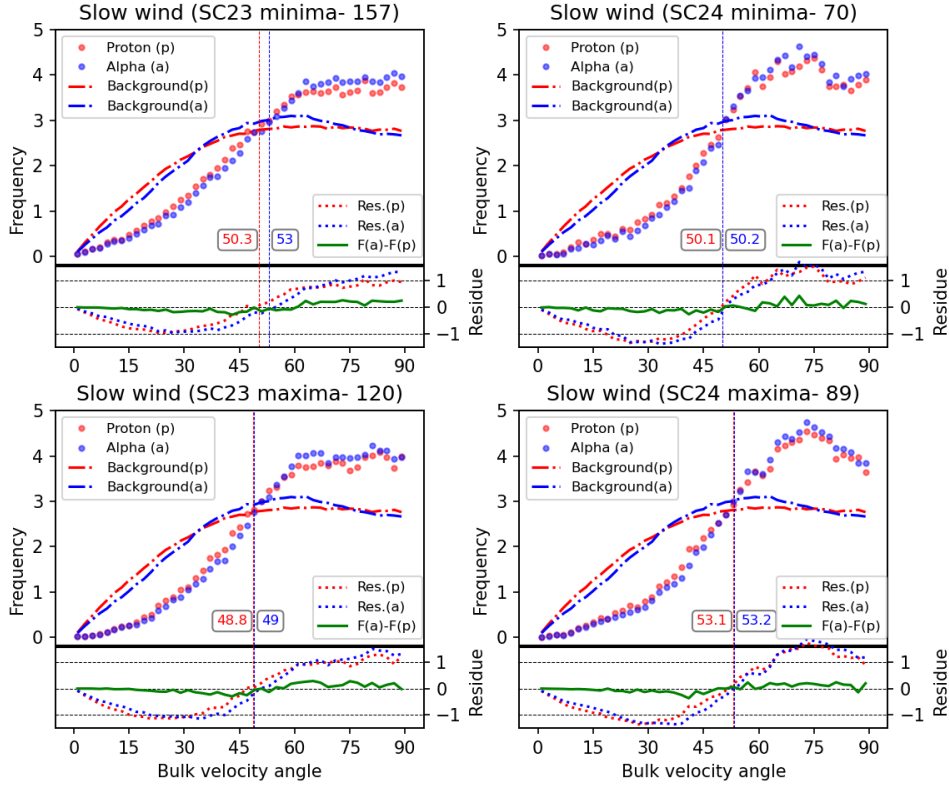


Figure 5.4: The BAD in the SWR for SC23 minima, SC23 maxima, SC24 minima, and SC24 maxima respectively are shown. The red and blue colours represent protons and alphas, respectively. The upper part of each panel shows the BAD for SWR and slow (<400 km/s) background wind while the lower part of each panel shows the differences (Residues) between them for alphas and protons. The green colour indicates the difference between the residues of the alphas and protons for the slow wind.

more protons and alpha particles for higher BAs than the background slow solar wind. The SC24 maxima show the highest shift of particles from lower BAs to higher BAs. The SC23 SWR distribution also shows a plateau region (no distinct sharp peaks in the BADs) for higher BAs in both maxima and minima. In contrast, distinct peaks can be seen in the case of SC24 SWR distribution during both maxima and minima. These aspects will be taken up in the discussion section.

The BADs for SWR are also calculated for the alphas in the solar wind (proton) frame. These are shown in Figure 5.5. It can be seen that the background and SWR BAD of alpha particles in the proton frame do not show significant

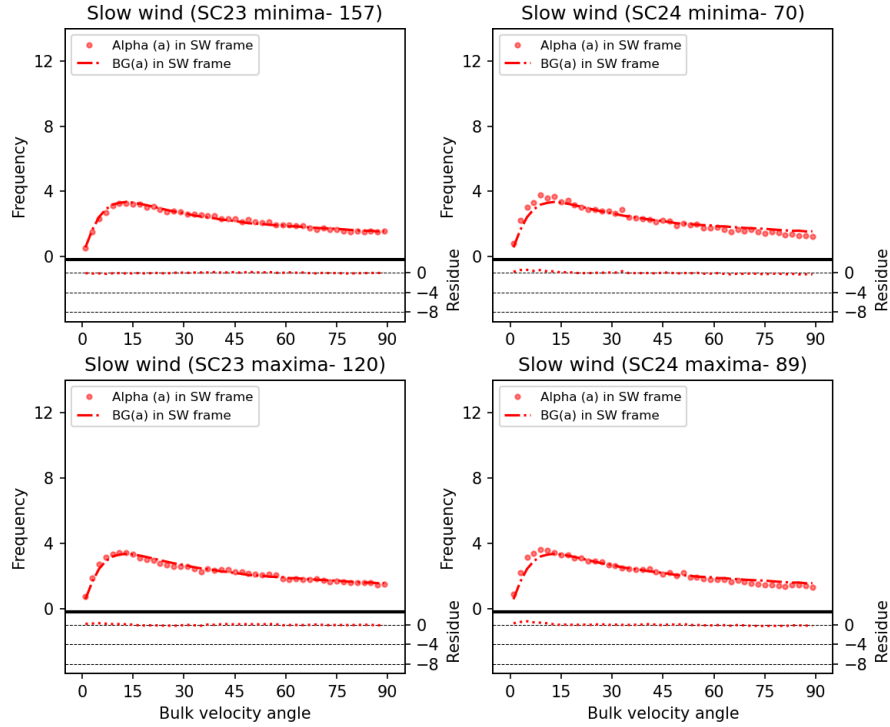


Figure 5.5: Same as Figure 5.4 but the BADs of alpha particles are shown here in solar wind (proton) frame. The dotted dashed and dotted lines are for the BADs for the background slow wind and SWR, respectively.

differences. These findings obtained from Figure 5.5 are consistent with those obtained from Figure 5.4 and therefore, the inferences drawn from Figure 5.4 are invariant even in the solar wind proton frame.

Similar analysis is also performed for the FWR. Figure 5.6 is analogous to figure 5.4 but applicable for FWR and background fast wind. Figure 5.6 reveals that a portion of the particle distribution with lower BAs in the background solar wind shifts towards higher BAs, similar to the SWR distribution. Unlike the slow solar wind, which has a single crossover point, the BADs for FWR and background fast wind exhibits at least two crossover points. The first crossover occurs at a lower angle, while the second occurs at a slightly higher value. The crossover BAs for protons are approximately 40° and 45° , except for SC23 minima, which have values of 31.1° (proton) and 37.6° (alpha). The difference between the crossover angles of protons and alphas is approximately 5 degrees, with alphas having higher crossover angles, indicating a higher shift of alpha particles towards

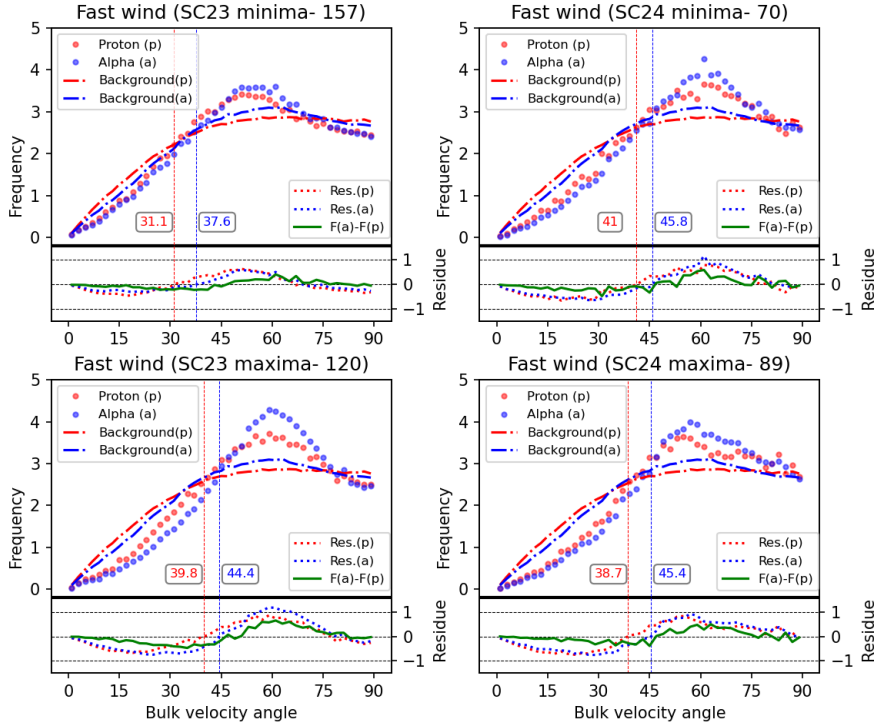


Figure 5.6: The BAD for the FWR for SC23 minima, SC23 maxima, SC24 minima, and SC24 maxima respectively are shown. The red and blue colours represent protons and alphas, respectively. The upper part of each panel shows the BADs for the fast wind region and fast (>500 km/s) background wind while the lower part of each panel shows the differences (Residues) between them for alphas and protons. The green colour indicates the difference between the residues of the alphas and protons for the FWR.

higher BAs. The green lines suggest that alphas are more dominant at higher BAs compared to protons.

At this juncture, the analysis shown in Figure 5.6 is repeated by taking an equal number of events in each maxima and minima of SC23 and SC24 to evaluate the impact of the effects of the sample size on the results. It can be seen that Figure 5.6 and Figure 5.7 show similar results except for the changes in the absolute numbers. Therefore, it can be concluded that the results reported here remain consistent regardless of the number of events considered.

BADs for alphas in the solar wind (proton) frame are also computed for the FWR and shown in Figure 5.8. Similar to Figure 5.6, the BADs for alphas in the solar wind frame show similar shift towards higher values. The results observed

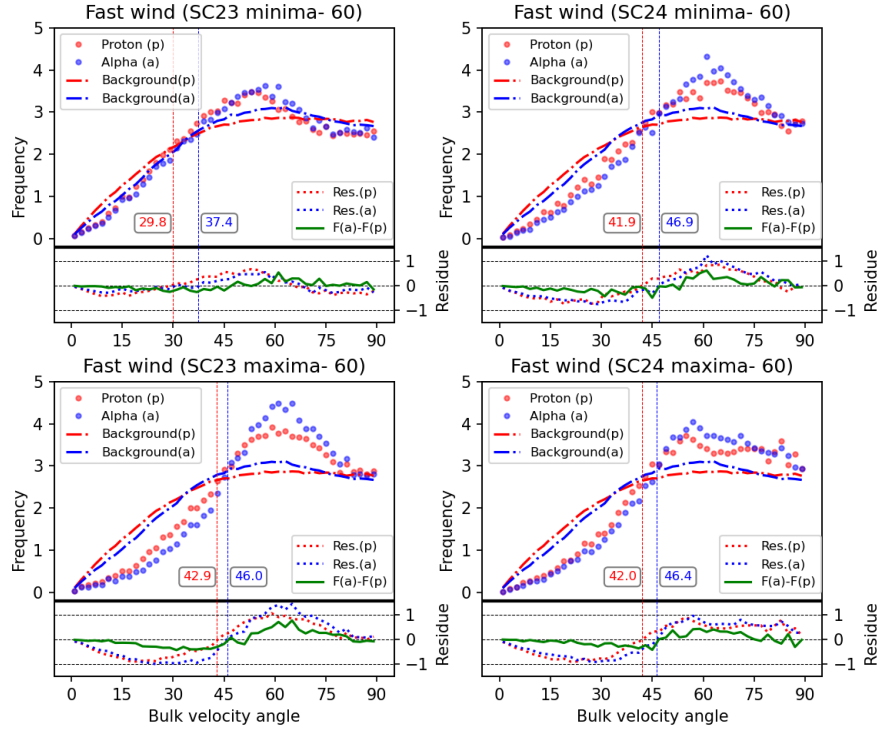


Figure 5.7: Similar to Figure 5.6 but for equal events (60). The results remain consistent regardless of the number of events considered.

in Figure 5.8, similar to Figure 5.6, suggests that the results reported in this work do not change in the solar wind frame.

In the context of Figure 5.5 and 5.8 one important point to be noted. Němeček et al. (2020) showed that the differential velocity angles are close to zero. It appears that this scenario is valid in the absence of stream interactions. The present investigation suggests that in the presence of stream interaction, the bulk velocity angles may change significantly. The different uncertainties in deriving proton and alpha velocities may additionally contribute to this difference as well.

5.3.4 Distribution of velocity difference between alphas and protons

In this subsection, we have analyzed another important parameter: the difference between alpha and proton velocities (Differential velocity). Similar to the previous subsection, the SIRs are divided into four parts based on solar activity

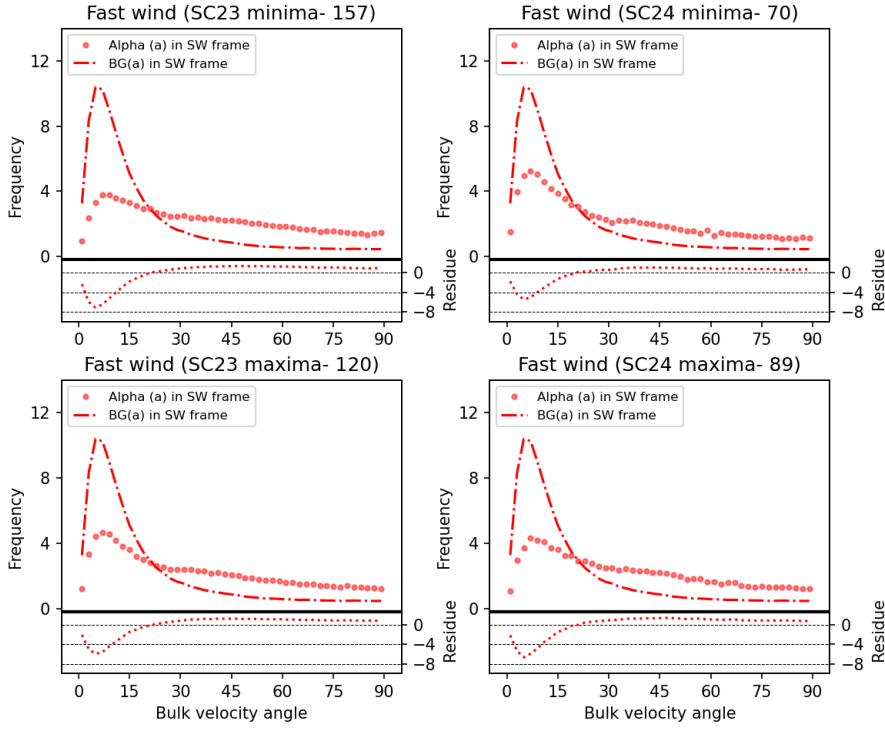


Figure 5.8: Same as Figure 5.6 but the BADs of alpha particles are shown here in solar wind (proton) frame. The dotted dashed and dotted lines are for the BADs for the background fast wind and FWR, respectively.

level. Figures 5.9 and 5.10 show the distribution of velocity differences for SWR and FWR, respectively. The red and blue colour in both the figures shows the differential velocity distribution for SWR and FWR, distribution of the background differential velocity, respectively. The green colour represents the difference (Residue) between the two distributions, i.e., differential velocity distribution for SIR and background differential velocity distribution. Figure 5.9 reveals that the distribution of SWR is nearly indistinguishable from the distribution corresponding to the background solar wind, except for the minor deviation at the center ($V_a - V_p = 0$) of the distribution.

In contrast to SWR, the FWR distribution of differential velocity shows more conspicuous changes. Similar to Figure 5.9, the red colour indicates the differential velocity distribution for the FWR in Figure 5.10. Blue colour represents the background distribution for the fast wind (velocity > 500 km/s). The green colour shows the difference between these two distributions. The background distribu-

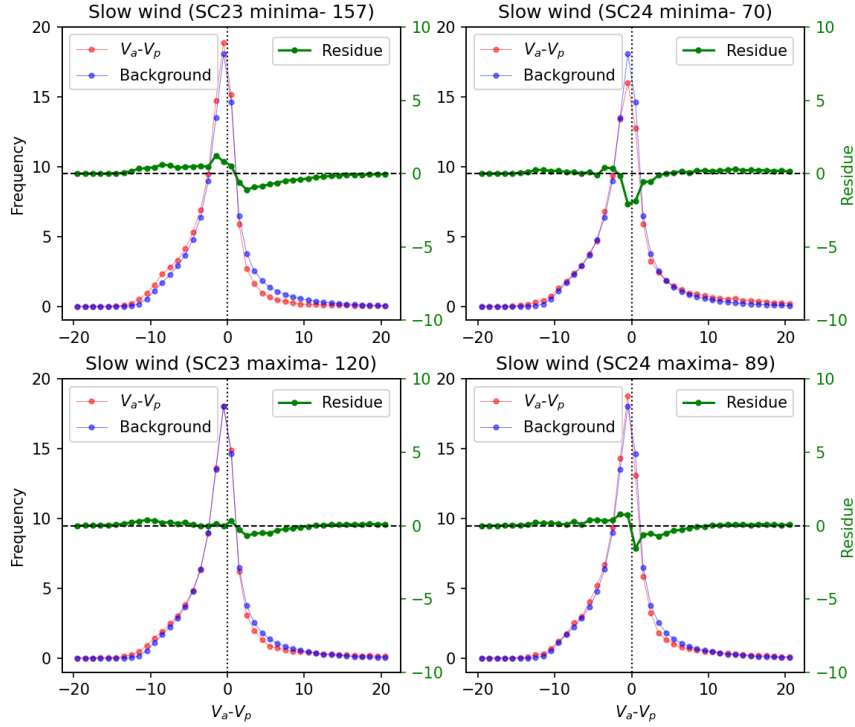


Figure 5.9: The distribution of differential velocity (alpha velocity – proton velocity) for SC23 minima, SC23 maxima, SC24 minima, and SC24 maxima, respectively, are shown for the slow wind region (SWR). The red and blue colours are used for the differential velocity distribution for the slow wind region in SIR and background slow wind, respectively. The green colour represents the difference between the SWR in SIR and the background slow wind distribution.

tion exhibits enhanced tails towards the positive side due to the higher velocity of alpha particles compared to protons in the background fast wind. In the case of FWR, the tail of the distribution towards the positive side is diminished compared to the background. This reduction indicates that faster alpha particles are slowed down in the interaction region and tend to accumulate near the centre ($V_\alpha = V_p$) of the distribution. The substantial enhancement of the residual curve in green near the center reflects this accumulation of alpha particles in the proton frame. This phenomenon is the primary cause of the enhanced helium abundance observed towards the FWR of SIRs. Another important observation to be made here is that [Marsch et al. \(1982\)](#) showed (Figure-10) the velocity difference to be almost zero in the 300-400 km/s velocity range at 1 AU. This velocity range contributes to 25% of the total solar wind, as shown in Chapter - 3. Therefore, it

is expected that zero differential velocity should be observed in $\sim 25\%$ of the total cases. Figures 5.9 and 5.10 show that the zero differential velocity contributes maximum ($\sim 20\%$) to the total observations and 80% of the total cases show significant differences in the alpha and proton velocities. Therefore, the results shown in Figures 5.9 and 5.10 are consistent with the results of Marsch et al. (1982).

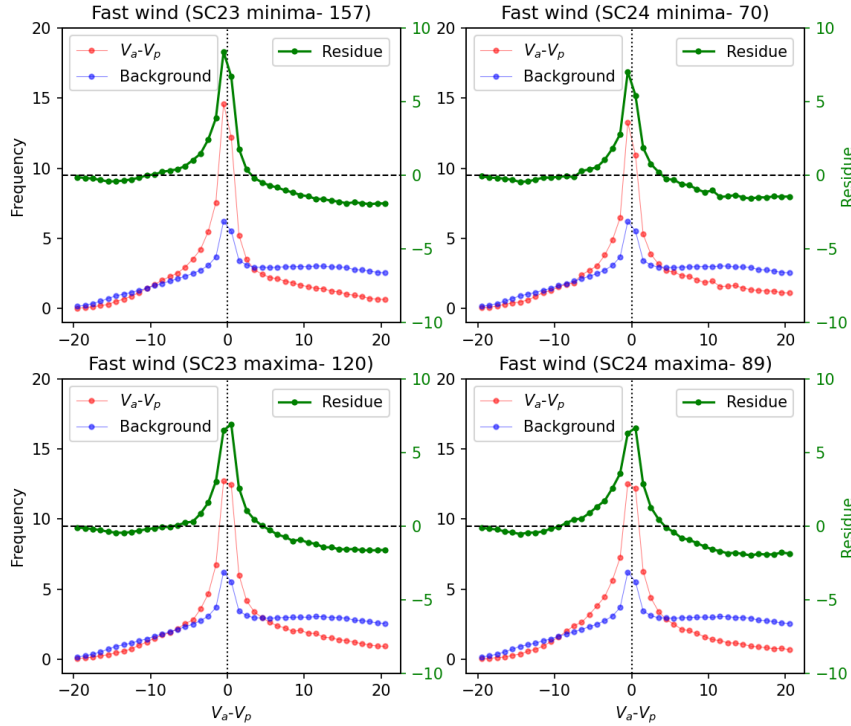


Figure 5.10: Same as Figure 5.9 but for the FWR.

This enhanced A_{He} near the centre ($V_a = V_p$) of the distribution is consistent with additional SI for alpha particles in Figure 5.3, indicating a preferential accumulation of alpha particles in the Fast Wind Region (FWR). Notably, the decoupling of these additional SI from the SI determined based on proton-related parameters such as number density, compressed magnetic field, flow deflection, and temperature increase (Chi et al., 2018) suggests that this additional SI is not a result of mixing processes. If mixing were the cause, additional SI would have also been observed in the Slow Wind Region (SWR) as well. Hence, alpha particles appear decoupled towards the FWR due to differential forcing resulting from differences in BA and velocity compared to protons.

Furthermore, we observe minimal disparity in the velocity differences at the maxima and minima of SC23 and SC24. Considering that SC24 was a weaker cycle compared to SC23, this implies that the alteration in the differential velocities between alpha particles and protons within SIRs is predominantly influenced by interplanetary processes. This aspect will be elaborated in the subsequent section.

5.3.5 Validity of magnetic mirror hypothesis

It should be noted that factors other than the magnetic mirror effect may also contribute to the variation of A_{He} within SIRs. While the SPA reveals distinct changes in A_{He} across SI, the influence of other processes occurring within the interaction region cannot be disregarded. One such process is the diffusive shock acceleration that can alter A_{He} within SIRs (Durovcová et al., 2019). However, as pointed out by Durovcová et al. (2019), variations in A_{He} are also observed for SIRs/CIRs not bounded by shocks. In such cases, the role of diffusive shock acceleration is not unambiguous.

Additionally, the simple magnetic mirror model overlooks the impact of turbulence and plasma waves in the solar wind, which may be associated with the passage of SIRs through the interplanetary medium. Further, the propagation of SIRs/CIRs through the interplanetary medium can introduce nonlinear effects related to magnetic field steepening and expansion (e.g., Burlaga and F.-Viñas, 2004; Durovcová et al., 2019). To accurately describe and model the behavior of helium within SIRs, these aspects need to be taken into consideration.

The SI of alpha shows different characteristics as compared to the SI of protons as seen in Figure 5.3. This may be due to the fact that although the mirroring hypothesis is reasonably effective in explaining the increase in alphas towards the FWR, a two fluid description is not enough to predict the behaviour of alphas at the stream interface region. One probably needs a three fluid description (protons, alpha and electrons as neutralising fluid) to understand the behaviour of alphas at the stream interface.

5.3.6 Uncertainties associated with alpha particle measurements

The derived alpha parameters generally have more uncertainties compared to proton parameters. Further, there can be significant overlap between the Velocity Distribution Functions (VDFs) of protons and alphas in the compression region. In this study, we have utilized the mean values of proton and alpha densities and velocities without considering the 1-sigma (standard deviation) variations. While this approach does not impact the conclusions drawn in this work, it does affect the specific characteristics of the BA and differential velocity distributions. For instance, considering 1-sigma variations would result in changes to the value of the crossover BA and the width of the residual curve centered around zero differential velocity.

5.4 Discussion

In this chapter, we present evidence that alpha particles and protons exhibit distinct behaviour within SIRs, and we observe an enhancement in A_{He} across the stream interface in FWR. Previous studies, such as [Gosling et al. \(1978\)](#), proposed that the A_{He} enhancement at the stream interface results from the different solar wind types (fast wind with high A_{He} and slow wind with low A_{He}). On the other hand, [Durovcová et al. \(2019\)](#) proposed that SIRs can be understood as magnetic bottles or mirror assemblies. In the magnetic bottle, the magnetic field and ion velocity govern the ion's motion. The magnetic mirror force depends on the ions' magnetic moment, given by $\mu = mV_{\perp}^2/2B$ where m and V represent the mass, and charge of ions (protons and alphas in this case), respectively. This force decelerates ions or causes ions with pitch angles higher than the loss cone angle to undergo bounce-back motions.

Our findings indicate that alpha particles and protons have similar BAs in the SWR, but in FWR, more alpha particles are distributed towards higher BAs than protons. It is worth noting that the mirror hypothesis is the most effective when BAs (ranging from 0 to 90 degrees) exceed the loss cone angle. Therefore,

the mirror hypothesis can be applied as long as the mean loss cone angle aligns closely with the BA crossover. The observed changes in A_{He} within SIRs in relation to the loss cone angle are discussed in detail by [Durovcová et al. \(2019\)](#). Another important aspect is that the BA crossover between the SIR and background distributions is similar for alpha particles and protons in SWR. However, in the FWR, this crossover differs by approximately 5 degrees. This change in distribution may play a significant role in the enhancement of alpha particles observed in the FWR of SIRs.

In addition to BA, the velocity of the solar wind also plays an important role in determining the number density of particles. Typically, protons and alpha particles have similar velocities in the SWR, while alpha particles are faster than protons in the FWR. Due to their higher velocity and mass, alpha particles possess a higher magnetic moment. As a result, they experience a greater magnetic curvature or mirror force compared to protons. The implication of this increased force can be observed in [Figure 5.10](#), where the frequencies of alpha particles faster than protons are reduced in the FWR of SIRs. Consequently, this difference in curvature force between alpha particles and protons leads to a second peak of alpha particles towards the FWR of SIRs.

The additional important point that comes out from this work is that the BAD for SWR in SC24 shows overall similarities with the BAD of FWR. This includes the peak at higher BAs in the BAD of SWR similar to BAD of FWR. On the contrary, the SWR BAD distribution in SC23 shows a plateau at higher BAs. This indicates the changes in the sources of slow solar wind in SC24 compared to SC23. This is consistent with the suggestion made in [chapter 3](#) wherein this was indicated based on the results obtained on the changes in the abundance of solar wind helium. The results presented above indicate that the solar activity levels do not primarily determine variations in helium abundance in SIR. Solar activity can influence the level of A_{He} enhancement in the SWR by altering the background value of helium abundance in the slow solar wind. This can be observed in [Figure 5.3](#), where the enhancement level in helium differs in the SWR, while it remains approximately same in the FWR. Rather, the BA and differential velocity are

found to be important factors influencing helium abundance in SIR.

One particular observation provides additional credence to this argument. When considering the SWR of SIRs, no notable changes are observed in terms of BA and differential velocity. This lack of significant variation in SWR may result in similar enhancement observed in both alphas and protons in this region. However, in the case of the FWR, there are significant disparities in the BA and differential velocity distributions between alphas and protons. The crossover points between the background distribution and the FWR distribution for alphas occur at a higher angle than protons. This indicates that a larger proportion of alpha particles are shifted towards higher BAs compared to protons, resulting in a considerable increase in the alpha number density. This seems to contribute to the generation of a second peak in the distribution of alphas in the FWR. Moreover, the differences in the BAD of SC23 (plateau) and SC24 (peak) suggest additional variations in the source of slow wind during these cycles. On the contrary, the differential velocities of alphas and protons do not exhibit significant changes in SC23 and SC24. This suggests that SIRs play a primary role in determining the differential velocities.

In addition to the magnetic mirror hypothesis, collisionality in both slow and fast solar winds plays a crucial role in determining the velocity difference between protons and alphas. The difference in velocity between alpha particles and protons in the slow wind disappears, possibly due to the higher collisionality of the slow solar wind. Conversely, the fast solar wind, characterized by lower collisionality, behaves differently. The higher collisionality explains the similar behavior of alpha and protons towards the SWR. However, in the FWR, alpha particles are piled up due to negligible collisionality. Exploring these aspects using collisional age is beyond the scope of this thesis and could be investigated in the future.

5.5 Conclusion

1. Alphas and protons exhibit similar behaviour in the SWR of SIRs, while they demonstrate contrasting behaviour in the FWR.
2. The crossover between the BAD of the SIR and the background indicates a higher concentration of alphas at elevated BAs in the FWR.
3. In the SWR, there is minimal difference in the differential velocity distribution between the SIR and the background.
4. In the FWR, there is a significant disparity in the differential velocity distribution between the SIR and the background.
5. The levels of enhancement differ among the minima and maxima of SC23 and SC24.
6. The bulk velocity angle and differential velocity distributions show relatively minor changes across different phases of the solar cycles, suggesting that the observed behavioural changes are primarily influenced by the interactions occurring in the interplanetary medium.

Chapter 6

Very Low Helium Abundances in the solar wind: Insights

Abstract

The abundance of helium ($A_{He} = 100 * N_a/N_p$) in the solar wind exhibits variations ranging from 2-5% with respect to solar cycle activity and solar wind velocity. However, there are instances where the observed A_{He} is exceptionally low ($< 1\%$). These occurrences of low A_{He} levels are detected both near the Sun and at 1 AU. These low A_{He} events are generally observed near the heliospheric current sheet. We use 28 such events from the WIND spacecraft and 4 such events from the Parker Solar Probe (PSP) to understand the origin of these events. The backtracking of these events using the ADAPT-WSA model shows that these events originated from the coronal hole boundaries. We also show that the coronal holes and the core of the streamer cannot produce this kind of very low helium abundance. The legs of the streamers are the most probable source candidates for these events. The association of these legs with coronal hole boundaries can produce very low helium abundances. We propose that the freezing of A_{He} at higher heights within the streamer legs can explain very low A_{He} events.

6.1 Introduction

Helium abundance in solar wind, represented as $A_{He}=100 * N_a/N_p$, varies significantly in the solar atmosphere. Depending on the sources, coronal and interplanetary modulations, A_{He} can vary from 0.1% to more than 30%. A_{He} follows the solar cycle (SC) and varies with solar wind velocity (Kasper et al., 2007; Alterman and Kasper, 2019). It is 8% in the photosphere and gets reduced to 4-5% in the solar corona. It can go up to 30% in coronal mass ejections (Fu et al., 2020, and references therein). It also varies in the interplanetary (IP) medium depending on the interaction between the different solar wind streams (Durovcová et al., 2019). The variation in the helium abundance can tell us about the different processes occurring near the solar surface and interplanetary medium. Based on remote-sensing observations, Moses et al. (2020) showed that helium is not uniformly distributed in the solar atmosphere. The variation of A_{He} in the solar wind, CMEs etc., has been explored by various researchers (Kasper et al., 2007; Alterman and Kasper, 2019; Fu et al., 2018, etc.). However, there are very few works on the very low ($< 1\%$) helium abundances in the solar wind. This is an important problem as understanding very low helium abundances may shed important lights on how the solar wind is generated and comes out of the Sun.

Borrini et al. (1981) showed that the helium abundance is low near the sector boundaries in the interplanetary (IP) medium. They also showed that these regions are generally associated with higher proton and electron densities, IP field polarity reversals, low bulk velocity, low alpha and proton temperature, minimum in the alpha-proton temperature ratio (T_a/T_p) and nearly equal hydrogen and helium speed. They suggested that these events may be related to the streamer belts. They indicated that these events might be associated with the solar current sheets. However, the processes that could decrease the amount of helium so drastically was not addressed. Also, it was unclear whether these reductions in the A_{He} were because of the interplanetary modulations or due to the processes that occurred closer to the Sun.

In recent times, a few other researcher (Sanchez-Diaz et al., 2016; Vasquez et al., 2017) also observed and indirectly studied the low helium abundance.

The low helium abundance was observed in the very slow solar winds (VSSW) (Sanchez-Diaz et al., 2016). These authors used the Helios data to understand the properties of the VSSWs. They showed that the A_{He} in VSSW also varies with the solar cycle (SC). They also suggested that the velocity of helium ions was less than the proton velocities in cases of VSSW events. During solar maxima, the A_{He} value in the VSSW was higher than that in the normal slow wind in case of a few events. Although their main objective was to understand the properties of VSSW, they showed that these events were related to the Heliospheric Current Sheets (HCS) and High-Density Regions (HDR). Vasquez et al. (2017) studied A_{He} in very slow ejecta and winds near solar minima of SC23. They showed that slow ejecta and winds show similar A_{He} variation. They also showed that these events follow the relationship between the A_{He} and velocity shown by Kasper et al. (2007) earlier. However, this relationship deviated at a very low speed. Although these authors studied the sources of the ejectas, the reason behind the low A_{He} events and their sources were not explored.

Suess et al. (2009) studied the quiescent current sheets in the solar wind and found that helium abundance is very low in the vicinity of the current sheets. Their main objective was to study the current sheets and the origin of slow wind. Woolley et al. (2021) recently found very low helium abundance observed by Parker Solar Probe (PSP). Despite these observations, the causes behind these low abundances remains relatively less explored so far.

The above discussion suggests that the low A_{He} events are generally observed near the HCS and the streamers, but the process causing this depletion is unclear to a great extent. In order to address this gap area, we have critically looked into the solar sources of these events. Interestingly, in some cases, the increment in the proton densities also contribute in the reduction in A_{He} . In this work, we present cases where significant reduction in A_{He} were majorly due to the reduction in the helium ions in the solar wind and not due to increase of the proton densities. We have also used the PSP data to see the origin of the low A_{He} events closer to the Sun. We have used the ADAPT-WSA (Air Force Data Assimilative Photospheric Flux Transport - Wang-Sheeley-Argé model) model to identify the solar sources

of these events. The data used and model details are presented in Section 6.2. Section 6.3 shows the results, and the probable reasons behind the reduction in A_{He} are discussed in Section 6.4.

6.2 Data Section and Model details

We have used OMNI data with 1-hour cadence for the selected events. OMNI data can be found at <https://cdaweb.gsfc.nasa.gov/index.html/>. The data utilized for our analysis spans from 1995 to 2021. We have chosen those events for which very low A_{He} ($< 1\%$) condition persists for more than 48 hours at the Sun-Earth L1 point. The data from Solar Wind Experiment (SWE) (Ogilvie et al., 1995) and Magnetic Field Investigations (MFI) (Lepping et al., 1995) instruments on board the Wind satellite are used for proton, alpha parameters and magnetic field respectively. All the events observed here are from the solar minimum epoch.

In this work, we have also used data from Solar Probe Analyzer for Ions (SPAN-I), which is a subsystem of the Solar Wind Electrons Alphas and Protons (SWEAP) (Kasper et al., 2016) onboard Parker Solar Probe (PSP). The SPAN-I instrument provides the alpha and proton parameters, whereas the magnetic field observations are used from the FIELDS instrument suite (Bale et al., 2016).

In addition to the above observations, we have used the ADAPT-WSA model to identify the sources of these low A_{He} solar wind events. This model combines both empirical and physics-based approaches. This model is an upgraded version of the original WS model (Wang and Sheeley, 1992; Wang et al., 1995). The global full disc magnetograms are used as the input in this model. The global synchronic photospheric field maps generated by the ADAPT model are used in this work. The ADAPT model incorporates magnetic flux transport (Worden and Harvey, 2000) to account for differential rotation and can interpolate situations when observations are not available. After getting the input from ADAPT maps, the WSA uses the traditional PFSS model to determine the coronal fields from the source surface height, i.e., $2.5R_{\odot}$ (Hoeksema et al., 1983). The outputs of the PFSS model are used as the input to the Schatten Current Sheet (SCS)

model (Schatten, 1971). This SCS model will give us more realistic magnetic field topologies of the corona.

WSA along with ADAPT provide twelve solutions. These solutions represent the global state of the coronal field and connectivity from a spacecraft to $1R_{\odot}$ for a given time. The best output is determined through a comparison between the magnetic field and solar wind speed obtained from the model and the corresponding observed values. Further details regarding the model can be found in the work by Wallace et al. (2019, 2020).

In this work, we are using the WIND data to see the variation in solar wind parameters because of the availability of high cadence data. However, Advanced Composition Explorer data is also used to compare the model output and interplanetary data. The Wind and ACE observations have a high correlation in the case of most of the events. Data from the Solar Wind Ion Composition Spectrometer (SWICS; Gloeckler et al., 1998) onboard ACE are used to understand compositional changes during the events.

6.3 Results

6.3.1 In-situ measurements of Low helium abundance events

The low ($<1\%$) helium abundance (A_{He}) events are identified using the data compiled at OMNI web and using the PSP data. We chose 28 events from the OMNI data (duration higher than 48 hours) and four from the Parker solar probe (PSP).

The events identified based on the Parker Solar Probe (PSP) data have shorter durations. This is because the position of PSP changes very fast. The PSP events are chosen based on the SPAN instrument's data coverage, i.e., when alpha and proton measurements are both available. The details regarding the selection criteria of the PSP events can also be seen in Mostafavi et al. (2022). These observation criteria are used to avoid the misinterpretation of the PSP data. We found four such events from encounters 4 (2 events), 9 and 11. The details regarding WIND and PSP events are provided in the Table 6.1.

In this section, we will discuss one event observed from each spacecraft, i.e. WIND and PSP. The other events are also analyzed similarly and the results are provided in the Table 6.1. The event from December 2019 is shown in Figure 6.1 below. The panels a-f of Figure 6.1 represents various parameters, i.e., magnetic field components, velocity (alpha and proton), number density (proton and alpha), helium abundance, the temperature of the proton (T_p) and alpha (T_a), and differential velocity. It can be seen from Figure 6.1 that this event has low velocity (average $\sim 310\text{km/s}$). All the other events have similarly significantly less speed. The blue and red horizontal dashed lines in Figure 6.1c show the solar cycle (SC) average of proton and alpha number density, respectively. It is seen that the proton number density is usually higher or equal to the average value for almost all the time. In contrast, the helium number density is (with a few occasional spike-like increases) significantly less than the average A_{He} value during the interval marked by the vertical red dashed lines. Similar feature is observed for the other 28 events as well. This suggests that the reduction in alpha number density causes these very low A_{He} events. Another point that can be noted is that the velocities of alphas and protons are almost equal for the duration of the event. In fact, almost all the events characteristically show low alpha density, slow speed and negligible alpha and proton velocity difference. Therefore, it appears that all the events originated from the same source or underwent some interplanetary modulations. To further confirm these characteristics, we have used PSP observations.

Figure 6.2 shows PSP event number two from the Table 6.1. The variation of all the parameters shown in the Figure 6.2 are in the instrument frame. The panels a-f of Figure 6.2 show magnetic field components, bulk velocity of alphas and protons, alpha and proton number density, helium abundance, T_p , T_a and difference in the bulk velocities of alpha and proton. The event shown here is the encounter 4 when PSP was at a distance of 0.13 AU ($27.8 R_{\odot}$).

It can be seen from Figure 6.2 that the low A_{He} (except occasional spikes) interval is not only confined to the interval of encounter 4 but also extended more than 12 hours before and after the encounter interval. It can be seen that,

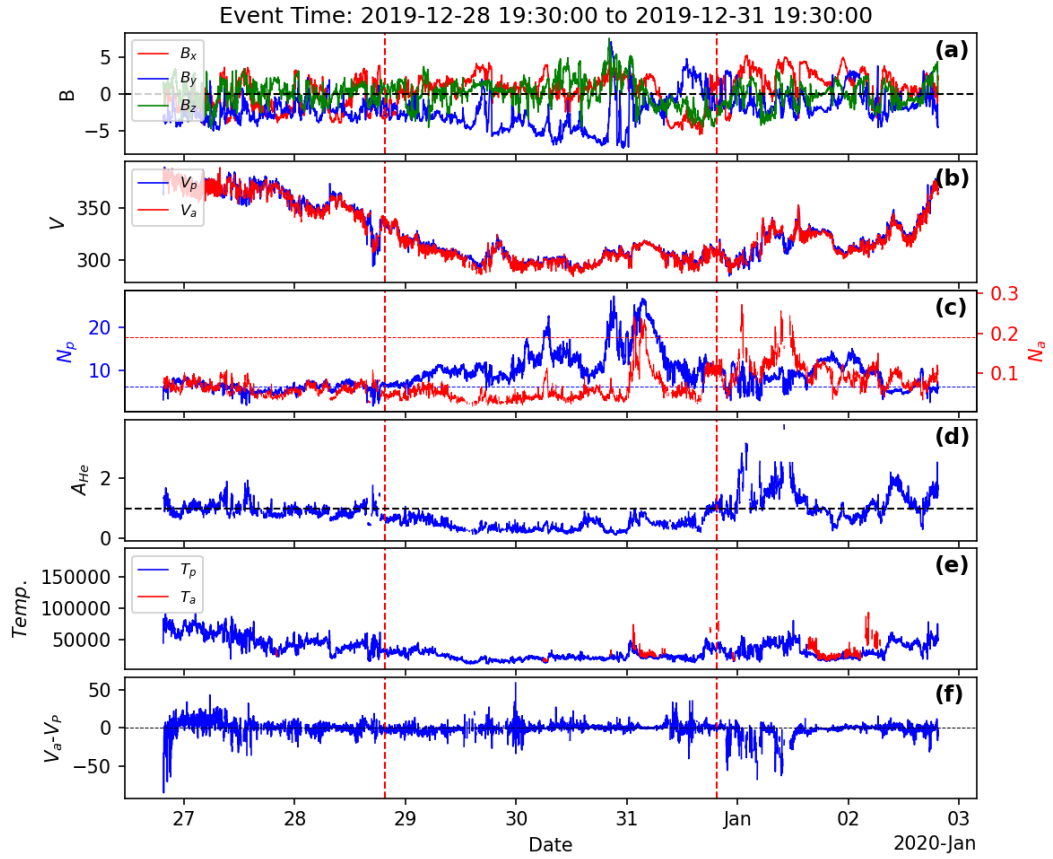


Figure 6.1: The low helium abundance event observed by Wind spacecraft in December 2019. The variations of the parameters, i.e., magnetic field components, velocity (alpha and proton), number density (proton and alpha), helium abundance, proton and alpha temperature (T_p , T_a), and differential velocity, are shown in panels a to f. The blue and red horizontal lines in panel c represent the average number density of protons and alpha particles over two SCs. The panel c shows that the proton density (N_p) are higher than average value of N_p (6.29) over the two solar cycles. On the contrary, the densities of alpha particles are lower compared to the two solar cycle averaged value. There is significantly less velocity difference between the alpha and protons (see panel f).

unlike Figure 6.1, there is a finite velocity difference between the alphas and protons in the event duration. Interestingly, this velocity difference is reduced after the event. Solar wind is also slower. This extended part also shows similar properties to the events observed at the L1 point by WIND with the exception of temperature of protons and alphas (T_p and T_a). This is understandable as the temperatures observed at the L1 point and near the Sun are expected to be

different.

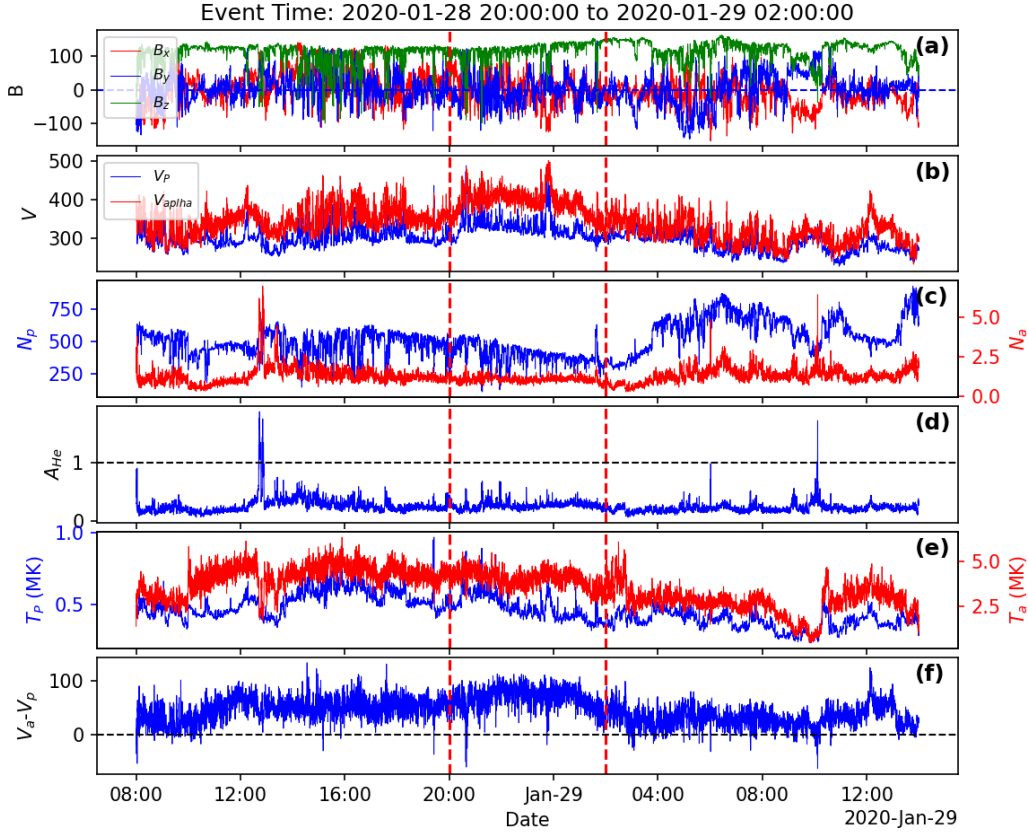


Figure 6.2: The low helium abundance event observed by PSP in January 2020. Similar to previous Figure, the variations in the solar wind parameters, i.e., magnetic field components, velocity (alpha and proton), number density (proton and alpha), helium abundance, proton and alpha temperature (T_p , T_a), and differential velocity, are shown in panels a to f. It can be seen the low A_{He} persist more than 12 hours before and 12 hours after the marked duration. The events time is selected based on the presence of alpha and protons in the field of view of the SPAN-I instrument onboard PSP.

Figure 6.2 shows that lower A_{He} events are also observed near the Sun. In the next section, all the events are traced back to the solar surface to understand the nature of the solar source. The ADAPT-WSA model is used for this purpose.

6.3 Results

Sr. No.	Start time		End time		Duration Hours	Average A_{He}	Average $N_p(6.29)$	Average $Na(0.19)$	Average Velocity (p)	Average Velocity (a)	Proton Temp.	Alpha Temp.	$V(p)-V(a)$	O^{7+}/O^{6+}	Fe/O
	Date	Time	date	Time											
	Wind Events														
1	1995-07-01	20:30:00	1995-07-03	21:30:00	49	0.54 ± 0.24	14.38 ± 4.95	0.082 ± 0.047	341.74 ± 12.11	340.49 ± 11.56	34048.4	77149.7	0.14	nan	nan
2	1996-04-06	15:30:00	1996-04-08	17:30:00	50	0.41 ± 0.29	14.41 ± 5.73	0.061 ± 0.047	309.23 ± 13.95	308.06 ± 13.67	16228.1	43921.1	0.51	nan	nan
3	2006-10-18	00:30:00	2006-10-20	02:30:00	50	0.63 ± 0.43	11.87 ± 4.79	0.068 ± 0.040	322.76 ± 17.49	321.55 ± 17.38	17024.2	18704.9	1.36	0.23	0.18
4	2007-03-20	16:30:00	2007-03-23	08:30:00	64	0.40 ± 0.18	11.41 ± 3.17	0.045 ± 0.025	285.48 ± 18.70	284.78 ± 17.94	17510.5	25856.4	1.23	0.174	0.22
5	2007-09-11	05:30:00	2007-09-13	11:30:00	54	0.46 ± 0.19	7.31 ± 1.74	0.031 ± 0.011	286.20 ± 14.68	287.92 ± 15.97	10924.8	14344.5	0.69	0.098	0.38
6	2007-10-09	21:30:00	2007-10-12	10:30:00	61	0.45 ± 0.31	11.25 ± 4.66	0.048 ± 0.043	271.79 ± 9.53	273.69 ± 13.16	11538.3	10332.2	2.64	0.17	0.16
7	2007-11-05	18:30:00	2007-11-08	02:30:00	56	0.42 ± 0.25	10.66 ± 1.28	0.044 ± 0.029	268.05 ± 12.92	271.08 ± 12.29	13173.1	16152.5	-0.81	0.192	0.17
8	2008-09-12	21:30:00	2008-09-14	23:30:00	50	0.44 ± 0.39	11.55 ± 7.55	0.062 ± 0.097	308.79 ± 21.38	307.70 ± 21.82	20149	47918.9	0.72	0.147	0.24
9	2008-11-12	03:30:00	2008-11-15	06:30:00	75	0.47 ± 0.13	6.99 ± 2.15	0.035 ± 0.011	311.55 ± 17.70	308.94 ± 19.45	22780.4	nan	0.5	0.098	0.18
10	2009-02-06	11:30:00	2009-02-08	12:30:00	49	0.52 ± 0.21	7.93 ± 2.16	0.041 ± 0.015	314.06 ± 7.87	312.02 ± 7.85	20728.9	21348.1	1.2	0.084	0.16
11	2009-08-15	00:30:00	2009-08-17	21:30:00	69	0.47 ± 0.21	8.09 ± 3.16	0.042 ± 0.022	283.92 ± 11.51	282.51 ± 13.06	17609.9	nan	2.17	0.203	0.29
12	2009-11-10	02:30:00	2009-11-12	04:30:00	50	0.68 ± 0.25	5.45 ± 0.86	0.036 ± 0.009	322.96 ± 28.08	320.31 ± 29.99	23808.7	12472.8	-1.09	0.058	0.18
13	2009-12-08	13:30:00	2009-12-11	00:30:00	59	0.66 ± 0.18	7.20 ± 0.98	0.046 ± 0.013	292.19 ± 13.51	292.88 ± 13.97	20989.4	20091.7	-0.22	0.053	0.22
14	2010-08-11	04:30:00	2010-08-13	05:30:00	49	0.55 ± 0.17	6.16 ± 2.15	0.031 ± 0.006	385.04 ± 52.11	385.77 ± 52.42	35160.6	nan	-2.19	0.187	0.19
15	2017-06-08	18:30:00	2017-06-11	15:30:00	69	0.54 ± 0.26	12.62 ± 5.41	0.067 ± 0.036	301.55 ± 18.32	299.59 ± 17.69	18581.2	17544.5	0.54	0.222	0.29
16	2018-01-06	02:30:00	2018-01-08	09:30:00	55	0.50 ± 0.29	14.82 ± 9.09	0.091 ± 0.131	298.42 ± 15.81	297.16 ± 15.73	19311.1	35658.2	1.62	0.251	0.18
17	2018-06-15	20:30:00	2018-06-17	22:30:00	50	0.52 ± 0.30	11.81 ± 6.25	0.066 ± 0.085	305.67 ± 9.98	304.63 ± 10.40	20821.3	56401	2.34	0.149	0.32
18	2018-10-19	09:30:00	2018-10-21	12:30:00	51	0.48 ± 0.27	11.42 ± 6.29	0.052 ± 0.044	302.50 ± 11.52	300.54 ± 11.85	20801.6	53313.3	0.75	0.138	0.28
19	2019-03-22	22:30:00	2019-03-25	01:30:00	51	0.63 ± 0.56	9.69 ± 6.58	0.070 ± 0.103	279.33 ± 17.51	281.45 ± 18.02	17336.5	42725.2	2.63	0.175	0.38
20	2019-06-06	02:30:00	2019-06-08	18:30:00	64	0.51 ± 0.36	11.91 ± 11.44	0.074 ± 0.180	303.38 ± 17.22	302.11 ± 17.87	20394	32727.5	0.17	0.126	0.31
21	2019-12-28	19:30:00	2019-12-31	19:30:00	72	0.48 ± 0.20	11.98 ± 4.55	0.058 ± 0.036	305.79 ± 9.51	304.49 ± 10.44	22735.6	27528.1	0.06	nan	nan
22	2020-05-13	08:30:00	2020-05-15	10:30:00	50	0.46 ± 0.25	12.39 ± 3.56	0.056 ± 0.028	297.73 ± 7.28	297.67 ± 7.12	17621.3	19362.8	1.01	nan	nan
23	2020-05-16	14:30:00	2020-05-18	22:30:00	56	0.53 ± 0.19	8.65 ± 1.99	0.048 ± 0.022	307.24 ± 11.62	306.31 ± 12.62	25843.1	nan	1.23	nan	nan
24	2020-06-05	12:30:00	2020-06-07	16:30:00	52	0.60 ± 0.27	11.47 ± 5.36	0.075 ± 0.074	319.55 ± 12.59	317.76 ± 13.08	31391.9	69127.9	0.28	nan	nan
25	2020-06-20	00:30:00	2020-06-23	16:30:00	88	0.48 ± 0.22	8.84 ± 4.10	0.037 ± 0.014	309.10 ± 16.78	304.70 ± 16.73	21309.9	21634.2	1.5	nan	nan
26	2020-09-19	19:30:00	2020-09-21	22:30:00	51	0.43 ± 0.38	9.88 ± 3.98	0.048 ± 0.053	294.89 ± 11.06	296.61 ± 10.31	16079.7	189721	0.75	nan	nan
27	2020-10-13	18:30:00	2020-10-16	10:30:00	64	0.47 ± 0.24	10.73 ± 3.67	0.050 ± 0.026	284.84 ± 13.49	285.23 ± 13.33	18221.9	25273.6	1.27	nan	nan
28	2021-08-22	21:30:00	2021-08-24	22:30:00	49	0.64 ± 0.90	13.03 ± 3.11	0.085 ± 0.110	305.92 ± 12.43	304.51 ± 13.10	25252.6	60986.2	2.36	nan	nan
PSP Events															
1	2020-01-28	00:00:00	2020-01-28	05:30:00	5.5	0.74 ± 0.44	157.18 ± 41.23	1.05 ± 0.26	529.79 ± 36.89	418.84 ± 45.54	730288.43	6285990.00	110.95		
2	2020-01-28	20:00:00	2020-01-29	02:00:00	6	0.27 ± 0.7	398.55 ± 73.73	1.04 ± 0.19	327.07 ± 29.42	395.44 ± 32.57	480635.34	4034057.67	68.37		
3	2021-08-09	00:00:00	2021-08-09	11:00:00	11	0.94 ± 0.25	2968.65 ± 798.08	27.76 ± 10.29	289.16 ± 31.73	325.64 ± 49.72	408999.30	2446157.92	36.47		
4	2022-02-24	08:30:00	2022-02-24	16:00:00	7.5	0.84 ± 0.27	1605.35 ± 370.90	12.92 ± 2.88	367.23 ± 39.50	443.35 ± 48.58	577080.97	4295912.54	76.12		

Table 6.1: The low helium abundance events ($A_{He} < 1\%$) observed by WIND and PSP spacecrafts are shown below. The duration of events observed by WIND is greater than 48 hours. The PSP events are of shorter duration and chosen based on the 360° observations of alpha and protons in the SPAN-I instrument. The start and end times, duration, average A_{He} , N_p , N_a , Average velocities of alphas and protons, proton temperature, alpha temperature and velocity difference between alphas and protons are shown for WIND and PSP events. O^{7+}/O^{6+} and Fe/O (using ACE data) are shown in the case of WIND only. The majority of events show higher proton number density (N_p) compared to the average value of Np over the two SCs (6.29), while the densities of alpha particles are decreased. In addition, the velocity difference is almost zero in WIND events, whereas the PSP event shows a finite difference between the alpha and proton velocities. The proton and alpha temperatures are low for these events.

6.3.2 Sources of low A_{He} events

Figures 6.3 and 6.4 represent the WIND and PSP events (discussed in the previous section) traced back to the Sun. We have used the ADAPT-WSA model for the global coronal magnetic field. The top panel in Figure 6.3 shows connectivity between the projection of WIND/PSP's location at $5 R_{\odot}$ and open field foot-points at $1 R_{\odot}$. The top panel represents the derived coronal holes together with the filed line connectivity. The middle panel shows the photospheric magnetic field. This coronal magnetic field at $5 R_{\odot}$ can be seen in the bottom panel of Figure 6.3. The dates labelled in red are satellite subpoints corresponding to when and from where the solar wind left the Sun at $5 R_{\odot}$. These red-coloured dates are joined with red/white tick marks representing the location of the satellite subpoints in all three panels of Figure 6.3. The black lines in panel 1 of Figure 6.3 are track of sub-satellite points at $1 R_{\odot}$. These black lines reveal the Model-generated source regions of the solar wind, which the WIND/PSP observed. The colour code represents the velocity in the same panel. The three panels are shown for the whole Carrington rotation (Left: CR-2225, right: CR-2226). The top panel of Figure 6.3 shows that solar wind originated from the coronal hole boundaries and reached the WIND/PSP.

Before tracking the specific lines of each event connected to the spacecraft, the best ADAPT-WSA solution from the 12 is selected for the period of interest. This is done by comparing the WSA-generated solar wind speed and magnetic field polarity for all 12 solutions with the observation from 4-6 days/ 1-3 days (solar wind travel time to reach WIND/PSP) after the solar wind left the Sun. The best realization is presented in Figure 6.4. The figure shows the model-derived solar wind (blue), and spacecraft observed (black) solar wind speed. The above two events, i.e. WIND/PSP, are well produced by the WSA model. There are a few events where the model output was not consistent with the satellite observations. This kind of events are listed in Table 6.2. Out of 4 PSP events, the first two are well predicted, and 3rd event was at the time when PSP was on the far side of the sun. For event 3 the magnetogram constructed by the ADAPT model has more importance because of the lack of observations. Looking qualitatively at Event

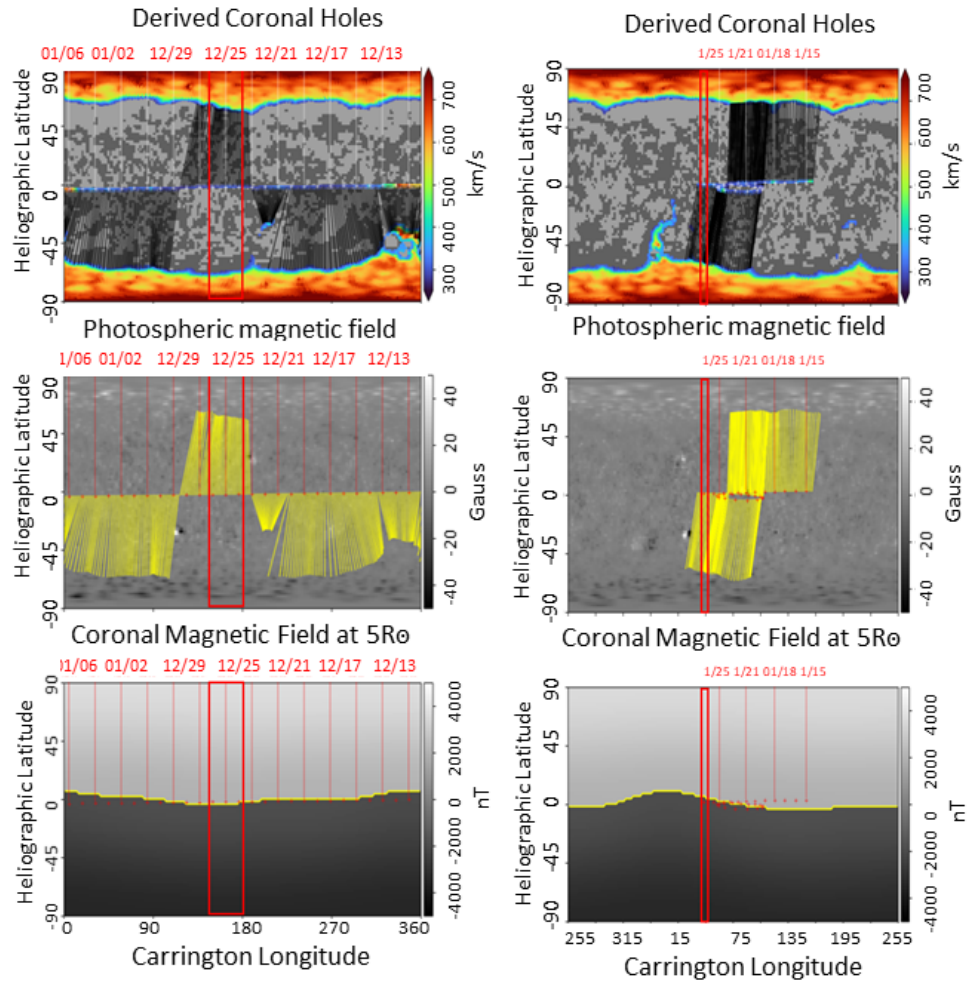


Figure 6.3: ADAPT-WSA model output for CR 2225 (Left) and CR 2226 (Right). The left and right model runs are for WIND and PSP satellite events (Figures 6.1 & 6.2). The white (top panel) and red (middle and bottom panel) tick-marks or vertical lines are subsatellite points with dates labelled in red. These lines represent the back projection of the WIND/PSP satellite at $5 R_{\odot}$. The top panel shows a WSA-derived open field at $1 R_{\odot}$ with model-derived solar wind speed in colour scale. Black lines indicate the magnetic connectivity between the projection of the observing satellite location at $5 R_{\odot}$ and the solar wind source region at $1 R_{\odot}$. The light and dark grey contours in the upper panel indicate the field polarity at the photosphere, with light corresponding to positive polarity and dark representing negative polarity. The photospheric field can be seen in the middle panel. This panel's yellow lines again show the the connectivity of satellite's projection to the photosphere. The bottom panel shows the WSA-derived coronal field at $5 R_{\odot}$. The yellow contour represents the heliospheric current sheet, derived from the model, which indicates the boundary where the overall coronal field undergoes a change in polarity.

3 is challenging, but we have recorded the event's details in Table 6.2. For event 4, the velocity did not match accurately, but the magnetic field polarity was well matched.

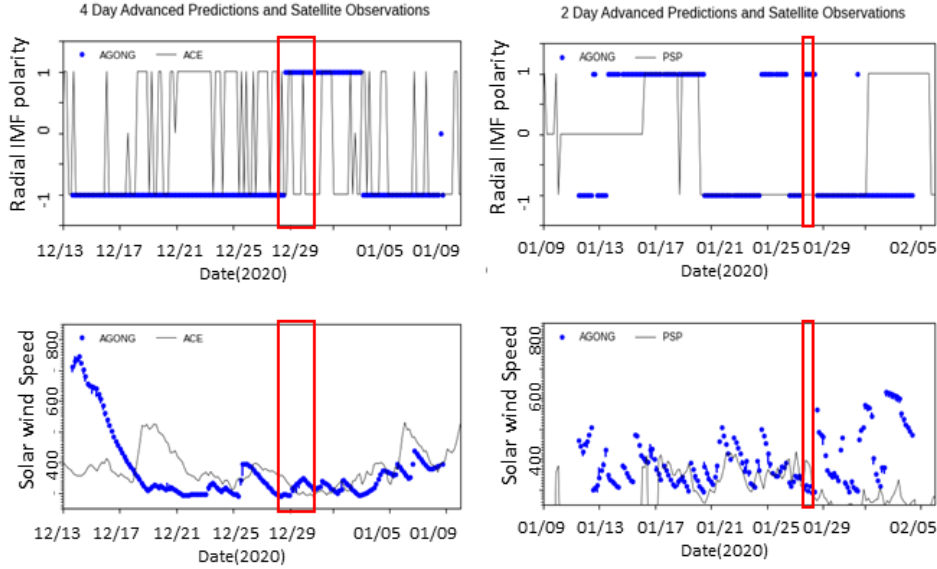


Figure 6.4: The left column is for the WIND event, and the right column is for the PSP event. The ADAPT-WSA model output (blue) vs the satellite observation (black) are shown. The upper panel is for the radial magnetic field's polarity, and the lower panel is for the solar wind velocity. Each solar wind represents the solar wind parcel connected to the WIND (ACE)/PSP.

The other parameters are calculated after the field lines are identified for each event. It is important to note that we are looking for in situ measurements of a solar wind parcel, which is a 3D structure, whereas the modelling of each structure only represents a 2D slice of a more extensive system. In addition, the model calculations are best matched for the events' duration compared to other parts of the Carrington rotation. The model also provides the speed of solar wind parcels that originate from each field line along the subsatellite track. The blue colour in Figure 6.4 represents the model-predicted solar wind speed and IMF of solar wind parcel coming out from a specific source region. This process of finding sources is repeated for all 28 and 4 events. The parameters given by the models are listed in Table 6.2. The model-derived parameters are mentioned for the events for which the model and observation show good consistency.

Sr. No.	Model comments	Model Start time		Model end time		SW Speed Km/s	Current sheet dist. (Deg)	B foot point (G)	Lon. footprint Deg ($1R_{\odot}$)	Lat. footprint Deg ($1R_{\odot}$)	Coronal hole distance	Expansion factor #/#
1	no good match											
2	no good match											
3	no good match											
4	OK	2007-03-21	01:32:44	2007-03-23	08:04:59	306.1	8.3	3.1	207.586	-56.4761	1.72	12.08
5	OK	2007-09-11	03:47:22	2007-09-13	11:40:59	329.4	8.7	-6.7	33.6719	67.0835	1.97	40.87
6	OK	2007-10-10	00:47:48	2007-10-12	11:55:14	308	3.1	-2.6	95.2329	35.828	1.51	61.94
7	no good match											
8	OK	2008-09-12	23:29:45	2008-09-15	05:19:06	311.9	5.7	2.4	225.403	-24.3759	2.77	13.56
9	OK	2008-11-12	18:10:56	2008-11-15	13:58:48	323.7	5.1	3.3	164.23	-44.266	2.04	15
10	OK	2009-02-06	11:39:50	2009-02-08	22:12:17	383.9	6	5.2	108.244	-62.4254	2.16	24.72
11	OK	2009-08-14	23:50:21	2009-08-17	00:33:50	300.2	2	0.5	98.1343	-0.102527	2.01	14.78
12	OK	2009-11-10	17:14:47	2009-11-12	02:47:28	304.6	0.7	-0.7	72.7918	23.4695	1.59	32.93
13	OK	2009-12-08	12:34:50	2009-12-11	00:27:47	315.9	0.8	-4.5	42.4134	45.7142	1.35	97.73
14	OK	2010-08-11	09:53:34	2010-08-13	00:44:03	395.1	22.2	5.3	28.2727	-15.954	2.67	13.45
15	OK	2017-06-08	20:11:45	2017-06-11	16:33:53	309.4	1.2	-8.6	246.407	-66.6461	1.72	63.98
16	no good match											
17	no good match											
18	OK	2018-10-19	07:50:52	2018-10-21	14:19:23	309.2	2.7	-5.2	170.384	-48.4465	1.6	21.76
19	no good match											
20	OK	2019-06-06	06:01:17	2019-06-07	21:07:11	325.3	6.6	-5.4	349.507	-62.4436	1.8	18.43
21	OK	2019-12-28	23:18:05	2019-12-31	21:47:05	309.3	1.5	3.4	169.611	31.566	1.31	64.23
22	OK	2020-05-13	05:02:23	2020-05-15	07:58:04	304	1.13	-4.2	185.314	-53.1052	1.51	24.25
23	OK	2020-05-16	20:15:47	2020-05-18	22:19:20	295.1	1.05	-6.1	115.559	-58.1145	1.6	51.19
24	OK	2020-06-05	15:53:25	2020-06-07	13:32:35	321.1	1.9	-3.3	213.795	-35.5714	2.49	12.19
25	OK	2020-06-19	21:40:45	2020-06-23	05:29:28	321.5	2.3	-3.8	25.1138	-53.8343	2.38	14.61
26	OK	2020-09-19	18:33:50	2020-09-21	21:53:25	312	1.2	4.8	264.988	20.334	1.48	166
27	OK	2020-10-14	00:56:09	2020-10-16	09:21:53	312.3	1.7	-4.2	303.273	-42.7406	1.44	17.88
28	OK	2021-08-22	20:36:05	2021-08-24	20:59:42	296.7	2	8	113.458	54.271	1.39	62.12
							PSP El					
1	OK	2020-01-27	22:55:37	2020-01-28	06:29:57	303.35	1.3	1.8524	70.2608	55.153	0.9653	13.8666
2	OK	2020-01-28	18:45:56	2020-01-29	03:44:29	481.8	2.7	-6.12905	58.1647	-59.6251	2.6508	23.7742
3	Far side	2021-08-09	12:42:11	2021-08-09	12:42:11	358.875	13.425	-63.7942	53.1081	-17.8024	1.939	141.075
4	No good match	2022-02-24	14:22:33	2022-02-24	14:22:33	508.2	20.2	-99.6912	36.1212	-20.2573	3.7119	71.5252

Table 6.2: The solar wind sources of the events shown in the table 6.1 are presented. The match between the model output and observed solar wind is shown in column 2. The solar wind start and end times estimated by the model are presented in columns 2 and 3. The outputs of the model, i.e., solar wind speed, distance from the current sheet, the magnetic field at the foot points, longitude and latitude of foot points, distance from coronal holes and expansion factors, are shown in the rest of the columns.

Table 6.2 shows the solar wind speed, distance from the current sheet, the magnetic field at the foot point, longitude, latitude of foot points, coronal hole distance and expansion factor.

It can be seen from Table 6.2 that the sources of almost all the events are coronal hole boundaries, as the distance from coronal holes is less than 2° or it is nearby 2° . Note, 2° is the resolution of our model calculations. Out of 23 events, 16 show relatively smaller expansion factor, i.e. close to 30 or less. This is also an additional support to the inference that the sources are coronal hole boundaries, as the expansion factors are higher inside the coronal holes. Except for a few, all the events are observed near the current sheet (see current sheet distance). This suggests that these observations are from helmet, quiet, or flat streamers.

Therefore, it can be seen that most of the events originated from the solar coronal hole boundaries and are observed near current sheets, i.e., streamer belts. The interesting point is that the sources of these events are independent of the observation point, i.e. PSP or WIND. The role of these source regions in the context of low helium abundance events is discussed in the next section.

6.4 Discussion

The low helium abundance events are important events as these events can provide critical information regarding the sources of solar wind. It is well known that coronal hole boundaries are also an important source region for the slow solar wind (Schwadron et al., 2005). The slow solar winds usually have a lesser and variable A_{He} than the fast wind (Bame et al., 1977). The analysis presented in the previous section represents the sources of the very low helium events that are associated with streamers. A detailed discussion regarding the association of the low A_{He} events with the streamers can also be found in Suess et al. (2009). On the other hand, Borrini et al. (1981) showed that low helium abundances are observed near the current sheets. Interestingly, our work also reveals that the low A_{He} events are detected near the heliospheric current sheet. Similar observations are also reported in Suess et al. (2009). Also, Suess et al. (2009) suggested

that three potential locations associated with streamers, can produce low helium abundance. These locations are coronal hole, streamer core just below the magnetic cusp and the streamer legs (See Figure 11 of [Suess et al., 2009](#)). These three sources can supply the low A_{He} plasma in the following manner. One, there is a probability that the plasma from the coronal holes adjacent to streamers can enter the streamer region via Kelvin-Helmholtz instability. Two, the streamer core region located just below the cusp can release plasma from a specific side leading to a depletion of A_{He} on that side of the HCS and three, the streamer legs can provide plasma to the streamers. The probable roles of these sources towards the low A_{He} events are discussed below.

In this section, to understand the contribution of the coronal hole plasma, we compare the Fe/O vs. A_{He} density distribution for the fast-solar wind events (Left panel of Figure 6.5) with that during the slow wind events (Right panel of Figure 6.5). In order to construct this plot, data from ACE satellite during 1998-2020 are used. The right panel of Figure 6.5 is pertinent for the low A_{He} events. Figure 6.5 indicates that the Fe/O ratio of the slow wind events are predominantly located at the higher values of Fe/O in the density distribution. The red patches in both the panels of Figure 6.5 are A_{He} and Fe/O values averaged for the entire duration of the low A_{He} events considered in the pre-sent work. Interestingly, these patches are outside the observed distribution of the fast wind but inside the distribution corresponding to slow wind. Further, these events significantly deviate from the distribution of fast wind, suggesting minimal contribution from coronal hole plasma and/or dominance of other processes. The slow wind events exhibit higher Fe/O value indicating substantial influence of the First Ionization Potential (FIP) effect. This also suggests that the plasma comes from the longer loops resulting into higher level of FIP processing. However, as suggested by [Laming et al. \(2019\)](#), FIP effect alone cannot explain the low helium abundances and therefore, in the subsequent sections, we explore other possibilities as well.

The second possibility is that the low A_{He} plasma comes from the cores of the streamers. This is unlikely as the cores of the streamers are expected to be in strict static equilibrium [Suess et al. \(2009\)](#). Interestingly, core outflow in the streamers

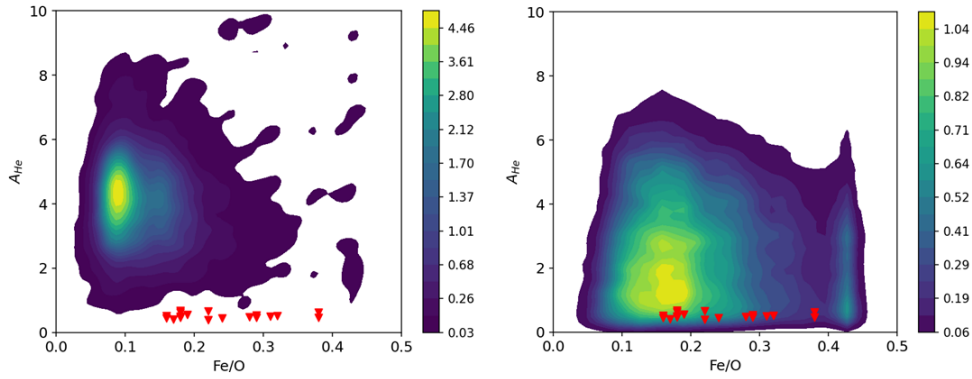


Figure 6.5: The Fe/O vs A_{He} density distributions are plotted. The ACE data is used from 1998 to 2020. The left and right panels are for the fast wind (>600 km/s) and slow solar wind (<450 km/s), respectively. The red coloured patches show our events' average A_{He} and Fe/O values. It can be observed that the events show higher Fe/O ratios as compared to most of the fast wind observations. In addition, the red patches are outside the observed distribution of the fast wind but inside the distribution corresponding to slow wind.

is not unlikely as this has been observed by [Noci and Gavryuseva \(2007\)](#). In addition, [Suess et al. \(2009\)](#) also showed a good correlation between O/H and He/H and argued that O/H is reduced in the core of the streamers compared to the legs. Therefore, they suggested that streamer cores could be potential sources of low A_{He} winds. However, in the same work, the authors rejected this hypothesis as all Current Sheets (CS) do not show the A_{He} depletion. Therefore, these low A_{He} events were proposed as transient events. Further, depleted helium abundance is mostly observed towards one edge of the CS. This consistent release of core plasma towards one edge only is surprising and hard to believe. Therefore, it appears that legs may potentially be the sources of these transient low A_{He} events.

[Suess et al. \(2009\)](#) suggested that plasma blobs are released through the legs of the streamers. The sharply pinched magnetic field confines the plasma, and this plasma can be released easily by small pressure pulses. These small perturbations cause an episodic release of low A_{He} plasma. These plasma blobs from each leg of streamer may not get mixed if there is a small difference between the blob velocity originating from the different legs. There are finite chances of different velocities

in legs because the sources or locations of origin in both legs differ. Therefore, these blobs can be observed at one side of the CS. These one-sided depletions are discussed in [Suess et al. \(2009\)](#). Although the depletion of A_{He} in one edge of CS is explained, the problem of these low plasma A_{He} blobs remains unresolved in the work by [Suess et al. \(2009\)](#). In our work, we show that the coronal hole boundaries are the sources of low A_{He} in most of the cases. The coronal boundaries are possible sources of the slow solar wind. Further, the coronal hole boundaries can be the potential legs of the helmet streamer containing the HCS. We propose a possible scenario in which the low A_{He} plasma is released from higher heights inside the coronal hole boundaries (see [Figure 6.6](#)).

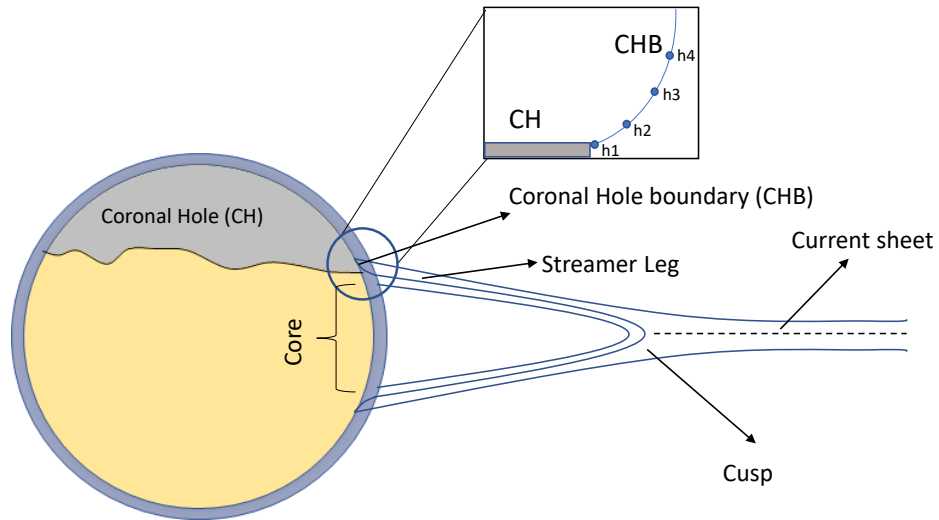


Figure 6.6: The schematic structure of the streamers. The zoomed view of the coronal boundary is shown. The reduction in helium abundance in the solar wind is attributed to the freezing of plasma composition at higher altitudes e.g., the solar wind coming from h4 will have lesser A_{He} as compared to wind from h1.

[Figure 6.6](#) shows three potential sources of solar wind similar to [Suess et al. \(2009\)](#). Following this [Figure](#), if we consider gravitational stratification around the boundary region of coronal hole in which the helium abundance is reduced at a higher height. It can be seen from [Figure 6.6](#) that the solar wind coming from h4 will have lesser A_{He} as compared to wind from h1 because of the enhanced helium abundance at h1 due to gravitational settling. As the solar wind comes from the upper heights and the long length of these loop originating from edges of

the coronal hole causes enhanced FIP effect, A_{He} is reduced significantly. In this scenario, the interplanetary modulation causing the low A_{He} events is ignored as these events are observed by PSP near the Sun. [McComas et al. \(2002\)](#) showed inverse relationship between the temperature calculated using O^{7+}/O^{6+} and the velocity of solar wind at the coronal hole boundaries. They also showed the transition of solar wind composition from chromospheric to coronal compositions at the boundary of the coronal hole. This provides additional support to the proposition made here that suggests that the freezing of the solar wind composition occurs at higher heights.

During the solar minimum, it is observed that there are longer durations with lower A_{He} values compared to the solar maximum. This intriguing feature can be attributed to two key factors. First, during the solar maximum, there is an expansion of lower-height plasma driven by the energy released through reconnections. This expansion leads to the mixing of different plasma populations, resulting in higher A_{He} values. Second, the reduction in the extent of coronal holes towards the equatorial latitudes causing the reduction in the solar wind from the coronal hole boundary. Furthermore, the dominant presence of solar wind originating from streamers, which typically exhibit lower A_{He} values, can also contribute to explain the SC variation in A_{He} .

Finally, the low A_{He} events can be considered as transient events ([Suess et al., 2009](#)). They require specific conditions to be met in order to be observed in the solar wind. The present investigation suggests that this aspect requires more detailed modelling of the coronal hole boundary regions and the altitudes of the solar wind from where it originates. This aspect can be taken up in future.

6.5 Conclusions

1. Very low helium abundance events ($<1\%$) are unique features of slow solar wind.
2. These events show slow velocity, low temperature and small V_a - V_p .
3. Analysis using the ADAPT-WSA model indicates that these events origi-

nate from the boundaries of coronal holes.

4. Coronal holes and the streamer core below the cusp are unlikely to be responsible for generating these events.
5. The streamer legs associated with the coronal hole boundaries contribute to these low helium abundance events. The fixing of A_{He} at higher altitudes within the streamer legs explains this phenomenon.

Chapter 7

Summary and Future works

7.1 Summary

The abundance of doubly ionized helium ions (alpha particles) to singly ionized hydrogen ions (protons), expressed as $A_{He} = 100 * n_{\alpha}/n_p$ (in percentage), varies significantly in different layers of the Sun. In this thesis, the variation in alpha-proton ratio in the solar wind (at solar cycle time scale), in the Interplanetary Coronal Mass Ejections (ICMEs) and Stream (or Co-rotating) Interaction regions (SIRs/CIRs) are explored. It is shown that the changes in coronal large-scale magnetic field configuration and/or solar wind sources, starting from solar cycle 23 affected the helium processing in the solar atmosphere that led to significant changes in A_{He} solar cycle 24. One of the major objectives of the thesis was to address the frequent enhancements in the helium abundance in interplanetary coronal mass ejection (ICME) structures. It is shown that although the background conditions, FIP effect, and coronal temperature contribute to A_{He} enhancements in ICMEs to certain degrees, the interplay between gravitational settling and chromospheric evaporation significantly determine the enhancements (more than 8%) observed in A_{He} abundance in ICMEs. The thesis also examines the role of angle between bulk velocity vector and local magnetic field (bulk velocity angle) and differential velocity of protons and alphas in modifying helium abundance within Stream (or Co-rotating) Interaction Regions. It was shown that bulk velocity angle distributions and differential velocity distribution in the in-

terplanetary medium play important roles in the helium enhancements, although these parameters did not change significantly in the time scale of solar cycles. Moreover, the thesis focuses on identifying the potential factors contributing to very low helium abundance events and brings out importance of the streamer legs associated with coronal hole boundaries and the fixing of helium abundance at higher altitudes within the streamer legs. Therefore, in summary, it can be said that this thesis work addresses the whole range of variations in the helium abundance in the solar wind in various time scales, structures and provide insights on possible physical mechanisms.

7.2 Future works

The thesis explores various aspects of the variations of helium abundance in the solar wind and the associated physical processes. Many of these processes occur closer to the Sun and some of these occur in the interplanetary medium. It is, therefore, difficult to understand these processes comprehensively based on measurements from a single spacecraft. Multi-spacecraft operations open up opportunities to sample various parts of the ICME, SIR/CIR and background solar wind structures paving the way for understanding the variation in helium abundance in these structures. This information can be tied together to build the bigger picture that link the solar processes to the point of measurement and this, in turn, can provide the end-to-end understanding of the physics of the solar wind. In addition, these observations need to be complemented by the model outputs (e.g. ADAPT-WSA) to dig deeper into the processes which cannot be understood based on observations only. If needed, suitable earth-based solar telescope observations also can be made use of to understand the solar processes which may be indirectly helpful to understand the physics of the solar wind. Therefore, although this theme is explored in this thesis primarily using in-situ variations in the helium abundance in the solar wind, other compositional proxies, measurements, model runs can be made use of to achieve the eventual goal of understanding the origin, acceleration and propagation of solar wind through the

interplanetary medium. This understanding, in turn, will help to evaluate how efficiently we understand the space weather in the vicinity of the earth, other planets and in the heliosphere.

A few immediate science problems that arose during the course of this thesis work and that can be taken up for further investigation are listed below:

1. The evolution of solar wind helium abundance in Interplanetary medium based on multi-spacecraft (i.e., PSP, Solar Orbiter, Wind, ACE, STEREO etc.) measurements. An associated question is - do these measurements throw light on how the background solar wind structures originate and evolve as they propagate through heliosphere.
2. An extension of the previous question is to address the spatial evolution of the transients that include ICMEs, SIRs/CIRs using measurements of helium abundance measurements from multi-spacecraft.
3. While we associate enhanced helium abundance with the ICMEs, there are ICMEs which do not show any enhancement in the helium abundance. This question has been touched upon in this thesis by invoking the interplay of timing of occurrence of solar flares and time constants associated with chromospheric evaporation, FIP and gravitational settling processes. This aspect needs more investigation in future so that we understand the interplay of these processes in greater detail. This understanding will also lead to better space weather forecasting framework based on measurements of helium abundance from the L1 point.
4. Although oxygen and hydrogen have similar FIP values, the present work shows that the ratios He/O and He/H do not show significant correlation. This suggests that there are processes other than FIP that may be operational. This aspect needs critical attention.
5. It is observed that carbon did not demonstrate any correlation with He/H regardless of the choice of the charge states, charge state ratio, or its ratio with oxygen. Interestingly, a depletion in the C/O ratio is often observed

during the onset of ICMEs. The underlying processes leading to these depletions need further attention.

6. The thesis highlights the significance of bulk velocity angle and velocities of alphas and protons in comprehending the changes in A_{He} within SIRs. Multi-vantage point observations can help in gaining the insights into the evolution of bulk velocity angles and velocities within SIRs. Such investigations can provide valuable information about the dynamics and processes occurring within these regions.
7. In chapter 5, the results are mainly dependent on the SPA and limitation of SPA is that it tends to wash out signatures at different length scales. In future, this aspect will be investigated.
8. We have used only the magnetic mirror assembly to explain the behaviour of alpha and protons in the SIRs. The collisional age can also alter the variation of the alpha and protons. The role of the differences between the collisional ages of protons and alphas in determining the helium abundances in SIRs will be investigated in future.
9. The presence of streamer structures associated with the boundaries of coronal holes has been found to contribute to low helium abundance events. Pseudo-streamers or unipolar streamers, which separate coronal holes of the same polarity without a current sheet in the outer corona, are very interesting structures that can be studied to evaluate their role in low A_{He} events.
10. One aspect that has not been touched upon in this thesis is the temperature anisotropy of the solar wind. Temperature anisotropy of helium and how it is different from hydrogen are important science problems that can be taken up in future. This exercise can be done for single spacecraft as well as for multiple spacecrafts to understand the variations of temperature anisotropy in heliosphere.
11. The wave-particle interaction can change the thermal properties of the solar

wind ions. Usually, the heavier ions have a higher temperature as compared to the protons. The increase or decrease in the energy of ions can lead to a change in the velocity of the heavy ions in the proton frame. These changes in velocity can cause the accumulation or dispersion of the particles. Then, in turn, can change the abundance of the elements e.g. Helium, Iron, Carbon etc. However, the effect of temperature anisotropy on helium abundance is not seen in the literature. This can only be taken up as a future study as this constitutes a very detailed investigation.

12. Not much is known about the directional anisotropy in helium abundances in the background solar wind as well as in the transients like ICMEs, SIRs/CIRs. This aspect can be addressed by the directional measurements of helium from the Aditya Solar wind EXperiment (ASPEX) on-board Aditya-L1 mission of India. This mission is coming up shortly and the measurements from this mission can be invaluable to address this and other science aspects.
13. Long term measurements of helium abundances can be used to train machine learning algorithms leading to development of efficient space weather forecasting tools. This is an area that can be tapped in future.

Bibliography

- Aellig, M.R., Lazarus, A.J., Steinberg, J.T., 2001. The solar wind helium abundance: Variation with wind speed and the solar cycle. *Geophys. Res. Lett.* 28, 2767–2770. doi:[10.1029/2000GL012771](https://doi.org/10.1029/2000GL012771).
- Alfvén, H., 1942. Existence of Electromagnetic-Hydrodynamic Waves. *Nature* 150, 405–406. doi:[10.1038/150405d0](https://doi.org/10.1038/150405d0).
- Alterman, B.L., Kasper, J.C., 2019. Helium Variation across Two Solar Cycles Reveals a Speed-dependent Phase Lag. *ApJ* 879, L6. doi:[10.3847/2041-8213/ab2391](https://doi.org/10.3847/2041-8213/ab2391), [arXiv:1906.12273](https://arxiv.org/abs/1906.12273).
- Alterman, B.L., Kasper, J.C., Leamon, R.J., McIntosh, S.W., 2021. Solar Wind Helium Abundance Heralds Solar Cycle Onset. *Sol. Phys.* 296, 67. doi:[10.1007/s11207-021-01801-9](https://doi.org/10.1007/s11207-021-01801-9), [arXiv:2006.04669](https://arxiv.org/abs/2006.04669).
- Antia, H.M., Basu, S., 2013. Contrasting the solar rotation rate of cycles 23 and 24, in: *Journal of Physics Conference Series*, p. 012018. doi:[10.1088/1742-6596/440/1/012018](https://doi.org/10.1088/1742-6596/440/1/012018).
- Aptekar, R.L., Frederiks, D.D., Golenetskii, S.V., Ilynskii, V.N., Mazets, E.P., Panov, V.N., Sokolova, Z.J., Terekhov, M.M., Sheshin, L.O., Cline, T.L., Stilwell, D.E., 1995. Konus-W Gamma-Ray Burst Experiment for the GGS Wind Spacecraft. *Space Sci. Rev.* 71, 265–272. doi:[10.1007/BF00751332](https://doi.org/10.1007/BF00751332).
- Arge, C.N., Henney, C.J., Koller, J., Compeau, C.R., Young, S., MacKenzie, D., Fay, A., Harvey, J.W., 2010. Air Force Data Assimilative Photospheric Flux Transport (ADAPT) Model, in: Maksimovic, M., Issautier, K., Meyer-Vernet,

- N., Moncuquet, M., Pantellini, F. (Eds.), Twelfth International Solar Wind Conference, pp. 343–346. doi:[10.1063/1.3395870](https://doi.org/10.1063/1.3395870).
- Asplund, M., Grevesse, N., Sauval, A.J., Scott, P., 2009. The Chemical Composition of the Sun. *ARA&A* 47, 481–522. doi:[10.1146/annurev.astro.46.060407.145222](https://doi.org/10.1146/annurev.astro.46.060407.145222), [arXiv:0909.0948](https://arxiv.org/abs/0909.0948).
- Bale, S.D., Goetz, K., Harvey, P.R., Turin, P., Bonnell, J.W., Dudok de Wit, T., Ergun, R.E., MacDowall, R.J., Pulupa, M., Andre, M., Bolton, M., Bougeret, J.L., Bowen, T.A., Burgess, D., Cattell, C.A., Chandran, B.D.G., Chaston, C.C., Chen, C.H.K., Choi, M.K., Connerney, J.E., Cranmer, S., Diaz-Aguado, M., Donakowski, W., Drake, J.F., Farrell, W.M., Fergeau, P., Fermin, J., Fischer, J., Fox, N., Glaser, D., Goldstein, M., Gordon, D., Hanson, E., Harris, S.E., Hayes, L.M., Hinze, J.J., Hollweg, J.V., Horbury, T.S., Howard, R.A., Hoxie, V., Jannet, G., Karlsson, M., Kasper, J.C., Kellogg, P.J., Kien, M., Klimchuk, J.A., Krasnoselskikh, V.V., Krucker, S., Lynch, J.J., Maksimovic, M., Malaspina, D.M., Marker, S., Martin, P., Martinez-Oliveros, J., McCauley, J., McComas, D.J., McDonald, T., Meyer-Vernet, N., Moncuquet, M., Monson, S.J., Mozer, F.S., Murphy, S.D., Odom, J., Oliverson, R., Olson, J., Parker, E.N., Pankow, D., Phan, T., Quataert, E., Quinn, T., Ruplin, S.W., Salem, C., Seitz, D., Sheppard, D.A., Siy, A., Stevens, K., Summers, D., Szabo, A., Timofeeva, M., Vaivads, A., Velli, M., Yehle, A., Werthimer, D., Wygant, J.R., 2016. The FIELDS Instrument Suite for Solar Probe Plus. Measuring the Coronal Plasma and Magnetic Field, Plasma Waves and Turbulence, and Radio Signatures of Solar Transients. *Space Sci. Rev.* 204, 49–82. doi:[10.1007/s11214-016-0244-5](https://doi.org/10.1007/s11214-016-0244-5).
- Bame, S.J., Asbridge, J.R., Feldman, W.C., Fenimore, E.E., Gosling, J.T., 1979. Solar wind heavy ions from flare-heated coronal plasma. *Sol. Phys.* 62, 179–201. doi:[10.1007/BF00150143](https://doi.org/10.1007/BF00150143).
- Bame, S.J., Asbridge, J.R., Feldman, W.C., Gosling, J.T., 1977. Evidence for a structure-free state at high solar wind speeds. *J. Geophys. Res.* 82, 1487. doi:[10.1029/JA082i010p01487](https://doi.org/10.1029/JA082i010p01487).

- Basu, S., Antia, H.M., 2004. Constraining Solar Abundances Using Helioseismology. *ApJ* 606, L85–L88. doi:[10.1086/421110](https://doi.org/10.1086/421110), [arXiv:astro-ph/0403485](https://arxiv.org/abs/astro-ph/0403485).
- Belcher, J.W., Davis, Leverett, J., 1971. Large-amplitude Alfvén waves in the interplanetary medium, 2. *J. Geophys. Res.* 76, 3534. doi:[10.1029/JA076i016p03534](https://doi.org/10.1029/JA076i016p03534).
- Berger, L., Wimmer-Schweingruber, R.F., Gloeckler, G., 2011. Systematic Measurements of Ion-Proton Differential Streaming in the Solar Wind. *Phys. Rev. Lett.* 106, 151103. doi:[10.1103/PhysRevLett.106.151103](https://doi.org/10.1103/PhysRevLett.106.151103).
- Bochsler, P., 2000. Abundances and charge states of particles in the solar wind. *Reviews of Geophysics* 38, 247–266. doi:[10.1029/1999RG000063](https://doi.org/10.1029/1999RG000063).
- Bochsler, P., 2007. Solar abundances of oxygen and neon derived from solar wind observations. *A&A* 471, 315–319. doi:[10.1051/0004-6361:20077772](https://doi.org/10.1051/0004-6361:20077772).
- Borrini, G., Gosling, J.T., Bame, S.J., Feldman, W.C., 1982. Helium abundance enhancements in the solar wind. *J. Geophys. Res.* 87, 7370–7378. doi:[10.1029/JA087iA09p07370](https://doi.org/10.1029/JA087iA09p07370).
- Borrini, G., Gosling, J.T., Bame, S.J., Feldman, W.C., Wilcox, J.M., 1981. Solar wind helium and hydrogen structure near the heliospheric current sheet: A signal of coronal streamers at 1 AU. *J. Geophys. Res.* 86, 4565–4573. doi:[10.1029/JA086iA06p04565](https://doi.org/10.1029/JA086iA06p04565).
- Bougeret, J.L., Kaiser, M.L., Kellogg, P.J., Manning, R., Goetz, K., Monson, S.J., Monge, N., Friel, L., Meetre, C.A., Perche, C., Sitruk, L., Hoang, S., 1995. Waves: The Radio and Plasma Wave Investigation on the Wind Spacecraft. *Space Sci. Rev.* 71, 231–263. doi:[10.1007/BF00751331](https://doi.org/10.1007/BF00751331).
- Burlaga, L.F., 1974. Interplanetary stream interfaces. *Journal of Geophysical Research (1896-1977)* 79, 3717–3725. doi:<https://doi.org/10.1029/JA079i025p03717>.
- Burlaga, L.F., F.-Viñas, A., 2004. Multiscale structure of the magnetic field and speed at 1 au during the declining phase of solar cycle 23 described by

- a generalized tsallis probability distribution function. *Journal of Geophysical Research: Space Physics* 109. doi:<https://doi.org/10.1029/2004JA010763>.
- Bürgi, A., 1992. Proton and alpha particle fluxes in the solar wind: Results of a three-fluid model. *Journal of Geophysical Research: Space Physics* 97, 3137–3150. doi:<https://doi.org/10.1029/91JA02833>.
- Cane, H.V., Richardson, I.G., 2003. Interplanetary coronal mass ejections in the near-Earth solar wind during 1996-2002. *Journal of Geophysical Research (Space Physics)* 108, 1156. doi:[10.1029/2002JA009817](https://doi.org/10.1029/2002JA009817).
- Chandrasekhar, S., 1943. Dynamical Friction. I. General Considerations: the Coefficient of Dynamical Friction. *ApJ* 97, 255. doi:[10.1086/144517](https://doi.org/10.1086/144517).
- Chen, P.F., 2011. Coronal Mass Ejections: Models and Their Observational Basis. *Living Reviews in Solar Physics* 8, 1. doi:[10.12942/lrsp-2011-1](https://doi.org/10.12942/lrsp-2011-1).
- Chi, Y., Shen, C., Luo, B., Wang, Y., Xu, M., 2018. Geoeffectiveness of Stream Interaction Regions From 1995 to 2016. *Space Weather* 16, 1960–1971. doi:[10.1029/2018SW001894](https://doi.org/10.1029/2018SW001894).
- Choudhuri, A.R., Chatterjee, P., Jiang, J., 2007. Predicting Solar Cycle 24 With a Solar Dynamo Model. *Phys. Rev. Lett.* 98, 131103. doi:[10.1103/PhysRevLett.98.131103](https://doi.org/10.1103/PhysRevLett.98.131103), [arXiv:astro-ph/0701527](https://arxiv.org/abs/astro-ph/0701527).
- Cranmer, S.R., 2009. Coronal Holes. *Living Reviews in Solar Physics* 6, 3. doi:[10.12942/lrsp-2009-3](https://doi.org/10.12942/lrsp-2009-3), [arXiv:0909.2847](https://arxiv.org/abs/0909.2847).
- Cranmer, S.R., 2014. Ensemble Simulations of Proton Heating in the Solar Wind via Turbulence and Ion Cyclotron Resonance. *ApJS* 213, 16. doi:[10.1088/0067-0049/213/1/16](https://doi.org/10.1088/0067-0049/213/1/16), [arXiv:1406.0678](https://arxiv.org/abs/1406.0678).
- Cranmer, S.R., Gibson, S.E., Riley, P., 2017. Origins of the Ambient Solar Wind: Implications for Space Weather. *Space Sci. Rev.* 212, 1345–1384. doi:[10.1007/s11214-017-0416-y](https://doi.org/10.1007/s11214-017-0416-y), [arXiv:1708.07169](https://arxiv.org/abs/1708.07169).

- Crooker, N.U., Antiochos, S.K., Zhao, X., Neugebauer, M., 2012. Global network of slow solar wind. *Journal of Geophysical Research (Space Physics)* 117, A04104. doi:[10.1029/2011JA017236](https://doi.org/10.1029/2011JA017236).
- Durovcová, T., Němeček, Z., Šafránková, J., 2019. Evolution of the α -proton Differential Motion across Stream Interaction Regions. *ApJ* 873, 24. doi:[10.3847/1538-4357/ab01c8](https://doi.org/10.3847/1538-4357/ab01c8).
- Dusenbery, P.B., Hollweg, J.V., 1981. Ion-cyclotron heating and acceleration of solar wind minor ions. *J. Geophys. Res.* 86, 153–164. doi:[10.1029/JA086iA01p00153](https://doi.org/10.1029/JA086iA01p00153).
- Elliott, H.A., Valek, P., McComas, D.J., Delamere, P.A., Bagenal, F., Gladstone, G.R., Olkin, C.B., Spencer, J., Stern, S.A., Young, L.A., Weaver, H.A., Ennico, K., Horizons Plasma, N., Particle Team, 2018. Determining the Alpha to Proton Density Ratio for the New Horizons Solar Wind Observations. *ApJ* 866, 85. doi:[10.3847/1538-4357/aadba6](https://doi.org/10.3847/1538-4357/aadba6).
- Feldman, U., 1998. FIP Effect in the Solar Upper Atmosphere: Spectroscopic Results. *Space Sci. Rev.* 85, 227–240. doi:[10.1023/A:1005146332450](https://doi.org/10.1023/A:1005146332450).
- Feldman, U., Schühle, U., Widing, K.G., Laming, J.M., 1998. Coronal Composition above the Solar Equator and the North Pole as Determined from Spectra Acquired by the SUMER Instrument on SOHO. *ApJ* 505, 999–1006. doi:[10.1086/306195](https://doi.org/10.1086/306195).
- Feldman, W.C., Asbridge, J.R., Bame, S.J., Gosling, J.T., 1978. Long-term variations of selected solar wind properties: Imp 6, 7, and 8 results. *J. Geophys. Res.* 83, 2177–2189. doi:[10.1029/JA083iA05p02177](https://doi.org/10.1029/JA083iA05p02177).
- Fenimore, E.E., 1980. Solar wind flows associated with hot heavy ions. *ApJ* 235, 245–257. doi:[10.1086/157628](https://doi.org/10.1086/157628).
- Fisk, L.A., 2003. Acceleration of the solar wind as a result of the reconnection of open magnetic flux with coronal loops. *Journal of Geophysical Research (Space Physics)* 108, 1157. doi:[10.1029/2002JA009284](https://doi.org/10.1029/2002JA009284).

- Fletcher, L., Dennis, B.R., Hudson, H.S., Krucker, S., Phillips, K., Veronig, A., Battaglia, M., Bone, L., Caspi, A., Chen, Q., Gallagher, P., Grigis, P.T., Ji, H., Liu, W., Milligan, R.O., Temmer, M., 2011. An Observational Overview of Solar Flares. *Space Sci. Rev.* 159, 19–106. doi:[10.1007/s11214-010-9701-8](https://doi.org/10.1007/s11214-010-9701-8), [arXiv:1109.5932](https://arxiv.org/abs/1109.5932).
- Forbes, T.G., Linker, J.A., Chen, J., Cid, C., Kóta, J., Lee, M.A., Mann, G., Mikić, Z., Potgieter, M.S., Schmidt, J.M., Siscoe, G.L., Vainio, R., Antiochos, S.K., Riley, P., 2006. CME Theory and Models. *Space Sci. Rev.* 123, 251–302. doi:[10.1007/s11214-006-9019-8](https://doi.org/10.1007/s11214-006-9019-8).
- Fu, H., Harrison, R.A., Davies, J.A., Xia, L., Zhu, X., Li, B., Huang, Z., Barnes, D., 2020. The High Helium Abundance and Charge States of the Interplanetary CME and Its Material Source on the Sun. *ApJ* 900, L18. doi:[10.3847/2041-8213/abb083](https://doi.org/10.3847/2041-8213/abb083), [arXiv:2008.08816](https://arxiv.org/abs/2008.08816).
- Fu, H., Madjarska, M.S., Li, B., Xia, L., Huang, Z., 2018. Helium abundance and speed difference between helium ions and protons in the solar wind from coronal holes, active regions, and quiet Sun. *MNRAS* 478, 1884–1892. doi:[10.1093/mnras/sty1211](https://doi.org/10.1093/mnras/sty1211), [arXiv:1805.02880](https://arxiv.org/abs/1805.02880).
- Fu, H., Madjarska, M.S., Xia, L., Li, B., Huang, Z., Wangguan, Z., 2017. Charge States and FIP Bias of the Solar Wind from Coronal Holes, Active Regions, and Quiet Sun. *ApJ* 836, 169. doi:[10.3847/1538-4357/aa5cba](https://doi.org/10.3847/1538-4357/aa5cba), [arXiv:1701.07610](https://arxiv.org/abs/1701.07610).
- Galvin, A.B., 1997. Minor ion composition in CME-related solar wind. Washington DC American Geophysical Union Geophysical Monograph Series 99, 253–260. doi:[10.1029/GM099p0253](https://doi.org/10.1029/GM099p0253).
- Gary, G.A., 2001. Plasma Beta above a Solar Active Region: Rethinking the Paradigm. *Sol. Phys.* 203, 71–86. doi:[10.1023/A:1012722021820](https://doi.org/10.1023/A:1012722021820).
- Gary, S.P., Yin, L., Winske, D., Reisenfeld, D.B., 2000. Electromagnetic alpha/proton instabilities in the solar wind. *Geophys. Res. Lett.* 27, 1355–1358. doi:[10.1029/2000GL000019](https://doi.org/10.1029/2000GL000019).

- Geiss, J., Gloeckler, G., von Steiger, R., 1995. Origin of the Solar Wind From Composition Data. *Space Sci. Rev.* 72, 49–60. doi:[10.1007/BF00768753](https://doi.org/10.1007/BF00768753).
- Geiss, J., Hirt, P., Leutwyler, H., 1970. On Acceleration and Motion of Ions in Corona and Solar Wind. *Sol. Phys.* 12, 458–483. doi:[10.1007/BF00148028](https://doi.org/10.1007/BF00148028).
- Gloeckler, G., Balsiger, H., Bürgi, A., Bochsler, P., Fisk, L.A., Galvin, A.B., Geiss, J., Gliem, F., Hamilton, D.C., Holzer, T.E., Hovestadt, D., Ipavich, F.M., Kirsch, E., Lundgren, R.A., Ogilvie, K.W., Sheldon, R.B., Wilken, B., 1995. The Solar Wind and Suprathermal Ion Composition Investigation on the Wind Spacecraft. *Space Sci. Rev.* 71, 79–124. doi:[10.1007/BF00751327](https://doi.org/10.1007/BF00751327).
- Gloeckler, G., Cain, J., Ipavich, F.M., Tums, E.O., Bedini, P., Fisk, L.A., Zurbuchen, T.H., Bochsler, P., Fischer, J., Wimmer-Schweingruber, R.F., Geiss, J., Kallenbach, R., 1998. Investigation of the composition of solar and interstellar matter using solar wind and pickup ion measurements with SWICS and SWIMS on the ACE spacecraft. *Space Sci. Rev.* 86, 497–539. doi:[10.1023/A:1005036131689](https://doi.org/10.1023/A:1005036131689).
- Gold, R.E., Krimigis, S.M., Hawkins, S. E., I., Haggerty, D.K., Lohr, D.A., Fiore, E., Armstrong, T.P., Holland, G., Lanzerotti, L.J., 1998. Electron, Proton, and Alpha Monitor on the Advanced Composition Explorer spacecraft. *Space Sci. Rev.* 86, 541–562. doi:[10.1023/A:1005088115759](https://doi.org/10.1023/A:1005088115759).
- Gopalswamy, N., Mäkelä, P., Akiyama, S., Xie, H., Yashiro, S., Reinard, A.A., 2013. The Solar Connection of Enhanced Heavy Ion Charge States in the Interplanetary Medium: Implications for the Flux-Rope Structure of CMEs. *Sol. Phys.* 284, 17–46. doi:[10.1007/s11207-012-0215-2](https://doi.org/10.1007/s11207-012-0215-2), [arXiv:1212.0900](https://arxiv.org/abs/1212.0900).
- Gosling, J.T., Asbridge, J.R., Bame, S.J., Feldman, W.C., 1978. Solar wind stream interfaces. *J. Geophys. Res.* 83, 1401–1412. doi:[10.1029/JA083iA04p01401](https://doi.org/10.1029/JA083iA04p01401).
- Gosling, J.T., Asbridge, J.R., Bame, S.J., Feldman, W.C., Zwickl, R.D., 1980. Observations of large fluxes of He⁺ in the solar wind following an interplanetary shock. *J. Geophys. Res.* 85, 3431–3434. doi:[10.1029/JA085iA07p03431](https://doi.org/10.1029/JA085iA07p03431).

- Grevesse, N., Sauval, A.J., 1998. Standard Solar Composition. *Space Sci. Rev.* 85, 161–174. doi:[10.1023/A:1005161325181](https://doi.org/10.1023/A:1005161325181).
- Gruesbeck, J.R., Lepri, S.T., Zurbuchen, T.H., 2012. Two-plasma Model for Low Charge State Interplanetary Coronal Mass Ejection Observations. *ApJ* 760, 141. doi:[10.1088/0004-637X/760/2/141](https://doi.org/10.1088/0004-637X/760/2/141).
- Gruesbeck, J.R., Lepri, S.T., Zurbuchen, T.H., Antiochos, S.K., 2011. Constraints on Coronal Mass Ejection Evolution from in Situ Observations of Ionic Charge States. *ApJ* 730, 103. doi:[10.1088/0004-637X/730/2/103](https://doi.org/10.1088/0004-637X/730/2/103).
- Hahn, M., 2020. Tracing the origins of the solar wind with helium. *Nature Astronomy* 4, 1128–1129. doi:[10.1038/s41550-020-1166-4](https://doi.org/10.1038/s41550-020-1166-4).
- Hansteen, V.H., Leer, E., Holzer, T.E., 1994. Coupling of the Coronal Helium Abundance to the Solar Wind. *ApJ* 428, 843. doi:[10.1086/174293](https://doi.org/10.1086/174293).
- Hansteen, V.H., Leer, E., Holzer, T.E., 1997. The Role of Helium in the Outer Solar Atmosphere. *ApJ* 482, 498–509. doi:[10.1086/304111](https://doi.org/10.1086/304111).
- Hathaway, D.H., 2015. The Solar Cycle. *Living Reviews in Solar Physics* 12, 4. doi:[10.1007/lrsp-2015-4](https://doi.org/10.1007/lrsp-2015-4), [arXiv:1502.07020](https://arxiv.org/abs/1502.07020).
- Henke, T., Woch, J., Mall, U., Livi, S., Wilken, B., Schwenn, R., Gloeckler, G., von Steiger, R., Forsyth, R.J., Balogh, A., 1998. Differences in the O^{7+}/O^{6+} ratio of magnetic cloud and non-cloud coronal mass ejections. *Geophys. Res. Lett.* 25, 3465–3468. doi:[10.1029/98GL02632](https://doi.org/10.1029/98GL02632).
- Henke, T., Woch, J., Schwenn, R., Mall, U., Gloeckler, G., von Steiger, R., Forsyth, R.J., Balogh, A., 2001. Ionization state and magnetic topology of coronal mass ejections. *J. Geophys. Res.* 106, 10597–10614. doi:[10.1029/2000JA900176](https://doi.org/10.1029/2000JA900176).
- Hirshberg, J., 1973. Helium Abundance of the Sun. *Reviews of Geophysics and Space Physics* 11, 115. doi:[10.1029/RG011i001p00115](https://doi.org/10.1029/RG011i001p00115).

- Hirshberg, J., Alksne, A., Colburn, D.S., Bame, S.J., Hundhausen, A.J., 1970. Observation of a solar flare induced interplanetary shock and helium-enriched driver gas. *J. Geophys. Res.* 75, 1. doi:[10.1029/JA075i001p00001](https://doi.org/10.1029/JA075i001p00001).
- Hirshberg, J., Bame, S.J., Robbins, D.E., 1972. Solar flares and solar wind helium enrichments: July 1965 July 1967. *Sol. Phys.* 23, 467–486. doi:[10.1007/BF00148109](https://doi.org/10.1007/BF00148109).
- Hoeksema, J.T., Wilcox, J.M., Scherrer, P.H., 1983. The structure of the heliospheric current sheet: 1978-1982. *J. Geophys. Res.* 88, 9910–9918. doi:[10.1029/JA088iA12p09910](https://doi.org/10.1029/JA088iA12p09910).
- Hu, Y.Q., Habbal, S.R., 1999. Resonant acceleration and heating of solar wind ions by dispersive ion cyclotron waves. *J. Geophys. Res.* 104, 17045–17056. doi:[10.1029/1999JA900193](https://doi.org/10.1029/1999JA900193).
- Huang, J., Kasper, J.C., Larson, D.E., McManus, M.D., Whittlesey, P., Livi, R., Rahmati, A., Romeo, O., Klein, K.G., Sun, W., van der Holst, B., Huang, Z., Jian, L.K., Szabo, A., Verniero, J.L., Chen, C.H.K., Lavraud, B., Liu, M., Badman, S.T., Niembro, T., Paulson, K., Stevens, M., Case, A.W., Pulupa, M., Bale, S.D., Halekas, J.S., 2023. Parker Solar Probe Observations of High Plasma β Solar Wind from the Streamer Belt. *ApJS* 265, 47. doi:[10.3847/1538-4365/acbcd2](https://doi.org/10.3847/1538-4365/acbcd2), [arXiv:2302.07230](https://arxiv.org/abs/2302.07230).
- Hudson, H., Fletcher, L., McTiernan, J., 2014. Cycle 23 Variation in Solar Flare Productivity. *Sol. Phys.* 289, 1341–1347. doi:[10.1007/s11207-013-0384-7](https://doi.org/10.1007/s11207-013-0384-7), [arXiv:1401.6474](https://arxiv.org/abs/1401.6474).
- Hundhausen, A.J., Gilbert, H.E., Bame, S.J., 1968. Ionization state of the interplanetary plasma. *J. Geophys. Res.* 73, 5485–5493. doi:[10.1029/JA073i017p05485](https://doi.org/10.1029/JA073i017p05485).
- Ipavich, F.M., Lundgren, R.A., Lambird, B.A., Gloeckler, G., 1978. Measurements of pulse-height defect in AuSi detectors for H, He, C, N, O, Ne, Ar, Kr from ≈ 2 to ≈ 400 keV/nucleon. *Nuclear Instruments and Methods* 154, 291–294. doi:[10.1016/0029-554X\(78\)90412-3](https://doi.org/10.1016/0029-554X(78)90412-3).

- Janardhan, P., Bisoi, S.K., Ananthakrishnan, S., Tokumaru, M., Fujiki, K., 2011. The prelude to the deep minimum between solar cycles 23 and 24: Interplanetary scintillation signatures in the inner heliosphere. *Geophys. Res. Lett.* 38, L20108. doi:[10.1029/2011GL049227](https://doi.org/10.1029/2011GL049227), [arXiv:1110.0437](https://arxiv.org/abs/1110.0437).
- Janardhan, P., Fujiki, K., Ingale, M., Bisoi, S.K., Rout, D., 2018. Solar cycle 24: An unusual polar field reversal. *A&A* 618, A148. doi:[10.1051/0004-6361/201832981](https://doi.org/10.1051/0004-6361/201832981), [arXiv:1805.06654](https://arxiv.org/abs/1805.06654).
- Kasper, J.C., 2002. Solar wind plasma: kinetic properties and micro-instabilities. Ph.D. thesis. Massachusetts Institute of Technology.
- Kasper, J.C., Abiad, R., Austin, G., Balat-Pichelin, M., Bale, S.D., Belcher, J.W., Berg, P., Bergner, H., Berthomier, M., Bookbinder, J., Brodu, E., Caldwell, D., Case, A.W., Chandran, B.D.G., Cheimets, P., Cirtain, J.W., Cranmer, S.R., Curtis, D.W., Daigneau, P., Dalton, G., Dasgupta, B., DeTomaso, D., Diaz-Aguado, M., Djordjevic, B., Donaskowski, B., Effinger, M., Florinski, V., Fox, N., Freeman, M., Gallagher, D., Gary, S.P., Gauron, T., Gates, R., Goldstein, M., Golub, L., Gordon, D.A., Gurnee, R., Guth, G., Halekas, J., Hatch, K., Heerikuisen, J., Ho, G., Hu, Q., Johnson, G., Jordan, S.P., Korreck, K.E., Larson, D., Lazarus, A.J., Li, G., Livi, R., Ludlam, M., Maksimovic, M., McFadden, J.P., Marchant, W., Maruca, B.A., McComas, D.J., Messina, L., Mercer, T., Park, S., Peddie, A.M., Pogorelov, N., Reinhart, M.J., Richardson, J.D., Robinson, M., Rosen, I., Skoug, R.M., Slagle, A., Steinberg, J.T., Stevens, M.L., Szabo, A., Taylor, E.R., Tiu, C., Turin, P., Velli, M., Webb, G., Whittlesey, P., Wright, K., Wu, S.T., Zank, G., 2016. Solar Wind Electrons Alphas and Protons (SWEAP) Investigation: Design of the Solar Wind and Coronal Plasma Instrument Suite for Solar Probe Plus. *Space Sci. Rev.* 204, 131–186. doi:[10.1007/s11214-015-0206-3](https://doi.org/10.1007/s11214-015-0206-3).
- Kasper, J.C., Bale, S.D., Belcher, J.W., Berthomier, M., Case, A.W., Chandran, B.D.G., Curtis, D.W., Gallagher, D., Gary, S.P., Golub, L., Halekas, J.S., Ho, G.C., Horbury, T.S., Hu, Q., Huang, J., Klein, K.G., Korreck, K.E., Larson, D.E., Livi, R., Maruca, B., Lavraud, B., Louarn, P., Maksimovic,

- M., Martinovic, M., McGinnis, D., Pogorelov, N.V., Richardson, J.D., Skoug, R.M., Steinberg, J.T., Stevens, M.L., Szabo, A., Velli, M., Whittlesey, P.L., Wright, K.H., Zank, G.P., MacDowall, R.J., McComas, D.J., McNutt, R.L., Pulupa, M., Raouafi, N.E., Schwadron, N.A., 2019. Alfvénic velocity spikes and rotational flows in the near-Sun solar wind. *Nature* 576, 228–231. doi:[10.1038/s41586-019-1813-z](https://doi.org/10.1038/s41586-019-1813-z).
- Kasper, J.C., Lazarus, A.J., Gary, S.P., 2008. Hot Solar-Wind Helium: Direct Evidence for Local Heating by Alfvén-Cyclotron Dissipation. *Phys. Rev. Lett.* 101, 261103. doi:[10.1103/PhysRevLett.101.261103](https://doi.org/10.1103/PhysRevLett.101.261103).
- Kasper, J.C., Lazarus, A.J., Steinberg, J.T., Ogilvie, K.W., Szabo, A., 2006. Physics-based tests to identify the accuracy of solar wind ion measurements: A case study with the Wind Faraday Cups. *Journal of Geophysical Research (Space Physics)* 111, A03105. doi:[10.1029/2005JA011442](https://doi.org/10.1029/2005JA011442).
- Kasper, J.C., Maruca, B.A., Stevens, M.L., Zaslavsky, A., 2013. Sensitive Test for Ion-Cyclotron Resonant Heating in the Solar Wind. *Phys. Rev. Lett.* 110, 091102. doi:[10.1103/PhysRevLett.110.091102](https://doi.org/10.1103/PhysRevLett.110.091102).
- Kasper, J.C., Stevens, M.L., Lazarus, A.J., Steinberg, J.T., Ogilvie, K.W., 2007. Solar Wind Helium Abundance as a Function of Speed and Heliographic Latitude: Variation through a Solar Cycle. *ApJ* 660, 901–910. doi:[10.1086/510842](https://doi.org/10.1086/510842).
- Kasper, J.C., Stevens, M.L., Maruca, B.A., Zaslavsky, A., 2012. Signatures of Local and Coronal Ion Heating Embedded in Solar Wind Observations, in: AGU Fall Meeting Abstracts, pp. SH32A–06.
- Kilpua, E., Koskinen, H.E.J., Pulkkinen, T.I., 2017. Coronal mass ejections and their sheath regions in interplanetary space. *Living Reviews in Solar Physics* 14, 5. doi:[10.1007/s41116-017-0009-6](https://doi.org/10.1007/s41116-017-0009-6).
- King, J.H., Papitashvili, N.E., 2005. Solar wind spatial scales in and comparisons of hourly Wind and ACE plasma and magnetic field data. *Journal of Geophysical Research (Space Physics)* 110, A02104. doi:[10.1029/2004JA010649](https://doi.org/10.1029/2004JA010649).

- Laming, J.M., 2009. Non-Wkb Models of the First Ionization Potential Effect: Implications for Solar Coronal Heating and the Coronal Helium and Neon Abundances. *ApJ* 695, 954–969. doi:[10.1088/0004-637X/695/2/954](https://doi.org/10.1088/0004-637X/695/2/954), [arXiv:0901.3350](https://arxiv.org/abs/0901.3350).
- Laming, J.M., 2012. Non-WKB Models of the First Ionization Potential Effect: The Role of Slow Mode Waves. *ApJ* 744, 115. doi:[10.1088/0004-637X/744/2/115](https://doi.org/10.1088/0004-637X/744/2/115), [arXiv:1110.4357](https://arxiv.org/abs/1110.4357).
- Laming, J.M., 2015. The FIP and Inverse FIP Effects in Solar and Stellar Coronae. *Living Reviews in Solar Physics* 12, 2. doi:[10.1007/lrsp-2015-2](https://doi.org/10.1007/lrsp-2015-2), [arXiv:1504.08325](https://arxiv.org/abs/1504.08325).
- Laming, J.M., 2017. The First Ionization Potential Effect from the Ponderomotive Force: On the Polarization and Coronal Origin of Alfvén Waves. *ApJ* 844, 153. doi:[10.3847/1538-4357/aa7cf1](https://doi.org/10.3847/1538-4357/aa7cf1), [arXiv:1707.05378](https://arxiv.org/abs/1707.05378).
- Laming, J.M., Feldman, U., 2001. The Solar Helium Abundance in Polar Coronal Holes as Measured by SOHO/SUMER, in: *American Astronomical Society Meeting Abstracts*, p. 88.06.
- Laming, J.M., Feldman, U., 2003. The Variability of the Solar Coronal Helium Abundance: Polar Coronal Holes Compared to the Quiet Sun. *ApJ* 591, 1257–1266. doi:[10.1086/375395](https://doi.org/10.1086/375395).
- Laming, J.M., Vourlidas, A., Korendyke, C., Chua, D., Cranmer, S.R., Ko, Y.K., Kuroda, N., Provornikova, E., Raymond, J.C., Raouafi, N.E., Strachan, L., Tun-Beltran, S., Weberg, M., Wood, B.E., 2019. Element Abundances: A New Diagnostic for the Solar Wind. *ApJ* 879, 124. doi:[10.3847/1538-4357/ab23f1](https://doi.org/10.3847/1538-4357/ab23f1), [arXiv:1905.09319](https://arxiv.org/abs/1905.09319).
- Landi, E., Gruesbeck, J.R., Lepri, S.T., Zurbuchen, T.H., Fisk, L.A., 2012. Charge State Evolution in the Solar Wind. II. Plasma Charge State Composition in the Inner Corona and Accelerating Fast Solar Wind. *ApJ* 761, 48. doi:[10.1088/0004-637X/761/1/48](https://doi.org/10.1088/0004-637X/761/1/48).

- Lang, K.R., 2000. The Sun from space. volume 1. Springer.
- Lepping, R.P., Acuña, M.H., Burlaga, L.F., Farrell, W.M., Slavin, J.A., Schatten, K.H., Mariani, F., Ness, N.F., Neubauer, F.M., Whang, Y.C., Byrnes, J.B., Kennon, R.S., Panetta, P.V., Scheifele, J., Worley, E.M., 1995. The Wind Magnetic Field Investigation. *Space Sci. Rev.* 71, 207–229. doi:[10.1007/BF00751330](https://doi.org/10.1007/BF00751330).
- Lepri, S.T., Zurbuchen, T.H., 2004. Iron charge state distributions as an indicator of hot ICMEs: Possible sources and temporal and spatial variations during solar maximum. *Journal of Geophysical Research (Space Physics)* 109, A01112. doi:[10.1029/2003JA009954](https://doi.org/10.1029/2003JA009954).
- Levine, R.H., Alschuler, M.D., Harvey, J.W., 1977. Solar sources of the interplanetary magnetic field and solar wind. *J. Geophys. Res.* 82, 1061. doi:[10.1029/JA082i007p01061](https://doi.org/10.1029/JA082i007p01061).
- Lin, R.P., Anderson, K.A., Ashford, S., Carlson, C., Curtis, D., Ergun, R., Larson, D., McFadden, J., McCarthy, M., Parks, G.K., Rème, H., Bosqued, J.M., Coutelier, J., Cotin, F., D’Uston, C., Wenzel, K.P., Sanderson, T.R., Henrion, J., Ronnet, J.C., Paschmann, G., 1995. A Three-Dimensional Plasma and Energetic Particle Investigation for the Wind Spacecraft. *Space Sci. Rev.* 71, 125–153. doi:[10.1007/BF00751328](https://doi.org/10.1007/BF00751328).
- Lundin, R., Guglielmi, A., 2006. Ponderomotive Forces in Cosmos. *Space Sci. Rev.* 127, 1–116. doi:[10.1007/s11214-006-8314-8](https://doi.org/10.1007/s11214-006-8314-8).
- Manchester, W., Kilpua, E.K.J., Liu, Y.D., Lugaz, N., Riley, P., Török, T., Vršnak, B., 2017. The Physical Processes of CME/ICME Evolution. *Space Science Reviews* 212, 1159–1219. doi:[10.1007/s11214-017-0394-0](https://doi.org/10.1007/s11214-017-0394-0).
- Marsch, E., Rosenbauer, H., Schwenn, R., Muehlhaeuser, K.H., Neubauer, F.M., 1982. Solar wind helium ions: observations of the Helios solar probes between 0.3 and 1 AU. *J. Geophys. Res.* 87, 35–51. doi:[10.1029/JA087iA01p00035](https://doi.org/10.1029/JA087iA01p00035).

- Mason, G.M., Gold, R.E., Krimigis, S.M., Mazur, J.E., Andrews, G.B., Daley, K.A., Dwyer, J.R., Heuerman, K.F., James, T.L., Kennedy, M.J., Lefevre, T., Malcolm, H., Tossman, B., Walpole, P.H., 1998. The Ultra-Low-Energy Isotope Spectrometer (ULEIS) for the ACE spacecraft. *Space Sci. Rev.* 86, 409–448. doi:[10.1023/A:1005079930780](https://doi.org/10.1023/A:1005079930780).
- Mauas, P.J.D., Andretta, V., Falchi, A., Falciani, R., Teriaca, L., Cauzzi, G., 2005. Helium Line Formation and Abundance in a Solar Active Region. *ApJ* 619, 604–612. doi:[10.1086/426428](https://doi.org/10.1086/426428), [arXiv:astro-ph/0412058](https://arxiv.org/abs/astro-ph/0412058).
- McComas, D.J., Alexander, N., Angold, N., Bale, S., Beebe, C., Birdwell, B., Boyle, M., Burgum, J.M., Burnham, J.A., Christian, E.R., Cook, W.R., Cooper, S.A., Cummings, A.C., Davis, A.J., Desai, M.I., Dickinson, J., Dirks, G., Do, D.H., Fox, N., Giacalone, J., Gold, R.E., Gurnee, R.S., Hayes, J.R., Hill, M.E., Kasper, J.C., Kecman, B., Klemic, J., Krimigis, S.M., Labrador, A.W., Layman, R.S., Leske, R.A., Livi, S., Matthaeus, W.H., McNutt, R.L., Mewaldt, R.A., Mitchell, D.G., Nelson, K.S., Parker, C., Rankin, J.S., Roelof, E.C., Schwadron, N.A., Seifert, H., Shuman, S., Stokes, M.R., Stone, E.C., Vandegriff, J.D., Velli, M., von Rosenvinge, T.T., Weidner, S.E., Wiedenbeck, M.E., Wilson, P., 2016. Integrated Science Investigation of the Sun (ISIS): Design of the Energetic Particle Investigation. *Space Sci. Rev.* 204, 187–256. doi:[10.1007/s11214-014-0059-1](https://doi.org/10.1007/s11214-014-0059-1).
- McComas, D.J., Bame, S.J., Barker, P., Feldman, W.C., Phillips, J.L., Riley, P., Griffee, J.W., 1998. Solar Wind Electron Proton Alpha Monitor (SWEPAM) for the Advanced Composition Explorer. *Space Sci. Rev.* 86, 563–612. doi:[10.1023/A:1005040232597](https://doi.org/10.1023/A:1005040232597).
- McComas, D.J., Elliott, H.A., Schwadron, N.A., Gosling, J.T., Skoug, R.M., Goldstein, B.E., 2003. The three-dimensional solar wind around solar maximum. *Geophys. Res. Lett.* 30, 1517. doi:[10.1029/2003GL017136](https://doi.org/10.1029/2003GL017136).
- McComas, D.J., Elliott, H.A., von Steiger, R., 2002. Solar wind from high-latitude coronal holes at solar maximum. *Geophys. Res. Lett.* 29, 1314. doi:[10.1029/2001GL013940](https://doi.org/10.1029/2001GL013940).

- Mishra, W., Srivastava, N., Wang, Y., Mirtoshev, Z., Zhang, J., Liu, R., 2019. Mass loss via solar wind and coronal mass ejections during solar cycles 23 and 24. *Monthly Notices of the Royal Astronomical Society* 486, 4671–4685. doi:[10.1093/mnras/stz1001](https://doi.org/10.1093/mnras/stz1001), [arXiv:1904.09898](https://arxiv.org/abs/1904.09898).
- Möbius, E., Kistler, L.M., Popecki, M.A., Crocker, K.N., Granoff, M., Turco, S., Anderson, A., Demain, P., Distelbrink, J., Dors, I., Dunphy, P., Ellis, S., Gaidos, J., Googins, J., Hayes, R., Humphrey, G., Kästle, H., Lavoisier, J., Lund, E.J., Miller, R., Sartori, E., Shappirio, M., Taylor, S., Vachon, P., Vosbury, M., Ye, V., Hovestadt, D., Klecker, B., Arbinger, H., Künne, E., Pfeiffermann, E., Seidenschwang, E., Gliem, F., Reiche, K.U., Stöckner, K., Wiewesiek, W., Harasim, A., Schimpfle, J., Battell, S., Cravens, J., Murphy, G., 1998. The Solar Energetic Particle Ionic Charge Analyzer (SEPICA) and the Data Processing Unit (S3DPU) for SWICS, SWIMS and SEPICA. *Space Sci. Rev.* 86, 449–495. doi:[10.1023/A:1005084014850](https://doi.org/10.1023/A:1005084014850).
- Moses, J.D., Antonucci, E., Newmark, J., Auchère, F., Fineschi, S., Romoli, M., Telloni, D., Massone, G., Zangrilli, L., Focardi, M., Landini, F., Pancrazzi, M., Rossi, G., Malvezzi, A.M., Wang, D., Leclec’h, J.C., Moalic, J.P., Rouesnel, F., Abbo, L., Canou, A., Barbey, N., Guennou, C., Laming, J.M., Lemen, J., Wuelser, J.P., Kohl, J.L., Gardner, L.D., 2020. Global helium abundance measurements in the solar corona. *Nature Astronomy* 4, 1134–1139. doi:[10.1038/s41550-020-1156-6](https://doi.org/10.1038/s41550-020-1156-6).
- Mostafavi, P., Allen, R.C., McManus, M.D., Ho, G.C., Raouafi, N.E., Larson, D.E., Kasper, J.C., Bale, S.D., 2022. Alpha-Proton Differential Flow of the Young Solar Wind: Parker Solar Probe Observations. *ApJ* 926, L38. doi:[10.3847/2041-8213/ac51e1](https://doi.org/10.3847/2041-8213/ac51e1), [arXiv:2202.03551](https://arxiv.org/abs/2202.03551).
- Ness, N.F., 1970. Magnetometers for Space Research. *Space Sci. Rev.* 11, 459–554. doi:[10.1007/BF00183028](https://doi.org/10.1007/BF00183028).
- Neugebauer, M., 1981. Observations of Solar-Wind Helium. *Fund. Cosmic Phys.* 7, 131–199.

- Neugebauer, M., Goldstein, B.E., Smith, E.J., Feldman, W.C., 1996. Ulysses observations of differential alpha-proton streaming in the solar wind. *J. Geophys. Res.* 101, 17047–17056. doi:[10.1029/96JA01406](https://doi.org/10.1029/96JA01406).
- Neugebauer, M., Goldstein, R., 1997. Particle and field signatures of coronal mass ejections in the solar wind. Washington DC American Geophysical Union Geophysical Monograph Series 99, 245–251. doi:[10.1029/GM099p0245](https://doi.org/10.1029/GM099p0245).
- Neugebauer, M., Reisenfeld, D., Richardson, I.G., 2016. Comparison of algorithms for determination of solar wind regimes. *Journal of Geophysical Research (Space Physics)* 121, 8215–8227. doi:[10.1002/2016JA023142](https://doi.org/10.1002/2016JA023142).
- Neugebauer, M.M., Feldman, W.C., 1979. Relation between superheating and superacceleration of helium in the solar wind. *Sol. Phys.* 63, 201–205. doi:[10.1007/BF00155710](https://doi.org/10.1007/BF00155710).
- Noci, G., Gavryuseva, E., 2007. Plasma Outflows in Coronal Streamers. *ApJ* 658, L63–L66. doi:[10.1086/513506](https://doi.org/10.1086/513506).
- Němeček, Z., Ďurovcová, T., Šafránková, J., Němec, F., Matteini, L., Stansby, D., Janitzek, N., Berger, L., Wimmer-Schweingruber, R.F., 2020. What is the Solar Wind Frame of Reference? *ApJ* 889, 163. doi:[10.3847/1538-4357/ab65f7](https://doi.org/10.3847/1538-4357/ab65f7).
- Ogilvie, K.W., Chornay, D.J., Fritzenreiter, R.J., Hunsaker, F., Keller, J., Lobell, J., Miller, G., Scudder, J.D., Sittler, E. C., J., Torbert, R.B., Bodet, D., Needell, G., Lazarus, A.J., Steinberg, J.T., Tappan, J.H., Mavretic, A., Gergin, E., 1995. SWE, A Comprehensive Plasma Instrument for the Wind Spacecraft. *Space Sci. Rev.* 71, 55–77. doi:[10.1007/BF00751326](https://doi.org/10.1007/BF00751326).
- Ogilvie, K.W., Hirshberg, J., 1974. The solar cycle variation of the solar wind helium abundance. *J. Geophys. Res.* 79, 4595. doi:[10.1029/JA079i031p04595](https://doi.org/10.1029/JA079i031p04595).
- Owens, A., Baker, R., Cline, T.L., Gehrels, N., Jermakian, J., Nolan, T., Ramaty, R., Seifert, H., Shephard, D.A., Smith, G., Stilwell, D.E., Teegarden, B.J., Cork, C.P., Landis, D.A., Luke, P.N., Madden, N.W., Malone, D., Pehl, R.H., Yaver, H., Hurley, K., Mathias, S., Post, A. H., J., 1995. A High-Resolution GE

- Spectrometer for Gamma-Ray Burst Astronomy. *Space Sci. Rev.* 71, 273–296. doi:[10.1007/BF00751333](https://doi.org/10.1007/BF00751333).
- Owens, M.J., Crooker, N.U., Lockwood, M., 2014. Solar cycle evolution of dipolar and pseudostreamer belts and their relation to the slow solar wind. *Journal of Geophysical Research (Space Physics)* 119, 36–46. doi:[10.1002/2013JA019412](https://doi.org/10.1002/2013JA019412).
- Parker, E.N., 1958. Dynamics of the Interplanetary Gas and Magnetic Fields. *ApJ* 128, 664. doi:[10.1086/146579](https://doi.org/10.1086/146579).
- Parker, E.N., 1963. Interplanetary dynamical processes. Interscience Publishers.
- Parker, E.N., 1965. Dynamical Theory of the Solar Wind. *Space Sci. Rev.* 4, 666–708. doi:[10.1007/BF00216273](https://doi.org/10.1007/BF00216273).
- Patchett, B.E., Norman, K., Gabriel, A.H., Culhane, J.L., 1981. The Coronal Helium Abundance Experiment on SPACELAB-2. *Space Sci. Rev.* 29, 431–437. doi:[10.1007/BF00239488](https://doi.org/10.1007/BF00239488).
- Pottasch, S.R., 1963. The Lower Solar Corona: Interpretation of the Ultraviolet Spectrum. *ApJ* 137, 945. doi:[10.1086/147569](https://doi.org/10.1086/147569).
- Priest, E.R., Forbes, T.G., 2002. The magnetic nature of solar flares. *A&A Rev.* 10, 313–377. doi:[10.1007/s001590100013](https://doi.org/10.1007/s001590100013).
- Rakowski, C.E., Laming, J.M., 2012. On the Origin of the Slow Speed Solar Wind: Helium Abundance Variations. *ApJ* 754, 65. doi:[10.1088/0004-637X/754/1/65](https://doi.org/10.1088/0004-637X/754/1/65), [arXiv:1204.2776](https://arxiv.org/abs/1204.2776).
- Ramesh, K.B., Vasantharaju, N., 2014. Temporal offsets among solar activity indicators. *Ap&SS* 350, 479–487. doi:[10.1007/s10509-014-1804-3](https://doi.org/10.1007/s10509-014-1804-3), [arXiv:1401.3990](https://arxiv.org/abs/1401.3990).
- Reinard, A.A., Zurbuchen, T.H., Fisk, L.A., Lepri, S.T., Skoug, R.M., Gloeckler, G., 2001. Comparison between average charge states and abundances of ions in CMEs and the slow solar wind, in: Wimmer-Schweingruber, R.F. (Ed.), Joint SOHO/ACE workshop “Solar and Galactic Composition”, pp. 139–144. doi:[10.1063/1.1433992](https://doi.org/10.1063/1.1433992).

- Reisenfeld, D.B., Gary, S.P., Gosling, J.T., Steinberg, J.T., McComas, D.J., Goldstein, B.E., Neugebauer, M., 2001. Helium energetics in the high-latitude solar wind: Ulysses observations. *J. Geophys. Res.* 106, 5693–5708. doi:[10.1029/2000JA000317](https://doi.org/10.1029/2000JA000317).
- Richardson, I.G., 2018. Solar wind stream interaction regions throughout the heliosphere. *Living Reviews in Solar Physics* 15, 1. doi:[10.1007/s41116-017-0011-z](https://doi.org/10.1007/s41116-017-0011-z).
- Richardson, I.G., Cane, H.V., 2004. Identification of interplanetary coronal mass ejections at 1 AU using multiple solar wind plasma composition anomalies. *Journal of Geophysical Research (Space Physics)* 109, A09104. doi:[10.1029/2004JA010598](https://doi.org/10.1029/2004JA010598).
- Richardson, I.G., Cane, H.V., 2010. Near-Earth Interplanetary Coronal Mass Ejections During Solar Cycle 23 (1996 - 2009): Catalog and Summary of Properties. *Sol. Phys.* 264, 189–237. doi:[10.1007/s11207-010-9568-6](https://doi.org/10.1007/s11207-010-9568-6).
- Richardson, J.D., Richardson, I.G., Kasper, J.C., Cane, H.V., Crooker, N.U., Lazarus, A.J., 2003. Helium variation in the solar wind, in: Wilson, A. (Ed.), *Solar Variability as an Input to the Earth's Environment*, pp. 521–526.
- Robbins, D.E., Hundhausen, A.J., Bame, S.J., 1970. Helium in the solar wind. *J. Geophys. Res.* 75, 1178. doi:[10.1029/JA075i007p01178](https://doi.org/10.1029/JA075i007p01178).
- Rodriguez, L., Woch, J., Krupp, N., FränZ, M., von Steiger, R., Forsyth, R.J., Reisenfeld, D.B., GlaßMeier, K.H., 2004. A statistical study of oxygen freezing-in temperature and energetic particles inside magnetic clouds observed by Ulysses. *Journal of Geophysical Research (Space Physics)* 109, A01108. doi:[10.1029/2003JA010156](https://doi.org/10.1029/2003JA010156).
- Sanchez-Diaz, E., Rouillard, A.P., Lavraud, B., Segura, K., Tao, C., Pinto, R., Sheeley, N.R., Plotnikov, I., 2016. The very slow solar wind: Properties, origin and variability. *Journal of Geophysical Research (Space Physics)* 121, 2830–2841. doi:[10.1002/2016JA022433](https://doi.org/10.1002/2016JA022433).

- Sarabhai, V., 1963. Some Consequences of Nonuniformity of Solar Wind Velocity. *Journal of Geophysical Research* 68, 1555–1557. doi:[10.1029/JZ068i005p01555](https://doi.org/10.1029/JZ068i005p01555).
- Schatten, K.H., 1971. Current sheet magnetic model for the solar corona. *Cosmic Electrodynamics* 2, 232–245.
- Schwadron, N.A., McComas, D.J., Elliott, H.A., Gloeckler, G., Geiss, J., von Steiger, R., 2005. Solar wind from the coronal hole boundaries. *Journal of Geophysical Research (Space Physics)* 110, A04104. doi:[10.1029/2004JA010896](https://doi.org/10.1029/2004JA010896).
- Shearer, P., von Steiger, R., Raines, J.M., Lepri, S.T., Thomas, J.W., Gilbert, J.A., Landi, E., Zurbuchen, T.H., 2014. The Solar Wind Neon Abundance Observed with ACE/SWICS and Ulysses/SWICS. *ApJ* 789, 60. doi:[10.1088/0004-637X/789/1/60](https://doi.org/10.1088/0004-637X/789/1/60).
- Smith, C.W., L’Heureux, J., Ness, N.F., Acuña, M.H., Burlaga, L.F., Scheifele, J., 1998. The ACE Magnetic Fields Experiment. *Space Sci. Rev.* 86, 613–632. doi:[10.1023/A:1005092216668](https://doi.org/10.1023/A:1005092216668).
- Song, H., Li, L., Sun, Y., Lv, Q., Zheng, R., Chen, Y., 2021. Solar Cycle Dependence of ICME Composition. *Sol. Phys.* 296, 111. doi:[10.1007/s11207-021-01852-y](https://doi.org/10.1007/s11207-021-01852-y), [arXiv:2106.03003](https://arxiv.org/abs/2106.03003).
- Stakhiv, M., Lepri, S.T., Landi, E., Tracy, P., Zurbuchen, T.H., 2016. On Solar Wind Origin and Acceleration: Measurements from ACE. *ApJ* 829, 117. doi:[10.3847/0004-637X/829/2/117](https://doi.org/10.3847/0004-637X/829/2/117).
- Steinberg, J.T., Lazarus, A.J., Ogilvie, K.W., Lepping, R., Byrnes, J., 1996. Differential flow between solar wind protons and alpha particles: First WIND observations. *Geophys. Res. Lett.* 23, 1183–1186. doi:[10.1029/96GL00628](https://doi.org/10.1029/96GL00628).
- Stone, E.C., Cohen, C.M.S., Cook, W.R., Cummings, A.C., Gauld, B., Kecman, B., Leske, R.A., Mewaldt, R.A., Thayer, M.R., Dougherty, B.L., Grumm, R.L., Milliken, B.D., Radocinski, R.G., Wiedenbeck, M.E., Christian, E.R., Shuman, S., Trexel, H., von Rosenvinge, T.T., Binns, W.R., Crary, D.J., Dowkontt, P.,

- Epstein, J., Hink, P.L., Klarmann, J., Lijowski, M., Olevitch, M.A., 1998a. The Cosmic-Ray Isotope Spectrometer for the Advanced Composition Explorer. *Space Sci. Rev.* 86, 285–356. doi:[10.1023/A:1005075813033](https://doi.org/10.1023/A:1005075813033).
- Stone, E.C., Cohen, C.M.S., Cook, W.R., Cummings, A.C., Gauld, B., Kecman, B., Leske, R.A., Mewaldt, R.A., Thayer, M.R., Dougherty, B.L., Grumm, R.L., Milliken, B.D., Radocinski, R.G., Wiedenbeck, M.E., Christian, E.R., Shuman, S., von Roseninge, T.T., 1998b. The Solar Isotope Spectrometer for the Advanced Composition Explorer. *Space Sci. Rev.* 86, 357–408. doi:[10.1023/A:1005027929871](https://doi.org/10.1023/A:1005027929871).
- Suess, S.T., Ko, Y.K., von Steiger, R., Moore, R.L., 2009. Quiescent current sheets in the solar wind and origins of slow wind. *Journal of Geophysical Research (Space Physics)* 114, A04103. doi:[10.1029/2008JA013704](https://doi.org/10.1029/2008JA013704).
- Vasquez, B.J., Farrugia, C.J., Simunac, K.D.C., Galvin, A.B., Berdichevsky, D.B., 2017. Concerning the helium-to-hydrogen number density ratio in very slow ejecta and winds near solar minimum. *Journal of Geophysical Research (Space Physics)* 122, 1487–1512. doi:[10.1002/2016JA023636](https://doi.org/10.1002/2016JA023636).
- Vauclair, S., Meyer, J.P., 1985. Diffusion in the Chromosphere, and the Composition of the Solar Corona and Energetic Particles, in: 19th International Cosmic Ray Conference (ICRC19), Volume 4, p. 233.
- Verscharen, D., Bourouaine, S., Chandran, B.D.G., 2013. Instabilities Driven by the Drift and Temperature Anisotropy of Alpha Particles in the Solar Wind. *ApJ* 773, 163. doi:[10.1088/0004-637X/773/2/163](https://doi.org/10.1088/0004-637X/773/2/163), [arXiv:1307.1823](https://arxiv.org/abs/1307.1823).
- Verscharen, D., Klein, K.G., Maruca, B.A., 2019. The multi-scale nature of the solar wind. *Living Reviews in Solar Physics* 16, 5. doi:[10.1007/s41116-019-0021-0](https://doi.org/10.1007/s41116-019-0021-0), [arXiv:1902.03448](https://arxiv.org/abs/1902.03448).
- Von Roseninge, T.T., Barbier, L.M., Karsch, J., Liberman, R., Madden, M.P., Nolan, T., Reames, D.V., Ryan, L., Singh, S., Trexel, H., Winkert, G., Mason,

- G.M., Hamilton, D.C., Walpole, P., 1995. The Energetic Particles: Acceleration, Composition, and Transport (EPACT) investigation on the WIND spacecraft. *Space Sci. Rev.* 71, 155–206. doi:[10.1007/BF00751329](https://doi.org/10.1007/BF00751329).
- Vourlidas, A., Howard, R.A., Plunkett, S.P., Korendyke, C.M., Thernisien, A.F.R., Wang, D., Rich, N., Carter, M.T., Chua, D.H., Socker, D.G., Linton, M.G., Morrill, J.S., Lynch, S., Thurn, A., Van Duyne, P., Hagood, R., Clifford, G., Grey, P.J., Velli, M., Liewer, P.C., Hall, J.R., DeJong, E.M., Mikic, Z., Rochus, P., Mazy, E., Bothmer, V., Rodmann, J., 2016. The Wide-Field Imager for Solar Probe Plus (WISPR). *Space Sci. Rev.* 204, 83–130. doi:[10.1007/s11214-014-0114-y](https://doi.org/10.1007/s11214-014-0114-y).
- Wallace, S., Arge, C.N., Pattichis, M., Hock-Mysliwiec, R.A., Henney, C.J., 2019. Estimating Total Open Heliospheric Magnetic Flux. *Sol. Phys.* 294, 19. doi:[10.1007/s11207-019-1402-1](https://doi.org/10.1007/s11207-019-1402-1), [arXiv:1903.12613](https://arxiv.org/abs/1903.12613).
- Wallace, S., Arge, C.N., Viall, N., Pihlström, Y., 2020. On the Relationship between Magnetic Expansion Factor and Observed Speed of the Solar Wind from Coronal Pseudostreamers. *ApJ* 898, 78. doi:[10.3847/1538-4357/ab98a0](https://doi.org/10.3847/1538-4357/ab98a0), [arXiv:2007.16168](https://arxiv.org/abs/2007.16168).
- Wang, Y.M., 2016. Role of the Coronal Alfvén Speed in Modulating the Solar-wind Helium Abundance. *ApJ* 833, L21. doi:[10.3847/2041-8213/833/2/L21](https://doi.org/10.3847/2041-8213/833/2/L21).
- Wang, Y.M., Sheeley, N. R., J., 1990. Solar Wind Speed and Coronal Flux-Tube Expansion. *ApJ* 355, 726. doi:[10.1086/168805](https://doi.org/10.1086/168805).
- Wang, Y.M., Sheeley, N. R., J., 1992. On Potential Field Models of the Solar Corona. *ApJ* 392, 310. doi:[10.1086/171430](https://doi.org/10.1086/171430).
- Wang, Y.M., Sheeley, N. R., J., Phillips, J.L., 1995. Coronal flux-tube expansion and the polar wind. *Advances in Space Research* 16, 365–365. doi:[10.1016/0273-1177\(95\)00371-K](https://doi.org/10.1016/0273-1177(95)00371-K).
- Wilson, Lynn B., I., Chen, L.J., Wang, S., Schwartz, S.J., Turner, D.L., Stevens, M.L., Kasper, J.C., Osmane, A., Caprioli, D., Bale, S.D., Pulupa,

- M.P., Salem, C.S., Goodrich, K.A., 2019. Electron Energy Partition across Interplanetary Shocks. I. Methodology and Data Product. *ApJS* 243, 8. doi:[10.3847/1538-4365/ab22bd](https://doi.org/10.3847/1538-4365/ab22bd), [arXiv:1902.01476](https://arxiv.org/abs/1902.01476).
- Wilson, Lynn B., I., Stevens, M.L., Kasper, J.C., Klein, K.G., Maruca, B.A., Bale, S.D., Bowen, T.A., Pulupa, M.P., Salem, C.S., 2018. The Statistical Properties of Solar Wind Temperature Parameters Near 1 au. *ApJS* 236, 41. doi:[10.3847/1538-4365/aab71c](https://doi.org/10.3847/1538-4365/aab71c), [arXiv:1802.08585](https://arxiv.org/abs/1802.08585).
- Wimmer-Schweingruber, R.F., Crooker, N.U., Balogh, A., Bothmer, V., Forsyth, R.J., Gazis, P., Gosling, J.T., Horbury, T., Kilchenmann, A., Richardson, I.G., Richardson, J.D., Riley, P., Rodriguez, L., von Steiger, R., Wurz, P., Zurbuchen, T.H., 2006. Understanding Interplanetary Coronal Mass Ejection Signatures. Report of Working Group B. *Space Sci. Rev.* 123, 177–216. doi:[10.1007/s11214-006-9017-x](https://doi.org/10.1007/s11214-006-9017-x).
- Wimmer-Schweingruber, R.F., von Steiger, R., Paerli, R., 1999. Solar wind stream interfaces in corotating interaction regions: New SWICS/Ulysses results. *J. Geophys. Res.* 104, 9933–9946. doi:[10.1029/1999JA900038](https://doi.org/10.1029/1999JA900038).
- Withbroe, G.L., 1981. Activity and Outer Atmosphere of the Sun, in: Praderie, F., Spicer, D.S., Withbroe, G.L. (Eds.), *Saas-Fee Advanced Course 11: Activity and Outer Atmosphere of the Sun and Stars*, p. 1.
- Woolley, T., Matteini, L., McManus, M.D., Berčić, L., Badman, S.T., Woodham, L.D., Horbury, T.S., Bale, S.D., Laker, R., Stawarz, J.E., Larson, D.E., 2021. Plasma properties, switchback patches, and low α -particle abundance in slow Alfvénic coronal hole wind at 0.13 au. *MNRAS* 508, 236–244. doi:[10.1093/mnras/stab2281](https://doi.org/10.1093/mnras/stab2281), [arXiv:2106.01075](https://arxiv.org/abs/2106.01075).
- Worden, J., Harvey, J., 2000. An Evolving Synoptic Magnetic Flux map and Implications for the Distribution of Photospheric Magnetic Flux. *Sol. Phys.* 195, 247–268. doi:[10.1023/A:1005272502885](https://doi.org/10.1023/A:1005272502885).
- Wurz, P., Wimmer-Schweingruber, R.F., Issautier, K., Bochsler, P., Galvin, A.B., Paquette, J.A., Ipavich, F.M., 2001. Composition of magnetic cloud

- plasmas during 1997 and 1998, in: Wimmer-Schweingruber, R.F. (Ed.), Joint SOHO/ACE workshop “Solar and Galactic Composition”, pp. 145–150. doi:[10.1063/1.1433993](https://doi.org/10.1063/1.1433993).
- Zhao, L., Landi, E., Lepri, S.T., Gilbert, J.A., Zurbuchen, T.H., Fisk, L.A., Raines, J.M., 2017. On the Relation between the In Situ Properties and the Coronal Sources of the Solar Wind. *ApJ* 846, 135. doi:[10.3847/1538-4357/aa850c](https://doi.org/10.3847/1538-4357/aa850c).
- Zirker, J.B., 1977. Coronal holes and high-speed wind streams. *Reviews of Geophysics and Space Physics* 15, 257–269. doi:[10.1029/RG015i003p00257](https://doi.org/10.1029/RG015i003p00257).
- Zurbuchen, T.H., Richardson, I.G., 2006. In-Situ Solar Wind and Magnetic Field Signatures of Interplanetary Coronal Mass Ejections. *Space Sci. Rev.* 123, 31–43. doi:[10.1007/s11214-006-9010-4](https://doi.org/10.1007/s11214-006-9010-4).
- Zurbuchen, T.H., Weberg, M., von Steiger, R., Mewaldt, R.A., Lepri, S.T., Antiochos, S.K., 2016. Composition of Coronal Mass Ejections. *ApJ* 826, 10. doi:[10.3847/0004-637X/826/1/10](https://doi.org/10.3847/0004-637X/826/1/10).
- Zwickl, R.D., Doggett, K.A., Sahm, S., Barrett, W.P., Grubb, R.N., Detman, T.R., Raben, V.J., Smith, C.W., Riley, P., Gold, R.E., Mewaldt, R.A., Maruyama, T., 1998. The NOAA Real-Time Solar-Wind (RTSW) System using ACE Data. *Space Sci. Rev.* 86, 633–648. doi:[10.1023/A:1005044300738](https://doi.org/10.1023/A:1005044300738).

List of Publications

Publications included in the thesis

1. **Yogesh**, D. Chakrabarty, N. Srivastava, Evidence for distinctive changes in the solar wind helium abundance in solar cycle 24, Monthly Notices of the Royal Astronomical Society: Letters, Volume 503, Issue 1, May 2021, Pages L17–L22, <https://doi.org/10.1093/mnrasl/slab016>
2. **Yogesh**, D Chakrabarty, N Srivastava, A holistic approach to understand helium enrichment in interplanetary coronal mass ejections: new insights, Monthly Notices of the Royal Astronomical Society: Letters, Volume 513, Issue 1, June 2022, Pages L106–L111, <https://doi.org/10.1093/mnrasl/slac044>
Yogesh, D Chakrabarty, N Srivastava, Correction to: A holistic approach to understand helium enrichment in interplanetary coronal mass ejections: new insights, Monthly Notices of the Royal Astronomical Society: Letters, Volume 520, Issue 1, March 2023, Page L78, <https://doi.org/10.1093/mnrasl/slad011>
3. **Yogesh**, D Chakrabarty, N Srivastava, New insights on the behaviour of solar wind protons and alphas in the Stream Interaction Region in solar cycle 23 and 24 (Under Review - MNRAS Letters)
4. **Yogesh** et al. 2023, Important roles of Coronal hole boundary and First ionization Potential effect for very low ($< 1\%$) helium abundance in the solar wind (To be submitted soon).

Presentations at International/National Conferences

Invited

1. Yogesh, D. Chakrabarty, Nandita Srivastava, "Enrichment of Helium abundance in Interplanetary Coronal Mass Ejections: Insights" presented in the Workshop-3, 41st Annual Meeting of the Astronomical Society of India (ASI) " held at IIT Indore, India, during 1-5 March 2023 (Invited - In-person)
2. Yogesh, D. Chakrabarty, Nandita Srivastava, "Investigations on the alpha-proton ratio in solar wind using ASPEX measurements" in Aditya-L1 Science Support Cell (AL1SSC) workshop held from June 27 to July 6, 2022, at ARIES, Nainital, India (Invited - In-person)

Oral Presentations

1. Yogesh, D. Chakrabarty, Nandita Srivastava, "Helium abundance in Stream Interaction Regions - insights" presented in the 41st Annual Meeting of the Astronomical Society of India (ASI) " held at IIT Indore, India, during 1-5 March 2023 (In person)
2. Yogesh, D. Chakrabarty, Nandita Srivastava, "Investigations on helium abundance in background solar wind and interplanetary coronal mass ejections" presented in the AGU-2022 held at Chicago, USA, during 12-16 December 2022 (In-person)
3. Yogesh, D. Chakrabarty, Nandita Srivastava, "Helium abundance variation in Interplanetary Coronal Mass Ejections spanning over solar cycle 23 and 24" presented in the Workshop-3, 40th Annual Meeting of the Astronomical Society of India (ASI) "held at IIT Roorkee, India, during 25-29 March 2022 (ONLINE)

4. Yogesh, D. Chakrabarty, Nandita Srivastava, "Helium abundance in solar wind and coronal mass ejections" presented in the 15th Quadrennial Solar-Terrestrial Physics Symposium (STP-15)" held at IIG Alibag, India, during 21-25 February 2022 (ONLINE)
5. Yogesh, D. Chakrabarty, Nandita Srivastava, "Investigation on Helium abundance variation in solar wind during last four solar cycles" presented in the 1st Indian Space Weather Conference (ISWC-2022) held at Physical Research Laboratory, India, during 11-12 January 2022 (ONLINE)

Poster Presentations

1. Yogesh, D. Chakrabarty, Nandita Srivastava, "Variation of Helium abundance in Stream Interaction Regions" presented in the 1st USO-PRL Solar Physics Workshop (USPW 2023) held at Udaipur Solar Observatory, PRL, India, during 3 - 5 April 2023 (In-person)
2. Yogesh, D. Chakrabarty, Nandita Srivastava, "On the variation of Helium abundance over solar cycles and ICMEs" presented in the 21st National Space Science Symposium (NSSS-2022) held at IISER Kolkata, India, during January 31 - February 4 2022 (ONLINE)

Schools Attended

1. Attended "5th IAGA School." Hosted by CSIR-NGRI, Hyderabad, India, on 16-20 August 2021 (ONLINE)
2. Attended "STFC Introductory Solar System Plasmas Summer School" held virtually by Hosted by University of Birmingham during 24 – 27 August 2020 (ONLINE)

Publications attached with thesis

1. **Yogesh**, D. Chakrabarty, N. Srivastava, Evidence for distinctive changes in the solar wind helium abundance in solar cycle 24, Monthly Notices of the Royal Astronomical Society: Letters, Volume 503, Issue 1, May 2021, Pages L17–L22, <https://doi.org/10.1093/mnrasl/slab016>
2. **Yogesh**, D Chakrabarty, N Srivastava, A holistic approach to understand helium enrichment in interplanetary coronal mass ejections: new insights, Monthly Notices of the Royal Astronomical Society: Letters, Volume 513, Issue 1, June 2022, Pages L106–L111, <https://doi.org/10.1093/mnrasl/slac044>
Yogesh, D Chakrabarty, N Srivastava, Correction to: A holistic approach to understand helium enrichment in interplanetary coronal mass ejections: new insights, Monthly Notices of the Royal Astronomical Society: Letters, Volume 520, Issue 1, March 2023, Page L78, <https://doi.org/10.1093/mnrasl/slad011>



Evidence for distinctive changes in the solar wind helium abundance in solar cycle 24

Yogesh ^{1,2*} D. Chakrabarty^{1*} and N. Srivastava³

¹Physical Research Laboratory, Navrangpura, Ahmedabad 380009, India

²Indian Institute of Technology Gandhinagar, Gandhinagar 382424, India

³Udaipur Solar Observatory, Physical Research Laboratory, Udaipur 313001, India

Accepted 2021 February 8. Received 2021 February 2; in original form 2021 January 4

ABSTRACT

The relative abundance of alpha particles with respect to protons, usually expressed as $A_{\text{He}} = (n_{\alpha}/n_p) \times 100$, is known to respond to solar activity, although changes in its behaviour in the last four solar cycles are not known. In this letter, by systematically analysing inter-calibrated A_{He} data obtained from the first Lagrangian point of the Sun–Earth system, we show that A_{He} variations are distinctively different in solar cycle 24 as compared to the last three cycles. The frequency of $A_{\text{He}} = 2\text{--}3$ per cent events is significantly higher in slow/intermediate solar winds in solar cycle 24 as opposed to the dominance of the typical $A_{\text{He}} = 4\text{--}5$ per cent events in the previous three cycles. Further, the occurrence of $A_{\text{He}} > 10$ per cent events is significantly reduced in cycle 24. Not only that the changes in delay of A_{He} with respect to peak sunspot numbers are less sensitive to changes in solar wind velocity in cycle 24. The investigation suggests that the coronal magnetic field configuration started undergoing systematic changes starting from cycle 23 and this altered magnetic field configuration affected the way helium got processed and depleted in the solar atmosphere.

Key words: magnetic fields; Sun: abundances – Sun: activity – solar wind; sunspots; Sun: corona.

1 INTRODUCTION

Doubly ionized helium (He^{2+} or α particle) is the second most abundant species in the solar wind after the singly ionized hydrogen (H^+ or proton). Despite helium being the second most abundant element in the solar wind, doubly ionized helium atom abundance in the quiet solar wind does not exceed 4–5 per cent (Laming & Feldman 2001) and is strongly regulated by a number of processes occurring in the chromosphere, transition region, and corona. Helium is four times heavier than hydrogen and, as a consequence, it constitutes 25 per cent of the solar wind mass flux. The first ionization potential (FIP) of helium is the highest among the solar elements; therefore, helium gets ionized later than any other element and this occurs at the topside of the chromosphere. It is believed that the FIP effect (Laming 2015) primarily depletes the helium abundance in the chromosphere and the transition region. Processes like gravitational settling, Coulomb collisions, and other wave–particle interactions also contribute in varying degrees to the helium depletion process at different heights (Moses et al. 2020).

The variation of A_{He} with solar activity was first indicated by Hirshberg (1973) and Ogilvie & Hirshberg (1974) by comparing it with the variations in sunspot numbers (SSNs). These authors used multiple satellite data to show the relationship between A_{He} and SSNs. Subsequently, Feldman et al. (1978) used *IMP* satellite data to extend the result of Ogilvie & Hirshberg (1974) and indicated a possible delay between the variations in A_{He} and SSNs. Aellig,

Lazarus & Steinberg (2001) extended the solar cycle variation of A_{He} using *Wind* data and found out a linear relationship between the SSNs and A_{He} for the slow solar wind. No such strong relationship was found to exist for the fast solar wind. It was also found that the linear relationship between the solar wind velocity and A_{He} for the slow solar wind is strong during minima, but weak during maxima. Further, in order to understand the variation of A_{He} for the slow solar wind, Kasper et al. (2007, 2012) investigated the solar activity variation of A_{He} for approximately one full solar cycle. The above studies suggest the possible association between the sources of the solar wind and solar activity variation of A_{He} . In addition to this, right from the work of Feldman et al. (1978), it is suggested that there exists a delay (hysteresis) between A_{He} and SSNs. In recent times, Alterman & Kasper (2019) investigated the delay in A_{He} variation with respect to the variations in SSNs and found a linear relationship between the solar wind velocity and the delay. Although the solar activity dependence of A_{He} and the hysteresis between A_{He} and SSNs were shown, it is not known whether helium abundance in solar wind behaved identically in the last four solar cycles. The answer to this question can shed light on the long-term changes in the way helium got processed in the coronal magnetic field of the Sun. This is an important question as many authors showed declining solar activity from cycle 23 onwards (Janardhan et al. 2011). The results presented in this work provide evidence that the variation of helium abundance started changing from cycle 23 onwards and is conspicuously different in cycle 24.

* E-mail: yphy22@gmail.com (Y); dipu@prl.res.in (DC)

2 DATA SET

The low-resolution OMNI data base used in this work contains multispacecraft data (such as *IMP*, *Wind*, *ACE*, and *Geotail*) having 1-h cadence. Some of these satellites are in earth orbit and for these satellites, the measurements made outside the terrestrial magnetosphere are considered. The plasma data from some spacecraft and parameters are compared and cross-normalized with respect to the *Wind/SWE/NLF* data. For the present investigation wherein proton and alpha measurements are used, primarily four multisource data are used. These are *IMP6/IMP7/IMP8* satellite data during 1971–1978, *IMP8* data during 1973–2001, *IMP8/ISEE3* data during 1978–1982, and *IMP8/Wind/ACE/Geotail* data during 1995–2019. These aspects are detailed comprehensively at https://omniweb.gsfc.nasa.gov/html/ow_data.html. One can also find the discussions on the time shifting of the data set for various satellites, data averaging scheme, spacecraft prioritization, cleaning of source data, as well as the possible sources of random and systematic differences between hourly averages of pairs of like parameters obtained by two spacecraft in this link. In addition, [King & Papitashvili \(2005\)](#) and references cited therein also provide the nuances of the normalization scheme for *ACE* and *Wind* satellites that are major contributors to this OMNI data base. Although the OMNI data base starts from 1963, the A_{He} data set is available since 1971. The data are parsed to create data for solar cycles 21–24 marked by the years 1976–1986, 1987–1996, 1997–2008, and 2009–2019, respectively.

3 RESULTS

Solar cycle 24 turns out to be the weakest cycle in the last 100 yr ([Hathaway 2015](#)). In order to evaluate the changes, if any, in the solar wind helium abundance in cycle 24 compared to the previous three cycles, we performed a number of extensive analyses of A_{He} data taken at 1-h cadence and available on the OMNI data base (<https://cdaweb.gsfc.nasa.gov/index.html>) spanning over almost half a century and encompassing the last four solar cycles (cycles 21–24).

3.1 Frequency of A_{He} events (≤ 10 per cent and > 10 per cent) in the last four solar cycles

As a first step, we divided the 1-h A_{He} data for each solar cycle in five velocity bins, viz. (1) $< 300 \text{ km s}^{-1}$, (2) $300\text{--}400 \text{ km s}^{-1}$, (3) $400\text{--}500 \text{ km s}^{-1}$, (4) $500\text{--}600 \text{ km s}^{-1}$, and (5) $\geq 600 \text{ km s}^{-1}$. For a given velocity bin, we evaluated the frequency distributions of A_{He} events. We note that the frequency distributions can be well approximated by lognormal distributions for all the velocity bins except for bin $< 300 \text{ km s}^{-1}$ (Fig. 1).

$$\text{Frequency} = \frac{A}{\sigma\sqrt{2\pi}} \exp\left\{-\frac{(\log(A_{\text{He}}) - \mu)^2}{2\sigma^2}\right\}, \quad (1)$$

$$m = \exp(\mu). \quad (2)$$

In equation (1), A is the normalization factor, σ is the standard deviation (shape parameter), and μ is the centre (median) of the lognormal distribution. Equation (2) is used to convert μ from log scale to linear scale. This linear counterpart of μ is marked as m and this is basically the median value. The corresponding values of A , m , and μ are mentioned in each subplot of Fig. 1. It can be noted that the median value of A_{He} monotonically decreases for $300\text{--}400$ and $400\text{--}500 \text{ km s}^{-1}$ velocity bins as one goes from cycle 21 to cycle 24. However, for the other two velocity bins, the median value increases in cycle 22 before dropping again in cycles 23 and 24. The most important feature to be noted is the shift of peak A_{He}

from the usual 4–5 per cent (in cycles 21 and 22) to 2–3 per cent in the $400\text{--}500 \text{ km s}^{-1}$ velocity range and increase in the frequency in the $300\text{--}400 \text{ km s}^{-1}$ velocity range in cycle 24. Interestingly, these two velocity bins contain around 80 per cent of the total data points. Based on Fig. 1, we fix the upper limit of A_{He} at 10 per cent and proceed to evaluate the velocity dependence of A_{He} for the four solar cycles in Sections 3.2 and 3.3.

We also evaluate the yearly frequency of events with $A_{\text{He}} > 10$ per cent vis-à-vis yearly averaged SSNs for the four solar cycles (Fig. 2) and note that these events start reducing significantly from cycle 23 and by cycle 24, the frequency of these events does not exceed 2 per cent.

3.2 Solar cycle variation of $A_{\text{He}} \leq 10$ per cent

In Fig. 3, we divide the solar wind velocity in each cycle into 12 quantiles and neglect the fastest and slowest quantiles to avoid possible measurement uncertainties and spreading out of the velocity range. Therefore, this work is primarily applicable for slow and intermediate solar wind velocities. For each velocity bin, both A_{He} and SSNs are first averaged for 250 d and plotted for the four cycles separately. The legend in each cycle shows the mid-point of each quantile and the corresponding Spearman rank correlation coefficient, $\rho(A_{\text{He}}, \text{SSN})$, between A_{He} and SSNs. Fig. 3 reveals that $\rho(A_{\text{He}}, \text{SSN})$ maximizes at 369 , 372 , and 373 km s^{-1} in cycles 21, 22, and 23, respectively. However, in cycle 24, the $\rho(A_{\text{He}}, \text{SSN})$ value maximizes at 401 km s^{-1} and it does not change significantly at higher velocity unlike other cycles. Therefore, ρ maximizes at a higher velocity in cycle 24 compared to the previous three solar cycles.

We also note that there is an apparent phase offset (delay) between the A_{He} and SSN, but this offset starts decreasing in cycle 23 and eventually becomes negligible in cycle 24. The dependence of this phase offset with the solar wind velocity is taken up for further scrutiny for the four solar cycles.

3.3 Delay between A_{He} and SSNs

In order to derive the phase offsets between A_{He} and SSNs for four solar cycles, both the time series are first subjected to 1-d average followed by 13 months' smoothing. This is done to remove the discreteness in the data and also to eliminate the influence of the orientation of the heliospheric current sheet with respect to the satellites. SSNs are shifted in steps of 10 d starting from 0 to 600 and peak $\rho(A_{\text{He}}, \text{SSN})$ values are obtained for each velocity bin with the corresponding delay times. These results are plotted in Fig. 4 that shows $\rho(A_{\text{He}}, \text{SSN})$ without delay by a dashed blue line and peak $\rho(A_{\text{He}}, \text{SSN})$ with delay by a solid blue line for each velocity quantile. The delays at different velocity quantiles are marked with filled black circles joined by a dashed line to aid the eye. Positive delay means changes in A_{He} follow the changes in SSNs. The standard deviations are calculated by considering 1 per cent variation of peak $\rho(A_{\text{He}}, \text{SSN})$ and the associated delays. It can be observed that $\rho(A_{\text{He}}, \text{SSN})$ maximizes between 350 and 400 km s^{-1} in all four cycles. However, the slopes of the linear fits (the fit equations are mentioned in Fig. 4) for delay are significantly reduced in cycles 23 and 24. We note that the delay for even the highest velocity quantile does not exceed 200 d and the differences in delay between the lowest and highest quantiles are not significantly different. We varied A_{He} from 4 per cent to 10 per cent and linear fit parameters are obtained in each case. This is tabulated and provided as a supplementary material. It is found that the slopes remain consistently higher (close to 1 or more) in cycles 21 and 22, and consistently lower (the highest value of slope is 0.64 at $A_{\text{He}} = 5$ per cent) in cycle 24 for all values of A_{He} .

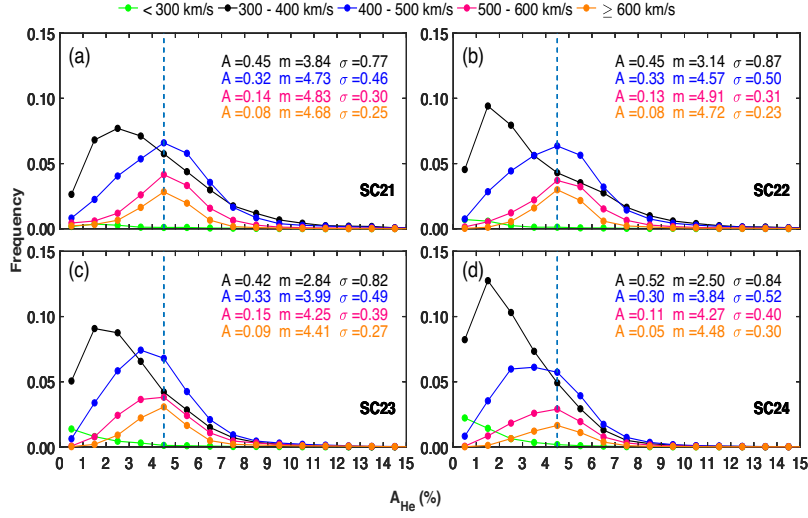


Figure 1. Frequency of distribution of A_{He} in different velocity bins in the last four solar cycles. Frequency distribution of A_{He} events with 1 per cent bin size for four velocity bins, viz. (1) $< 300 \text{ km s}^{-1}$, (2) $300\text{--}400 \text{ km s}^{-1}$, (3) $400\text{--}500 \text{ km s}^{-1}$, (4) $500\text{--}600 \text{ km s}^{-1}$, and (5) $\geq 600 \text{ km s}^{-1}$ in solar cycles 21 (a), 22 (b), 23 (c), and 24 (d). Each velocity window is marked with a different colour (with a filled circle joined by a solid line) and is shown at the top of the figure. The frequency distributions are approximated by lognormal distributions wherein A , σ , and m are the fit parameters, representing normalization coefficient, standard deviation and median in linear scale, respectively. It can be noted that m monotonically decreases for $300\text{--}400$ and $400\text{--}500 \text{ km s}^{-1}$ velocity bins as one goes from cycle 21 to cycle 24. Further, the shift of the peak A_{He} from the usual $4\text{--}5$ per cent (in cycles 21 and 22) to $2\text{--}3$ per cent in the $400\text{--}500 \text{ km s}^{-1}$ velocity range and increase in the frequency in the $300\text{--}400 \text{ km s}^{-1}$ velocity range in cycle 24 are also conspicuous. The vertical dashed lines mark A_{He} of 4.5 per cent. This figure also reveals that the frequency of occurrence for $A_{\text{He}} > 10$ per cent events is insignificant in statistical sense.

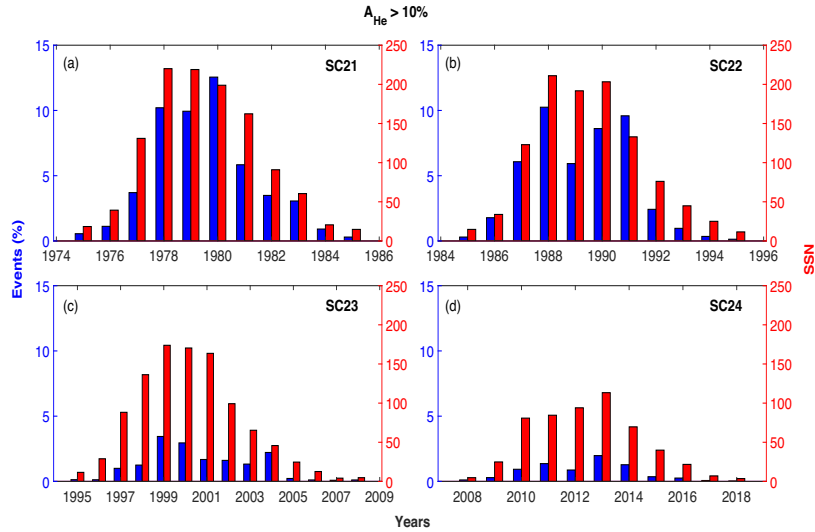


Figure 2. Frequency of $A_{\text{He}} > 10$ per cent events in the last four cycles. Year-wise frequency of $A_{\text{He}} > 10$ per cent events (marked by blue vertical bars) and yearly averaged sunspot numbers (SSNs) (marked by red vertical bars) in the last four solar cycles denoted by (a), (b), (c), and (d). This frequency is calculated with respect to the number of all A_{He} events in a particular year. Peak values of A_{He} frequencies are 12.55 per cent, 10.25 per cent, 3.44 per cent, and 1.98 per cent as one goes from cycle 21 to cycle 24.

4 DISCUSSION AND CONCLUSIONS

The helium abundance in the photosphere is taken to be nearly 8.5 per cent (Grevesse & Sauval 1998), but it generally remains about 4–5 per cent (Laming & Feldman 2001) in the solar corona. This suggests that the helium abundance is depressed by processes that occur in the chromosphere, transition region, and corona. As

helium is heavier than hydrogen, it undergoes enhanced gravitational settling (Hirshberg 1973). In addition, FIP effect (Laming 2015) can change the helium abundance. When the downward or upward propagating Alfvén waves encounter the chromosphere, these exert upward ponderomotive forces on the ions that raise the ions up in altitude (Laming 2012; Rakowski & Laming 2012). Subsequently,

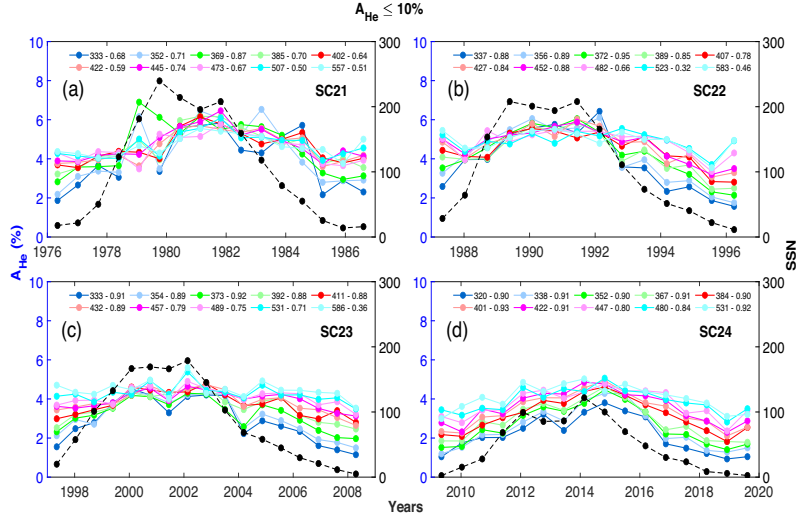


Figure 3. Variation of $A_{\text{He}} \leq 10$ per cent in the last four solar cycles: Spearman's rank correlation analysis between averaged (for 250 d) A_{He} and sunspot numbers (SSNs) for 12 velocity quantiles in the last four solar cycles. Results for cycles 21–24 are provided in (a), (b), (c), and (d), respectively. The Spearman's rank correlation coefficient, ρ (A_{He} , SSN), values, and the mid-point of each velocity quantile are shown on the top of each panel. Note that the highest and lowest velocity quantiles are removed from this representation. Each velocity quantile is marked by filled circles of different colours joined by solid lines, and SSN variations are marked by black filled circles joined by dashed lines. The ρ (A_{He} , SSN) values maximize at 369, 372, and 373 km s^{-1} in cycles 21, 22, and 23, respectively. However, in cycle 24, the ρ (A_{He} , SSN) value maximizes at 401 km s^{-1} . The apparent phase offset between A_{He} and SSNs becomes negligible in cycle 24.

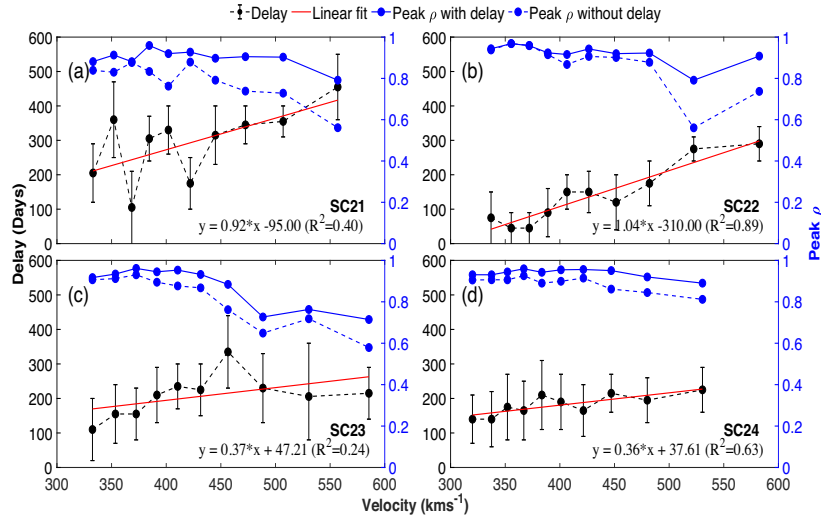


Figure 4. Delayed correlation between $A_{\text{He}} (\leq 10$ per cent) and SSNs in four solar cycles. Variation of delay (filled black dots joined by a dashed line) between SSNs and A_{He} for each velocity quantile in four solar cycles (21–24) is marked in (a), (b), (c), and (d), respectively. Peak ρ (A_{He} , SSN) values between SSNs and A_{He} with (blue solid dots joined by a solid blue line) and without (blue solid dots joined by a dashed blue line) delay for each velocity quantile are also plotted for each cycle. The standard deviations are calculated by varying peak ρ (A_{He} , SSN) by 1 per cent and considering the associated delays. The red lines mark the linear fits (equations and R^2 values are shown in each figure) for the delays in each cycle. Peak ρ (A_{He} , SSN) value maximizes between 350 and 400 km s^{-1} in all the four cycles. However, slopes of the linear fits in cycles 23 and 24, and particularly in cycle 24, are significantly less compared to cycles 21 and 22.

if the magnetic loops open up due to magnetic reconnection, the low FIP ions are released into the corona. While this effect enhances the abundance of lower FIP elements in the corona, it also conversely implies that it depletes the higher FIP elements.

Therefore, FIP effect suggests that if there are significant changes in the closed loop coronal magnetic field configuration from one cycle to other, it will have impact on the helium abundance as well as delay.

This investigation shows that the maximum correlation coefficient between A_{He} and SSNs is obtained at a different velocity bin in cycle 24 as compared to the previous three cycles. Given this, it is also important to evaluate the sources of the slow/intermediate solar winds and how these affect the helium abundance. It was proposed earlier that the slow solar wind originates from two primary sources, viz. streamer belt and active region (Kasper et al. 2007). While the active region has stronger magnetic fields compared to the streamer belt, the latter has longer magnetic loops that facilitate enhanced processing of the solar wind helium. This leads to the delay in A_{He} with respect to the SSNs. Interestingly, this delay is solar wind velocity dependent and, in general, more for higher velocities (Alterman & Kasper 2019). However, as shown by our analysis starting from cycle 23, this processing seems to have become less sensitive to the solar wind velocity. At this juncture, it may be noted that the time lag of the order of hundreds of days suggests that He fractionation is a slow process. Whether it indicates the dominant role of gravitational settling in the He fractionation is a question that requires further attention. Interestingly, as discussed by Laming et al. (2019), extreme He depletions reported by earlier works (Kasper et al. 2012; Kepko et al. 2016) are unlikely to be reproduced by ponderomotive force and thus gravitational settling appears to be the most dominant mechanism. Therefore, the reduced time lag across the velocity bins and systematic shift of A_{He} frequency to lower A_{He} values in cycle 24 may be suggestive of systematic changes in ponderomotive force as well as the gravitational settling in closed magnetic loops. It is to be noted that the length of the magnetic loop is also important for He processing. Although these are speculative scenarios, there are indications that systematic changes did occur in the Sun starting from cycle 23. One such example is the changes in the occurrence and characteristics of pseudo-streamers and dipole streamers. Pseudo-streamers are known to be additional sources of slow solar wind (Crooker et al. 2012). Interestingly, occurrence of pseudo-streamers was found to be significantly higher during the minimum of the solar cycle 23 unlike cycles 21 and 22 when these structures almost disappeared (Owens, Crooker & Lockwood 2014). On the other hand, the dipole streamers were shown (Owens et al. 2014) to be less tightly confined to the solar equator at the end of cycle 23 compared to the previous two cycles. This difference in the pseudo-streamers and dipole streamers at the end of solar cycle 23 indicates towards the possible change in the processing of the slow solar wind at the end of cycle 23.

Some of the earlier works (Levine, Altschuler & Harvey 1977; Wang & Sheeley 1990) suggest that the origin of slow solar wind is the boundary of the coronal holes. As the magnetic flux tubes from the boundary of the coronal hole are expanded, the bulk speed of the slow solar wind decreases. This reduces the proton flux beyond $2.5 R_{\odot}$ and, as a result, the alpha particle enrichment in the solar wind decreases through reduced momentum transfer via Coulomb collisions (Bürgi 1992). This scenario is particularly valid for solar minimum when the magnetic flux tubes undergo strong overexpansion. We suggest that large-scale magnetic flux tube topologies are quite different (in statistical sense) in solar cycle 24 (starting from solar cycle 23), which affected the processing as well as the velocity dependence of the helium enrichment process in the solar wind. This proposition gets indirect support from the fact that the polar field went through unusual reversal in solar cycle 24 (Janardhan et al. 2018).

The higher A_{He} events are, in general, thought to be associated with transient coronal disturbances like solar flare and eruptive prominences (Borrini et al. 1982). Many of these processes are believed to throw helium-rich plasma from the lower solar corona to the interplanetary medium causing helium abundance enhancements.

The frequency of occurrences of such transient disturbances is approximately in phase with the solar cycle (Borrini et al. 1982). Further, it is known that the number of X, M, and C-class flares dropped drastically in cycle 23 compared to the earlier cycles (Hudson, Fletcher & McTiernan 2014). The number of such flares is even less in cycle 24. This may be one of the reasons for the lower frequency of higher A_{He} events in cycle 24 compared to the previous three cycles. As stated earlier, solar cycle 24 turns out to be the weakest in the last century and the Sun was unusually quiet since the deep minimum of cycle 23. Many authors highlighted the declining solar activity from solar cycle 23 onwards based on observations (Janardhan et al. 2011) or dynamo models (Choudhuri, Chatterjee & Jiang 2007). Observations during Ulysses first (cycle 22) and third orbit (cycle 23) revealed that solar wind in the minimum of cycle 23 was weaker characterized by significantly less dense, cooler wind with less mass, and momentum flux compared to the first orbit during the solar minimum in cycle 22 (McComas et al. 2008). The peculiarities of solar cycle 24 have also been highlighted by earlier workers (Antia & Basu 2013). Therefore, we believe that the large-scale coronal magnetic field topology and dynamics of the Sun went through significant changes in cycle 24 that affected the way helium was processed in the solar wind. Recent helium abundance measurements (Moses et al. 2020) in the solar corona provide credence to this proposition. Further modelling investigations are needed to explain the changes in the helium abundance in cycle 24 and to predict the possible variation in cycle 25.

ACKNOWLEDGEMENTS

We would like to thank the managing team of OMNI data set (<https://cdaweb.gsfc.nasa.gov/team.html>). We thank and acknowledge the significant efforts put forward by the Principal Investigators (PIs) of all the satellites, data of which are used to generate this integrated, cross-calibrated OMNI data set. This work is supported by the Department of Space, Government of India.

DATA AVAILABILITY

The data can be obtained from <https://cdaweb.gsfc.nasa.gov/index.html>.

REFERENCES

- Aellig M. R., Lazarus A. J., Steinberg J. T., 2001, in Wimmer-Schweingruber R. F., eds, *AIP Conf. Proc.*, Vol. 598, New York, p. 89
- Alterman B. L., Kasper J. C., 2019, *ApJ*, 879, L6
- Antia H. M., Basu S., 2013, *J. Phys.: Conf. Ser.*, 440, 012018
- Borrini G., Gosling J. T., Bame S. J., Feldman W. C., 1982, *J. Geophys. Res.: Space Phys.*, 87, 7370
- Bürgi A., 1992, *J. Geophys. Res.: Space Phys.*, 97, 3137
- Choudhuri A. R., Chatterjee P., Jiang J., 2007, *Phys. Rev. Lett.*, 98, 131103
- Crooker N. U., Antiochos S. K., Zhao X., Neugebauer M., 2012, *J. Geophys. Res.: Space Phys.*, 117, A4
- Feldman W., Asbridge J., Bame S., Gosling J., 1978, *J. Geophys. Res.: Space Phys.*, 83, 2177
- Grevesse N., Sauval A., 1998, *Space Sci. Rev.*, 85, 161
- Hathaway D. H., 2015, *Living Rev. Sol. Phys.*, 12, 4
- Hirshberg J., 1973, *Rev. Geophys. Space Phys.*, 11, 115
- Hudson H., Fletcher L., McTiernan J., 2014, *Sol. Phys.*, 289, 1341
- Janardhan P., Bisoi S. K., Ananthakrishnan S., Tokumaru M., Fujiki K., 2011, *Geophys. Res. Lett.*, 38, 20
- Janardhan P., Fujiki K., Ingale M., Bisoi S. K., Rout D., 2018, *A&A*, 618, A148

Kasper J. C., Stevens M. L., Lazarus A. J., Steinberg J. T., Ogilvie K. W., 2007, *ApJ*, 660, 901
Kasper J. C., Stevens M. L., Korreck K. E., Maruca B. A., Kiefer K. K., Schwadron N. A., Lepri S. T., 2012, *ApJ*, 745, 162
Kepko L., Viall N. M., Antiochos S. K., Lepri S. T., Kasper J. C., Weberg M., 2016, *Geophys. Res. Lett.*, 43, 4089
King J. H., Papitashvili N. E., 2005, *J. Geophys. Res.: Space Phys.*, 110, A2
Laming J. M., 2012, *ApJ*, 744, 115
Laming J. M., 2015, *Living Rev. Sol. Phys.*, 12, 2
Laming J. M., Feldman U., 2001, *ApJ*, 546, 552
Laming J. M. et al., 2019, *ApJ*, 879, 124
Levine R. H., Altschuler M. D., Harvey J. W., 1977, *J. Geophys. Res.*, 82, 1061
McComas D. J., Ebert R. W., Elliott H. A., Goldstein B. E., Gosling J. T., Schwadron N. A., Skoug R. M., 2008, *Geophys. Res. Lett.*, 35, 18
Moses J. et al., 2020, *Nat. Astron.*, 4, 12
Ogilvie K. W., Hirshberg J., 1974, *J. Geophys. Res. Space Phys.*, 79, 4595
Owens M. J., Crooker N. U., Lockwood M., 2014, *J. Geophys. Res.: Space Phys.*, 119, 36
Rakowski C. E., Laming J. M., 2012, *ApJ*, 754, 65

Wang Y. M., Sheeley N. R. J., 1990, *ApJ*, 355, 726

SUPPORTING INFORMATION

Supplementary data are available at [MNRASL](https://www.mnrasl.org) online.

Table S1 Linear fit parameters between the delay and velocity for different A_{He} limits: The limit of A_{He} is varied from 4 per cent to 10 per cent and the corresponding delays are estimated.

Please note: Oxford University Press is not responsible for the content or functionality of any supporting materials supplied by the authors. Any queries (other than missing material) should be directed to the corresponding author for the article.

This paper has been typeset from a $\text{\TeX}/\text{\LaTeX}$ file prepared by the author.

Table 1: **Linear fit parameters between the delay and velocity for different A_{He} limits:** The limit of A_{He} is varied from 4% to 10% and the corresponding delays are estimated. The A_{He} limit of 10% means all the A_{He} data upto $A_{He} = 10\%$ are considered. The linear fit parameters are stated in the table. The fit parameters include slope (m), intercept (c) and the goodness of fit coefficient (R^2). The rows corresponding to the slope in each cycle are marked in bold fonts. It is found that the slopes remain consistently higher (close to 1 or more) in cycle 21 and 22 and consistently lower (highest value of slope is 0.64 at $A_{He} = 5\%$) in cycle 24 for all values of A_{He} .

SC	Modelled parameters	A_{He} limit						
		4%	5%	6%	7%	8%	9%	10%
21	m	1.85	1.12	1.34	1.58	1.35	1.11	0.92
	c	-508.24	-56.89	-157.70	-285.37	-262.95	-143.45	94.93
	R^2	0.39	0.22	0.42	0.54	0.61	0.61	0.40
22	m	2.06	2.22	2.04	1.69	1.27	1.08	1.04
	c	-671.54	-756.51	-688.91	-543.61	-389.24	-310.99	-309.99
	R^2	0.75	0.0.84	0.82	0.64	0.86	0.85	0.89
23	m	0.99	1.90	1.66	1.95	0.60	0.30	0.30
	c	-153.54	-498.31	-419.18	-531.84	-28.42	78.65	47.21
	R^2	0.56	0.97	0.75	0.94	0.35	0.16	0.24
24	m	0.35	0.64	0.62	0.55	0.43	0.32	0.36
	c	55.19	-54.05	-50.91	-22.36	16.14	56.87	37.61
	R^2	0.21	0.81	0.69	0.50	0.63	0.41	0.63

A holistic approach to understand helium enrichment in interplanetary coronal mass ejections: new insights

Yogesh^{1,2}*, D. Chakrabarty¹ and N. Srivastava³

¹Physical Research Laboratory, Navrangpura, Ahmedabad 380009, India

²Indian Institute of Technology-Gandhinagar, Gandhinagar 382055, India

³Udaipur Solar Observatory, Physical Research Laboratory, Udaipur 313001, India

Accepted 2022 April 13. Received 2022 April 4; in original form 2022 February 3

ABSTRACT

Despite helium abundance ($A_{\text{He}} = n_{\text{H}}/n_{\text{He}}$) being ~ 8 per cent at the solar photospheric/chromospheric heights, A_{He} can be found to exceed 8 per cent in interplanetary coronal mass ejections (ICMEs) on many occasions. Although various factors like interplanetary shocks, chromospheric evaporation, and ‘sludge removal’ have been separately invoked in the past to address the A_{He} enhancements in ICMEs, none of these processes could explain the variability of A_{He} in ICMEs comprehensively. Based on an extensive analysis of 275 ICME events, we show that there is a solar activity variation of ICME averaged A_{He} values. We also found that the first ionization potential effect and localized coronal heating due to magnetic reconnection are not the major contributing factors for A_{He} enhancements in ICMEs. Investigation on concurrent solar flares and ICME events for 63 cases reveals that chromospheric evaporation in tandem with gravitational settling determines the A_{He} enhancements and variabilities beyond 8 per cent in ICMEs. While chromospheric evaporation releases the helium from chromosphere into the corona, the gravitationally settled helium is thrown out during the ICMEs. We show that the intensity and timing of the preceding flares from the same active region from where the CME erupts are important factors to understand the A_{He} enhancements in ICMEs.

Key words: Sun: abundances – Sun: activity – Sun: coronal mass ejections (CMEs) – Sun: flares – solar wind.

1 INTRODUCTION

The abundance of helium with respect to hydrogen, expressed as $A_{\text{He}} = n_{\text{H}}/n_{\text{He}}$ percent in general, varies significantly in different layers of the Sun. While A_{He} is ~ 8 per cent in the photosphere, it remains 4–5 per cent in the corona. On the other hand, A_{He} varies from 2 to 5 per cent in the quiet solar wind (SW) depending upon the phase of the solar activity and SW velocity (Kasper et al. 2007; Alterman & Kasper 2019; Yogesh, Chakrabarty & Srivastava 2021). Interestingly, on many occasions, A_{He} is found to increase significantly and exceed the photospheric abundance of ~ 8 per cent (Grevesse & Sauval 1998; Asplund et al. 2009) in the interplanetary coronal mass ejection (ICME) structures. This suggests that other processes are operational for the elevated A_{He} abundances in the ICME structures. The nature of these processes is poorly understood till date (Manchester et al. 2017). While elevated A_{He} is observed in many ICMEs, the absence of A_{He} enhancements is also noted in some ICMEs. This unresolved dichotomy is also intricately connected with the question of efficacy of A_{He} as one of the ICME indicators (Hirshberg, Bame & Robbins 1972; Borrini et al. 1982; Zurbuchen & Richardson 2006) in the heliosphere.

In the past, enhanced A_{He} at 1 au has been found to be associated with interplanetary (IP) shocks (e.g. Borrini et al. 1982). However, A_{He} enhancement without preceding IP shock has also been found in many cases (e.g. Fenimore 1980). Based on the high ionization temperature associated with the A_{He} enhancement events, Borrini

et al. (1982) suggested that enhanced A_{He} in the SW at 1 au indicates the arrival of plasma ejecta from the solar eruptive events. As the ejecta are thrown from the lower corona, these bring out additional loads of gravitationally settled helium (Hirshberg et al. 1970). Therefore, the ‘sludge effect’ proposed by Neugebauer & Goldstein (1997) is primarily an extension of this gravitational settling argument. Since gravitational settling is always present, it is not clear how the sludge effect can selectively enhance A_{He} in certain CMEs only. On the other hand, Fu et al. (2020) suggested an important role of chromospheric evaporation for the enhancement in A_{He} in CMEs. However, as the photospheric abundance of A_{He} is ~ 8 per cent (Grevesse & Sauval 1998), it is not clear how this process can enhance A_{He} beyond 8 per cent. Therefore, despite the important roles of the above processes being qualitatively acknowledged, the relative roles of these processes governing the variability of A_{He} enhancements, particularly beyond 8 per cent, remain elusive till date. In this work, we evaluate all these processes in totality and show that primarily chromospheric evaporation along with gravitational settling controls the variabilities of A_{He} in ICMEs.

2 DATA AND ICME SELECTION

The measurements from the Solar Wind Ion Composition Spectrometer (SWICS; Gloeckler et al. 1998) instrument onboard *Advanced Composition Explorer (ACE)* satellite are used in this study. We have used the two-hourly data of different elemental compositions and charge states here. This data set contains data from 1998 February 4 to 2011 August 21 for several elements and their charge states. On 2011 August 22, *ACE/SWICS* entered into a different state

* E-mail: yphy22@gmail.com, dipu@prl.res.in

due to hardware degradation caused by radiation-induced defects. After this incident, another approach (Shearer et al. 2014) was used to get the compositional data. A few compositional observations were possible using this indirect and modified approach. Details on the data prior to and after the change in approach can be found at <http://www.srl.caltech.edu/ACE/ASC/level2/index.html>. The one-hourly helium and hydrogen ratios are also used from the OMNI data set (King & Papitashvili 2005).

In this work, the ICME catalogue (<http://www.srl.caltech.edu/ACE/ASC/DATA/level3/icmetable2.html>) compiled by Richardson & Cane (2004, 2010) is used to select the ICME events and their arrival at the L1 point. The details regarding the selection criteria can be found in Richardson & Cane (2004). A total of 275 events have been compiled. The ICME list is classified into three different categories: (1) ICMEs with magnetic cloud (Burlaga et al. 1981) having properties like high magnetic field strength, smooth rotation in components and low beta, etc. (MC, 86 events); (2) ICMEs showing the magnetic rotation but lacking a few properties like magnetic field enhancements (referred to as partial MC, 92 events); and (3) ICME without most of the MC characteristics (termed as ejecta, 97 events). We have considered only those events for which the composition data are available for more than 6 h. Relevant details like the start and end times of the duration of passage of the ICMEs through the L1 point are given in the Richardson and Cane catalogue. For a selected ICME event, the average A_{He} between the start and end times is considered. The SOHO/LASCO CME catalogue (Gopalswamy et al. 2009, and references therein) is used to find the details on the flares associated with these CMEs and the NOAA active region identifier from where the flares erupt. The SOHO/LASCO Halo CME catalogue details can be found at <https://cdaw.gsfc.nasa.gov/CME.list/halo/halo.html>.

3 RESULTS AND DISCUSSIONS

3.1 Solar activity variation of A_{He} in ICMEs

Since A_{He} in SW varies with solar activity level (Kasper et al. 2007; Alterman & Kasper 2019; Yogesh et al. 2021), it is important to check whether the variation of A_{He} in ICMEs also shows variation with solar cycle. Solar cycle (cycles 23 and 24) variation of A_{He} during ICME events is analysed in order to address this aspect. In Fig. 1(a) (upper panel), the red and black lines depict the individual ICME averaged A_{He} and sunspot number (SSN). The lines joining red and black dots are the yearly averaged SSN and A_{He} averaged (with $\pm 1\sigma$ variations) over the ICME durations for a given year. Interestingly, the yearly ICME averaged A_{He} (varies from 1 to 6) and SSN show a good correlation ($R^2 = 0.63$) as brought out in Fig. 1(b) (lower panel). This suggests that the processes controlling the A_{He} in background SW modulate the ICME averaged A_{He} values also. Another important point that emerges from Fig. 1 is the higher value of ICME averaged A_{He} in the year 2005. An increase in the number of flare occurrence (Hudson, Fletcher & McTiernan 2014) and CME (Mishra et al. 2019) for the same duration 2004–2005 was reported earlier. This is indicative of the important role of solar flares in the A_{He} enhancement. This aspect will be exclusively taken up in a subsequent section.

3.2 Relationship of A_{He} with FIP elemental ratios, average charge states, and charge state ratios

It is, in general, observed (Zurbuchen et al. 2016) that the low-FIP (first ionization potential) elements are enhanced during the ICMEs as compared to the ambient SW. These authors suggested that

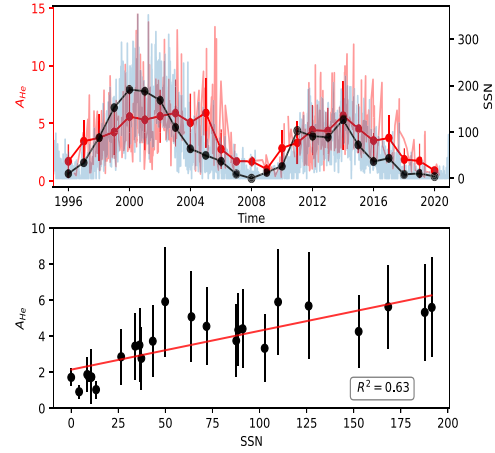


Figure 1. Solar activity variation of ICME averaged A_{He} . Panel (a): The red and black coloured lines in the background show the individual ICME averaged A_{He} and SSN. The filled red and black circles joined by lines are the yearly averaged A_{He} (with $\pm 1\sigma$ variations) and SSN for the ICME duration only. Panel (b): The correlation between the annual averaged A_{He} and SSN for the ICME duration is shown.

either FIP bias is more significant during the CME or different type of plasma is injected into the CME. Further, the magnetic energy is converted into thermal and kinetic energies through magnetic reconnection in the corona during the CME initiation process (Forbes et al. 2006; Wimmer-Schweingruber et al. 2006) and the flares associated with these events. The charge states and the charge state ratios get frozen in the corona and the CME throws out these plasma from the corona into the SW (Gruesbeck et al. 2011; Gruesbeck, Lepri & Zurbuchen 2012). Therefore, it is worthwhile to evaluate the relationship of A_{He} with FIP elemental ratios, average charge states, and charge state ratios.

We thus tested the relationship of A_{He} with different FIP proxies (like Mg/O, Fe/O, Si/O, C/O, Ne/O, and He/O) for background SW, ejecta, partial MC, and MC varieties of ICMEs. As the FIPs of Mg, Fe, Si, C, Ne, He, and O are 7.65, 7.9, 8.2, 11.3, 21.6, 24.6, and 13.6 eV, respectively, the correlation results of Mg/O, Fe/O, Si/O, C/O, Ne/O, and He/O with respect to A_{He} for the four categories (ambient SW, ejecta, partial MC, and MC) are summarized from top to bottom in Table 1. The corresponding plots are provided as supplementary Fig. S1. Two types of correlation coefficients are considered. One is the linear correlation coefficient (CC – parametrized by the coefficient of determination, R^2) and the other is the Spearman's correlation coefficient (SpCC). It is noted that the FIP proxies are uncorrelated with A_{He} in the ambient SW. However, with the exception of He/O and C/O, R^2 improves for the MC category compared to the non-MC category. It is also noted that SpCCs are higher than R^2 , indicating control of processes other than FIP. This is because SpCC is a measure of monotonic relationship and does not necessarily imply a linear relationship. As we show later, A_{He} is additionally controlled by gravitational settling unlike other proxies and therefore certain degree of non-linearity can be expected between A_{He} and other proxies.

In the intermediate section of Table 1, we have tabulated the linear correlation coefficients (CC parametrized as R^2), and SpCC between the average charge state of C, O, Mg, Si, Fe, and A_{He} , respectively. The corresponding plots are provided as supplementary Fig. S2. A few important points can be inferred in this case. First, R^2 is

Table 1. The results from the detailed correlation analysis of A_{He} with FIP elemental ratios, average charge states, and charge state ratios. Linear correlation coefficient (CC – parametrized by the coefficient of determination, R^2) and the Spearman's correlation coefficients (Sp CC) are calculated and tabulated for ambient SW, ejecta, partial MC as well as MC. The corresponding figures are provided as supplementary materials. The correlation of A_{He} in ICME is non-existent for ambient SW and maximum for MC.

	Ambient SW (184)		Ejecta (97)		Partial MC (92)		MC (86)	
	FIP proxies							
	CC	Sp CC	CC	Sp CC	CC	Sp CC	CC	Sp CC
Mg/O	0.06	-0.29	0.05	0.27	0.19	0.35	0.32	0.54
Fe/O	0.03	0.12	0.13	0.40	0.23	0.35	0.33	0.56
Si/O	0.00	-0.01	0.06	0.32	0.15	0.33	0.32	0.56
C/O	0.08	-0.28	0.26	-0.57	0.12	-0.38	0.07	-0.26
Ne/O	0.03	-0.22	0.20	0.52	0.31	0.49	0.42	0.58
He/O	0.12	0.36	0.02	0.13	0.09	0.30	0.15	0.39
	Average charge states							
	CC	Sp CC	CC	Sp CC	CC	Sp CC	CC	Sp CC
Q_C	0.01	0.08	0.02	-0.15	0.02	0.08	0.00	0.00
Q_O	0.07	0.20	0.19	0.51	0.34	0.56	0.32	0.57
Q_{Mg}	0.11	0.33	0.28	0.63	0.42	0.65	0.35	0.57
Q_{Si}	0.05	0.21	0.29	0.58	0.44	0.66	0.42	0.65
Q_{Fe}	0.05	0.22	0.26	0.56	0.44	0.62	0.36	0.61
	Charge state ratios							
	CC	Sp CC	CC	Sp CC	CC	Sp CC	CC	Sp CC
C^{+6}/C^{+4}	0.01	0.07	0.00	0.00	0.05	0.25	0.03	0.17
C^{+6}/C^{+5}	0.01	0.06	0.01	-0.08	0.04	0.15	0.02	0.12
O^{+7}/O^{+6}	0.06	0.19	0.21	0.57	0.31	0.60	0.39	0.63

significantly less for the ambient SW. Secondly, the R^2 values are significantly higher for ejecta, partial MC, and MC as compared to ambient SW for Q_{Si} , Q_{Fe} , Q_{Mg} , and Q_O but nearly zero for Q_C . Thirdly, R^2 values for ejecta are less than their MC and partial MC counterparts. The increased R^2 for MC categories (partial and full) compared to ejecta and ambient SW suggests modification in A_{He} by localized coronal heating associated with magnetic reconnection processes. This is because R^2 can increase from an improved linear relationship between A_{He} and averaged charge state proxies. Since average charge state proxies are dependent on localized coronal heating, the increased R^2 may suggest modification in A_{He} by localized coronal heating. However, as Sp CCs are more than CC values, factors other than localized coronal heating for the A_{He} enhancements in ICMEs assume importance.

In order to further explore the role of localized coronal heating for the A_{He} enhancements during ICMEs, CC and Sp CC between the charge state ratios of C, O, and A_{He} are explored. This is also captured in Table 1 and the plots are provided as supplementary Fig. S3. Similar to previous cases, we again find that negligible correlations exist between the charge state ratios and A_{He} for the ambient SW. In addition, the number density of carbon charge states (C^{+6}/C^{+4} and C^{+6}/C^{+5}) also does not show a significant correlation with A_{He} . However, the oxygen charge states, O^{+7}/O^{+6} , show much higher correlations with A_{He} , particularly for MC. Similar to what has been noted earlier, the Sp CCs are higher than CCs for ejecta, partial MC, and MC in the case of O^{+7}/O^{+6} . This indicates contributions from factors other than localized coronal heating for the A_{He} enhancements in ICMEs.

One way to verify these results is to perform tests on similar proxies and check if the correlation coefficients increase significantly. Following this line of thinking, we found very high correlation coefficients ($R^2 = 0.67$) between Mg/O and Fe/O as well as Si/O

and Fe/O ($R^2 = 0.80$) in the case of MC. Note that Mg, Si, and Fe have FIPs less than 10 eV. Therefore, the Mg/O, Si/O, and Fe/O are expected to get enhanced due to the FIP effect (Laming 2015). In addition, the CC values are also found to be closer to Sp CC as one considers ICMEs. These results are also provided as supplementary Fig. S4. This exercise suggests that if the underlying process is identical (in this case, FIP effect), one can expect significantly higher correlations. We can deduce that because A_{He} is dependent not only on FIP but on multiple processes (discussed in ensuing sections), its correlation with proxies that primarily depend on one process (e.g. Mg/O fractionation primarily depends on FIP) is expected to be poorer than correlation between proxies dependent on identical processes (e.g. Mg/O and Fe/O). One can see Table 1 in favour of this argument. Further, it is possible that CC is higher for MC (Table 1) because the MCs offer well-defined flux ropes to be intercepted by the *in-situ* S/C, while partial MC or ejecta may be a consequence of flank encounters with the S/C and thus all the properties of the ICMEs (MC) are not captured efficiently, leading to relatively poor correlation.

Based on these arguments, we infer that the processes like localized coronal heating that determine the average charge states and charge state ratios or the FIP effect in the chromosphere may contribute to the processes that determine A_{He} in ICMEs up to a certain degree. The enhanced Sp CC (compared to the linear CC) strongly suggests the presence of non-linear contribution from other processes.

3.3 Chromospheric evaporation and sludge effect

Recently, it has been suggested by Fu et al. (2020) that the chromospheric evaporation associated with a flare can alter the A_{He} values. Interestingly, the thermal energy release during a flare can influence the charge states as well as the frozen-in signatures.

Therefore, we evaluate the relationship between the occurrence of flares and observed A_{He} enhancements in associated ICMEs. The number of flares associated with each active region is considered along with the strength of the flares during the course of the CME development. The information on the associated flare and source active region of this flare for each CME is available for 63 cases. Out of these 63 cases, 17 cases are associated with X-class flares, 29 with M-class, 16 with C-class, and 1 with B-class flare. We find that 88 per cent (15/17) of the ICMEs associated with X-class flares show A_{He} enhancement at the L1 point for at least an hour. The corresponding numbers for ICMEs with M- and C-class flares are ~ 76 per cent and 50 per cent, respectively. Also, the MCs have highest probability (21/27 ~ 78 per cent) of A_{He} enhancement as compared to partial MC (16/22 ~ 73 per cent) and ejecta (9/14 ~ 64 per cent) for the 63 ICMEs. In totality, 46 out of 63 ICME events (~ 73 per cent) show $A_{\text{He}} > 8$ per cent for at least 1 h in the presence of flares, and this number increases to 59 (~ 94 per cent) if an additional 12 h is considered beyond the ICME start and end times, respectively. As the ICME start and end times at the L1 point can differ significantly if one goes by compositional boundaries or magnetic field boundaries (Gopalswamy et al. 2013, also see the Richardson and Cane catalogue), consideration of additional 12 h takes care of the uncertainties involved in identifying the passage of ICMEs at the L1 point. Further, we have verified that if we change the duration of A_{He} enhancement from 1 to 6 h or more, the percentage of occurrence of A_{He} enhanced ICME events changes from 73 per cent (46/63) to 55.6 per cent (35/63).

Since the occurrence of A_{He} enhancement is more likely linked with the strength of the flare, we infer that stronger flares lead to stronger chromospheric evaporation contributing to the higher A_{He} enhancements. These statistical results are also provided as supplementary Table S5. However, chromospheric evaporation can enhance A_{He} only up to the chromospheric/photospheric abundance limit (8 per cent). Therefore, A_{He} values greater than 8 per cent in ICMEs at the L1 point on many occasions cannot be explained by chromospheric evaporation alone. The work by Geiss, Hirt & Leutwyler (1970) suggests that A_{He} accumulates in the chromosphere and/or in the lower corona by inefficient Coulomb drag exerted by protons on helium. This inefficient Coulomb drag is the cause behind the bulging of helium in the chromosphere and/or lower corona. More importantly, helium being heavier than hydrogen, gravitational settling (Hirshberg et al. 1970; Laming et al. 2019) contributes significantly to the piling up of helium at lower coronal heights. In fact, the large lags (of the order of 100 d) reported by Yogesh et al. (2021) strongly suggest the dominant role played by gravitational settling at lower heights. SW brings out this excess helium through CMEs mediated by a process akin to ‘sludge removal’ (Neugebauer & Goldstein 1997) or ‘cleaning out’ (Wimmer-Schweingruber et al. 2006). We here suggest that chromospheric evaporation along with the ‘cleaning out’ of the gravitationally settled helium-enriched sludge (or, to some extent settled by inefficient Coulomb drag) CMEs can contribute to the higher values of A_{He} greater than 8 per cent. However, it is obvious that this may not happen for all CMEs.

To understand when the ICME events with $A_{\text{He}} > 8$ per cent are a possibility, we divide the CME events into three classes and build up a statistical picture. This is captured in the supplementary Table S5. Under class 1, we consider the CMEs (20 events) with a nearly concurrent flare event prior to the CME and no previous flare activities from the same active region (except the concurrent one) for 12 h prior to the CME. Under class 2, we consider CMEs (20 events) with multiple flares (without additional CMEs) prior to the CME from the vicinity of the same active region. The class 3 is

for the multiple CMEs (23 events–11 active regions, on an average of two or more CMEs per active region) erupting from a single active region. One typical example of classes 1 and 2 is shown in the first (panels a and a’) and second (panels b and b’) rows of Fig. 2. The third (Figs 2c and c’) and fourth (Figs 2d and d’) rows are examples of class 3. The left-hand column (panels a–d) of Fig. 2 shows the GOES X-ray flux variation in sky blue lines for four representative cases (2014 April 2, 2014 February 12, 2001 March 28–29, and 2004 September 12–14). The green vertical dashed lines mark the flares that originated from the same active region where the CME originated. The dark blue vertical dashed lines mark the eruption times of the CMEs. The class (mentioned in rectangular boxes) of the flares that erupted just before the CME is also marked in Figs 2(a)–(d). The right-hand column of Fig. 2 (panels a’–d’) shows the variation of A_{He} in the ICMEs as measured from the L1 point for the four cases shown in the left-hand column. In Figs 2(a’–(d’), the vertical solid and dashed lines mark the start and end times of the passage of an ICME at the L1 point. Two ICMEs are marked by red and blue colours, respectively. The horizontal blue dashed lines mark the $A_{\text{He}} = 8$ per cent level. $A_{\text{He}} > 8$ per cent are considered enhancements. We observe the highest percentage (80 per cent) of A_{He} enhancement events falling under class 2. On the contrary, the class-1 events show the lowest percentage (65 per cent) of A_{He} enhancement events. Class 3 shows A_{He} enhancements in 74 per cent of the cases. Therefore, these analyses reveal that CMEs with the near-simultaneous occurrence of multiple flares from the same active region (class 2) predominantly have $A_{\text{He}} > 8$ per cent as compared to CMEs with a single flare from the nearby location (class 1). This suggests that the CMEs with higher helium abundance at the L1 point carry more helium-rich plasma from the lower coronal region released by chromospheric evaporation processes occurring during multiple flares.

To understand the effect of gravitational settling, the events shown in Figs 2(c) and (d) are chosen. These two events are selected based on the time difference between the two CMEs. The first event (Fig. 2c) has the time difference of 21.5 h (less than 1 d) between the two CMEs, whereas the second event has a time difference of 57.5 h (more than 2 d). As the gravitational settling time for helium is ~ 1.5 d (Laming et al. 2019), if the second CME erupts before the helium gets gravitationally settled, the second CME can be expected to have lesser helium abundance than the first one. We speculate that this must have happened for the case shown in Fig. 2(c’). On the contrary, if the second CME erupts sufficiently later than the first one (as in Figs 2d and d’), the helium abundance in the second CME can be more (in this case) or less depending upon the accumulation of helium. We got only two cases in our filtered data base with a time difference between CMEs of less than 1.5 d. More such cases in future will strengthen our argument. We note here that the time-scale for the gravitational settling is more than that of chromospheric evaporation (approximately less than an hour; Zurbuchen et al. 2016) and less than that of FIP bias (a few days; Zurbuchen et al. 2016). Therefore, if an intense flare (and the associated CME) occurs at an opportune time when sufficient helium has settled down, it will throw out significant helium into the ICMEs through chromospheric evaporation. Therefore, these results strongly indicate the primary role of the combined effects of chromospheric evaporation and ‘sludge removal’ for the enhanced A_{He} abundance in CMEs. Although the evidence for the combined roles of solar flare and sludge removal in A_{He} enhancement is compelling, there exists a small subset of ICMEs that do not show any A_{He} enhancement whatsoever. This class of ICMEs need separate investigations.

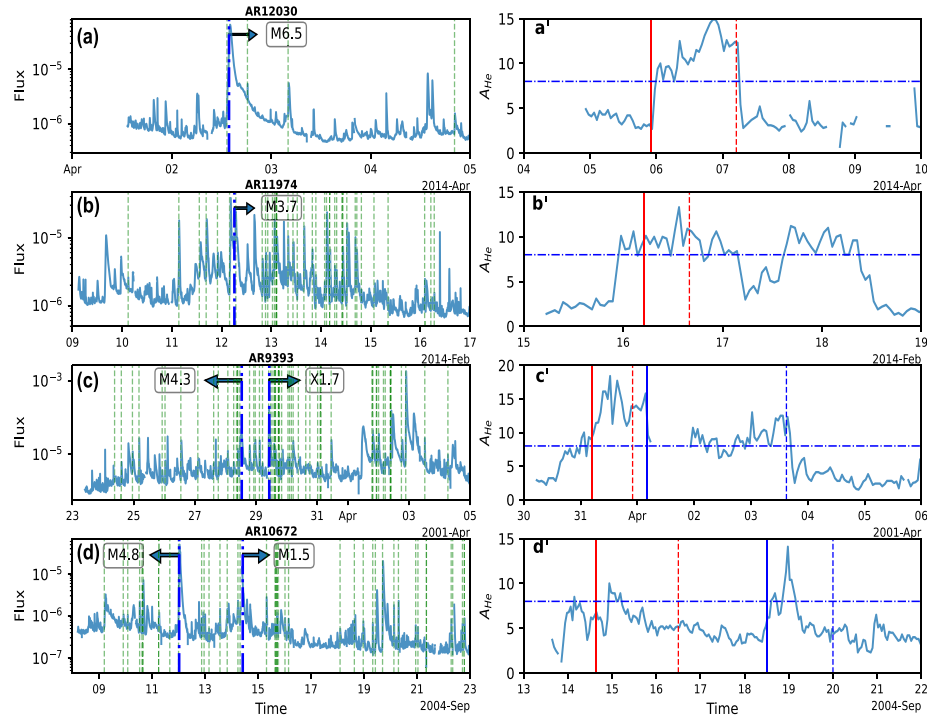


Figure 2. Solar flares and A_{He} enhancements in ICMEs. Panels (a)–(d): GOES X-ray flux variation shown by sky blue curves for four representative cases (2014 April 2, 2014 February 12, 2001 March 28–29, and 2004 September 12–14). The dark blue vertical lines indicate the CME time from the NOAA active regions from where the flares erupted. The green dashed vertical lines are the time of occurrence of flares from the same NOAA active region. The class of the flare just preceding the CME is mentioned. Panels (a')–(d'): A_{He} variation for the associated ICMEs at the L1 point. The vertical solid and dashed lines mark the start and end times of the passage of an ICME at the L1 point. Two ICMEs are marked by red and blue colours, respectively. The horizontal blue dashed lines mark the $A_{\text{He}} = 8$ per cent level. Note that $A_{\text{He}} > 8$ per cent are considered enhancements here.

4 CONCLUSIONS

This investigation shows that although solar activity variation, FIP effect, and localized coronal heating contribute in certain degrees towards A_{He} enhancements in ICMEs at the L1 point, it is the chromospheric evaporation during solar flares assisted by gravitational settling of helium that determines the enhancement of A_{He} in ICMEs. It is shown that while chromospheric evaporation is important in releasing the helium in CMEs, gravitationally settled helium thrown out of the corona during chromospheric evaporation process helps the A_{He} levels to exceed the 8 per cent photospheric/chromospheric level. It is suggested that the time constants of chromospheric evaporation and gravitational settling are important parameters to understand the A_{He} enhancement events.

ACKNOWLEDGEMENTS

We would like to thank the managing team of OMNI data set (<https://cdaweb.gsfc.nasa.gov/team.html>). We thank and acknowledge the significant efforts put forward by the principal investigators (PIs) of all the satellites, data of which are used to generate this integrated, cross-calibrated OMNI data set. We thank the PIs of SWICS (*ACE*) and ACE Science Centre for providing the *ACE* data. We acknowledge NOAA and GOES for their open data policy. We would like to thank Richardson and Cane for the ICME catalogue. This work is supported by the Department of Space, Government of India.

DATA AVAILABILITY

The solar wind data can be obtained from <https://cdaweb.gsfc.nasa.gov/index.html>. The GOES X-ray flux are obtained from <https://satdat.ngdc.noaa.gov/sem/goes/data/avg/>.

REFERENCES

- Altermann B. L., Kasper J. C., 2019, *ApJ*, 879, L6
 Asplund M., Grevesse N., Sauval A. J., Scott P., 2009, *ARA&A*, 47, 481
 Borriani G., Gosling J. T., Bame S. J., Feldman W. C., 1982, *J. Geophys. Res.*, 87, 7370
 Burlaga L., Sittler E., Mariani F., Schwenn R., 1981, *J. Geophys. Res.*, 86, 6673
 Fenimore E. E., 1980, *ApJ*, 235, 245
 Forbes T. G. et al., 2006, *Space Sci. Rev.*, 123, 251
 Fu H., Harrison R. A., Davies J. A., Xia L., Zhu X., Li B., Huang Z., Barnes D., 2020, *ApJ*, 900, L18
 Geiss J., Hirt P., Leutwyler H., 1970, *Sol. Phys.*, 12, 458
 Gloeckler G. et al., 1998, *Space Sci. Rev.*, 86, 497
 Gopalswamy N., Yashiro S., Michalek G., Stenborg G., Vourlidis A., Freeland S., Howard R., 2009, *Earth Moon Planets*, 104, 295
 Gopalswamy N., Mäkelä P., Akiyama S., Xie H., Yashiro S., Reinard A. A., 2013, *Sol. Phys.*, 284, 17
 Grevesse N., Sauval A., 1998, *Space Sci. Rev.*, 85, 161
 Gruesbeck J. R., Lepri S. T., Zurbuchen T. H., Antiochos S. K., 2011, *ApJ*, 730, 103
 Gruesbeck J. R., Lepri S. T., Zurbuchen T. H., 2012, *ApJ*, 760, 141

- Hirshberg J., Alksne A., Colburn D. S., Bame S. J., Hundhausen A. J., 1970, *J. Geophys. Res.*, 75, 1
- Hirshberg J., Bame S. J., Robbins D. E., 1972, *Sol. Phys.*, 23, 467
- Hudson H., Fletcher L., McTiernan J., 2014, *Sol. Phys.*, 289, 1341
- Kasper J. C., Stevens M. L., Lazarus A. J., Steinberg J. T., Ogilvie K. W., 2007, *ApJ*, 660, 901
- King J. H., Papitashvili N. E., 2005, *J. Geophys. Res.: Space Phys.*, 110, A02104
- Laming J. M., 2015, *Living Rev. Sol. Phys.*, 12, 2
- Laming J. M. et al., 2019, *ApJ*, 879, 124
- Manchester W., Kilpua E. K. J., Liu Y. D., Lugaz N., Riley P., Török T., Vršnak B., 2017, *Space Sci. Rev.*, 212, 1159
- Mishra W., Srivastava N., Wang Y., Mirtoshev Z., Zhang J., Liu R., 2019, *MNRAS*, 486, 4671
- Neugebauer M., Goldstein R., 1997, in Crooker N., Joselyn J. A., Feynman J., eds, *AGU Geophysical Monograph Series, vol. 99, Coronal Mass Ejections*. John Wiley & Sons, U.S., p. 245
- Richardson I. G., Cane H. V., 2004, *J. Geophys. Res.: Space Phys.*, 109, A09104
- Richardson I. G., Cane H. V., 2010, *Sol. Phys.*, 264, 189
- Shearer P., von Steiger R., Raines J. M., Lepri S. T., Thomas J. W., Gilbert J. A., Landi E., Zurbuchen T. H., 2014, *ApJ*, 789, 60
- Wimmer-Schweingruber R. F. et al., 2006, *Space Sci. Rev.*, 123, 177
- Yogesh, Chakrabarty D., Srivastava N., 2021, *MNRAS*, 503, L17
- Zurbuchen T. H., Richardson I. G., 2006, *Space Sci. Rev.*, 123, 31
- Zurbuchen T. H., Weberg M., von Steiger R., Mewaldt R. A., Lepri S. T., Antiochos S. K., 2016, *ApJ*, 826, 10

SUPPORTING INFORMATION

Supplementary data are available at [MNRASL](https://www.mnrasl.org/) online.

Figure S1. A_{He} and FIP proxies – Relationship of the FIP elemental ratios with A_{He} is explored in this figure.

Figure S2. A_{He} and charge states – Relationships of the average charge state of different elements with A_{He} are explored in this figure.

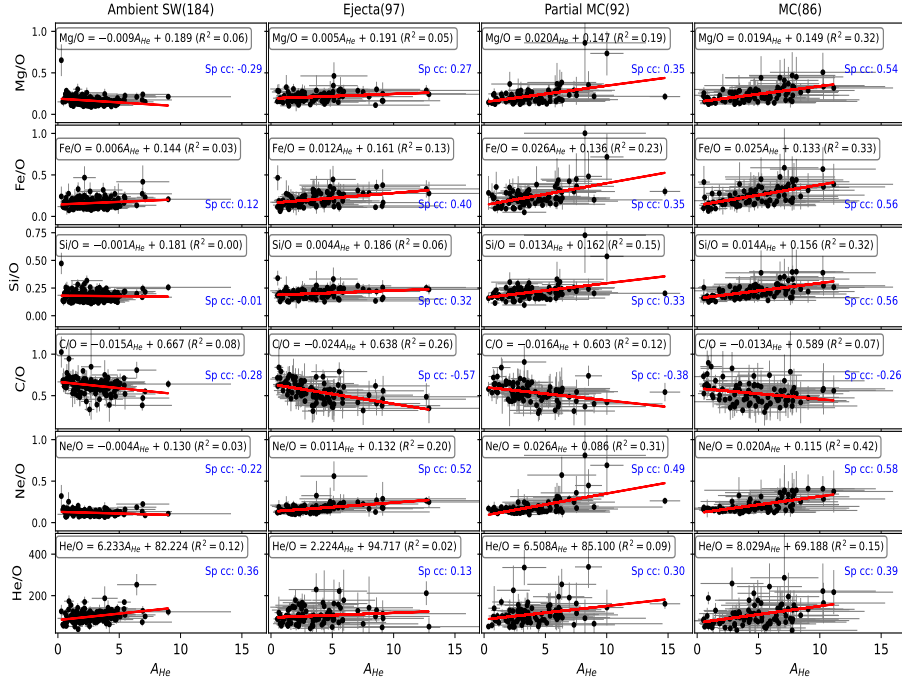
Figure S3. A_{He} and charge state ratios – Relationship of the number density ratios of the different charge states of carbon and oxygen with A_{He} is explored in this figure.

Figure S4. Correlations of Mg/O, Si/O, Ne/O, with Fe/O – Relationships of the average element abundance ratio (Mg/O, Si/O, and Ne/O) with Fe/O are explored.

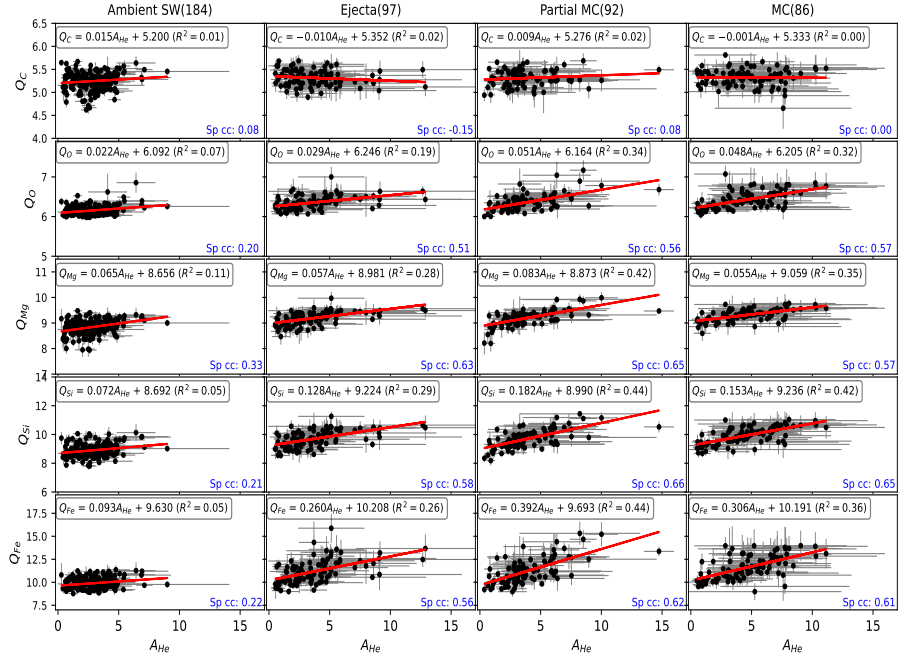
Table S5. The distribution of events according to the associated flare class (in red).

Please note: Oxford University Press is not responsible for the content or functionality of any supporting materials supplied by the authors. Any queries (other than missing material) should be directed to the corresponding author for the article.

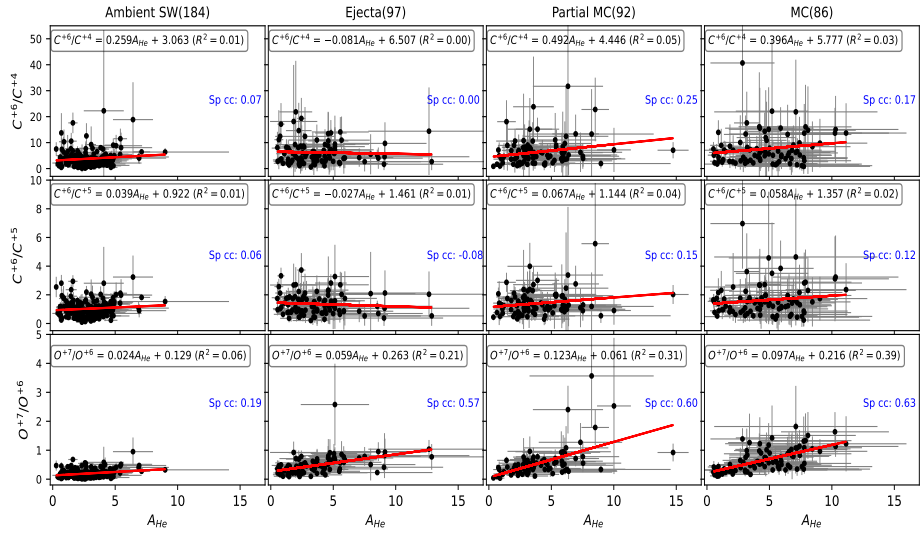
This paper has been typeset from a $\text{\TeX}/\text{\LaTeX}$ file prepared by the author.



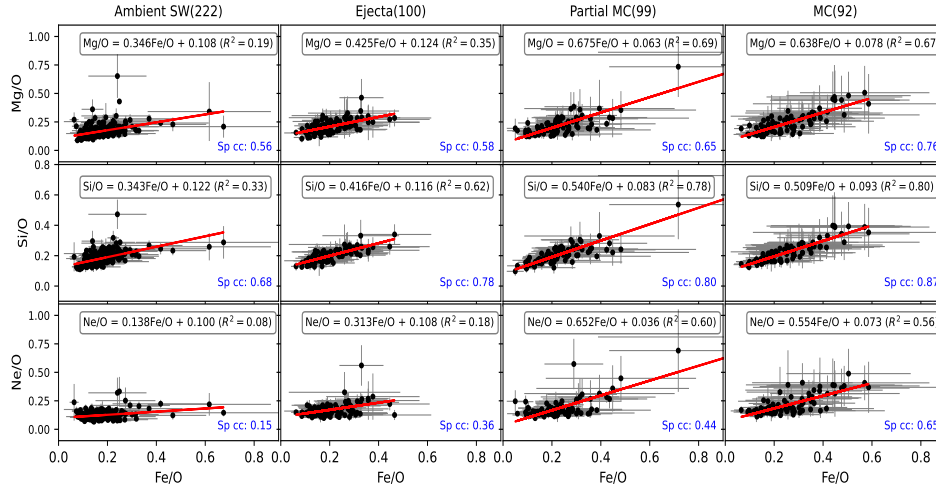
Supplementary Figure S1: A_{He} and FIP proxies - Relationship between the FIP elemental ratios with A_{He} is explored in this figure. The Mg/O, Fe/O, Si/O, C/O, Ne/O, and He/O are plotted with A_{He} in rows from top to bottom. Column 1: Ambient solar wind (184) for the duration 1998-2011, Column 2: Ejecta events (97), Column 3: partial MC events (92), Column 4: ICMEs with MC characteristics (86). The linear fits and the corresponding correlation coefficients (i.e., expressed by R^2) values are shown in each plot. Spearman's correlation coefficients (Sp. CC) are mentioned in blue color. A significant enhancement in correlation can be seen between FIP proxies and average A_{He} for the MCs except for He/O and C/O. Since O and H have similar FIP values, higher R^2 are expected for correlations of He/O and C/O with A_{He} . However, This does not happen. These results indicate FIP bias is not the major process.



Supplementary Figure S2: A_{He} and Charge States - Relationships between the average charge state of different elements with A_{He} are explored in this Figure. Average charge states of Carbon (C), Oxygen (O), Magnesium (Mg), Silicon (Si), and Iron (Fe) are shown in rows starting from the top to the bottom. Similar to Figure S2, the four columns pertain to the ambient solar wind, Ejecta, Partial MC, and MC events from left to right. Spearman's correlation coefficients (Sp. CC) are mentioned in blue color. It can be noted that except for Carbon, the other average charge states show reasonable correlations with A_{He} . This correlation enhances in MC as compared to ejectas. Higher Sp. CCs suggest significant role of processes other than localized coronal heating.



Supplementary Figure S3: - A_{He} and Charge States Ratios -Relationship between the number density ratios of the different charge states of Carbon, oxygen with A_{He} are explored in this Figure. The C^{6+}/C^{4+} , C^{6+}/C^{5+} , and O^{7+}/O^{6+} are shown in rows starting from the top to the bottom. Similar to Figures S2 and S3, the four columns pertain to the ambient solar wind, Ejecta, Partial MC, and MC events from left to right. Spearman's correlation coefficients (Sp. CC) are mentioned in blue color. Reasonable correlations can be found between O^{7+}/O^{6+} and the event-averaged A_{He} . Negligible correlation exists between the number density ratios of different charge states of Carbon, (average C^{6+}/C^{4+} and average C^{6+}/C^{5+}) and average A_{He} . In this case also, higher Sp. CCs suggest significant role of processes other than localized coronal heating.



Supplementary Figure S4: - Correlations of Mg/O, Si/O, Ne/O with Fe/O - Relationships between the average elements abundance ratio (Mg/O, Si/O, and Ne/O) with Fe/O are explored. Similar to Figures S2, S3 and S4, the four columns pertain to the ambient solar wind, Ejecta, Partial MC, and MC from left to right. Spearman's correlation coefficients (Sp. CC) are mentioned in blue color. It can be seen that all the ICME events show higher correlation coefficients (R^2) compared to the ambient solar wind. The Mg/O and Si/O show an excellent correlation with Fe/O. Also, the difference between linear CC and Sp CC are narrow down particularly for MCs and partial MCs. This probably because of the FIP effect as the First ionisation potentials are not significantly different for Mg(7.65 eV), Si (8.15), and Fe(7.9 eV). However, Ne/O shows good correlation with Fe/O in partial and full MC events. The reason behind this is not clear as the Ne (21.56 eV) is a high FIP element.

Supplementary Table S5: - The distribution of events according to the associated flare class (in red). The column shows the percentage of enhancements of A_{He} for at least one hour for ICMEs associated with different class of flares. It can be seen that chances (88%) of A_{He} enhancement are highest in CMEs associated with X-class flares. The chances of A_{He} enhancements are related to the strength of associated flares. The statistics for three classes of CMEs (described in the main text) can be seen in rows. The last column (blue color) shows the total statistics for CME classes irrespective of the associated flare-strength. The 2nd class shows the highest probability (80%) of A_{He} enhancement. This may be because of the continuous supply of He-rich material from the lower coronal heights due to continuous chromospheric evaporation caused by multiple flares. First class shows the lower probability (65%) of enhancement as single flare is connected to these CMEs. The class-3 is an intermediate class as it is based on the multiple CMEs from a single active region and not on the flare occurrence. Overall, 73% of flare-associated CMEs show enhancement.

	X	M	C	B	
Class 1	3/3 (100%)	5/6 (83.3%)	5/11 (45.5%)		13/20 (65%)
Class 2	5/5 (100%)	7/10 (70%)	3/4 (75%)	1/1 (100%)	16/20 (80%)
Class 3	7/9 (78%)	10/13 (77%)	0/1 (0%)		17/23 (74%)
	15/17 (88%)	22/29 (76%)	8/16 (50%)	1/1 (100%)	46/63 (73%)

Correction to: A holistic approach to understand helium enrichment in interplanetary coronal mass ejections: new insights

This is a correction to: Yogesh, D Chakrabarty, N Srivastava, A holistic approach to understand helium enrichment in interplanetary coronal mass ejections: new insights, *Monthly Notices of the Royal Astronomical Society: Letters*, Volume 513, Issue 1, June 2022, Pages L106–L111, <https://doi.org/10.1093/mnras/slac044>

The paper ‘A holistic approach to understand helium enrichment in interplanetary coronal mass ejections: new insights’ was published in MNRASL, 513, L106–L111. There is a typographical mistake in the paper. We have written $AHe = nH/nHe$ which is incorrect. The correct representation is $AHe = (nHe/nH) * 100$.

This paper has been typeset from a \TeX/L\AA\TeX file prepared by the author.

New insights on the behaviour of solar wind protons and alphas in the stream interaction region in solar cycle 23 and 24

Yogesh ^{1,2*} D. Chakrabarty¹ and Nandita Srivastava³

¹Physical Research Laboratory, Navrangpura, Ahmedabad 380009, India

²Indian Institute of Technology-Gandhinagar, Gandhinagar 382055, India

³Udaipur Solar Observatory, Physical Research Laboratory, Udaipur 313001, India

Accepted 2023 August 2, Received 2023 July 11; in original form 2023 April 1

ABSTRACT

Although the enhancements in the alpha–proton ratio in the solar wind (expressed as $A_{\text{He}} = N_{\alpha}/N_{\text{p}} \times 100$) in the interplanetary coronal mass ejections have been studied in the past, A_{He} enhancements at the stream interface region received very little attention so far. In this letter, by extensively analysing the stream interaction region (SIR) events observed in solar cycle 23 and 24, we show that the stream interface of alphas starts separating out from that of protons from the minimum of solar cycle 23. The population of alpha particles are enhanced compared to protons at higher angles between bulk velocity and local magnetic field (henceforth, bulk velocity angle) in the fast wind region of SIRs if the background solar wind is taken as reference. The analysis of differential velocities between alphas and protons also reveals that the faster alpha particles accumulate near the fast wind side of the stream interface region leading to enhancement of A_{He} . The investigation brings out, for the first time, the salient changes in A_{He} in SIRs for the two solar cycles and highlight the importances of bulk velocity angle and differential velocity in the fast wind region for the changes in A_{He} in SIRs.

Key words: Sun: abundances – Sun: activity – Sun: coronal mass ejections (CMEs) – Sun: heliosphere – Sun: magnetic fields – Solar wind.

1 INTRODUCTION

The stream interaction regions (SIRs) are large-scale and long lasting structures in the interplanetary (IP) medium. SIRs influence the dynamics of near-Earth solar wind properties and hence, associated space weather impact. The SIRs are formed by the interaction of high-speed solar wind stream with the preceding slow solar wind. The increase in plasma density, magnetic field strength, and plasma pressure indicate compressed plasma in the SIR. SIRs have three parts – slow-wind region, stream interface region, and fast-wind region. The stream interface (SI) is usually characterized by an abrupt drop in density, an increase in the temperature/pressure, and a change in velocity with a large gradient at 1 au (Belcher & Davis 1971; Burlaga 1974). Earlier researchers have studied the changes in solar wind plasma parameters, i.e. density, magnetic field, dynamic pressure, etc. (Richardson 2018, and references therein) associated with SIR. However, there are very few studies (e.g. Gosling et al. 1978; Āurovcova, Nemecek & Šafrankova 2019) on how SIR would alter the solar wind plasma composition in general and alpha–proton ratio (expressed as $A_{\text{He}} = N_{\alpha}/N_{\text{p}} \times 100$) in particular. This is probably because large enhancement in A_{He} in SIRs is rare unlike interplanetary coronal mass ejections (ICMEs) wherein significant enhancements in A_{He} are observed quite frequently (Richardson & Cane 2010; Fu et al. 2020; Yogesh, Chakrabarty & Srivastava 2022, etc.). Nevertheless, how A_{He} varies across the SI can be very useful in characterizing SIR structures and to evaluate their space weather impact.

It is also worthwhile to mention here that A_{He} can provide indication about the source region of the solar wind (e.g. Borrini et al. 1982; Kasper et al. 2007). It is also known that although the A_{He} is 8 per cent in the photosphere, it gets depleted in corona and solar wind and gets fixed at a 4–5 per cent level (Laming 2004). Yogesh, Chakrabarty & Srivastava (2021) showed that this scenario got changed in solar cycle 24 when A_{He} shifted towards lower values (2–3 per cent) indicating changes in the helium processing in the corona in the last cycle. Further, A_{He} varies in solar wind according to solar wind speed and the solar activity level (Kasper et al. 2007; Alterman & Kasper 2019; Yogesh et al. 2021). Usually, the fast wind shows higher A_{He} as compared to the slow wind. A_{He} values are more variable in slow solar wind, whereas it does not vary significantly in the case of fast wind. Yogesh et al. (2022) also showed that the possible interplay of chromospheric evaporation and gravitational settling determines the enhanced A_{He} level in ICMEs reported earlier (e.g. Borrini et al. 1982; Fu et al. 2020, etc.). However, very little has been reported for the A_{He} variations in SIR. It was thought earlier that changes (generally increase) in helium abundance in SIR structures are only because of the transition in the type of solar wind (Gosling et al. 1978; Wimmer-Schweingruber, von Steiger & Paerli 1997). Gosling et al. (1978) also showed that alpha flow speeds relative to protons change abruptly at the interface. Recently, Āurovcova et al. (2019) suggested that the pitch angles and velocity of alphas in the proton frame are important factors to be accounted to explain the enhancement in A_{He} in SIRs.

In this letter, we investigate a large number of SIR events spanning over solar cycle 23 and 24 (henceforth, SC23 and SC24) in the context of slow/fast wind and solar maxima/minima. This has not been attempted so far.

* E-mail: yphy22@gmail.com, dipu@prl.res.in

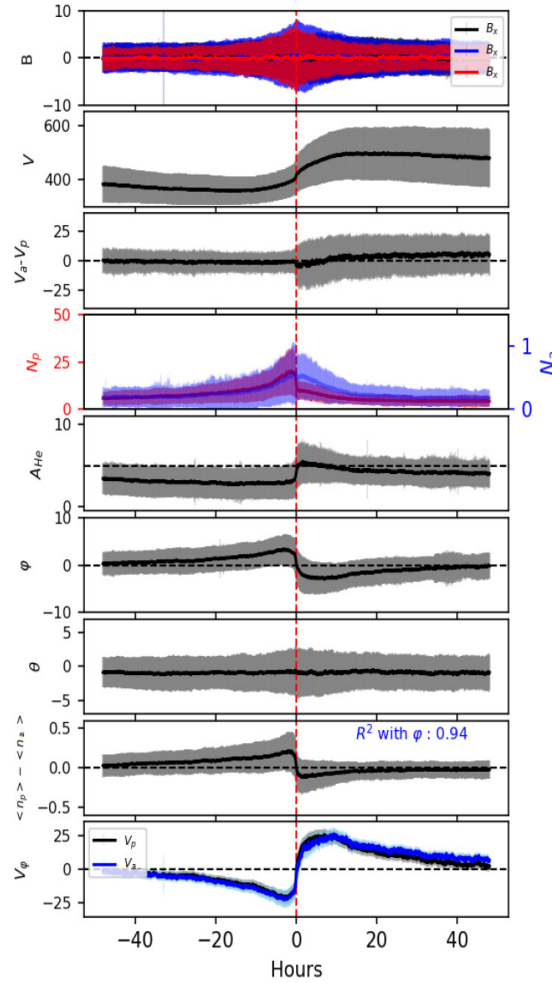


Figure 1. Superposed epoch analysis (SPA) of the 436 SIR events. The red vertical dashed line is the epoch time. The SI is chosen as the epoch time. The upper seven rows show the magnetic field components (B_x , B_y , B_z), velocity (V), the difference between the alpha and proton velocities ($V_a - V_p$), number density of alpha and proton (N_a , N_p), Helium abundance (A_{He}), East-West GSE bulk flow angle (ϕ), and North-South flow angle (θ). The row number eight shows the difference between scaled proton number density (Scaled density = $\langle N \rangle = (n - n_{min}) / (n_{max} - n_{min})$) and scaled alpha number density ($\langle N_p \rangle - \langle N_a \rangle$). The row number nine shows the East-West velocity of alphas and protons ($V_\phi(a)$, $V_\phi(p)$). The ϕ and V_ϕ are good indicators for the change in the solar wind type, i.e. from slow to the fast wind. Note, R^2 (coefficient of determination) between $\langle N_p \rangle - \langle N_a \rangle$ and ϕ is very high (more than 90 per cent). This suggests that the proton pile-up dominates slow wind, whereas the alpha pile-up dominates fast wind.

2 DATA AND SELECTION OF SIR EVENTS

For the present investigation, we have used the Solar Wind Experiment (SWE) data on board the *WIND* spacecraft (Ogilvie et al. 1995). The data set has a resolution of approximately 92 s. The magnetic field measurements are taken from the Magnetic Field Investigation experiment (Lepping et al. 1995).

The SIR events are taken from the catalogue compiled in Chi et al. (2018). The details regarding the selection of events and the start and end times of the events at the spacecraft can be found in Chi et al. (2018) and references therein. This catalogue contains 866 SIR events observed during 1995–2016. We have removed the events which do not have continuous coverage of data. The SIR events, having possible mix-up with ICMEs within one day before the start time and one day after the end time, are also removed to make sure

that only pure SIR events are considered. The ICME events are taken from the Richardson & Cane catalogue (Richardson & Cane 2010). The above criteria lead to 436 events that are used eventually for the present investigation.

We have divided the SIR events into four categories, i.e. SC23 minima (1996–1998; 2006–2009), SC23 maxima (1999–2005), SC24 minima (2010–2011; 2016), and SC24 maxima (2012–2015). Note, SIR events beyond 2016 are not available in this catalogue making the number of SIR events considered in SC24 much less compared to SC23. Nevertheless, by considering identical number of SIR events, we have verified (see supplementary Fig. S1 and compare with Fig. 4) that the scientific inferences reported in this work remain invariant. Therefore, in this work, we exploit the full available data base.

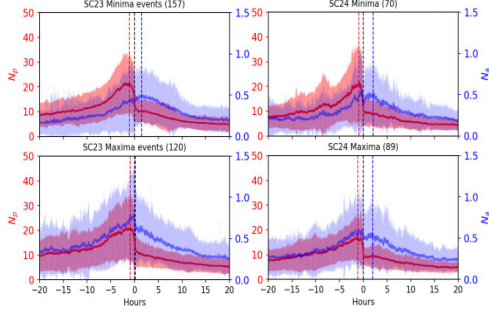


Figure 2. SPA of number densities of alphas (blue) and protons (red) in SC23 and SC24 are shown with one sigma error bar for SC23 minima, SC24 maxima, SC24 minima, and SC24 maxima. The number of events considered are also mentioned at the top of each panel. The dashed black, red, and blue vertical lines represent the SI, the peak value of proton density towards the slow wind region (SWR), and the peak value of alpha density towards the fast wind region (FWR), respectively. The additional peaks of alpha particles towards fast wind (in SC23 minimum and SC24) suggest the differential behaviour between the alphas and protons across SI.

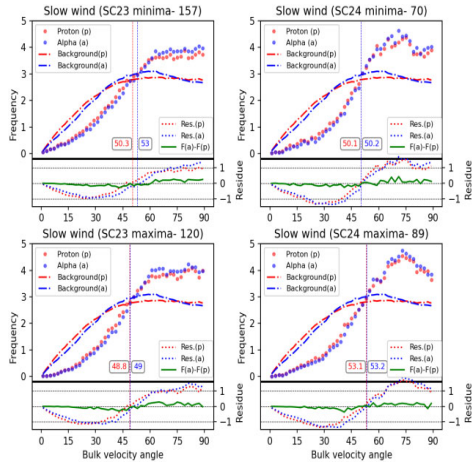


Figure 3. The bulk velocity angle distribution (BAD) for minima and maxima for SC23 and SC24 are shown only for the SWR. The red and blue colours are used for protons and alphas, respectively. The upper part of each panel shows the BAD for SWR of SIR and slow background wind. The lower part of each panel shows the difference between SIR BAD and the background slow wind. The green colour indicates the difference between alpha and proton BAD for SWR.

3 RESULTS AND DISCUSSION

3.1 Superposed epoch analysis (SPA) of the total events during solar maxima and minima

Fig. 1 shows the SPA of the SIR events used in this work. The cadence of data is changed from the 92 s to 2 min to generate the SPA outputs. The SI is the boundary between the slow and fast wind. The SPA is carried out with respect to the zero-epoch line which, in this case, is the SI. Henceforth, the slow wind side of SI will be referred to as the SWR, and the fast wind side will be described as the FWR. It can be noted from Fig. 1 that although SPA mixes together measurements from inside the SIRs with those from outside the SIRs, the characteristic changes related to SI occur mostly within

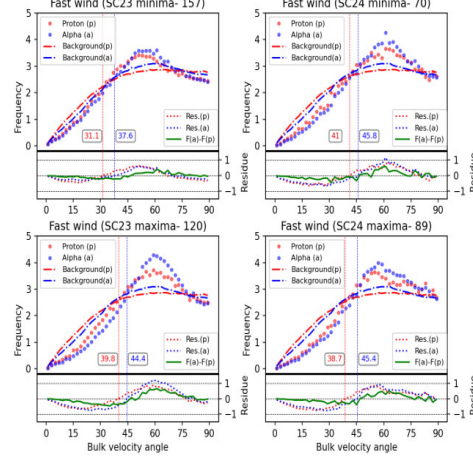


Figure 4. The BAD for minima and maxima for SC23 and SC24 are shown only for the FWR. The red and blue colours are used for protons and alphas, respectively. The upper part of each panel shows the BAD for FWR of SIR and background fast wind. The lower part of each panel shows the difference between SIR BAD and background fast wind. The green colour indicates the difference between alpha and proton BAD for FWR.

an interval of ± 10 h with respect to zero-epoch line. Note, in our investigation, the duration of 80 per cent of SIR events are more than 20 h. Therefore, we believe that results presented in this work are statistically valid.

The change in the magnetic field, number density, and velocity can be observed in the SPA (Fig. 1). The change in East–West flow angle (ϕ) is a good indicator for SI identification (Rout et al. 2017; Mayank, Vaidya & Chakrabarty 2022). An important point that emerges from this figure is that the difference between the scaled proton number density (scaled density = $\langle N \rangle = (n - n_{\min}) / (n_{\max} - n_{\min})$) and scaled alpha density show very high correlation (See Fig. 1) with the East–West flow angle (ϕ). This differential scaled density also suggests that the pile-up of protons is dominant over alphas in SWR, whereas the alphas pile-up dominates towards FWR. Therefore, it becomes apparent from the SPA that this differential pile-up is the primary cause of relative enhancement of A_{He} in the FWR of SIRs. The possible reasons for this differential pile-up and the variations in A_{He} in minima and maxima of SC23 and SC24 are taken up in the ensuing sections.

3.2 Superposed epoch analysis (SPA) of number densities of alphas and protons in SC23 and SC24

In this section, we show the SPA of the number density of alphas and protons (N_a and N_p) corresponding to maxima and minima of SC23 and SC24 (Fig. 2). The SI (dashed black line) is used as the zero-epoch time. The duration of 20 h before and 20 h after the zero-epoch time is shown. The variations in protons and alphas are shown in red and blue colour respectively, with one sigma error bar. The red and blue dashed vertical lines represent the peak value of proton number density towards SWR and the peak alpha number density towards FWR.

It can be observed from Fig. 2 that alphas have distinct additional SIs towards FWR during SC24 (both minima and maxima) and this additional SI seems to be absent in SC23. In SC23, the SI of alphas either coincides with SI of protons (maxima) or lies distinctly separated (primary SI) in the FWR region (minima). Whether it is

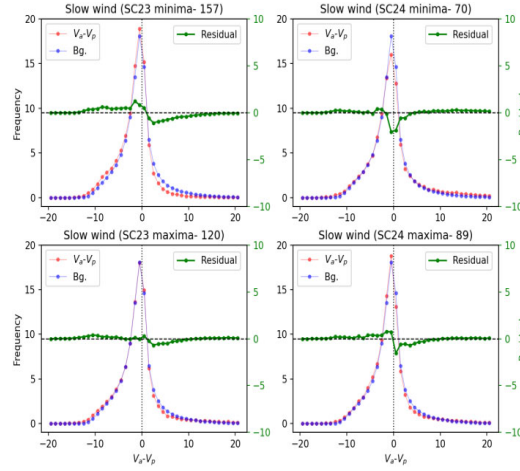


Figure 5. The distribution of differential velocity (alpha velocity–proton velocity) for minima and maxima for SC23 and 24 are shown only for the SWR. The red and blue colours are used for differential velocity distribution for the SWR in SIR and background (Bg.) slow wind, respectively. The green colour shows the difference between the SWR in SIR and the background slow wind distribution.

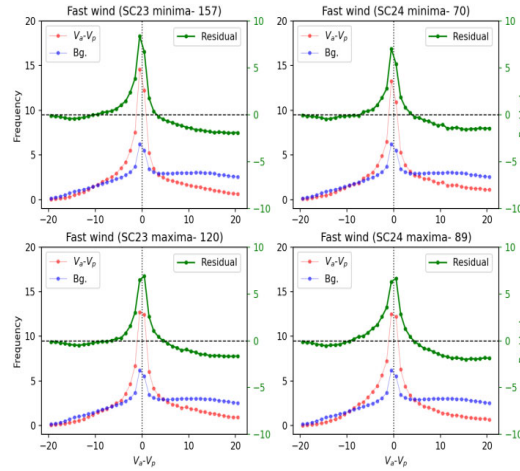


Figure 6. The distribution of differential velocity (alpha velocity–proton velocity) for minima and maxima for SC23 and 24 are shown only for the FWR. The red and blue colours are used for differential velocity distribution for the FWR of SIR and background (Bg.) fast wind, respectively. The green colour shows the difference between the FWR of SIR and background fast wind distribution.

primary or additional alpha SI, both are separated by ~ 2 h from the proton SI. Therefore, as the alpha SIs are well separated (with the exception of SC23 maxima) based on statistically significant data set, we treat these alpha SIs as real. In addition, there is no abrupt decline in the alpha number density similar to proton density across the SI. This suggests that an enhanced helium abundance can be expected in the FWR of SIRs. It is now known that SC24 is a weaker cycle and the declining solar activity could be observed from the SC23 minima (deep minimum) itself while the maximum of SC23 was relatively stronger (Hathaway 2015). Therefore, it appears that the enhanced helium abundance at the SWR of SC23 maxima is associated with the SC23 solar activity.

Đurovová et al. (2019) considered the SIRs as analogous to a magnetic mirror assembly. The important parameters which control the motion of charged particles in curved magnetic fields are the pitch angle and the velocity of ions. In this work, instead of pitch angle,

we have considered angle between bulk velocity vector and local magnetic field vector and differential velocity between alphas and protons. We have evaluated how these parameters affect the alpha and proton number density for different phases of SC23 and SC24. It can be noted from Fig. 2 that the behaviour of alphas and protons are different in the SWR and FWR of SIR. Therefore, these regions are investigated individually in the upcoming subsections.

3.3 Bulk velocity angle distribution (BAD)

We define bulk velocity angle with respect to the local magnetic field (in short, BA) for both protons and alphas and construct BAD. Note, BAD is different from pitch angle distribution or PAD as BAD deals with the angle of bulk velocity of ions with respect to the local magnetic field direction while PAD deals with the angles between the individual ion velocity with respect to the local magnetic field

direction. BA is defined as follows

$$BA = \cos^{-1}\left(\frac{\vec{B} \cdot \vec{V}}{|\vec{B}| |\vec{V}|}\right). \quad (1)$$

Here, B is the magnetic field vector and V is the bulk velocity vector. The BAD from 0° to 90° is only considered here and this is ensured by taking modulus in the denominator. This is done as the BAD between 90° to 180° is expected to be the mirror image of the BAD between 0° to 90° . To start with, we have grouped the BA data (~ 92 s cadence) from SWR and FWR of all the SIR events separately. Subsequently, a BAD is constructed by taking a bin size of 2° . Fig. 3 shows the BAD in minima and maxima of SC23 and SC24 in SWR. To understand the effect of the stream interaction, the BAD of SIRs is compared with the BAD of the background slow and fast winds in absence of SIR. Solar wind velocities less than 400 km s^{-1} and higher than 500 km s^{-1} are used to construct the references for the slow and fast background wind, respectively. The solar wind having velocities between $400\text{--}500 \text{ km s}^{-1}$ is not considered to maintain the sanctity of the references. In addition, the ICME events are also removed from the data to estimate the background references. Note the references are constructed based on data during 1996–2016 to make it consistent with the SIR catalogue. The red and blue colours are for protons and alphas, respectively.

3.3.1 Slow Wind Region (SWR)

In each panel of Fig. 3, the upper part shows the BAD (of protons and alphas) in SWR of SIR in dotted lines whereas the dotted dashed lines capture the BAD for the background wind. The dashed vertical lines show the crossover of the SWR of SIR and the background BAD. The lower part of each panel shows the difference between the BAD in SWR of SIR and background slow solar wind. The green line shows the difference or residual between the BAD of alphas and protons in the SWR of SIR.

A few important points can be noted from Fig. 3. A part of the lower BAs (before the crossover) distribution seems to have shifted towards the higher values (after the crossover). This shift seems to maximize in the maxima of the SC24. The crossover point is nearly at 50° in SC23 and SC24. The alphas and protons have similar crossover points except for SC23 minima wherein a difference of 2.7° is noticed. The SC24 maxima shows the highest shift of particles from lower BAs to higher BAs. Another important feature is that the SWR distribution shows a plateau region (lack of distinctly sharp peaks in the BAD) for both maxima and minima for higher BAs in SC23. In contrast, conspicuous peaks are noticed in the case of SWR distribution during both maxima and minima in SC24. Despite all the above features, the green line is near zero which means there is little difference between the alpha and proton BAD. Therefore, there is no significant difference between the BAD of alphas and protons in the SWR of SIR although there are higher number of protons or alpha particles for higher BAs than the background slow solar wind.

3.3.2 Fast Wind Region (FWR)

A similar analysis is also performed for FWR in SIR. Fig. 4 is analogous to Fig. 3 but with the properties of FWR and background fast wind. It can be observed from Fig. 4 that a part of particle distribution having lower BAs than the background solar wind seems to have shifted towards higher values similar to SWR. However, one difference is noticed. The BAD for FWR and background fast wind have at least two distinct crossover points unlike the slow solar wind

when only one crossover point is seen. The first crossover point is at the lower BA, whereas the second is at a very high value. The crossover BAs are nearly 40° and 45° for protons except for SC23 minima (31.1° proton and 37.6° alpha). The proton and alpha BAs crossover points have a difference of approximately 5° . The alphas have higher crossover angles, suggesting that more alpha particles are shifted towards higher BAs. Unlike SC23, the variation in the green line (in the lower panels) in this case suggests that alphas are more at higher BAs than protons. This alpha and proton distribution difference is the least in the SC23 minima. Note, SC23 is characterized by a deep minimum period (Hathaway 2015). Based on these results, it can be stated that the alphas behave differently than protons in the case of the FWR. In addition, the BA crossovers are different from those for SWR.

We have also repeated this exercise for helium ions in solar wind (proton) frame. These results are presented in supplementary figs S2 and S3. It can be seen from S2 and S3 that the alpha particles are shifted towards higher BAs in FWR whereas this feature is absent for SWR. This is consistent with Figs 3 and 4.

3.4 Distribution of differential velocity between alphas and protons in SC23 and 24

The variation in the difference between the alpha and proton velocities (differential velocity) are shown in Figs 5 and 6 for SWR and FWR in SC23 and 24 similar to Figs 3 and 4. Figs 5 and 6 show the distribution of velocity difference for SWR and FWR respectively. The red colour in both the Figures shows the differential velocity distribution for SWR and FWR for SIRs. The blue colour indicates the distribution for the background differential velocity. The green colour is the difference between the two distributions, i.e. differential velocity distribution for SIR and background velocity. It can be observed from Fig. 5 that there is hardly any difference in the distribution for SWR in SIR and in the background solar wind barring slight differences at the distribution centre ($V_a - V_p = 0$).

The FWR distribution for differential velocity shows significant changes than the SWR distribution. The background distribution shows relatively enhanced tails towards the positive side because of the fact that alphas have higher velocity than protons in the background fast wind. Or in other words, velocities of alpha particles get reduced in the case of the FWR of SIRs. Therefore, the faster alpha particles are slowed down in the interaction region and accumulate near the centre ($V_a = V_p$) of the distribution. This is captured by the substantial enhancement of the residual curve in green near the centre, suggesting the accumulation of alpha particles in the proton frame. This is the primary cause of the enhanced helium towards the FWR of SIRs and it is probably consistent with additional SI found in Fig. 2. The additional SI for alphas in Fig. 2 suggests preferential accumulation of alpha particles in the FWR. The decoupling of this additional SI from the SI determined based on proton number density, compressed magnetic field at the interface, flow deflection, and temperature increase (Chi et al. 2018) suggest that these additional alpha SI is not because of mixing. If it were the case, additional SI would have been found in SWR also. Therefore, it appears that alpha particles get decoupled towards the FWR owing to differential forcing arising out of the differences in BA and velocity with respect to protons.

We also note that there is little difference in the behaviours of velocity differences in the maxima and minima of SC23 and SC24. This suggests that unlike N_a and BA, the change in the differential velocities between alphas and protons in SIRs with respect to the

background solar wind is due to primarily IP processes. This aspect will be discussed further in the next section.

3.5 Validity of magnetic mirror hypothesis

It must be mentioned that processes other than magnetic mirror may also contribute in the variation of A_{He} within SIRs. As the SPA shows distinctive changes in A_{He} around SI, the role of other processes operational within the interaction region cannot be neglected. Therefore, the finite role of diffusive shock acceleration in changing A_{He} in SIR may be hypothesized (Đurovcová et al. 2019). However, as Đurovcová et al. (2019) pointed out, changes in A_{He} are also observed for SIRs/CIRs that are not bounded by shocks. Under this scenario, the role of diffusive shock acceleration is not unambiguous. Further, the simple magnetic mirror model disregards the effects of turbulence and plasma waves in the solar wind that may be associated with the passage of SIR through IP medium. Note, propagation of SIR/CIR through IP medium can bring in non-linear effects associated with magnetic field steepening and expansion (e.g. Burlaga & F-Viñas 2004; Đurovcová et al. 2019). For an accurate description and modelling of the behaviour of helium inside SIRs, these aspects need to be considered.

3.6 Uncertainties associated with alpha particle measurements

The derived alpha parameters, in general, come with larger uncertainties than proton parameters. In addition, in the compression region, there can be significant overlap between proton and alpha velocity distribution functions. In the present work, we have considered the mean values of proton, alpha densities, and velocities without considering the 1σ (standard deviation) variations. This will not affect the inferences drawn in this paper although the exact nature of BA and differential velocity distributions will be affected. For example, if we consider $1\text{-}\sigma$ variations, the value of the crossover BA will change as well as the width of the residual curve centred around zero differential velocity will get affected.

4 SUMMARY

In this letter, we show that alphas and protons show different behaviour in the SIRs and enhancement in A_{He} occurs across the SI in the FWR. Gosling et al. (1978) suggested that the enhancement in A_{He} at the SI is caused by the difference in the type (fast or slow wind having high and low A_{He} , respectively) of solar wind. The SIRs can be considered as magnetic bottles or mirror assemblies (Đurovcová et al. 2019). It is well known that the magnetic field and the velocity of the ions play important roles in controlling the bounce motion of particles. The magnetic mirror force depends on the ions' magnetic moment, $m = mV_{\perp}^2/2B$. This force slows down the ions or the ions having a BA higher than the loss cone angle tend to have bounce-back motions. Our results suggest that alphas and protons have similar BAs in SWR, but in the case of FWR, more alpha particles are distributed towards higher BAs as compared to protons. It may be noted that the mirroring hypothesis works best when BAs (varying 0 to 90° in this case) exceed the loss cone angle. Therefore, as long as the mean loss cone angle is closer to the BA crossover shown in Figs 3 and 4, the mirroring hypothesis can be applied. The observed changes in A_{He} in SIR with respect to loss cone angle is discussed in detail in Đurovcová et al. (2019). Another aspect to be noted is that the BA crossover between SIR distribution and background distribution is similar for alpha and protons for SWR. This crossover differs by approximately 5° in the case of FWR of SIRs. This change in

distribution may play an important role in causing the enhancement of alpha particles in the FWR of SIR.

In addition to BA, solar wind velocity also plays a vital role in deciding the number density. In general, protons and alphas have similar speeds in the slow wind, whereas alphas are faster than protons in the fast wind. The alphas have a higher magnetic moment because of the higher velocity and mass. So, alpha particles experience more magnetic curvature or mirror force than protons. The implication of this higher force can be seen in Fig. 6 as the frequencies of alpha particles faster than protons are reduced in the case of FWR of SIRs. So, this difference in curvature force for alphas and proton causes a generation of the second peak of alpha particles towards FWR.

The additional important point that emerges from this work is that the SWR BAD in SC24 shows similarities with the overall FWR BAD as these show peaks at higher BAs. On the contrary, the SWR distribution in SC23 shows a plateau region at higher BAs. This probably indicates additional influence of the changes in the sources of slow solar wind in SC24 compared to SC23.

The above results reveal that the variations in helium abundance near the SI are not primarily determined by the level of solar activity. Instead, it appears that the primary factors affecting helium abundance in this region are BA and differential velocity. The solar activity can determine the level of enhancement towards SWR because it changes the background value of helium abundance in the slow solar wind. This can be observed in Fig. 2, that the level of enhancement in helium differs in SWR whereas these levels are approximately the same in the FWR region.

In a nutshell, the SWR of SIRs does not show significant changes in BA and differential velocity. This may be the primary cause behind the similar enhancement in the alphas and protons in the case of SWR. In the case of FWR, the BA and differential velocity distribution show significant differences between alphas and protons. The crossover between background distribution and the FWR distribution for alphas is at a higher angle than protons. It means that more alphas are shifted towards higher BA than protons, causing a significant enhancement in the alpha number density. This probably causes the second peak of alphas in the FWR. The differences in the BAD for SC23 (plateau) and SC24 (peak) possibly indicate additional changes in the source of slow wind during SC23 and SC24. On the contrary, the differential velocities of alphas and protons do not show any significant change in SC23 and SC24. This suggest primary role of SIR in determining the differential velocities.

ACKNOWLEDGEMENTS

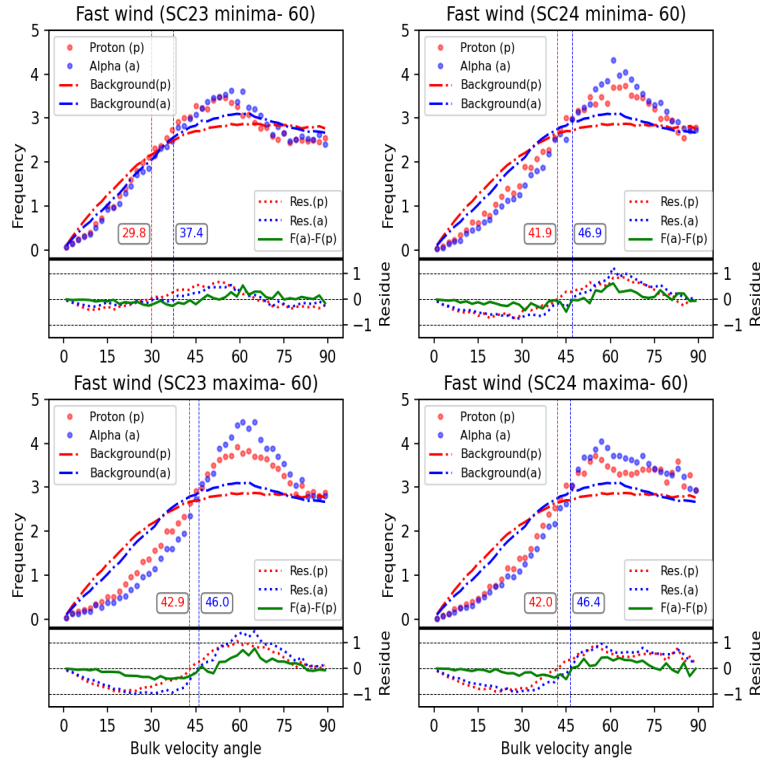
We thank the SWE (*WIND*) team for their efforts. We acknowledge Coordinated Data Analysis Web for its open data policy. This work is supported by the Department of Space, Government of India.

DATA AVAILABILITY

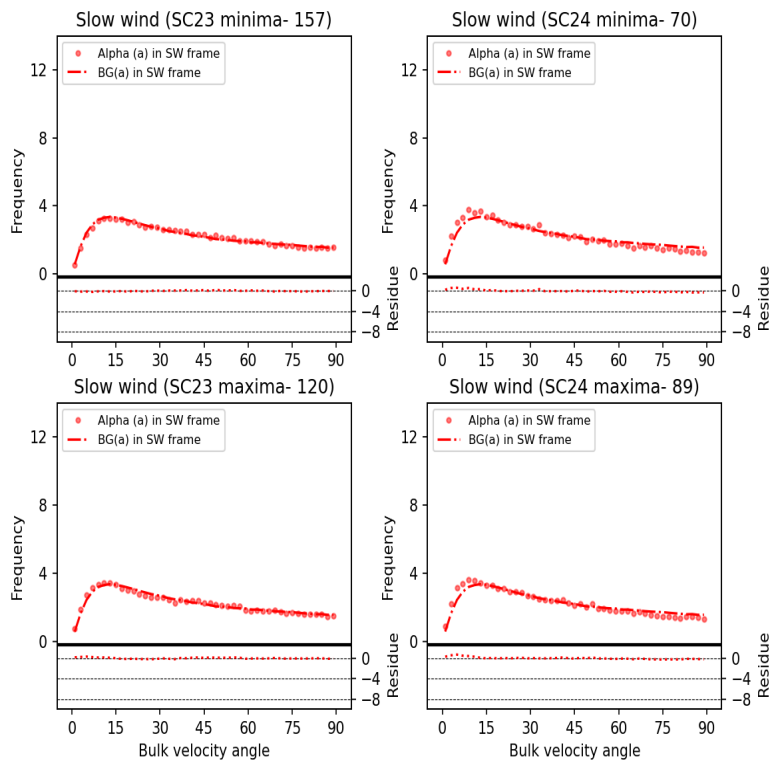
The data can be obtained from <https://cdaweb.gsfc.nasa.gov/index.html>.

REFERENCES

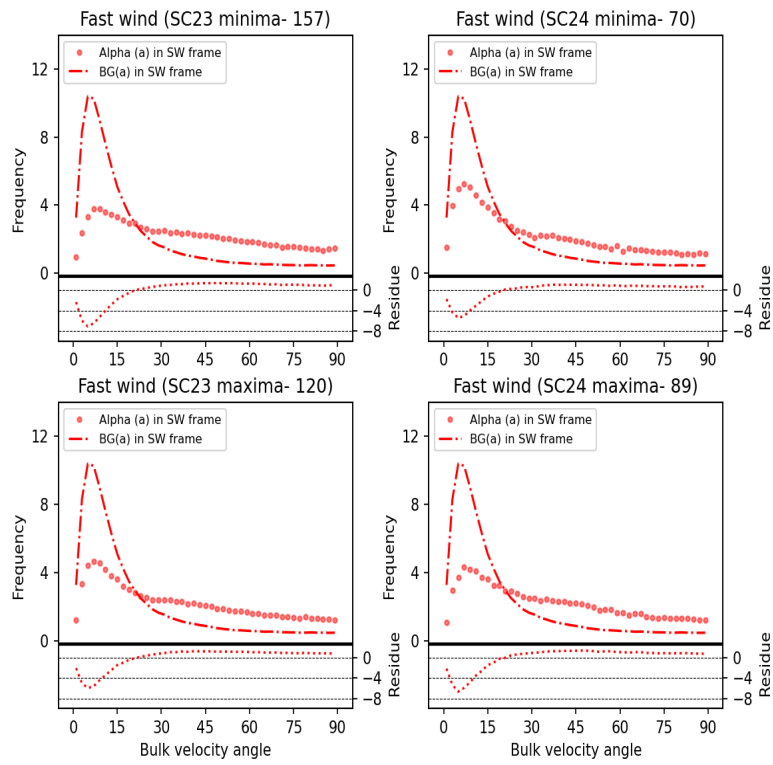
- Alterman B. L., Kasper J. C., 2019, *ApJ*, 879, L6
- Belcher J. W., Davis Leverett J., 1971, *J. Geophys. Res.*, 76, 3534
- Borini G., Gosling J. T., Bame S. J., Feldman W. C., 1982, *J. Geophys. Res.: Space Phys.*, 87, 7370
- Burlaga L. F., 1974, *J. Geophys. Res.*, 79, 3717



Supplementary Figure S1: Similar to figure 4, the Bulk velocity Angle Distribution (BAD) for minima and maxima for SC23 and 24 are shown only for the fast wind region (FWR). The number of events are taken equal (60) in maxima and minima of SC23 and SC24. The red and blue colors are used for protons and alphas, respectively. The upper part of each panel shows the BAD for FWR of SIR and background fast wind. The lower part of each panel shows the difference between SIR BAD and background fast wind. The green color indicates the difference between alpha and proton BAD for FWR. The difference in bulk velocity angle crossover point for alpha and protons can be observed. The results in this figure are almost similar to figure 4 irrespective of the change in number of events.



Supplementary Figure S2: Similar to figure 3 but in solar wind (proton) frame. The upper part of each panel shows the BAD for SWR and background slow wind. The lower part of each panel shows the difference between SWR BAD and background slow wind.



Supplementary Figure S3: Similar to figure 4 but in solar wind (proton) frame. The upper part of each panel shows the BAD for FWR and background fast wind. The lower part of each panel shows the difference between FWR BAD and background fast wind.

